# A Novel Crossed-Molecular-Beam Setup

Investigating state- and conformer-specific effects in bimolecular reactions

**Inauguraldissertation**

zur
Erlangung der Würde eines Doktors der Philosophie
vorgelegt der
Philosophisch-Naturwissenschaftlichen Fakultät
der Universität Basel

von

**Ludger Ploenes**

2022

Genehmigt von der Philosophisch-Naturwissenschaftlichen Fakultät

auf Antrag von

Prof. Dr. Stefan Willitsch, Prof. Dr. Markus Meuwly
und Prof. Dr. Piergiorgio Casavecchia

Basel, den 22. Februar 2022

Prof. Dr. Marcel Mayor

Dekan der Philosophisch - Naturwissenschaftlichen Fakultät

# Abstract

Chemical reactions are profoundly impacted by the properties of the interacting molecules, including their structure and quantum state. Crossed-beam setups have been proven to be a great tool for the investigation of such fundamental interactions occurring in bimolecular reactions under single-collision conditions. The information gained from these studies depends strongly on the experimental control which can be achieved over the reactants' properties. In recent years, tremendous progress has been made in that regard by manipulating molecules in supersonic beams with external electric and magnetic fields. However, the experimental techniques used were mainly limited to the control and manipulation of weak-field-seeking reactants.

This thesis presents the design, construction and characterisation of a novel crossed-molecular-beam setup suited for investigating bimolecular reactions of controlled strong-field-seeking molecules. The distinctive feature of the new setup is an electrostatic deflector integrated into one of the molecular beams, which exploits the interaction of polar molecules with its strongly inhomogeneous electric field. This enables the spatial separation of molecules in different rotational states as well as the selection of specific molecular conformations. This allows in particular the study of bimolecular reactions with isolated conformers, whose tendency to interconvert has provided strong experimental challenges in the past. The co-reactants to the prepared molecules are provided by a home-built discharge valve, which allows the generation of radicals and metastable-rare-gas atoms. A time-of-flight mass spectrometer allows the detection and identification of the reaction products as well as the determination of mass-specific relative integral cross sections. Differential cross sections of specific reaction products can be obtained by a mass-gated velocity-map-imaging detector.

The capabilities of the new setup are demonstrated with pioneering experiments of state- and conformationally-resolved chemi-ionisation reactions. Studying the reactive collisions of metastable neon atoms with rotational-state selected carbonyl sulfide (OCS) molecules revealed that the branching ratio between the reaction pathways resulting in the Penning ion ($OCS^+$) or the dissociative-ionisation product $S^+$ strongly depends on the initial rotational state of OCS. Also the investigation of the conformationally-resolved chemi-ionisation reaction of metastable neon with *trans*- and *cis*-hydroquinone showed a clear difference in the reactivity towards forming the Penning ion or the dissociative-ionisation products, which seems to be dependent on the initial conformational- and rotational state of hydroquinone.

The novel crossed-molecular-beam setup presented here should be applicable for the investigation of a broad range of different reactions of polyatomic molecules and by that will provide a useful tool for unravelling the fundamental details of geometry-specific effects in bimolecular reactions.

# Acknowledgments

Starting as a young PhD student of physical chemistry with an empty laboratory is both a challenging as well as a very daring task, as it demands of you to not only become an experimental scientist but first an engineer, who has to design, simulate and construct the new setup. A task which would have been impossible without the constant support and guidance of many people. As everything in science, also this project has been an immense team effort.

I am very grateful for the opportunity provided by Prof. Dr. Stefan Willitsch to be able to work on such an exciting project and for giving me enough space to develop and realise my own ideas regarding the new setup. Our constant discussions really moved this project along. I am thankful to Prof. Dr. Markus Meuwly for his refreshing comments and insights during my yearly research evaluations and to Prof. Dr. Piergiorgio Casavecchia for reviewing this thesis as the external examiner.

A sincere thank you to Prof. Dr. Jochen Küpper and his group for hosting me at DESY in Hamburg. Thank you for teaching me everything I needed to know about electrostatic deflection. Prof. Dr. Kopin Liu, the insights I gained at your laboratory in Taipei were invaluable to me and the new setup presented here greatly benefited from your experience and ideas. I will always cherish my stay in Taiwan.

I am not sure if I would have ever started a PhD-project without the mentors during my master studies. Thank you, Dr. Alix McCollam for your inspiring passion in science and Prof. Dr. Bas van de Meerakker for introducing me to the field of gas-phase collisions.

I want to acknowledge Dr. Daniel Rösch for his initial work on the Monte-Carlo simulations and Dr. Nabanita Deb for her valuable work in the lab. Dr. Hong Gao, I am very grateful for your impactful help and advice in the initial phase of constructing the new setup.

What would I have done during this time without the amazing technical support. Philipp and Grischa as well as all the apprentices, your abilities to put our often abstract ideas in finely crafted objects always amazed me. During my PhD, the workshop has always been one of my favourite places! Thank you, Georg, for all the countless hours you invested designing and building new electronic devices. Anatoly, for introducing me to the art of laser physics and Mike, for the excellent IT support. Markus, thank you for always being there when the lab was on fire or a car had crashed into our lab!

I also greatly thank Maya, Mariella and Daniela for their great and kind work in the *Administration and Human Resource* team of the physical-chemistry department.

## Acknowledgments

# Table of Contents

## Table of Contents

# 1

# Introduction

Imagine you find yourself in the woods, witnessing the amazing hustle and bustle of an ant colony. On a first glance, the collective actions might look like chaos, but after a short while it becomes apparent that everything follows clear and purposeful rules. If you would try to unravel the mysteries of the ant colony, you could proceed by observing the colony as a whole, trying to determine the overall principles which dictate the collaborative actions. The downside of this method would be that it is not sensitive to small important details, which might easily get lost or can not be observed at all while studying the colony in its entirety. Alternatively, you could focus on a single ant at a time and investigate the specific interaction of this individual with its peers. Both methods lead to valuable insights, which combined give a more comprehensive picture of the overall processes. Trying to understand the rules determining the efficient organisation of an ant colony is the scientific field of myrmecology [1].

Analogously, the matter surrounding us is build up out of atoms which combine to form molecules. Comprehending the interactions of these particles is the work of a chemist, who describes the recombination of atoms and molecules to form new products as chemical reactions [2]. Studying such reactions in thermal assemblies consisting of large numbers of atoms and molecules is an essential part of chemistry and the typical work of a chemist as often depicted by media, which excessively formulated and with a hint of irony consists out of mixing colourful liquids in Erlenmeyer flasks. Contrarily, looking at the interactions of isolated atoms and molecules is one of the core branches of chemical physics [3]. Creating an environment

---

in which such investigations are possible is a challenging task, as already the air around us consists out of numerous, fast moving particles. Therefore, the lab of a chemical physicist does usually not contain many flasks and fume hoods, but large vacuum setups which utilise physical methods such as electric and magnetic fields to isolate, control and detect single atoms and molecules. Continuously improving and rethinking these setups is a crucial task as it opens new possibilities towards studying the details of chemical reactions under single-collision conditions. Such a new setup, a novel crossed-molecular-beam apparatus specially designed for the investigation of conformational effects on chemical reactions, is described in this thesis.

The kinetics and dynamics of a chemical reaction strongly depend on the properties of the reactant molecules including their collision energy, internal quantum states, geometries as well as alignment and orientation. In the last decades, significant progress has been achieved in unravelling the details of bimolecular reactions under single-collision conditions [4, 5], notably by the development and continuous improvement of crossed-molecular-beam (CMB) experiments [6–19]. The information to be gained from such studies substantially depends on the ability to control and prepare the reactants. While in conventional molecular-beam setups the molecules are internally cooled to rotational and translational temperatures of typically a few Kelvin in supersonic gas expansions, they usually still populate a range of different quantum states and, in the case of complex species, even different molecular conformations. Reaction cross sections obtained in this way are thus averages over a range of quantum states and molecular configurations obscuring the precise influence of these degrees of freedom on chemical reactivity.

Significant progress in the control of the reactant molecules was recently achieved by utilising external electric or magnetic fields in molecular-beam experiments. Selection of individual rotational states has been achieved using electrostatic-multipole focusers [20–27]. The implementation of Stark [28–30] and Zeeman decelerators [31–35] in crossed-beam setups enabled the measurement of state-to-state scattering cross sections with unprecedented collision-energy resolution [36–40]. Moreover, the development of merged-beam experiments lead to an increased understanding of chemi-ionisation reactions of excited rare gas atoms with state-selected and even oriented atoms and molecules at very low collision energies [41–48].

All of these studies exploited the focusing effects obtained by the interaction of an inhomogeneous external field with the electric or magnetic dipole moment of molecules in weak-field seeking quantum states, i.e. states whose energy increases with increasing field strength, and focused on di- or small polyatomic systems. Of additional interest in chemistry are also larger polyatomic molecules featuring different stereoisomers.

Due to the coupling between their closely spaced rotational levels, these molecules are usually exclusively strong-field-seeking at experimentally relevant field strengths. Such strong-field-seekers are not amenable to the techniques described above because the laws of electrodynamics do not allow a maximum for static fields in free space and hence no transverse stability along the beam axis can be achieved [49–51].

For the manipulation of strong-field-seeking molecules in a beam, alternating-gradient focusers were developed which enabled the successful control of diatomic and small polyatomic molecules such as CO, YbF, CaF, $NH_3$ and OH [52–57], but also allowed for state selection and deceleration of larger species like benzonitrile [58, 59] and even spatial separation of conformers of molecules like 3-aminophenol [60, 61]. Alternatively, the selection of strong-field seeking states was achieved by microwave lens systems [62–65], while laser-based optical techniques were successfully applied for the deflection and deceleration of neutral, strong-field-seeking molecules [66–69].

A very versatile approach is the technique of electrostatic deflection which allows the separation of weak- and strong-field seeking molecules by exploiting the interaction of their effective dipole moments with static inhomogeneous fields [70–73]. This technique enabled not only the selection of individual rotational states in small systems [74–77], but also the spatial separation of individual conformers of more complex species like different aromatic compounds [60, 78, 79], 2,3-dibromo-1,3-butadiene [80], methyl vinyl ketone [81] and dipeptides [82].

This method of electrostatic deflection was successfully applied in our laboratory [83] to the study of ionic reactive collisions of conformationally selected 3-aminophenol molecules with trapped $Ca^+$ ions [84, 85] and different nuclear-spin isomers of water with $N_2H^+$ ions [86], revealing a strong dependence of the reactivity of molecules in different conformational or rotational states. Most recently, the same setup was used to investigate the cycloaddition reaction of *gauche-* and *s-trans*-2,3-dibromo-1,3-butadiene with sympathetically cooled propene ions [87], which showed that attractive long-range ion-molecule interactions resulted in an almost twofold larger rate constant for the *gauche*-compared to the *s-trans*-conformer.

This thesis reports an extension of this approach to the investigation of reactions in which all reactants are neutral and report the development of a novel crossed-molecular-beam setup featuring an electrostatic deflector. In contrast to previously reported crossed-molecular-beam setups, which are summarised in multiple reviews [10, 12–19], the new setup allows the preparation of strong-field seeking molecules in different rotational states and especially in different molecular conformations prior to the reaction. This enables the investigation of the dynamics and kinetics of a wide variety of reactions of state- and conformer-selected strong-field-seeking species with neutral reaction partners and allows for the characterisation of rotational and stereochemical

effects in a single-collision environment. The capabilities of the new setup will be demonstrated with two proof-of-principle experiments on the chemi-ionisation reaction of metastable neon atoms with rotational-state selected carbonyl sulfide (OCS) molecules and in a second reaction of metastable neon with conformer-selected hydroquinone.

The content of this dissertation is structured as follows. **Chapter** 2 provides essential theoretical background regarding the investigation of neutral bimolecular reactions under single-collision conditions in the gas-phase. The experimental setup of the novel crossed-molecular-beam is described in **Chapter** 3 together with relevant background information of the used experimental techniques as well as a thorough characterisation of key technical components. **Chapter** 4 focuses on electrostatic deflection. It starts with a theoretical description of molecules in external electric fields, which is followed by an overview of reported experimental realisations and how Monte-Carlo simulations are used to reproduce the trajectories of deflected molecules. The end of the chapter contains two experimental demonstrations on how the principle of electrostatic deflection can be used for the separation of rotational states and conformers on the example of OCS and hydroquinone, respectively. **Chapter** 5 reports measurements on the rotational-state resolved chemi-ionisation reaction of metastable neon with OCS using the new crossed-molecular-beam setup. The capability of the new setup to investigate also conformational effects in bimolecular reactions is demonstrated on the chemi-ionisation reaction of metastable neon with spatially separated *trans-* and *cis-*hydroquinone in **Chapter** 6. The dissertation is concluded by **Chapter** 7, which provides a summary of the most important aspects, contains an outlook for potential future experiments and discusses possible technical upgrades for the new setup.

# 2

# Atomic and molecular collisions in the gas phase

The purpose of the new crossed-molecular-beam setup is to probe the details of reactions in the gas-phase under single-collision conditions. This chapter aims to describe the relevant theoretical background necessary to understand the experiments performed in the context of this thesis. A detailed description of the theory of molecular collisions in the gas phase can be found e.g. in references [4] and [5]. Here only a reproducing summary of the most important aspects are given.

## 2.1 Elastic, inelastic and reactive collisions

Scattering events in the gas-phase are commonly divided into three categories. In an **elastic collision**, the total translational kinetic energy of the colliding particles remains constant throughout the collision event, while the kinetic energy of the individual collisions partners may change. Contrary, in an **inelastic collision** the total kinetic energy is not conserved, but energy is converted leading to e.g. electronical, vibrational or rotational (de)excitation of at least one of the collision participants. A **reactive collision** describes a process in which the particles after the collision are chemically distinct from the initial reactants, usually involving the formation and breaking of chemical bonds. Because the total kinetic energy is not conserved, the reactive scattering is just a special form of an inelastic scattering, but is usually classified individually due to its unique feature of resulting in chemical change [4, 5].

In principle, all three collision processes can be probed with the crossed-molecular-beam setup described here. As the experimental results described in Chapters 5 and 6 belong to reactive collisions, this chapter also focuses primarily on this category.

## 2.2 Kinematics of gas-phase collisions

Every collision process must obey the physical laws of energy and linear momentum conservation, which couple the final velocities of the reaction products to the initial velocities of the reactants [4, 5]. This section describes the scattering kinematics of two particles A and B with masses $m_{A,B}$ and velocities $\vec{v}_{A,B}$ colliding with a scattering angle $\beta$.

The total kinetic energy $E_{kin}$ of both particles is given by

$$E_{kin} = E_{kin,A} + E_{kin,B} = \frac{1}{2}m_A v_A^2 + \frac{1}{2}m_B v_B^2. \tag{2.1}$$

The behaviour of all particles during a collision process is most intuitively described in the centre-of-mass (COM) frame, in which the collision is seen from the viewpoint of an observer moving with the system's centre of mass. Its velocity $\vec{v}_{COM}$ follows from the conservation of momentum and is given by

$$\vec{v}_{COM} = \frac{m_A \vec{v}_A + m_B \vec{v}_B}{M}, \tag{2.2}$$

where M is the sum of the individual particle masses [4]. The velocities of the colliding particles in the COM-frame $\vec{u}_{A,B}$ are then defined as

$$\vec{u}_A = \vec{v}_A - \vec{v}_{COM} \quad \text{and} \quad \vec{u}_B = \vec{v}_B - \vec{v}_{COM}. \tag{2.3}$$

From the properties of the COM-system follows that the two particles collide head-on with a relative velocity $\vec{v}_{rel}$, which is the same in the COM- and laboratory frame of reference and is given by

$$\vec{v}_{rel} = \vec{v}_A - \vec{v}_B = \vec{u}_A - \vec{u}_B. \tag{2.4}$$

These definitions allow to express the total kinetic energy of the system in the COM-frame $E_{kin,COM}$, which can be expressed as [4]

$$E_{kin,COM} = \frac{1}{2}M\vec{v}_{COM}^2 + \frac{1}{2}m_{red}\vec{v}_{rel}^2, \tag{2.5}$$

with $m_{red}$ the reduced mass defined as

$$m_{red} = \frac{m_A m_B}{M}. \tag{2.6}$$

The first term in Equation (2.5) describes the kinetic energy of the moving centre of mass, which has to be conserved throughout the collision and hence can not be transferred into internal degrees of freedom of the products [4, 5]. The second term is associated with the relative motion of both particles towards each other and is available for internal excitation or to overcome energetic barriers of the reaction. It is therefore

also called the **collision energy**. For a given set of reactants the experimental collision energy can only be changed by tuning the velocity of the reactants or by adjusting the scattering angle. In the setup described here, the collision angle of the two interacting beams is fixed to $\beta = 90°$. For this special case, the collision energy $E_{\text{col}}$ can be written purely as function of the particle velocities as given by

$$E_{\text{col},90} = \frac{1}{2}m_{\text{red}}\vec{v}_{\text{rel}}^2 = \frac{1}{2}m_{\text{red}}(v_{\text{A}}^2 + v_{\text{B}}^2 - 2v_{\text{A}}v_{\text{B}}\cos(\pi/2)) = \frac{1}{2}m_{\text{red}}(v_A^2 + v_B^2). \quad (2.7)$$

Besides the collision energy and the internal energy of the reactants $E_{\text{int,reac}}$ (electronic, vibrational and rotational excitation), also the change in reaction energy $\Delta E_{\text{R}}$ has to be considered in the total energy balance of the reaction [5]. For an exothermic reaction ($\Delta E_{\text{R}} < 0$), the energy of the products is less than the combined energy of the reactants. The difference in energy is released and is available during the reaction process to contribute to the final translational and internal energy of the reaction products. Contrary, for an endothermic reaction ($\Delta E_{\text{R}} > 0$), energy is consumed by the formation of the products which is then not available during the collision process. The total available energy $E_{\text{avl}}$ of a single reaction event is then given by [4]

$$E_{\text{avl}} = E_{\text{col}} + E_{\text{int,reac}} - \Delta E_{\text{R}}. \quad (2.8)$$

The available energy directly impacts the kinetics of the reaction products as is demonstrated in the following on a few concrete examples. First, a bimolecular collision leading to two reaction products C and D is considered. Assuming that all the available energy is converted to translational motion of the final products, their post-collisional velocities are purely defined by the laws of conserved energy and linear momentum. In the COM-frame, the total linear momentum is zero, i.e. for the linear momentum of the reactants and products it has to be valid that

$$m_{\text{A}}\vec{u}_{\text{A}} + m_{\text{B}}\vec{u}_{\text{B}} = m_{\text{C}}\vec{u}_{\text{C}} + m_{\text{D}}\vec{u}_{\text{D}} = 0. \quad (2.9)$$

And the law of conserved energy dictates that

$$E_{\text{avl}} = \frac{1}{2}m_{\text{C}}\vec{u}_{\text{C}}^2 + \frac{1}{2}m_{\text{D}}\vec{u}_{\text{D}}^2. \quad (2.10)$$

Combining Equations (2.9) and (2.10) yields for the speed of product C (analogously for D)

$$u_{\text{C}} = \sqrt{\frac{2m_{\text{D}}E_{\text{avl}}}{m_{\text{C}}(m_{\text{C}} + m_{\text{D}})}}. \quad (2.11)$$

As parts of the available energy can also be used to break bonds and internally excite the products, the velocity of Equation (2.11) describes merely the maximum recoil velocity

the product can have after the collision. If the product gets internally excited during an inelastic scattering, less energy will be transferred into its translational motion. Because the internal energy levels of the products are quantised, also the reduction in kinetic energy and final velocities are quantised accordingly. The products can scatter towards all directions as long as the linear momentum is conserved, i.e. both collision products have to leave the interaction region in opposite directions. The kinematics of a bimolecular collision can be best summarised in a **Newton diagram**, which visualises the velocity vectors of all particles before and after the collision event. In such a Newton diagram, energetically possible recoil velocities of a product are represented by Newton spheres. The more energy is transferred away from translational motion, e.g. by exciting the collision products, the smaller the resulting Newton spheres. Figure 2.1 gives exemplary two-dimensional Newton diagrams for an elastic and inelastic scattering process (Fig. 2.1a) and for an endo- and exothermic reactive collision (Fig. 2.1b).
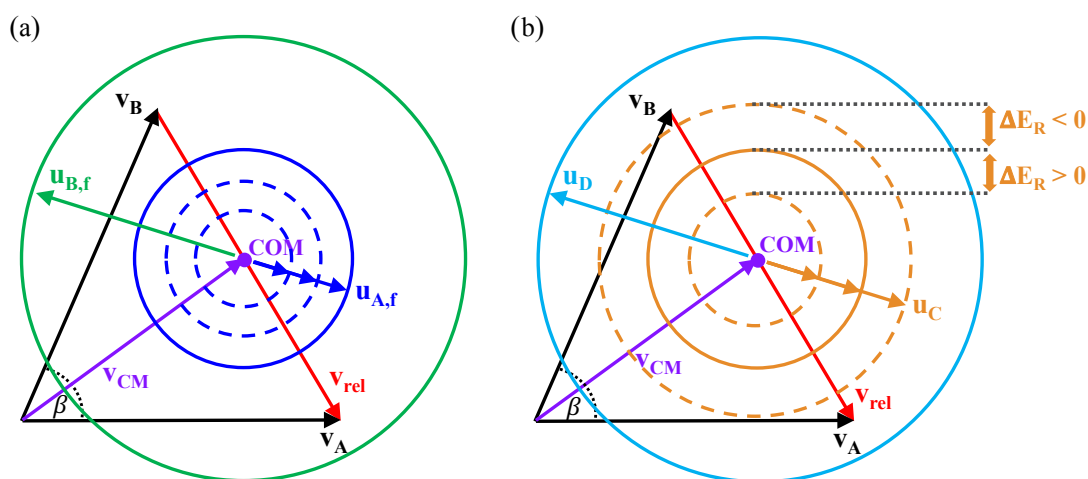


**Figure 2.1** (a) Two-dimensional Newton diagram for an elastic and inelastic scattering process of two colliding particles resulting in the same chemical species. The kinematics of an inelastic scattering is indicated for an internally excited product A by dashed circles. (b) Deviations for an exo- and endothermic reactive collision (dashed circles) from the kinetics of an elastic scattering process (solid circle). Symbols are explained in the text.

For the special case of an addition reaction for which the collision of the reactants (A,B) leads to the formation of only one stable product (C), the law of conserved linear momentum can be written as

$$m_A \vec{u}_A + m_B \vec{u}_B = m_C \vec{u}_C = 0. \tag{2.12}$$

It is obvious that product C has no net recoil velocity and hence has to travel with the system's centre of mass. This means that all energy which becomes available during the collision event ($E_{avl}$) leads to internal excitation of the formed complex. None of this energy can be transferred into translational kinetic energy as is possible when multiple reaction products are formed.

For the case that the collision results in more than 3 simultaneously formed reaction products, the conservation of energy and linear momentum are not enough to unambiguously define the recoil velocities of the products. The change in velocity and momentum of one particle can be counterbalanced by the other two particles resulting in infinite different scattering possibilities.

## 2.3 Cross sections, impact parameter and rate constant

The last section described the kinetic processes of two particles undergoing a collision in the gas phase. The probability of a collision between two approaching particles can be described by the collision cross section, which is most intuitive for two non-interacting hard spheres as schematically shown in Figure 2.2a. Two such spheres with diameters $d_A$ and $d_B$ only collide with each other when their relative separation is less than the arithmetic average of their individual diameters ($d_{AB} = (d_A + d_B)/2$), i.e. sphere A only collides with sphere B when its centre lies within the **collision cross section** $\sigma_c$ given by [5]

$$\sigma_c = \pi d_{AB}^2 = \pi \left( \frac{d_A + d_B}{2} \right)^2.$$

(2.13)

The collision cross section for all possible scattering angles is also known as the **integral cross section (ICS)** of a scattering process. The probability that a scattered particle leaves the interaction region along the solid angle $\Omega$ is given by the **differential cross section (DCS)** $\sigma_\Omega$ defined as

$$\sigma_\Omega = \frac{d\sigma_c}{d\Omega}.$$

(2.14)

Molecules and atoms do not behave like hard spheres but their interaction is governed by attractive and repulsive forces, which can lead to collision events even if their separation is larger than their physical dimensions. The perpendicular separation of two moving particles is described by the **impact parameter** $b$ which is given by the minimum separation between the intial trajectories of two particles [4, 5], as schematically

shown in Figure 2.2b.
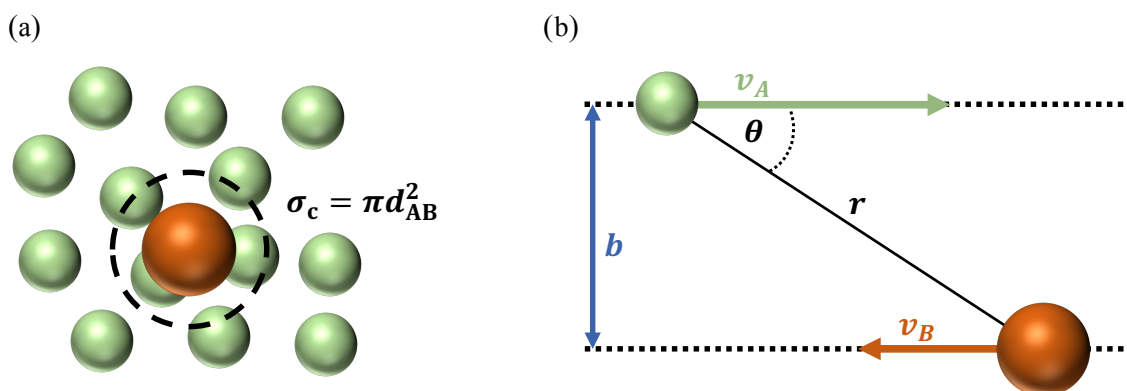


**Figure 2.2** (a) Schematic representation of the collision cross section of hard spheres moving with a relative velocity perpendicular to the image plane. A collision only occurs when the separation of the particles is smaller than their average diameter. (b) Sketch of collision geometry of two particles on trajectories separated by the impact parameter $b$ and a total distance $r$ [4,5].

The probability of the two particles reacting with each other depends on the impact parameter and is described by the opacity function P(b). The **reaction cross section** $\sigma_r$ of two particles can then be determined by integrating the opacity function over all angles and up to the maximum impact parameter $b_{max}$ for which the value of the opacity function vanishes. $\sigma_r$ is then given by [4,5]

$$\sigma_r = \int_0^{2\pi} \int_0^{b_{max}} P(b)\, b\, db\, d\Phi = 2\pi \int_0^{b_{max}} P(b)\, b\, db. \tag{2.15}$$

The probability of particles to react and hence the reaction cross section depends strongly on the velocity of the interacting particles. Therefore, to calculate the thermal rate constants $k(T)$ from the reactive cross sections of individuals reactions, the velocity distribution $f(v)$ of the particles at a given thermal temperature $T$ has to be considered. The thermal rate constant can then be determined by integrating the velocity-specific reaction cross section $\sigma_r(v)$ and the velocity distribution over all possible velocities of the sampled particles

$$k(T) = \int_0^\infty v\, f(v)\, \sigma_r(v)\, dv. \tag{2.16}$$

## 2.4 Potential energy and centrifugal barrier

The interaction of atoms and molecules is described by their **potential energy** $V(\vec{r})$, which depends on the distance and orientation of the interacting molecules. Once

the potential energy is known, the forces $\vec{F}$ acting on the particles are defined by the gradient of the potential energy. For a potential energy purely depending on the molecular distance vector $\vec{r}$, this relationship is given by

$$\vec{F}(\vec{r}) = -\vec{\nabla}V(\vec{r}). \tag{2.17}$$

The forces determine the subsequent motion of the particles and therefore fully define the dynamics of the reaction [4,5]. The potential energy of the interaction is therefore essential in understanding collision processes. The potential energy of two neutral species in the gas phase can be divided in a long-range attractive part and a short-range repulsive component. One exemplary interaction potential, which combines these two components, is the Lennard-Jones potential $V_{\mathrm{LJ}}(r)$ introduced in 1924 as

$$V_{\mathrm{LJ}}(r) = \epsilon \left( \left( \frac{r_0}{r} \right)^{12} - 2 \left( \frac{r_0}{r} \right)^{6} \right), \tag{2.18}$$

where $\epsilon$ is the well depth and $r_0$ the particle separation at the potential energy minimum [88]. The Lennard-Jones potential describes a chemical reaction proceeding without a barrier.

The orbital angular momentum introduces a barrier to the potential energy as kinetic energy has to be transferred to change the orbital motion of the particles [4,5]. This barrier is refereed to as the **centrifugal barrier**. The orbital angular momentum $L$ of two particles with relative velocity $\vec{v}_{\mathrm{rel}}$ is given by

$$|L| = |m_{\mathrm{red}}\vec{r} \times \vec{v}_{\mathrm{rel}}| = m_{\mathrm{red}}v_{\mathrm{rel}}r\sin(\theta), \tag{2.19}$$

with $\theta$ the angle between $\vec{v}_{\mathrm{rel}}$ and the distance vector $\vec{r}$ of the particles [4,5]. At long range the term $r\sin(\theta)$ becomes approximately equal to the impact parameter $b$ and the orbital angular momentum simplifies to $|L| \approx m_{\mathrm{red}}v_{\mathrm{rel}}b$. The height of the centrifugal barrier $E_{\mathrm{cent}}$ is defined by the rotational kinetic energy of the system and the total effective potential energy $V_{\mathrm{eff}}(r)$ then becomes [4,5]

$$V_{\mathrm{eff}}(r) = V(r) + E_{\mathrm{cent}} = V(r) + \frac{L^2}{2m_{\mathrm{red}}r^2} \approx V(r) + \frac{m_{\mathrm{red}}v_{\mathrm{rel}}^2 b^2}{2r^2}. \tag{2.20}$$

The centrifugal barrier increases for systems of heavy particles on trajectories with a large relative velocity and large impact parameters. Classically, only for collision energies larger than the centrifugal barrier a successful reaction can occur [4,5]. For a specific system interacting with a certain collision energy, the value of the maximum impact parameter $b_{\mathrm{max}}$ decides if a collision leads to a successful reaction event. For two particles on trajectories separated by an impact parameter larger than $b_{\mathrm{max}}$ the collision energy is not sufficient to overcome the centrifugal barrier. For the simplified

hard-sphere model, the opacity function is zero ($P(b > b_{\mathrm{max}}) = 0$) [5]. Contrary, if the particle trajectories are separated less than $b_{\mathrm{max}}$, the collision energy will exceed the centrifugal barrier allowing a successful reaction ($P(b < b_{\mathrm{max}}) = 1$) [5]. For direct head-on collisions ($b = 0$), the orbital angular momentum of the system vanishes and leads to no centrifugal barrier. The effective potential energy is then purely described by the interaction potential. These three cases are schematically illustrated in Figure 2.3.
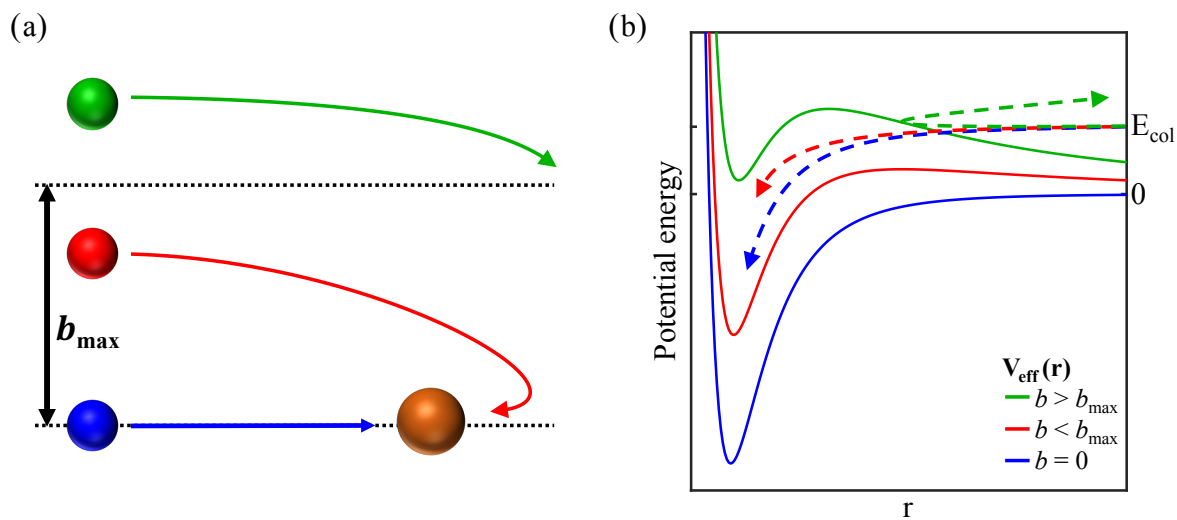


**Figure 2.3** (a) Schematic illustration of classical scattering trajectories with different impact parameters $b$ for the hard-sphere model. Blue: head-on collision with $b = 0$ ($L = 0$), red: reactive scattering with $b < b_{\mathrm{max}}$, green: non-reactive scattering with $b > b_{\mathrm{max}}$. (b) Effective potential energy based on the Lennard-Jones potential ($V_{\mathrm{eff}}(b{=}0) = V_{\mathrm{LJ}}(r)$). The centrifugal barrier increases with larger impact parameters. Only trajectories for which the collision energy $E_{\mathrm{col}}$ exceeds the height of the centrifugal barrier can lead to a successful reaction [4, 5].

## 2.5   The excitation function

The reactive cross section depends on the collision energy. This dependency is described by the **excitation function** $\sigma_{\mathrm{r}}(E_{\mathrm{col}})$ [4, 5]. So far only a barrierless interaction as, e.g. described by the Lennard-Jones potential, was considered. If the reaction proceeds via an energetic barrier of height $E_0$ for an head-on collision ($|L| = 0$) and an equilibrium distance $r_0$, a successful reaction can only occur when the collision energy exceeds the total energetic barrier of the reaction

$$E_{\mathrm{col}} - (E_0 + E_{\mathrm{cent}}) > 0. \tag{2.21}$$

For the hard-sphere model with the centrifugal energy as defined in Equation (2.20), a model excitation function can then be expressed as [5]

$$\sigma_{\mathrm{r}}(E_{\mathrm{col}}) = \pi b_{\mathrm{max}}^2 = \pi r_0^2 \left(1 - \frac{E_0}{E_{\mathrm{col}}}\right). \tag{2.22}$$

This excitation function is shown in Figure 2.4 together with the opacity function for hard spheres ($P(b < b_{\mathrm{max}}) = 1$ & $P(b > b_{\mathrm{max}}) = 0$) in the figure inset.

It has to be noted that the opacity function and hence the excitation function for interactions of atoms and molecules is more complex and depends on the specific interaction of the reaction partners. Furthermore, also quantum-mechanical tunnelling through the reaction barrier is possible, which can lead to reactions even for collision energies smaller than the barrier energy. In general, low collision energies are sensitive to the reaction barrier and the long-range attractive part of the potential, whereas high collisions energies probe the short-range repulsive part as visualised in Figure 2.4b.
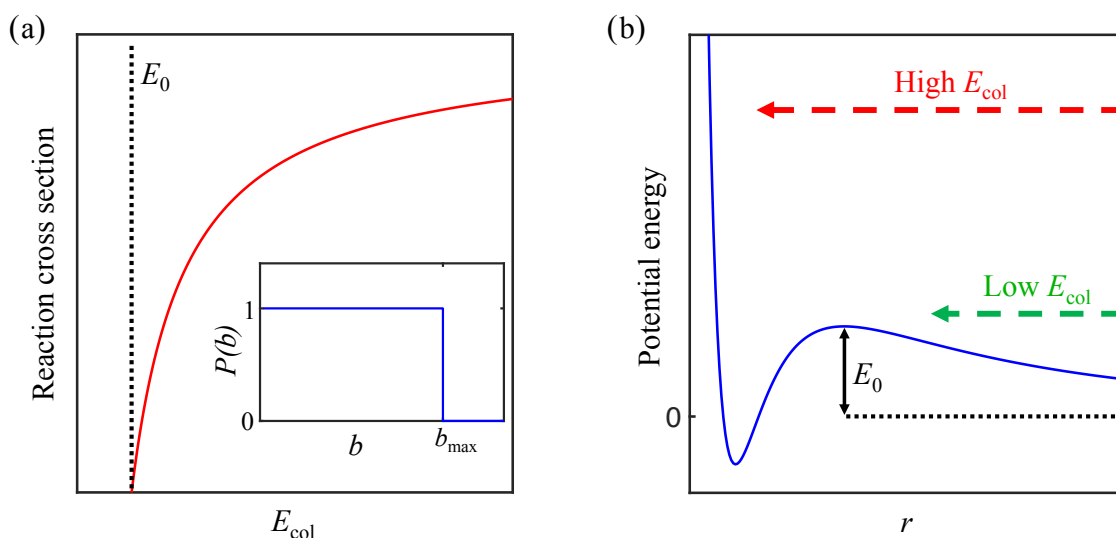


**Figure 2.4** (a) Excitation function $\sigma_{\mathrm{r}}(E_{\mathrm{col}})$ for a reaction with energetic barrier $E_0$ assuming the hard sphere model with the opacity function $P(b)$ as shown in the figure inset. (b) Differences of a collision event proceeding with a low and high collision energy $E_{\mathrm{col}}$. Low collision energies are more sensitive to the barrier and the attractive part of the potential, whereas high collision energies probe the repulsive part of the potential [4, 5].

## 2.6 Molecular reactions in the gas phase

For reactions involving atoms with molecules also the internal energy $E_{\mathrm{int}}$ of the reactants has to be considered. This is shown for the simplest case of a molecular reaction

between an atom A and a diatomic molecule BC in Figure 2.5a [4, 5]. In classical physics, the reaction can only proceed if the sum of the collision and internal energy (electronic, vibrational and rotational) exceeds the barrier height $E_{\rm b}$. If the reaction is exothermic (endothermic), the available energy $E_{\rm avl}$ for the products increases (decreases) by the reaction energy $|\Delta E_{\rm R}|$. The total available energy after the reaction is distributed among the internal $E_{\rm int}'$ and kinetic energy $E_{\rm kin}'$ of the reaction products. The total kinetic energy of the reaction has to fulfil the laws of conserved energy and linear momentum as discussed in Section 2.2. Also the total angular momentum of the system has to be conserved, i.e.

$$L + J_{\rm BC} = L' + J_{\rm AB}, \tag{2.23}$$

where the rotational angular momentum of the reactant and product molecules is denoted by $J_{\rm BC}$ and $J_{\rm AB}$ and the orbital angular momentum before and after the collision is given by $L$ and $L'$, respectively [4, 5]. If the reactants are internally cold, as it is usually the case in supersonic-beam experiments, the rotational angular momentum of the reactant molecule can be neglected ($L = L' + J_{\rm AB}$).

Figure 2.5b gives a typical potential energy along the entrance and exit channel of
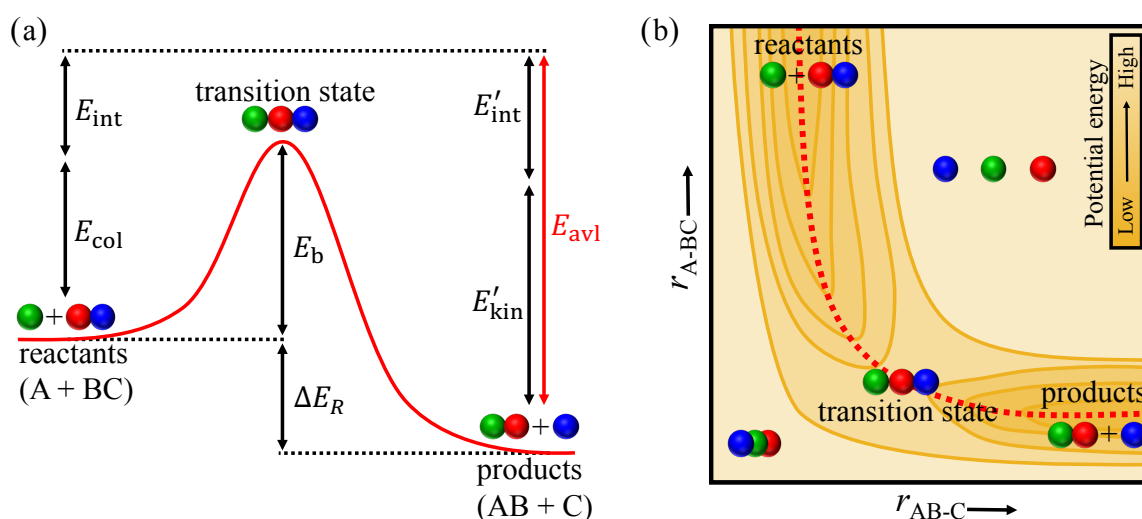


**Figure 2.5** (a) Schematic diagram of the reaction between an atom A and a diatomic molecule BC. The reaction can only proceed if enough energy is available to overcome the energetic barrier ($E_{\rm b}$) associate with the transition state of the reaction. Symbols as explained in the text. (b) Contour plot of an exemplary potential energy surface along the reaction entrance ($r_{\rm A-BC}$) and exit channel ($r_{\rm AB-C}$). The minimum energy path from the reactants along the transition state to the products is indicated by the red dashed line [4, 5].

the reaction depicted in Figure 2.5a together with the path of minimum energy from
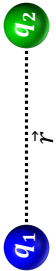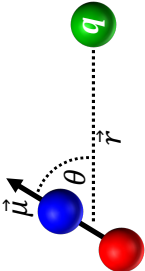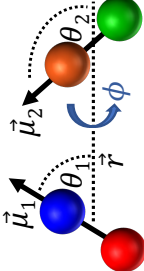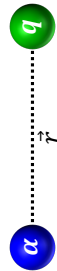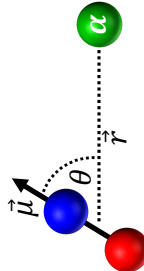
the reactants to the products (dashed red line). For the entrance channel, the intermolecular distance between A and BC ($r_{\text{A-BC}}$) decreases until the transition state at the saddle point of the potential is reached. If enough energy is available to overcome the barrier of the transition state, the reaction proceeds along the exit channel ($r_{\text{AB-C}}$) until the potential minimum associated with the reaction products is reached [4, 5]. This exemplary figure only displays the interactions as a function of the intermolecular distance of the reaction partners. As molecules have a three-dimensional structure, the interaction changes depending on the relative orientation of the reactants. The potential energy as function of all relevant coordinates is given by the **potential energy surface (PES)** of the reaction.

Crucial for describing molecular collisions in the gas phase is the potential energy which arises from charge distributions on the molecules, which give rise to long-range interactions between electrostatic multipoles [4, 5]. These interactions can roughly be divided into three categories; (i) the **electrostatic interactions** between permanent multipoles (e.g. charge, dipole moment) on both reactants, (ii) the **induced interactions** in which one reactant with a permanent multipole induces a temporary multipole in the other reactant and (iii) the **dispersion interaction** [89]. The dispersion interaction arises from temporary multipoles caused by charge fluctuations on one reactant which introduces a weakly induced multiple on the co-reactant leading to a weak, long-range coupling. All these interactions can be described analytically by a potential energy $V_{\text{multipole}}(r)$ of the form

$$V_{\text{multipole}}(r) = \frac{a}{r^n}. \tag{2.24}$$

The exponent $n$ determines the order of the attraction and depends on the character of the coupling. The numerator term $a$ describes the multipole interaction based on the properties of the particles such as their charges $q$, permanent dipole moments $\mu$ and polarisabilities $\alpha$. For quantities which are vectors, e.g. the permanent dipole moment, the interaction strongly depends on the relative orientation of the reactants and the term $a$ has to be expressed as function of the orientation angle $\theta$ between the quantity vector and the atom-molecule axis [89]. Table 2.1 gives the electrostatic and induced interaction terms of different multipoles in vacuum ($\epsilon = \epsilon_0$) [89]. The table gives both the interaction energies associated with a static orientation of the reactants as well as the thermally averaged energies over all orientations for rotating molecules. If one of the reactants does not feature a certain multipole, the corresponding term vanishes. E.g. for a complete neutral reaction all terms containing a particle charge are zero and the interaction is dominated by higher-order multipole moments.

**Table 2.1** Potential energy terms of permanent and induced multipoles [89]

| Interaction type | Static orientated | Thermally averaged |
|---|---|---|
| Charge - charge | $V(r) = \dfrac{q_1 q_1}{4\pi\epsilon_0}\dfrac{1}{r}$ | $V(r) = \dfrac{q_1 q_1}{4\pi\epsilon_0}\dfrac{1}{r}$ |
| Charge - dipole | $V(r,\theta) = -\dfrac{q\mu\cos(\theta)}{4\pi\epsilon_0}\dfrac{1}{r^2}$ | $V(r) = -\dfrac{q^2\mu^2}{6(4\pi\epsilon_0)^2 k_{\mathrm{B}T}}\dfrac{1}{r^4}$ |
| Dipole - dipole | $V(r,\theta_1,\theta_2,\phi) = -\dfrac{\mu_1\mu_2(2\cos(\theta_1)\cos(\theta_2) - \sin(\theta_1)\sin(\theta_1)\cos(\phi))}{4\pi\epsilon_0}\dfrac{1}{r^3}$ | $V(r) = -\dfrac{2}{3}\dfrac{\mu_1\mu_2}{(4\pi\epsilon_0)^2 k_{\mathrm{B}T}}\dfrac{1}{r^6}$ |
| Charge - induced dipole | $V(r) = \dfrac{q^2\alpha}{(4\pi\epsilon_0)^2}\dfrac{1}{r^4}$ | $V(r) = \dfrac{q^2\alpha}{(4\pi\epsilon_0)^2}\dfrac{1}{r^4}$ |
| Dipole - induced dipole | $V(r,\theta) = \dfrac{\mu^2\alpha(3\cos(\theta)^2 + 1)}{2(4\pi\epsilon_0)^2}\dfrac{1}{r^6}$ | $V(r) = \dfrac{\mu^2\alpha}{(4\pi\epsilon_0)^2}\dfrac{1}{r^6}$ |

The most important contribution to the dispersion interaction is the mutual induction of dipole moments described by the London relation $V_{\mathrm{London}}$ given by

$$V_{\mathrm{London}}(r) = -\frac{3\alpha_1'\alpha_2'}{2}\frac{E_{\mathrm{ion},1}E_{\mathrm{ion},2}}{E_{\mathrm{ion},1} + E_{\mathrm{ion},2}}\frac{1}{r^6}, \tag{2.25}$$

where $E_{\mathrm{ion},1}$ and $E_{\mathrm{ion},2}$ are the ionisation energies of the two interacting particles [90]. The dispersion energy is also often referred to as the **van-der-Waals (vdW) interaction**. The thermally averaged dipole-dipole interaction, the dipole-induced dipole term and the dispersion energy scale with the inverse sixth power of the distance and are therefore often summarised in the attractive part of the Lennard-Jones potential. The potential energy surface of most reactions is a combination of many different contributions depending on the reactants' properties and whose strength strongly changes with the intermolecular distance and reactant orientation. A full description of an atomic or molecular interaction can only be achieved by an ab-initio quantum-mechanical calculation of the potential energy surface. Despite great advances in the last decades a full quantum-mechanical treatment of reactive collision processes of systems with more than a few atoms keeps being challenging. Analytical models based on classical and semi-classical approaches might be less accurate and are not able to explain all interactions but are easier scalable and can provide a more intuitive approach to understand the underlying physical and chemical phenomena of atomic and molecular interactions. An example of an analytical potential energy surface describing the interaction of a highly polarisable atom with a molecule featuring a strong permanent dipole moment is given in Chapter 5.

## 2.7 The single-collision conditions

So far, the theory described in this chapter considered only isolated collision events of two particles in the gas phase. This is a strong simplification as particles at atmospheric pressures move with a velocity of hundreds of meters per second and undergo constant collisions. This provides a great experimental challenge as every secondary collision event leads inevitably to a loss of information of the primary collision process. Multiple sequential collision events prevent the observer from correlating the initial reactants and their properties to the measured reaction products.

The mean free path $\lambda_{\mathrm{col}}$ describes the average distance a particle travels between collisions. For a particle with an average velocity $v_{\mathrm{mean}}$ in a gas with particle density $n$, the mean free path is given by

$$\lambda_{\mathrm{col}} = v_{\mathrm{mean}}t_{\mathrm{col}} = \frac{1}{\sqrt{2}\sigma_{\mathrm{c}}n}, \tag{2.26}$$

where $t_{\text{col}}$ is the time between collision events and $\sigma_c$ the particle's cross section [3]. For an ideal gas the mean free path can be expressed in terms of the gas pressure $P$ and temperature $T$

$$\lambda_{\text{col}} = \frac{k_B T}{\sqrt{2}\sigma_c P},$$ (2.27)

with the Boltzmann constant $k_B$. A typical mean free path, e.g. of the helium atom ($\sigma_{c,\text{He}} = 0.21$ nm$^2$, [3]), at room temperature and atmospheric pressures is about $\lambda_{\text{col}} = 140$ nm, but increases to $\lambda_{\text{col}} = 1400$ m in high vacuum ($P = 10^{-7}$ mbar).

To be able to observe isolated reactions in the gas phase, the mean free path of the products has to be much longer than their path to the particle detector $\lambda_{\text{col}} >> d_{detection}$. This is known as the **single-collision condition** for physical detection of scattering products. Typical experimental detection distances are several centimetres up to one meter for which the single-collision condition can only be satisfied by low gas pressures. This is realised in crossed-beam setups in which particles react with each other in a small, well defined volume under high vacuum conditions [91]. The reaction products are extracted from the dense reaction volume before they can undergo a second scattering process and are then accelerate towards the detector. Secondary collisions of the products on the way to the detector are strongly suppressed by the high vacuum environment. The crossed-beam technique will be the topic of the next chapter.

# 3

# The novel crossed-molecular-beam setup

Investigating reactions in the gas phase under single-collision conditions provides a powerful tool to unravel the fundamental details of reaction mechanisms as it allows the investigation of individual bimolecular reactions rather than a statistical average of many interacting particles which is often the case in classical chemistry using thermalised systems.

Probing reactions at a single-collision level requires to detect the reaction products of a molecular collision before they can participate in a secondary scattering event. The development of the first crossed-beam setups during the 1950s and 60s was a milestone in experimentally investigating neutral reaction processes under single-collision conditions in the gas phase [6–9, 92–96]. In a crossed-beam setup, two collimated atomic or molecular beams intersect each other under a certain angle in a narrow, well-defined scattering volume, for which the great majority of scattered particles have left the scattering region before a second collision event can occur. For the insights gained by their new crossed-beam setup on elementary processes of chemical reactions, Dudley R. Herschbach and Yuan T. Lee were awarded the Nobel price in Chemistry in 1986 [11, 91], together with John C. Polanyi for his advancements using the infrared chemiluminescence method [97].

In an ideal gas-phase bimolecular reaction experiment, all relevant properties of the reactants and of the final reaction products are known to the observer. How much can

be learned from investigating chemical reactions using a crossed-beam setup hence depends on two main experimental factors; the accuracy to detect the final reaction products and the ability to control the properties of the reactants prior to the collision event. In both areas, tremendous progress has been made since the first experimental realisation in the 1950s.

The implementation of an electron-impact mass spectrometer in combination with ion-particle detectors during the 1960s added a universal way of detecting reaction products and made the crossed-beam technique applicable to a much wider range of reactions [9]. This was soon followed by the time-of-flight technique, which allowed product identification based on their mass-to-charge ratio [98]. This technique is also relevant to the experiments discussed in this thesis and is described in detail in Section 3.5.2. Quantum-state specific identification of the reaction products became possible with the introduction of laser-detection techniques [99, 100], which enabled the observation of state-resolved cross sections [101–103]. Angle-resolved cross sections could first only be gained by rotating the particle detector around the collision region to measure each scattering angle sequentially. This process got revolutionised first by the incorporation of the ion imaging technique [104] and later by velocity map imaging (VMI) [105]. The VMI technique allows recording differential cross sections of all scattering angles simultaneously by directly mapping the full velocity vector of the scattered collision partners [15]. The VMI technique will be the topic of Section 3.5.3. The introduction of supersonic beams was a great improvement over effusive beams as it allowed preparation of reactants with better defined translational and longitudinal velocities and strongly reduced the number of populated rotational and vibrational quantum states in the molecular beam [106, 107]. Supersonic beams will be discussed in Section 3.3. Rotating molecular beam sources enabled the continuous tuning of the collision energy by varying the scattering angle of the two beams [108]. Exploiting the interaction of polar reactants with magnetic or electric fields led to multiple experimental tools which further increased the control over the reactants. Multipole focusers allowed the selection of reactants in certain rotational states from the thermalised distribution of the molecular beam [21–23, 25–27, 109]. Electric and magnetic beam guides enabled the development of merged beam setups [41–48], an extension of the crossed-beam technique for probing reactions at very low collision energies by minimising the scattering angle of both reactants. This effect was also achieved by copropagating two supersonic beams from a dual-molecular beam source [110]. Actively reducing the forward velocity was enabled by switching electric fields in Stark- and Zeeman decelerators which allowed observation of state-to-state differential cross sections of elastic and inelastic collisions with unprecedented resolution [36–40]. The above developments of the last decades led to valuable insights of a wide range

of reactions which could only be achieved by exploiting the strengths of various different crossed-beam setups. Detailed overviews of the different techniques and investigated neutral reaction systems are provided, among others, by the reviews given in References [10, 12–19].

The new crossed-molecular-beam setup developed and constructed in the context of this thesis will be a valuable addition to the existing setups as it allows reactant preparation of polyatomic, strong-field seeking reactants. This will enable the investigation of state- and geometry-specific effects in bimolecular reactions under single-collision conditions for large reaction systems. This chapter focuses on the experimental details of the new crossed-molecular-beam setup.

## 3.1    General description of the experimental setup

A schematic of the novel crossed-molecular-beam apparatus is depicted in Fig. 3.1. The setup features two molecular beams which intersect at a collision angle of $\beta = 90°$ in the centre of an assembly of electrostatic ion-extraction electrodes. The products of the investigated reaction can be detected by time-of-flight mass spectrometry to obtain mass-specific relative integral cross sections. Differential cross sections can be obtained by mass-gated velocity-map imaging (VMI). The implementation of a femtosecond (fs) laser or a Dye-Nd:YAG laser combination allows the detection of neutral reaction products by universal multiphoton ionisation or state-specific resonance-enhanced multiphoton ionisation (REMPI), respectively. Ionic reaction products can be mass-specifically detected by pulsed ion-extraction fields.

The distinctive feature of the new setup is an electrostatic deflector integrated into one of the molecular beams. The interaction of the strongly inhomogeneous electric field of the deflector with the effective molecular dipole moments enables the spatial separation of different rotational states or conformers prior to the reaction [74].

The second molecular-beam source is equipped with a home-built discharge valve, which allows the generation of radicals and metastable-rare-gas reactants. All experiments are performed in a high-vacuum environment to enable the investigation of state- and geometry-specific effects under single-collision conditions.

This chapter provides detailed information of all relevant parts of the new crossed-molecular-beam setup and gives necessary background information of the used experimental techniques.
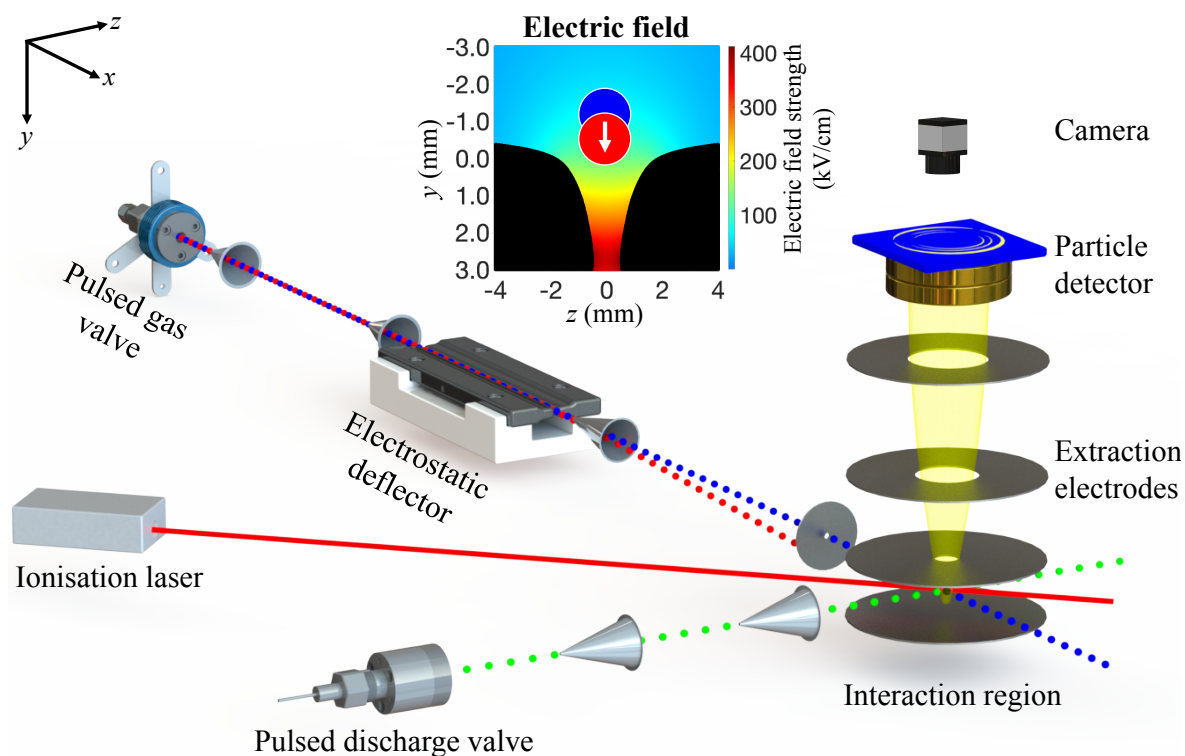
**Figure 3.1** Schematic of the novel crossed-molecular-beam setup for investigating state- and geometry-specific effects in bimolecular reactions under single-collision conditions. An electrostatic deflector enables the spatial separation of individual quantum states or conformers of molecules, schematically indicated by the red and blue dots, in a pulsed molecular beam. In the interaction region, the spatially separated molecules are overlapped with a second atomic beam containing metastable or radical co-reactants (green dots) produced by a pulsed discharge valve. Reaction products are detected by time-of-flight mass spectrometry and velocity-map imaging. The inset shows a cross section of the inhomogeneous electric field in the deflector and the approximate position of the molecular beam separating into different components [111].

## 3.2   Generating a high-vacuum environment

To investigate gas-phase reactions under single-collision conditions, the experiments have to be performed in a high-vacuum environment. The setup consist out of four stainless-steel chambers which are vacuum sealed by copper-gaskets between ConFlat (CF) flanges. A construction drawing of the vacuum setup is given in Figure 3.2.

Each source chamber features two magnetically levitated turbo pumps (Oerlikon Leybold MAG W 2200) with a pumping speed of 2200 l/s each. The collision and deflector chambers are differentially pumped with 2200 l/s and a 600 l/s magnetically levitated turbo pumps, respectively (Oerlikon Leybold MAG W 2200 and MAG W 600). All turbo pumps are backed up by a single oil-free and corrosion resistant double-stage

**Figure 3.2** Construction drawing of the vacuum setup of the crossed-molecular-beam apparatus. The setup consists out of four stainless-steel chambers which are vacuum-sealed by copper-gaskets between ConFlat (CF) flanges. A high-vacuum environment is achieved by several magnetically levitated turbo pumps as indicated in the figure. Gate valves on both sides of the deflector chamber allow separate venting of the deflector and the deflector-source chamber. Labels: ① Turbo pump (2200 l/s), ② Turbo pump (600 l/s),③ Vacuum gate valves, ④ $xyz$-translation stage, ⑤ Time-of-flight tube, ⑥ Camera with holder.

root pump (Pfeiffer A 604 H) with a total pumping speed of 560 m$^3$/h. Molecular beam skimmers between the chambers enable differential pumping of the individual chambers, which generates a pressure gradient from the gas-load intensive source chambers to the collision chamber, where the best vacuum conditions are needed. High-vacuum pressure gauges (Leybold PTR 90 N Penningvac) installed on all chambers allow real-time monitoring of the chamber pressures. All experiments described in this thesis are performed at an experimental repetition rate of 50 Hz, for which the pressure of both source chambers is typically maintained in the 10$^{-6}$ mbar range and the pressure of the collision chamber does not exceed 2·10$^{-7}$ mbar. The setup has been tested with both beam sources running at a repetition rate of 200 Hz which resulted in a collision-chamber pressure below 5·10$^{-7}$ mbar, which is still adequate for crossed-molecular-beam studies under single-collision conditions (see Sec. 2.7). All pumps are continuously

water cooled to keep them at ideal operating temperatures even under larger gas loads. Vacuum gate valves on both sides of the deflector chamber allow separate venting of the defector and the deflector-source chamber in case maintenance is required or new changes have to be incorporated into the experimental setup. A gate valve between the conventional source and collision chamber was omitted to be able to reduce the distance between the discharge source and the interaction region, which results in higher beam densities and ultimately in increased signal levels (see Sec. 3.3).

To prevent the vacuum system from damage while investigating reactions involving strongly corrosive agents, all turbo pumps are purged with dry $N_2$ using electronically controllable purge valves (Leybold 12133, flow rate: 36 sccm). The backing pump is continuously purged by 12 slm of dried air. Purging the full pumping system increases the pressure in the foreline of the turbo pumps from about $5\text{x}10^{-4}$ mbar to $2\text{x}10^{-2}$ mbar, but is does not effect the pressures in the vacuum chambers.

All essential features of the turbo pumps can be accessed by a self-written control program based on the *LabVIEW* software package from *National Instruments*. The program features a user-friendly graphical user interface which allows easy access to all important features of the turbo pumps, purge and vent valves of the setup and continuously monitors all relevant parameters as for example the frequency of the pump and its operation temperatures.

## 3.3   The atomic and molecular beam sources

Supersonic atomic and molecular beams are essential for every crossed-beam setup as it prepares the reactants with a well-defined velocity, reduces the internal energy of the reactants and by that provides the first experimental step in controlling the reactants' properties. In addition, cold molecular beams with a narrow velocity spread are crucial to achieve good experimental separation of rotational states and conformers by electrostatic deflection as demonstrated in Chapter 4.

### 3.3.1   Supersonic expansion of atoms and molecules

The use of atomic and molecular beams are nowadays standard in gas-phase studies and in-depth literature on this topic is available [106, 107, 112, 113]. This section only provides a short, reproducing summary of the most important aspects. A particle beam is generated by expanding gas from a high-pressure environment through a small opening, commonly known as the nozzle, into a low-pressure region. Thermodynamically, this process can be described by an adiabatic and isentropic expansion of an ideal gas, for which the total energy of the system has to be conserved. Considering an

initial gas prior expansion with an internal energy $U_{\mathrm{res}}$, molecular mass $m$ and a mean velocity $v_{\mathrm{res}}$ being contained inside a reservoir with volume $\mathcal{V}_{\mathrm{res}}$ and pressure $P_{\mathrm{res}}$, the conservation of total energy dictates that

$$U_{\mathrm{res}} + \mathcal{V}_{\mathrm{res}}P_{\mathrm{res}} + \frac{1}{2}mv^2_{\mathrm{res}} = U_{\mathrm{beam}} + \mathcal{V}_{\mathrm{beam}}P_{\mathrm{beam}} + \frac{1}{2}mv^2_{\mathrm{beam}}, \tag{3.1}$$

where the subscript *beam* denotes the properties of the particle beam after the expansion [114]. The nature of the expansion strongly depends on the initial stagnation conditions of the gas reservoir and the geometry of the expansion setup and is described by the Knudsen number $Kn$ [113], which relates the mean free path between particle collisions $\lambda_{\mathrm{col}}$ to the diameter of the expansion nozzle $d_{\mathrm{nozzle}}$

$$Kn = \frac{\lambda_{\mathrm{col}}}{d_{\mathrm{nozzle}}}. \tag{3.2}$$

Two limiting cases can be distinguished for $Kn >> 1$ and $Kn << 1$, which are called the effusive and supersonic regime, respectively [112]. In the effusive regime, the nozzle diameter is much smaller than the mean free path of the particles, i.e. during the expansion process barely any collisions are taking place and the velocity distribution of the resulting beam is comparable to the one of the thermal gas prior expansion [106]. For small nozzle sizes typically used, low backing pressures are required for the generation of effusive beams. Contrarily, the mean free path in a high-pressure environment is sufficiently small for the gas particles to undergo many collision events during the expansion process in the direct vicinity of the nozzle. These inelastic collisions result in an energy transfer from the internal to the kinetic energy of the particles resulting in a strong reduction of populated quantum states of the expanded atoms and molecules [112, 113]. For typical conditions leading to a supersonic beam, the pressure in the expansion region can be neglected and the term for the potential energy of the expanding gas vanishes ($V_{\mathrm{beam}}P_{\mathrm{beam}} \approx 0$). Further considering that the mean gas velocity in the reservoir is zero, the conservation of total energy given in Equation (3.1) can be simplified for a supersonic expansion process to

$$U_{\mathrm{res}} + \mathcal{V}_{\mathrm{res}}P_{\mathrm{res}} = U_{\mathrm{beam}} + \frac{1}{2}mv^2_{\mathrm{beam}}. \tag{3.3}$$

Rearranging in favour of the kinetic beam energy emphasises the conversion of the internal energy stored in the gas reservoir to forward motion of the expanding gas

$$\frac{1}{2}mv^2_{\mathrm{beam}} = (U_{\mathrm{res}} - U_{\mathrm{beam}}) + \mathcal{V}_{\mathrm{res}}P_{\mathrm{res}}. \tag{3.4}$$

Typical supersonic beams have a fast forward velocity exceeding the speed of sound, while at the same time having a narrow velocity spread as the randomised motion of the

particles gets assimilated during the collision process. Eventually, all particles travel with a similar velocity which strongly reduces the probability for collisions and finally results in a supersonic jet of barely interacting particles. The longitudinal velocity distribution $f_{\text{SB}}(v)$ of a supersonic beam can be described by a Maxwell-Boltzmann distribution adjusted for the mean velocity of the beam [107, 112, 115] and is given by

$$f_{\text{SB}}(v) = \left(\frac{v}{v_{\text{mean}}}\right)^2 \exp\left(-\left(\frac{v - v_{\text{mean}}}{\Delta v}\right)^2\right), \tag{3.5}$$

with the mean beam velocity $v_{mean}$ and the velocity spread $\Delta v$ respectively defined as

$$v_{mean} = \sqrt{\frac{2k_{\text{B}}}{m}\frac{\gamma}{\gamma - 1}(T_{\text{res}} - T_{\text{beam}})} \quad \text{and} \quad \Delta v = \sqrt{\frac{2k_{\text{B}}T_{\text{beam}}}{m}}. \tag{3.6}$$

Here, the temperature of the gas reservoir and the final beam are denoted by $T_{\text{res}}$ and $T_{\text{beam}}$, respectively. $k_{\text{B}}$ is the Boltzmann constant and $\gamma$ describes the adiabatic coefficient of the expanded gas. A comparison of the velocity distributions for a typical effusive and supersonic beam is shown in Figure 3.3 together with schematically visualisations of the expansion process for both regimes in the insets of the figure [116].
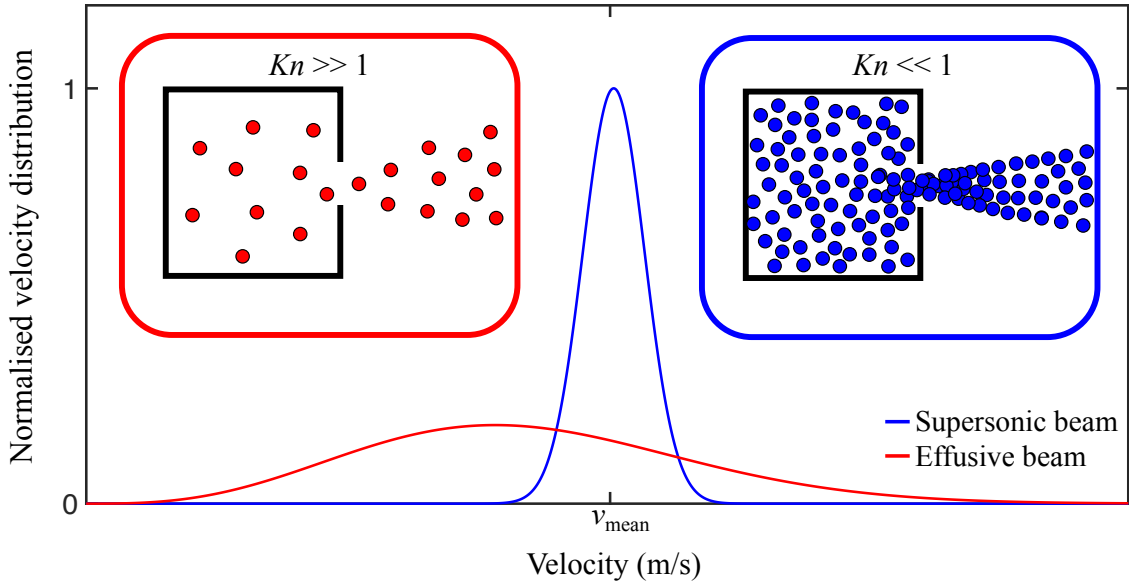


**Figure 3.3** Representative velocity distribution of an effusive and supersonic atomic beam [116]. The insets schematically show the different Knudsen regimes for an effusive ($Kn \gg 1$, red) and a supersonic expansion ($Kn \ll 1$, blue).

In a good supersonic expansion, almost all initial internal energy is transferred into kinetic energy of the beam, i.e. the final beam temperature can be neglected in

comparison to the initial temperature of the gas reservoir ($T_{\text{beam}} \ll T_{\text{res}}$). For this limiting case, the maximum mean velocity $v_{mean,max}$ a supersonic beam can reach is given by [115]

$$v_{mean,max} = \sqrt{\frac{2k_{\text{B}}}{m}\frac{\gamma}{\gamma-1}T_{\text{res}}}. \tag{3.7}$$

The final velocity of the beam hence depends on the mass of the expanded gas and the thermal temperature of the gas reservoir. The mass dependency is shown for all commonly used rare gases ($\gamma = 5/3$, [113]) in Figure 3.4a, while Figure 3.4b gives the impact of $T_{\text{res}}$ on the beam velocity for the two rare gases used in this thesis, helium and neon.
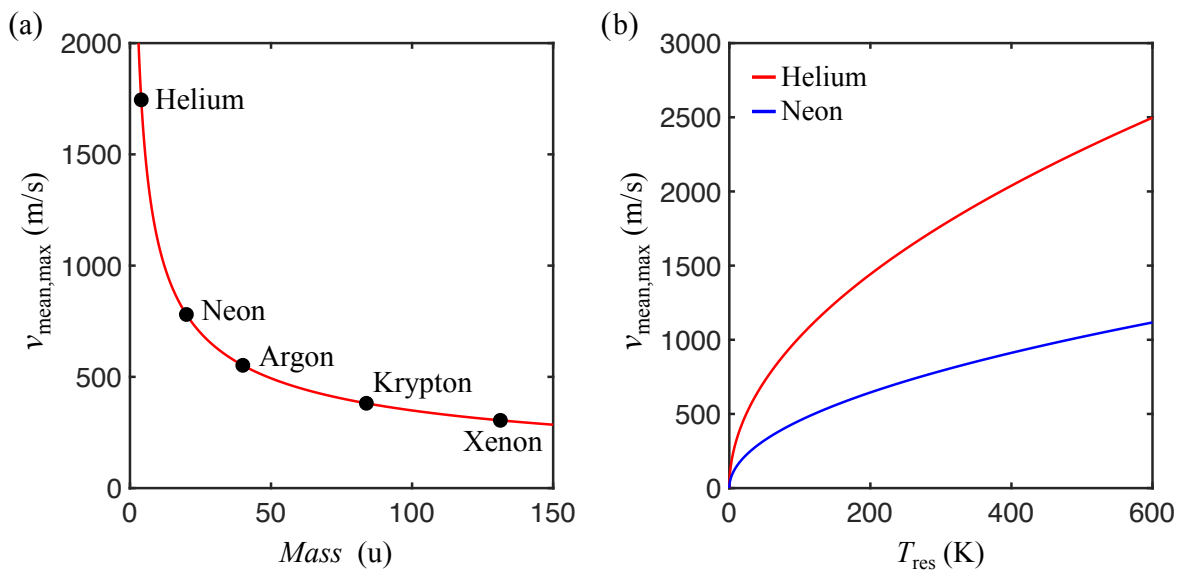


**Figure 3.4** (a) Maximum mean velocity $v_{mean,max}$ of a supersonic beam as function of the molecular mass at a reservoir temperature of $T_{\text{res}} = 293$ K. (b) Dependence of the maximum mean velocity $v_{mean,max}$ of a supersonic beam on the reservoir temperature for the rare gases helium and neon.

The transversal velocity of a supersonic beam is experimentally reduced by the utilisation of beam skimmers, which confine the beam along its propagation axis and by that select only the most intense part of the beam [112]. The transversal velocity distribution is then determined by the geometry of the setup accounting for all beam skimmers. The transversal velocity component of a supersonic beam passing several skimmers is approaching zero and its spatial cross section is comparable to the orifice of the last confining skimmer, as illustrated in Figure 3.5. Skimmers are also essential for differential pumping of the experimental setup as they prevent particles deviating from the core of the beam from proceeding to the next experimental stage.

$d_{\text{beam}} \approx d_{\text{Skimmer}}$

Skimmer 3        Skimmer 2        Skimmer 1        Valve
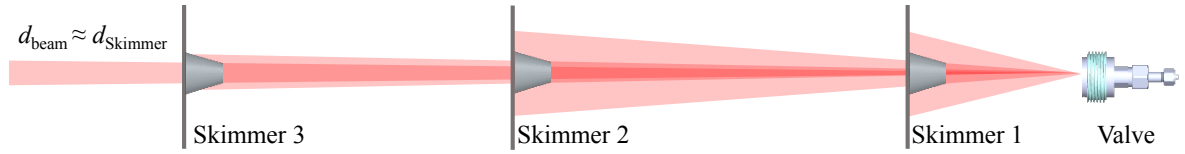
**Figure 3.5** Schematic illustration of the confinement of a supersonic beam by skimmers. After the last skimmer the transversal velocity of the beam is approaching zero and the size of the beam is comparable to the orifice of the last skimmer.

The transversal velocity leads to a dispersion of particles from the main propagation axis resulting in an overall decrease of its density. The particle density $C_{\text{beam}}(x)$ of a supersonic beam as function of the distance from the nozzle $x$ can be described by

$$C_{\text{beam}}(x) = C_0 \left( 1 + \frac{\gamma - 1}{2} M(x)^2 \right)^{-\frac{1}{\gamma - 1}} , \tag{3.8}$$

where $C_0$ is the initial beam density at the nozzle and $M(x)$ describes the dependence of the Mach number $M$ on $x$ [117]. According to Ref. [118], $M(x)$ for an monoatomic gas ($\gamma = 5/3$) can be estimated by

$$M(x) = 3.26 \left( \frac{x}{d_{\text{nozzle}}} - 0.075 \right)^{\frac{2}{3}} - 0.61 \left( \frac{x}{d_{\text{nozzle}}} - 0.075 \right)^{-\frac{2}{3}} , \tag{3.9}$$

with $d_{\text{nozzle}}$ the diameter of the nozzle opening. A typical decrease of density as function of the distance to the nozzle is given in Figure 3.6 for several initial particle densities at the nozzle and different nozzle openings. The main decrease in particle density occurs in the direct vicinity of the nozzle.

**Molecular beams** can be produced by directly expanding the pure gas or by co-expanding the target molecules with an inert carrier gas, a principle which is known as **seeding**. Usually atomic rare gases are chosen as carrier gases, but also non-interacting molecules like $SF_6$ or $H_2$ have been used in the past. Seeding allows tuning of the molecular-beam speed by choosing the carrier gas and by adjusting the seeding ratio of the target molecules to the inert gas. For sufficient low concentrations of the target molecule, the resulting molecular beam is dominated by the properties of the carrier gas [112]. Seeding also provides an efficient way to cool down the internal energy of the expanding molecules, as collisions with the seeding gas facilitate the transfer form vibrational and rotational energy to forward motion. As the energy level spacing of vibrational levels is larger compared to rotational levels, cooling of the vibrational levels is overall less effective. This is in particular the case for small, diatomic molecules with large energy spacing whereas for larger polyatomic molecules also the vibrational levels are cooled efficiently [112–115]. In a good supersonic expansion only the lowest rotational levels are populated, as experimentally shown in Chapter 4. Seeding a molecular
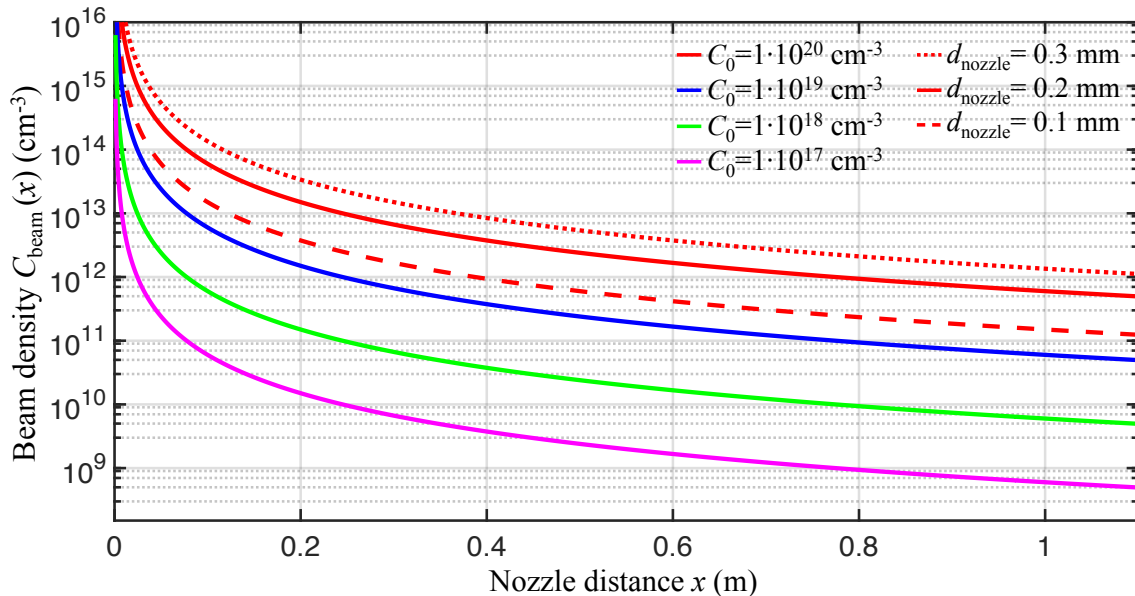
**Figure 3.6** Dependence of the particle density of a supersonic rare gas beam $C_{\mathrm{beam}}(x)$ on the distance to the expansion nozzle $x$. $C_{\mathrm{beam}}(x)$ is plotted for several initial densities $C_0$ and typical effective nozzle diameters $d_{\mathrm{nozzle}}$ of high-pressure beam valves as indicated in the legend.

species in an inert carrier gas also significantly reduces the formation of van-der-Waals clusters between molecules by reducing the probability of two cold molecules colliding with each other [107, 113]. The downside of seeding target molecules in an inert gas is the significantly reduced beam density compared to a pure expansion. Higher percentages of the target molecules increases the overall beam density and hence experimental signal levels, but also reduces the cooling of internal degrees of freedom. Because for electrostatic deflection experiments a cold molecular beam without molecular clusters is essential, the concentration of expanded molecules is usually kept below 1 % for the experiments described in this thesis, which results in a rotational temperature not exceeding a few Kelvin (see Ch. 4).

**Pulsed-molecular beams** can be generated by allowing the expansion process only for a well-defined time, which is experimentally done by repeatedly opening and closing the expansion nozzle. In contrast to **continuous beams** the gas load of pulsed beams and hence the requirements for the vacuum pumps are significantly reduced, which results in an overall lower background pressure and by that improves the expansion process [107]. The strong reduction in internal energy together with a well-defined velocity makes atoms and molecules in pulsed, supersonic beams ideal reactants for the investigation of gas-phase reactions. How such particle beams are generated experimentally for the novel crossed-molecular-beam setup is described in the next sections.

### 3.3.2 The Even-Lavie valve

Pulsed molecular beams which are guided into the electrostatic deflector to prepare reactants in certain rotational quantum states or conformers are generated by a commercial Even-Lavie valve [119–121]. The Even-Lavie valve belongs to the group of pulsed solenoid valves for which the nozzle of the gas reservoir is sealed by a magnetic plunger which is periodically pulled back by the magnetic field of a solenoid. Fast closing of the reservoir nozzle between the magnetic pulses is ensured by a mechanical loaded spring pushing the plunger back into its sealing position [120]. This results in the generation of well-defined and dense supersonic beams of molecules. The Even-Lavie valve can operate at high backing pressures up to 100 bar and repetition rates exceeding 1 kHz. In our setup, the valve is mounted in the deflector-source chamber, which is connected by a conical skimmer with a diameter of $d_{\mathrm{Skim}} = 3$ mm to the deflector chamber. A construction drawing of the implementation of the Even-Lavie valve in the CMB setup is given in Figure 3.7, together with a picture of the deflector-source chamber.
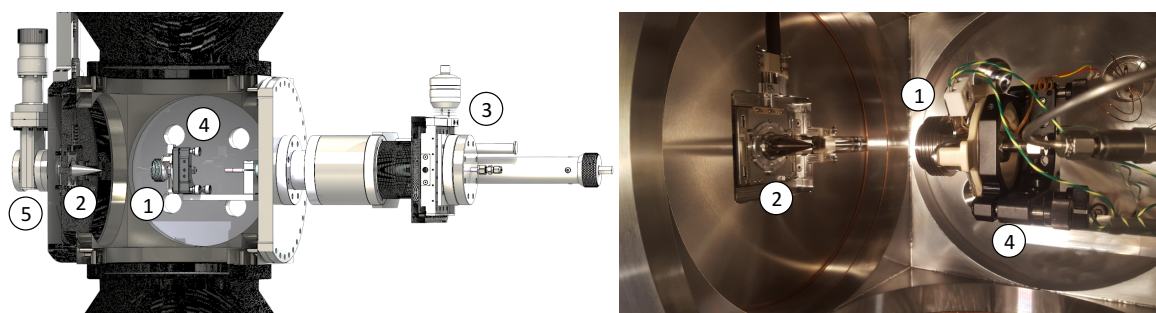


**Figure 3.7** (a) Construction drawing of the deflector-source chamber. The Even-Lavie valve is mounted in a mirror mount, which is placed on an *xyz*-translation stage. (b) Photographic image of the inside of the deflector-source chamber. Labels: ① Even-Lavie valve, ② Movable skimmer, ③ *xyz*-translation stage, ④ Mirror mount, ⑤ Vacuum gate valve.

The valve body is mounted inside a mirror mount which is placed on a *xyz*-translation stage. This arrangement enables proper alignment of the molecular beam axis with the deflector and the collision region as all three space directions and also the horizontal and vertical tilting of the valve can be controlled independently.

Typically temporal profiles of supersonic beams produced by the Even-Lavie valve in the CMB setup are shown in Figure 3.8 for the two molecules OCS and hydroquinone (HYQ) which are used as reactants in the context of this thesis (Ch. 5 and 6, respectively). Only highly diluted samples of OCS ($\approx$ 0.2 %) in an inert carrier gas are used to avoid molecular cluster formation and ensure good rotational cooling. Seeding OCS
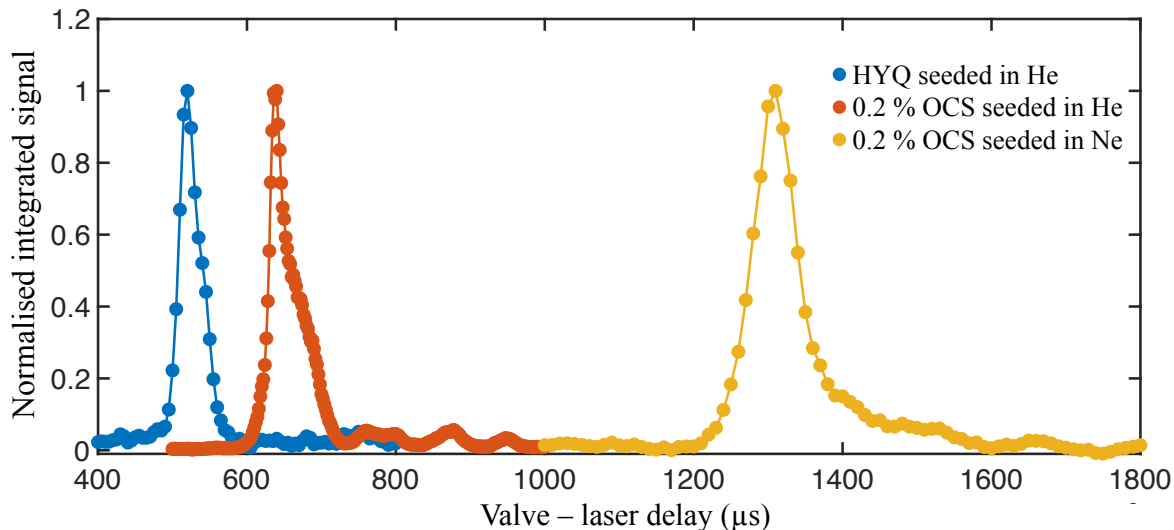
**Figure 3.8** Typical temporal profiles of pulsed molecular beams produced by the Even-Lavie valve for OCS seeded in helium and neon and for hydroquinone with helium as carrier gas. The amplitude of the profiles has been normalised for better comparison. For the molecular beam of HYQ the gas reservoir was heated to a temperature of $T_{\mathrm{res}} = 420$ K, resulting in a slightly faster beam compared to the OCS-He mixture.

in neon results in a significantly slower molecular beam compared to using helium as carrier gas. In contrast to OCS, hydroquinone is solid at room temperature and therefore has to be heated to generate a sufficiently dense molecular beam. An accurate value for its concentration in the beam can therefore not be given and only a rough estimate can be made. Based on experimental signal intensities the concentration of HYQ even after heating the sample should be significantly lower than the typical 0.2 % of OCS. For the beam profile of HYQ seeded in helium shown in Figure 3.8, the gas reservoir was heated to a temperature of $T_{\mathrm{res}} = 420$ K. Heating the gas reservoir increases the mean velocity of the beam according to Equation (3.7), resulting in the slightly faster beam of HYQ compared to the OCS-He mixture. Supersonic expansions by the Even-Lavie valve also result in excellent cooling of the internal degrees of freedom of the expanded molecules [119]. In the current setup typical rotational temperatures of $T_{\mathrm{rot}} \approx 0.5$ K and $T_{\mathrm{rot}} \approx$ 1-2 K were achieved for a molecular beam of OCS and hydroquinone, respectively, as demonstrated in Chapter 4.

For the expansion of liquid and solid samples, the Even-Lavie valve features a sample cartridge which is directly placed inside the valve housing. The valve body and the sample cartridge can be heated to control the vapour pressure of the sample and by that impact the density of the resulting molecular beam. Assuming a linear dependency of the vapour pressure $P_{\mathrm{vap}}$ in the gas reservoir and the measured signal intensity, the signal levels $I_{\mathrm{Signal}}$ as function of the reservoir temperature $T_{\mathrm{res}}$ should scale accord-

ing to the Antoine equation [122, 123] corrected by a normalisation constant $N_{\text{norm}}$. $I_{\text{Signal}}(T_{\text{res}})$ can then be expressed as

$$I_{\text{Signal}}(T_{\text{res}}) = N_{\text{norm}} \cdot P_{\text{vap}}(T_{\text{res}}) = N_{\text{norm}} \cdot 10^{A - \frac{B}{C + T_{\text{res}}}}, \tag{3.10}$$

with $A$, $B$ and $C$ being molecule-specific parameters. The experimental determined signal intensity of a beam of hydroquinone seeded in helium for different reservoir temperatures are shown in Figure 3.9a together with the normalised Antoine equation using the molecule-specific parameters for HYQ ($A = 5.8947$, $B = 3049.481$, $C = -40.485$ [124, 125]). The relative beam intensities of HYQ were measured by
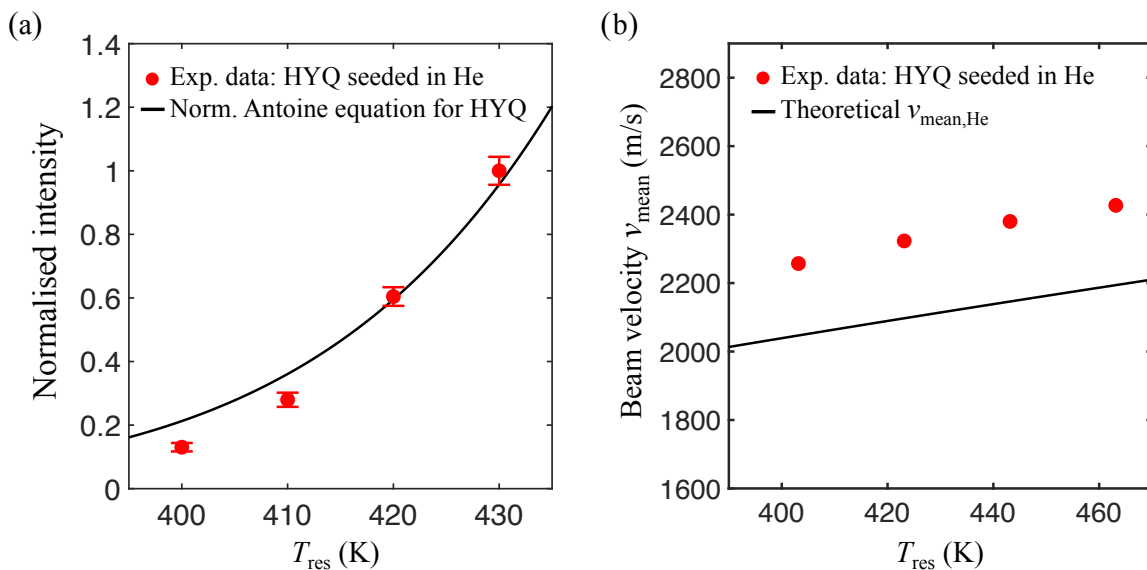


**Figure 3.9** (a) Relative signal intensities of a molecular beam of hydroquinone (HYQ) as function of the gas reservoir temperature $T_{\text{res}}$ of the Even-Lavie valve. The data was fitted with a normalised Antoine equation for the HYQ-specific parameters ($A = 5.8947$, $B = 3049.481$, $C = -40.485$ [124, 125]) with the normalisation constant $N_{\text{norm}}$ the only independent fitting parameter. The error bars represent the standard error of three individual measurements. (b) Experimental dependence of the mean beam velocity of a HYQ beam seeded in helium on the reservoir temperature together with the theoretical velocities of a pure helium beam. The discrepancy between experiment and theory is due to small systematic errors in the velocity determination and the valve temperature readout.

integrating the relevant peak in a time-of-flight mass spectrum obtained after fs-laser ionisation. Heating the sample increased the beam densities of the target molecules. It has to be noted that the Antoine equation does not accurately describe the vapour pressure in the vicinity of phase transitions and hence only data below the melting point of HYQ ($T_{\text{melt}} = 445$ K) is shown.

Heating the valve also impacts the final velocity of the molecular beam as shown in

Equation (3.7). The mean beam velocity of a beam of HYQ seeded in helium was determined for different reservoir temperatures using the velocity-map imaging technique. For solid samples, it can be assumed that the concentration of hydroquinone is so low that the final velocity of the beam is mainly determined by the properties of the carrier gas helium. Figure 3.9b gives the measured experimental beam velocities together with the theoretical maximum mean speeds of helium. The deviations between experimental and theoretical values can be accounted for by small systematic errors in the measurement of the velocity and reservoir temperature on the one side and shortcomings of the above presented theory.

### 3.3.3   The discharge source: the CRUCS valve

The second supersonic beam containing the reaction partners to the state- or conformer selected molecules is generated by a valve designed and developed by the Canadian Center for Research on Ultra-Cold Systems (CRUCS) [126]. This CRUCS valve is a solenoid-based pulsed valve and has a similar operating mechanism as the Even-Lavie valve. In our group, it was equipped with a discharge unit to be able to produce beams of metastable atoms and free radicals [127]. Both species feature a very high chemical reactivity which makes them preferred co-reactants in crossed-molecular-beam experiments as the resulting large reaction cross sections ensure sufficient signal levels [12–19, 128, 129].

The CRUCS valve is mounted in a separate source chamber, which extends by a hollow tube into the reaction chamber as schematically shown in Figure 3.10. The extension of the source chamber enables the CRUCS valve to move closer to the detection region, resulting in significantly higher beam densities in the overlap region of the two crossed beams (as demonstrated in Fig. 3.6). The atomic beam of the CRUCS valve first passes through a slit skimmer (1 mm×10 mm) separating the source from the reaction chamber, before it is confined to its final size by a conical skimmer ($d_{\text{Skim}} = 1.5$ mm) directly before the interaction region. The final distance between the valve nozzle and the centre of the interaction region is around 25-30 cm, which is close to the minimum possible distance while still employing two skimmers to achieve a nicely confined atomic beam. This includes a minimum distance of 10 cm between the valve nozzle and the first skimmer, which is essential for high-density gas valves, like the CRUCS valve used here, to prevent clogging of the skimmer [130]. Similar to the arrangement of the Even-Lavie valve, also the CRUCS valve is clamped inside a mirror-mount which is placed on a *xyz*-translation stage to allow optimum alignment of the atomic beam with the interaction region. All relevant dimensions and positions of the beam skimmers are
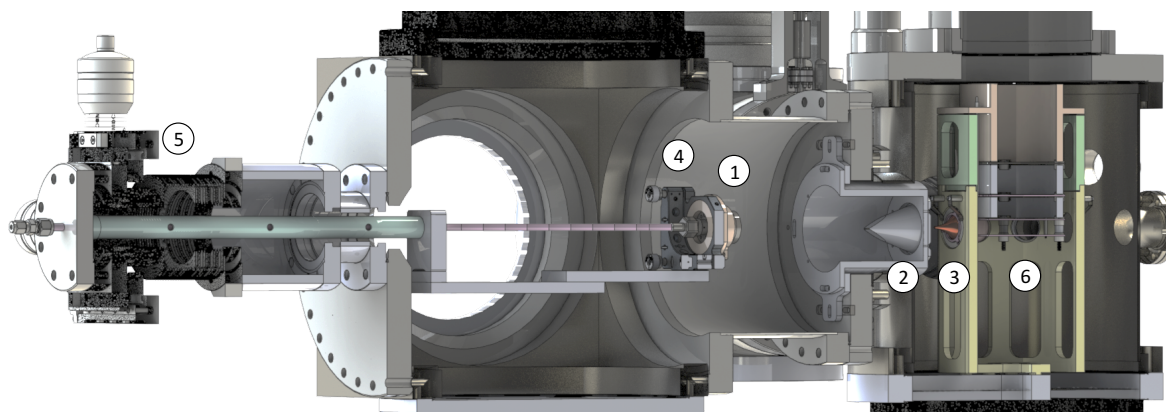
**Figure 3.10** Construction drawing of the source chamber containing the discharge unit. The CRUCS valve with attached plate-discharge is clamped in a mirror mount, placed on an *xyz*-translation stage. The source chamber extends into the reaction chamber to minimise the distance between nozzle and detection region. The atomic beam first passes through a slit skimmer (1 mm×10 mm) separating the source from the reaction chamber, before it is finally confined by a conical skimmer ($d_{\text{Skim}} = 1.5$ mm) placed in the octagonal support structure in the reaction chamber. Labels: ① CRUCS valve plus plate-discharge, ② Slit skimmer, ③ Conical skimmer, ④ Mirror mount, ⑤ *xyz*-translation stage, ⑥ Octagonal support structure with ion-extraction electrodes.

summarised for the complete crossed-molecular-beam setup at the end of this chapter in Figure 3.29.

The high reactivity of metastable atoms and radicals demands their production directly in the collision-free environment of an expanding particle beam, as otherwise they would directly recombine to chemically more stable species. For this purpose the expanding beam of the precursor species is electrically discharged directly after the nozzle of the CRUCS valve. The combination of two different discharge sources, a conventional plate discharge [126, 131–138] and a dielectric-barrier discharge (DBD) [126, 138–141], with the CRUCS valve and their characterisation for the production of an atomic beam of fluorine radicals was done by Patrik Straňák and the results are published in Ref. [127] and further detailed in his dissertation [142]. In short, both discharges succeeded in generating a cold and dense beam of fluorine radicals by dissociating the precursor molecule $F_2$ and operated reliably up to repetition rates of 200 Hz. The discharge efficiency (ratio of $F^*$ to $F_2$) was by a factor of 8 to 9 larger for the plate-discharge source compared to the dielectric-barrier discharge. Both discharge types generated predominantly fluorine radicals in the $^2P_{3/2}$ ground state, but overall the radical beam produced by the DBD-source was internally slightly colder compared to its plate-discharge counterpart [127]. The usage of corrosive-resistant materials such as stainless steel, MACOR and Teflon-sealing gaskets instead of commonly used Kapton-seals ensured excellent resistance to corrosion of both the valve and discharge sources.

Even for the highly corrosive $F_2$ precursor, the discharge sources could be operated reliable over weeks without maintenance. It has to be mentioned that discharge units of the same designs, but attached to a Nijmegen Pulsed Valve [143], were successful in the generation of dense and cold molecular beams of OH and NH radicals from the precursors $H_2O$ and $NH_3$, respectively [138, 144]. This allows the assumption that the combination of CRUCS valve and discharge unit presented here should be able to generate a wide variety of different atomic and molecular radicals increasing the range of possible reactions which can be investigate with the here introduced CMB setup.

In the context of this thesis, the generation of metastable species is more relevant and is discussed in the following. All experiments presented here utilise the plate discharge, mainly because it produces overall denser atomic beams but also because it is significantly less complex and easier to maintain than the dielectric-barrier discharge [142]. A schematic of the plate-discharge source is given in Figure 3.11b.
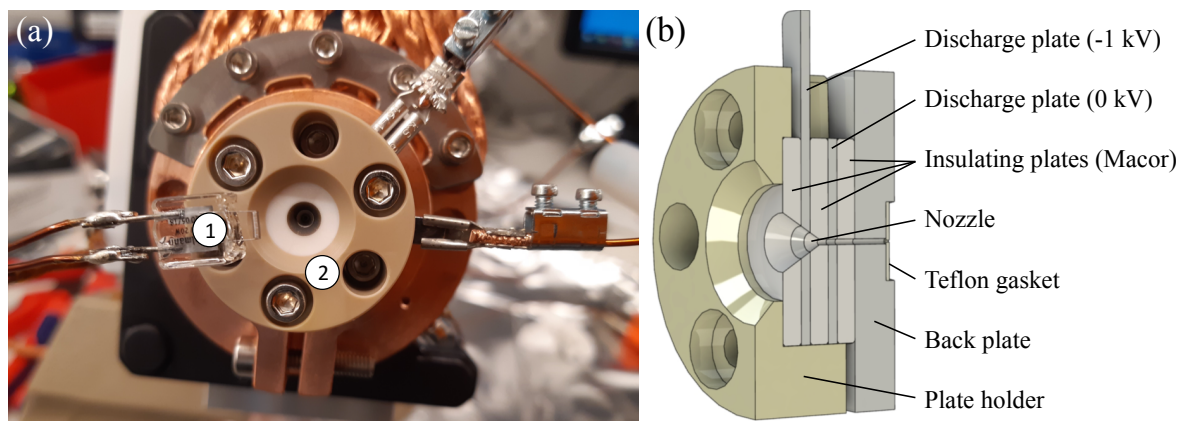


**Figure 3.11** (a) Photographic image showing the frontal view of the plate-discharge unit attached to the CRUCS valve and the electron-emitting tungsten filament. (Photograph taken by P. Straňák). (b) Schematic cross section of the plate-discharge source. The expanding atomic beam is discharged in the nozzle between two concentric plate electrodes (thickness 1 mm). The plates are separated by MACOR insulators (thickness 2 mm). The conically shaped nozzle features an opening angle of 60° and an inner diameter of 0.5 mm. The plate-discharge unit is mounted on the front plate of the CRUCS valve (not shown). Sealing between valve body and discharge unit is achieved by a corrosion-resistant Teflon gasket [127]. (Schematic by P. Straňák). Labels: ① Tungsten filament, ② Plate-discharge unit.

The expanding rare gas beam is excited by an electrical discharge occurring between two concentric plate electrodes placed in the throat of the expansion nozzle. The voltage applied to the electrodes is obtained from a home-built voltage driver, which provides nearly squared high-voltage pulses. A simplified schematic of the electronic circuit powering the discharge and a typical high-voltage pulse are shown in Figure 3.12a and

Figure 3.12b (blue trace), respectively.
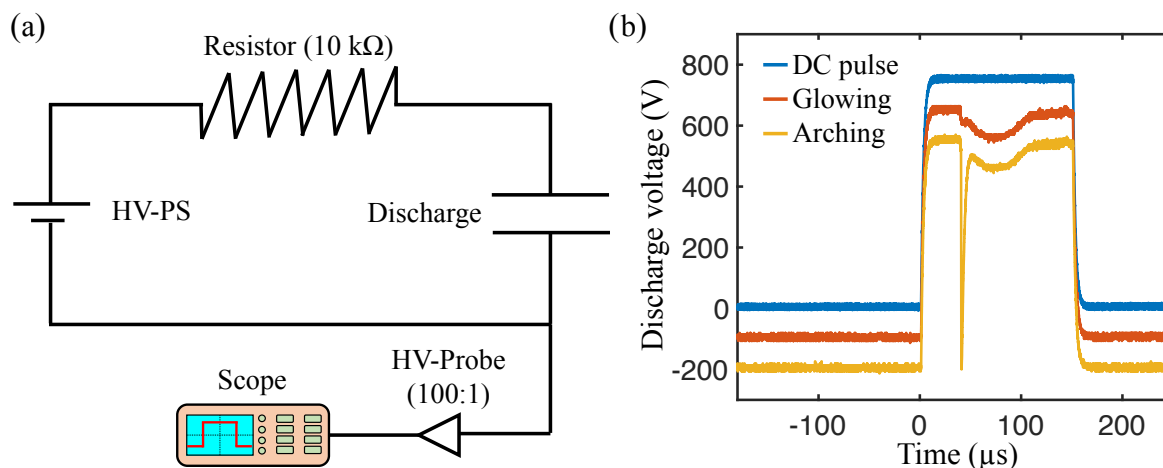


**Figure 3.12** (a) Electronic circuit of the plate discharge attached to the CRUCS valve. The applied voltage is continuously monitored by a fast oscilloscope. (b) The voltage across the discharge electrodes as monitored with the oscilloscope. Different traces show the raw HV-pulse in the absence of any discharge (blue), the voltage across the discharge electrodes in the presence of a glow discharge (red) and the large voltage drop occurring during arching events (yellow).

The different operation regimes of an electrical plate discharge depends on the size of the applied voltage across the electrodes and the size of the resulting current caused by breakdowns of the insulating vacuum between the electrodes [145, 146]. In the absence of an atomic beam, the vacuum between the discharge plates prevents any discharges of the electrodes which then function as a nearly perfect capacitor. If a discharge pulse with a sufficiently large voltage is timed simultaneously with the expansion of the atomic beam, the insulating character of the vacuum breaks down and a conductive plasma is generated in which electrons and cations are accelerated towards the anode and cathode, respectively. This results in a voltage drop of the potential applied across the electrodes [147], as can be seen in Figure 3.12b (red trace). In this regime, inelastic collisions between rare gas atoms and free electrons lead to the excitation of ground-state atoms into higher lying electronic states. Short-lived states decay back under emission of a photon. Therefore, this regime is called the glow regime of the discharge [145, 146]. Contrarily, states for which relaxation to the ground-state is forbidden due to quantum-mechanical selection rules are long-lived [148]. These long-lived metastable states can survive in the collision free region of an expanding atomic beam until they reach the collision chamber and thus can be used to investigate reactions with metastable reactants. Further increasing the discharge

voltage eventually results in significantly larger discharge currents occurring directly between the two electrodes, which can be observed by a sudden drop of the applied potential to zero as exemplary shown in Figure 3.12b (yellow trace) [146, 147]. This is called arching of the discharge and should be avoided for a long-term stable and reliable operation. For the plate-discharge attached to the CRUCS valve, a voltage difference between the electrodes of $800 - 1000$ V is usually ideal to operate it stably in the glow regime. Monitoring the discharge voltage allows adjusting the amplitude of the applied electronic pulse until an optimal value is reached for which the discharge works reliable in the glow regime and arching events are reduced to a minimum.

The discharge process can further be stabilised by the use of an electron-emitting filament placed in the vicinity of the discharge electrodes [134]. For this purpose, a tungsten filament is attached to the CRUCS valve body as shown in Figure 3.11a. The discharge process also leads to the generation of unwanted ions in the expanding beam, which can be ejected from the atomic jet by using an external electric field [140]. While initially using deflection plates directly placed after the discharge source, later the same effect was reached by applying a constant voltage of around 500 V to the first skimmer which separates the source from the reaction chamber. In dense beams of metastable species, intrabeam collisions can lead to the formation of ions also beyond the initial expansion region of the atomic beam [149]. These ions are more effectively discarded by the voltage on the skimmer compared to the deflection plates. Any unwanted ions formed in the beam after the first skimmer are prevented from reaching the reaction region by applying an electric clean-up pulse to the ion-extraction electrodes of the detector (more in Sec. 3.5.2).

So far, the plate-discharge source was used in our laboratory to generate metastable beams of helium and neon, but the same principle is extendable to all rare gases. Excitation of ground-state helium leads to the two long-lived states $(1s2s)^3S_1$ and $^2S_0$, whereas excitation of ground-state neon results into the metastable states $(2p^53s)^3P_2$ and $^3P_0$. Relaxation of these states to the ground-state is forbidden by electric-dipole selection rules [148]. Properties of the ground- and metastable states of helium and neon are summarised in Table 3.1 and their average lifetime is orders of magnitude longer than the the average arrival time of the atomic beam at the detection region ($\approx 200 - 500$ $\mu s$).

Typical temporal profiles of metastable beams of helium and neon produced with the CRUCS discharge nozzle are given in Figure 3.13. The inset shows a typical TOF mass spectrum of a metastable helium beam ionised by fs-laser radiation. When the plate-discharge is switched off, no helium peak can be observed in the spectrum as the power of the fs-laser radiation used is not sufficient to ionise ground-state helium atoms. Quenching of certain metastable states to allow beams of only a single excited state,

**Table 3.1** Metastable states of helium and neon

| Species | State | Energy | Lifetime |
|---------|-------|--------|----------|
| He | $^1S_0$ | 0 | ground-state |
| He | $2^3S_1$ | 19.82 eV [150] | 7870 s [151] |
| He | $2^1S_0$ | 20.62 eV [150] | 19.8 ms [152] |
| Ne | $^1S_0$ | 0 | ground-state |
| Ne | $^3P_2$ | 16.62 eV [153] | 14.32 s [154] |
| Ne | $^3P_0$ | 16.67 eV [153] | 430 s [155] |

e.g. by implementing optical quenching using a discharge lamp [156–159], by optical depletion using laser radiation [160–162] or by magnetic [163] or optical deflection [164], is not yet possible in the setup presented here, but should be implemented in the near future to allow the investigation of state- to state-prepared reactions.
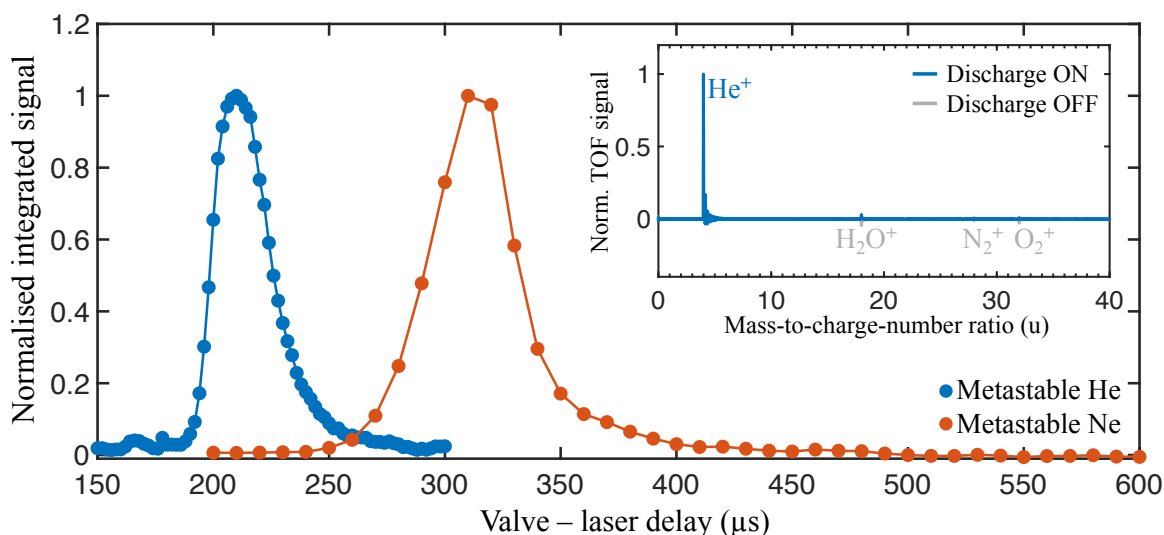


**Figure 3.13** Temporal profiles of the metastable atomic beams of neon and helium as produced by the CRUCS valve. Inset shows a typical TOF-MS trace of a metastable helium beam ionised by fs-laser radiation (blue trace). When the plate-discharge is switched off, no helium peak can be observed in the spectrum as the power of the used fs-laser radiation is not sufficient to ionise ground-state helium atoms (grey trace). The grey trace was inverted for clarity.

## 3.4 The electrostatic deflector

The electrostatic deflector enables spatial separation of individual rotational states or conformers of molecules by exploiting the interaction of their effective dipole moment with a strong inhomogeneous electric field [74]. Implementing an electrostatic deflector into a crossed-molecular-beam setup allows the investigation of state- and conformational effects on bimolecular reactions in the gas phase. The theory of electrostatic deflection of molecules is given in Chapter 4 together with an experimental demonstration of our deflection setup for the separation of individual rotational states of OCS (Sec. 4.4.1) and the *trans*- and *cis*-rotamers of hydroquinone (Sec. 4.4.2). This section merely deals with the experimental details of the electrostatic deflector and its implementation in the crossed-molecular-beam setup.

Figure 3.14a displays a construction drawing of the experimental setup relevant for the deflected molecular beam. A supersonic beam of molecules is generated in the deflector-source chamber by the Even-Lavie valve before it enters the deflector chamber through a skimmer with an orifice diameter of 3 mm. In the deflector chamber, the molecular beam is further confined by two conical skimmers ($d_{\mathrm{Skim}} = 1.5$ mm) placed directly before and after the electrostatic deflector (Fig. 3.14b). These two skimmers determine the position of the molecular beam axis, which is placed 2.7 mm above the centre of the high-voltage electrodes of the deflector as indicated in Figure 3.14d. As described in Chapter 4, the interaction of the inhomogeneous electric field of the deflector with the effective dipole moments of the investigated molecules leads to a spatial deflection along the $y$-axis, which further increases during a free flight over a distance of 45 cm between the end of the deflector and the reaction region. Along this way, the molecular beam passes through another collimator consisting of an aperture with a diameter of 1.5 mm placed 6.5 cm before the centre of the collision region. The total distance from valve to the interaction region with the second molecular beam is $\approx 1$ m, which is significantly longer than in conventional CMB setups [12, 15–19]. This results in low beam densities in the interaction region and hence a reduced number of collision events. Therefore, the present setup has been designed to operate at higher repetition rates than the typical 10 Hz used in many previous setups in order to compensate for the inherent loss in sensitivity by faster data accumulation. All relevant dimensions and positions of the beam skimmers are summarised for the complete crossed-molecular-beam setup at the end of this chapter in Figure 3.29.

The electrostatic deflector used in the present experiment was designed and built by the group of Jochen Küpper at DESY (Deutsches Elektronen-Synchrotron) in Hamburg and is described in detail in Ref. [165, 166]. Briefly, it consists of two parallel electrodes oriented along the molecular-beam axis with a total length of 15 cm spaced
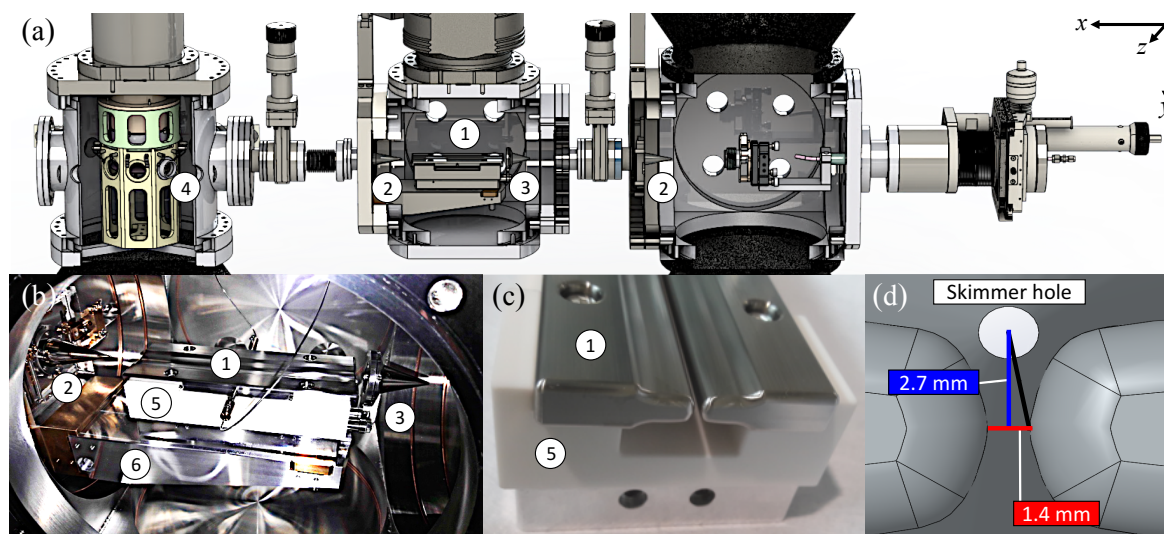
**Figure 3.14** Electrostatic deflector and its implementation in the CMB setup. (a) Construction drawing showing a cross section of the deflector-source chamber with the Even-Lavie valve, the deflector chamber housing the electrostatic deflector and the collision chamber with the octagonal support structure. (from right to left). (b) Photographic image of the electrostatic deflector implemented in the deflector chamber. The deflector is mounted on an alignment bridge between two 1.5 mm skimmers. (c) Frontal picture of the deflector electrodes. (d) Schematic CAD drawing of a cross section through the deflector electrodes. The position of the skimmers determines the axis of the molecular beam, which enters the deflector 2.7 mm above the centre of the high-voltage electrodes. Labels: ① Deflector electrodes, ② Movable skimmer, ③ Fixed skimmer, ④ Collimator, ⑤ MACOR insulator, ⑥ Deflector holder with alignment features.

1 mm apart as shown in Figure 3.14c. The shape of the geometries were optimised to maximise the gradient of the inhomogeneous electric field while still having an open mechanical structure to allow the deflection of dense supersonic molecular beams with large cross sections [165, 166]. The electrode design results in a fairly constant field gradient over the cross section of the molecular beam (see Fig. 4.3 in Sec. 4.3.2), which ensures a uniform deflection of all molecules independent of their spatial position in the beam.

The deflector electrodes are separated by a MACOR insulator, which is placed on a stainless-steel holder attached to the deflector chamber. The deflector holder posses several alignment features which allow to accurately adjust the position of the deflector electrodes in a very controlled fashion. For the same purpose two skimmers as indicated in Figure 3.14 are mounted on movable, high-vacuum sealed skimmer flanges, which allow adjusting the translational position of the skimmer without breaking the vacuum. Proper alignment of the deflector towards the molecular beam axis and the

collision region has been carried out carefully as it is crucial for proper electrostatic deflection experiments.

The strong inhomogeneous electric fields are produced by applying a constant electro-static potential difference of up to 40 kV between the deflector electrodes. The voltage is supplied by two commercial high-voltage power supplies (FUG HCP 14–20000 and HCP 35–35000 for the negative and positive electrode, respectively). To prevent any damages to the electrodes by unwanted electric discharges, the deflector is carefully con-ditioned every time after exposure to air. A resistor of 100 M$\Omega$ is integrated into the supply circuit of each electrode to limit potential harmful discharge currents. Two ac-curate multimeters (Digital-Multimeter FLUKE 87-V TRMS AC 10) monitor eventual discharge currents and enable a controlled electrostatic conditioning of the deflector electrodes.

Molecules passing through the electrostatic deflector are diverted from their initial path along the $y$-axis. Molecules in different rotational states or conformational iso-mers with different effective dipole moments are deflected to a different extent resulting in a broadened molecular beam (see Ch. 4). To be able to overlap different parts of the deflected molecular beam with the reaction region, the source chamber and the deflec-tor chamber are mounted on a movable frame which can be tilted with respect to the collision chamber as shown in Figure 3.15. By tilting the deflector assembly, different parts of the deflected molecular beam, which contain molecules in different rotational states or different conformers, can be overlapped with the second beam in the collision chamber so that state- or conformer-specific reaction effects can be studied (Inset of Fig. 3.15). The position of the frame can be read out at the tilt adjustment with an accuracy of 10 $\mu$m using a digital micrometer. The displacement of the molecular beam in the collision region, also referred to as the deflection coordinate $y_{\text{defl}}$, can be determined from the measured frame offset $y_{\text{frame}}$ by a purely geometrical relationship as indicated at the bottom of Figure 3.15. The deflection coordinate $y_{\text{defl}}$ is then given by

$$y_{\text{defl}} = -\frac{l_1}{l_2} \cdot y_{\text{frame}} = -\frac{580 \text{ mm}}{850 \text{ mm}} \cdot y_{\text{frame}}, \tag{3.11}$$

with $l_1$ and $l_2$ the distance between the adjustment wheel and the fixpoint of the frame and between the fixpoint and centre of the detection region, respectively.
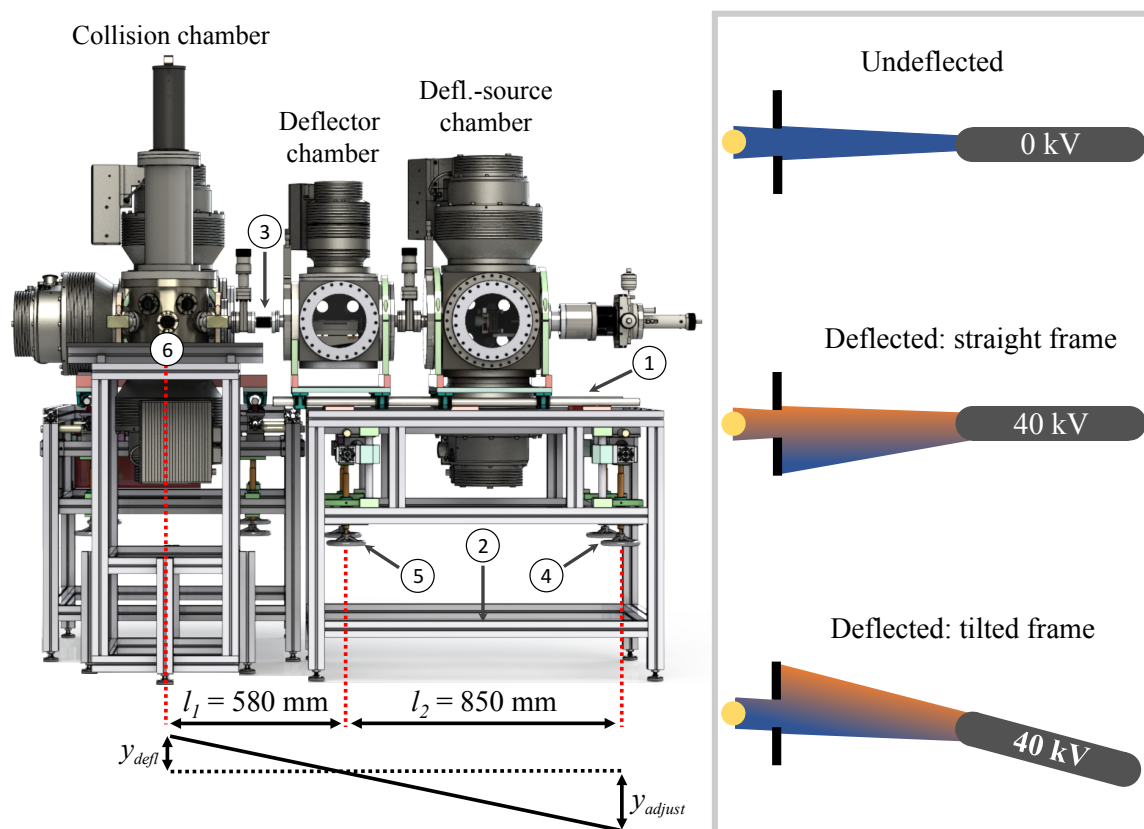
**Figure 3.15** Construction drawing of the CMB setup. The chambers housing the deflected molecular beam are mounted on a movable frame which can be tilted with an adjustment wheel. Thus, different parts of the deflected beam containing different compositions of conformers or rotational states can be overlapped with the second molecular beam in the collision region. The offset of the frame $y_{frame}$ can be read out at the tilt adjustment with an accuracy of 10 $\mu$m using a digital micrometer. The actual deflection coordinate $y_{defl}$ at the centre of the deflection region can be determined by a purely geometrical relationship as shown at the bottom of the figure. The inset schematically illustrates how different parts of the molecular beam can be overlapped with the collision centre by tilting the deflected molecular beam. Labels: ① Movable frame, ② Static frame, ③ Flexible bellow, ④ Tilt adjustment, ⑤ Fixpoint, ⑥ Centre of detection region.

## 3.5 The detection system

The crossed-molecular-beam setup aims to investigate reactions of polyatomic systems, for which the reactants are large enough to exhibit structural isomers. In such reactions a wide variety of products can be formed, whose identification is the first step in every experimental investigation. Therefore, the new setup features a time-of-flight mass spectrometer (TOF-MS), which allows identification of the reaction products based on their mass-to-charge ratio and enables the determination of relative branching ratios of different reaction products and pathways. The dynamics of the investigated reaction can be probed by the velocity-map-imaging (VMI) technique which allows to directly map the post-collisional velocity of the reaction product. The experimental setup of the detector is described in Section 3.5.1, and how it is used to obtain TOF-MS traces and velocity-mapped images is described in Sections 3.5.2 and 3.5.3, respectively.

### 3.5.1 The experimental setup of the detector

The time-of-flight mass spectrometer and velocity-map imaging detector share the same experimental setup as schematically illustrated in Figure 3.16.
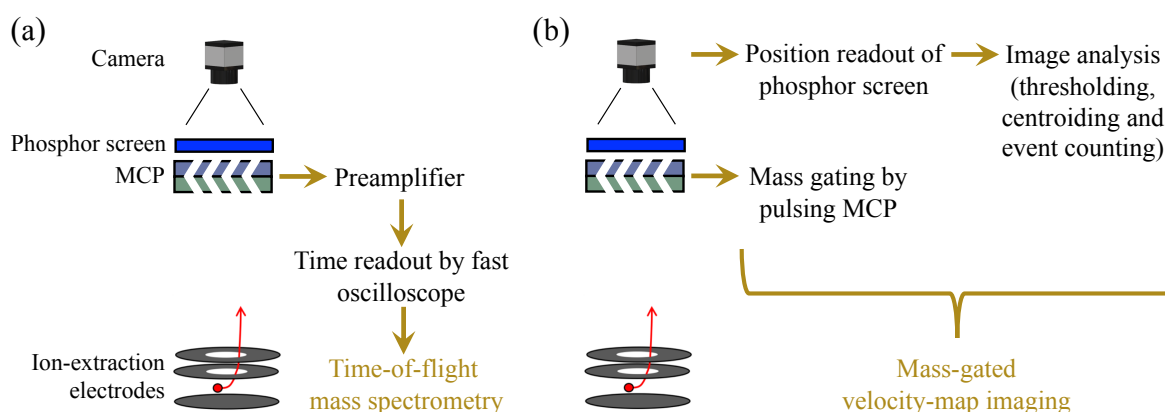


**Figure 3.16** Schematic illustration of the detector setup consisting out of ion-extraction electrodes, MCP coupled to a phosphor screen and a fast CMOS camera. (a) For time-of-flight mass spectrometry, the electronic signal of the MCP is first amplified and then read out by a fast oscilloscope. (b) In case of velocity-map imaging, the MCP are mass-gated and the impact position of the ion is read out by the camera. The signal is thresholded, centroided and event-counted resulting in the final mass-gated velocity-map image.

After ionisation of the reaction products, either by using a suitable laser or directly in chemi-ionisation reactions, the ions are accelerated by an electrostatic lens towards a position-sensitive detector consisting of a 75 mm diameter multichannel-plate (MCP) stack coupled to a phosphor (P46) screen (Photek). For TOF-MS, the electronic signal

of the MCP is enhanced by a home-built preamplifier (x10) before being processed by a fast oscilloscope (Teledyne LeCroy WaveRunner 8054). In VMI mode, the phosphor screen is read out by a fast CMOS camera (IDS UI-3040CP-M-GL Rev.2). The resulting image is thresholded, centroided and event-counted [167] in real-time by a home-written software package. To obtain images of only certain reaction products, the voltage of the particle detector can be gated by a fast HV-switch (Photek) to make it only sensitive during the arrival time of products with a specific mass.

The stack of ion-extraction electrodes is based on the design described in Ref. [168] and shown with all relevant dimensions in Figure 3.17.
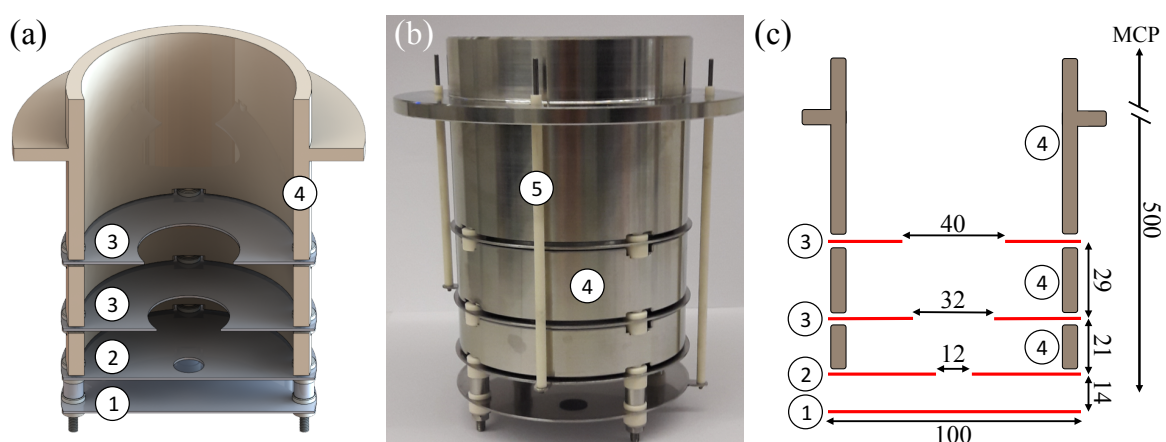


**Figure 3.17** (a) Constructional drawing showing a cross section of the ion-extraction electrodes as implemented in the crossed-molecular-beam setup. The stack consists of four circular electrodes, separated by electric insulators. The molecular beam enters the ion-extraction electrodes between the repeller and the extractor electrode. Grounded metallic shielding elements between the electrodes prevent distortions of the electric extraction field. (b) Photographic image of the ion-extraction stack. (c) Dimensions of the electrodes. The dimensions are based on the design of Ref. [168]. All dimensions are in millimetres. Labels: ① Repeller electrode, ② Extractor electrode, ③ Grounded electrodes, ④ Grounded shielding segments, ⑤ Electric wires with MACOR insulation.

Depending on the configuration of the applied voltages, the electrode stack allows the generation of ideal extracting fields for the acquisition of TOF-MS traces or ideal focusing fields for velocity-map imaging. For all experiments presented in this dissertation,voltage was only applied to the first two plates, which are called repeller and extractor electrode, respectively. The other two plates are grounded. In case of the investigation of reactions resulting directly into ions, e.g. chemi-ionisation reactions, the voltage applied to the electrostatic lens system can be pulsed within nanoseconds from ground to the required voltage by two independent Behlke switches (for details

see Sec. 3.5.2).

The stack of ion-extraction electrodes is mounted in an octagonal support structure similar to the one reported in Ref. [169]. It is centrally placed in the collision chamber and serves as the fixation and alignment point for both particle beams, for all lasers inserted into the experiment and for the extraction electrodes of the ion-detection system as shown in Figure 3.18. Each side of the octagon features clip mounts to which skimmers, collimators or optical lenses can be attached reproducibly without losing the alignment of the particle and laser beams. This renders the setup flexible for adjusting experimental parameters such as the size of the collision and laser-ionisation volumes which have a strong effect on signal levels, detector resolution and selection of different parts of the deflected molecular beam.
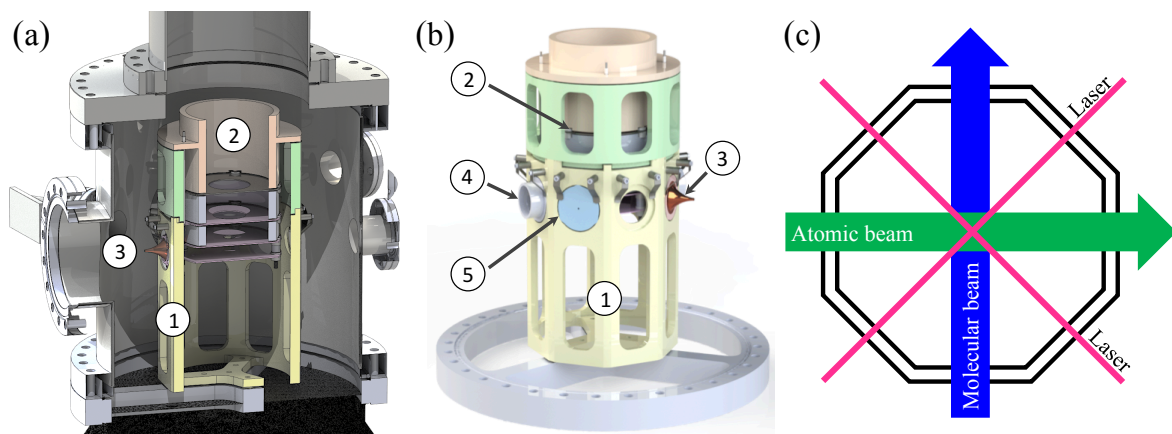


**Figure 3.18** (a) Construction drawing showing a cross section of the collision chamber with the octagonal support structure and the ion-extraction electrodes. (b) Construction drawing of the octagonal support structure which holds the ion-extraction electrodes and allows for easy mounting of skimmers, collimators and optical lenses [111]. (c) Schematic drawing of the top view of the octagonal support structure which determines the axes of the atomic, molecular and laser beam. Labels: ① Octagonal support structure, ② Ion-extraction electrodes, ③ Conical Skimmer, ④ Optical lens holder, ⑤ Beam collimator.

### 3.5.2 Time-of-flight mass spectrometry

The time-of-flight technique has a long history in analysing chemical compositions in gas-phase experiments based on their mass-to-charge ratio [170–177]. The TOF-MS technique used for the crossed-molecular-beam setup described here relies on the principles of the Wiley-McLaren mass spectrometer [98].

#### The Wiley-McLaren time-of-flight mass spectrometer

A typical setup of a Wiley-McLaren time-of-flight mass spectrometer is shown in Figure 3.19 [98]. Between three metallic grid-electrodes two homogeneous electric extraction fields $\mathcal{E}_1$ and $\mathcal{E}_2$ are generated which accelerate the ions from the ionisation region towards a time-sensitive particle detector. The electric field between the last, electrically grounded electrode and the particle detector is zero [98].
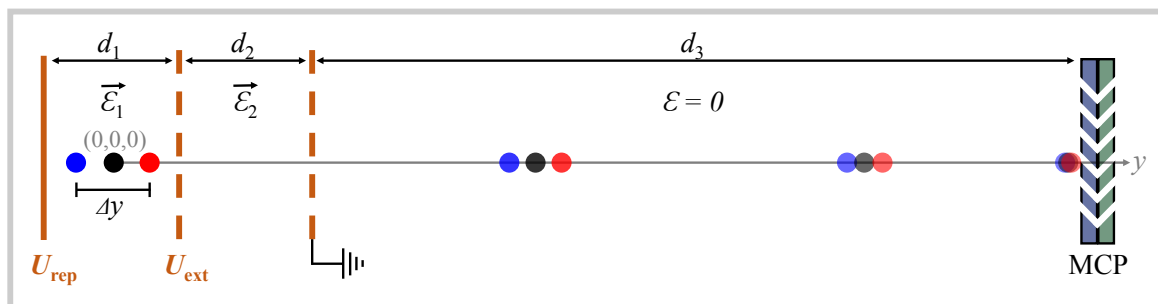


**Figure 3.19** Schematic setup of the Wiley-McLaren TOF–mass spectrometer [98]. Ions are accelerated by two homogeneous extraction fields towards a particle detector. The arrival time depends on the mass-to-charge ratio of the ions. The spread introduced by particles with different ionisation positions along the $y$-axis (red, black and blue dots) can be minimised by optimising the ratio of the two extraction fields. Symbols as explained in text.

For a particle with mass $m$, charge $q$ and a negligible initial kinetic energy ($E_{\text{kin}} \approx 0$) ionised in the exact centre of the electrode stack at position $y = 0$, the time of flight $t_{\text{TOF}}$ from the moment of ionisation till arrival at the detector is given by [98]

$$t_{\text{TOF}} = \sqrt{\frac{m}{q(d_1\mathcal{E}_1 + 2d_2\mathcal{E}_2)}} \left( 2\sqrt{k}d_1 + \frac{2\sqrt{k}}{\sqrt{k}+1}d_2 + d_3 \right), \tag{3.12}$$

with the distances $d_{1,2,3}$ as specified in Figure 3.19 and the parameter $k$ defined for convenience as

$$k = \frac{d_1\mathcal{E}_1 + d_2\mathcal{E}_2}{d_1\mathcal{E}_1}. \tag{3.13}$$

The arrival time of the extracted ions depends only on constant, experimental parameters and the mass-to-charge ratio of the detected species. Experimentally, this ratio is

often expressed as the mass-to-charge-number ratio $m/z$ in terms of atomic mass units $u$, with the charge number defined as $z = q/e$ and $e$ being the elementary charge. Deviations from the ideal ionisation position at $y = 0$ introduces a spread of the arrival time of the ions on the detector. The time of flight is then a function of the ionisation position $t_{\text{TOF}}(y)$. The time spread $\Delta t_{\Delta y}$ arising from two ions with an initial space separation of $\Delta y$ around $y = 0$ can be derived by performing a series expansion of $t_{\text{TOF}}(y)$ around $y = 0$ and is given by [98]

$$\Delta t_{\Delta y} = \sum_{n=1}^{\infty} \frac{1}{n!} \left( \frac{d^n t_{\text{TOF}}(y)}{dy^n} \right)_{y=0} (\Delta y)^n. \tag{3.14}$$

The effect of $\Delta t_{\Delta y}$ can be described qualitatively by two simultaneously ionised particles with different ionisation positions as shown schematically in Figure 3.19. The particle ionised closer to the repeller electrode is accelerated more strongly by the constant electric field and hence enters the field-free region with a higher velocity than the particle with an ionisation position closer to the extractor electrode. Eventually, the faster ion will catch up to the slower particle. At the point of overtaking the time spread caused by the initial ionisation position is zero. The point of overtaking can be tuned to coincide with the position of the particle detector by adjusting the ratio of the two extraction fields, which minimises the experimentally observed time spread $\Delta t_{\Delta y}$ and improves the resolution of the TOF-MS detector.

So far, only molecules with a negligible, initial kinetic energy were considered. An initial velocity parallel to the detector plane has no impact on the observed time of flight and only the kinetic-energy component along the detector axis $E_{\text{kin,y}}$ has to be taken into account. The time spread $\Delta T_E$ at the detector caused by two identical particles with opposite initial velocities can be described by the relation [98]

$$\Delta T_E = \frac{2\sqrt{2mE_{\text{kin,y}}}}{q\mathcal{E}_1}. \tag{3.15}$$

This time spread can not be compensated by the electric-field ratios and broadens the resulting time-of-flight peaks. The width of the recorded signal peaks hence contains information about the initial kinetic energy of the particles. E.g. particles ionised from molecular beams entering the detector parallel to its electrodes (along $x$ or $z$-axis) posses only a very small kinetic energy along $y$ and hence their resulting TOF peaks are narrow. In contrast, products from exothermic reactions or dissociation processes, in which chemical energy is transformed to kinetic energy, can have a large recoil velocity resulting in broad TOF peaks.

The resolution $R_{\text{m}}$ of a time-of-flight mass spectrometer can be estimated by the definition of the IUPAC nomenclature

$$R_{\text{m}} = \frac{m}{\Delta m}, \tag{3.16}$$

which relates the mass of a single charged ion $m$ to the full-width-half maximum (FWHM) $\Delta m$ of the resulting mass peak.

**Time-of-flight mass spectrometry after laser ionisation**

In contrast to the Wiley-McLaren spectrometer the setup described here features circular electrodes with open holes for the ions instead of metallic grids, because for velocity-map imaging the electric field has to function as an electrostatic lens system (see Sec. 3.5.3). The extraction fields are therefore not homogeneous as in a classical TOF mass spectrometer, which causes small deviations of the theory developed in the previous section and makes ion-trajectory simulations necessary.

For calibration purposes, a TOF-MS trace was recorded after ionising a pure beam of molecular oxygen by the 225 nm output of a frequency-doubled dye laser pumped by an Nd:YAG-laser. Two photons of the 225 nm radiation excites the oxygen molecule to the $3d\pi(^3\Sigma_{1g}^-)$ Rydberg state, from which the absorption of a third and fourth photon leads via various processes to auto-ionisation of $O_2^+$ or dissociative ionisation resulting into $O^+$. The details of these processes are described in Section 3.5.3 or in Ref. [178]. The resulting mass spectrum is given in Figure 3.20a. The inset shows the raw time-of-flight spectrum as obtained directly in our setup. The experimental time-of-flight spectrum can be transformed to the mass spectrum shown in Figure 3.20a via Equation (3.12).

For a well-resolved time-of-flight spectrum, it is essential to optimise the ratio of the two extraction fields to minimise the time spread at the detector caused by different ionisation positions. Experimentally, this is achieved by adjusting the potential $U_{\text{rep}}$ and $U_{\text{ext}}$ applied to the repeller and extractor electrode, respectively. The ideal ratio of the voltages was determined by simulating two ions with an initial spatial spread of $\Delta y = 0.5$ mm in SimIon as function of $U_{\text{ext}}/U_{\text{rep}}$ as shown in Figure 3.20b. The simulated time spread as function of the electrode voltages can be reproduced by the theoretically derived time spread $\Delta t_{\Delta y}$ of Equation (3.14). The ideal voltage ratio for our setup was determined to be $U_{\text{ext}}/U_{\text{rep}} = 0.85$. The experimental mass resolution of the spectrometer was determined from the molecular oxygen peak of the mass spectrum in Figure 3.20a to be $R = m/\Delta m \approx 32/0.09 = 355$.

In addition, the SimIon simulations allow to predict accurately the experimentally measured time of flight as shown exemplary for an oxygen atom as function of different repeller voltages in Figure 3.20c. The theoretical calculated $t_{\text{TOF}}$ slightly deviates from the experimentally measured data as the theoretical calculations are based on homogeneous extraction fields. Contrary, the simulated data points using inhomogeneous extraction fields reproduce the experimental data accurately.

(a)



(b)

(c)
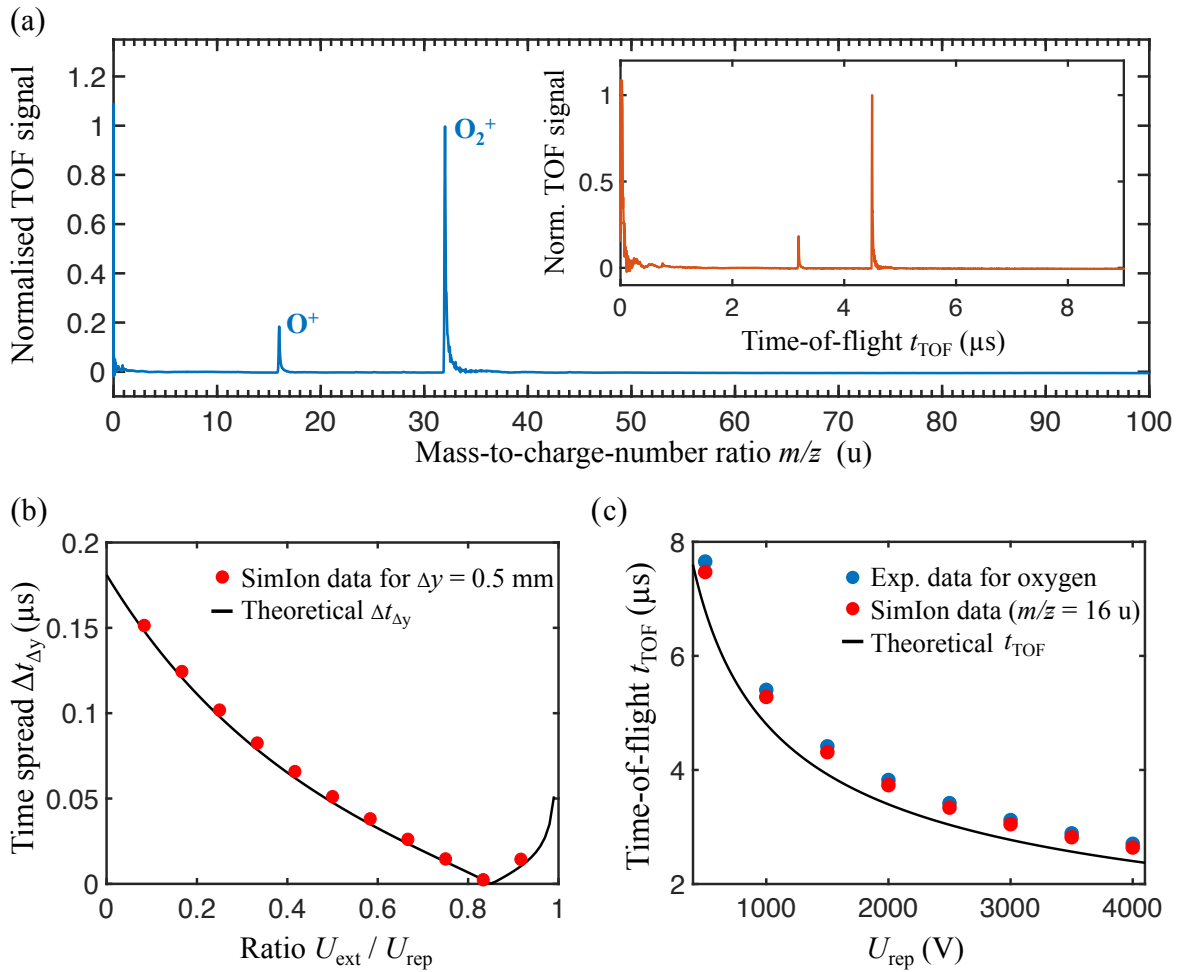


**Figure 3.20** (a) Time-of-flight mass spectrum of molecular oxygen ionised and dissociated by 225 nm laser radiation. The inset shows a raw TOF spectrum as obtained directly in the experiment. The x-axis of the plot was transformed from $t_{TOF}$ to the mass-to-charge-number ratio via Equation (3.12). Intensities are normalised with respect to the strongest signal. (b) Simulated and theoretical time spread at the detector between two identical molecules but with a different ionisation positions ($\Delta y = 0.5$ mm). The spread can be minimised by adjusting the ratio of the voltages applied to the extractor and repeller. The ideal ratio was determined to be $U_{ext}/U_{rep} \approx 0.85$. (c) Time of flight for different repeller voltages as observed in the experiment and simulated with SimIon. The extractor voltage was kept at $U_{ext} = 0.85 \cdot U_{rep}$. The theoretical values assume homogeneous extraction fieds resulting in a small deviation from the experimental and simulated values.

**Time-of-flight mass spectrometry after chemi-ionisation**

Neutral reaction products are ionised by laser radiation in the timescale of a laser pulse (ns-fs), which is negligible compared to the average flight time of the ions to the detector ($\mu$s). Therefore, in continuous extraction fields sufficient separation in the time of flight of particles with different mass-to-charge ratios can be achieved. This is not the case for chemi-ionisation reactions, in which the ionic reaction products are generated for the entire duration of the overlap between the crossed atomic and molecular beams, which is in the order of tens of microseconds. This timescale is significantly longer than the difference in flight time achieved for ions with different $m/q$-ratios and hence prevents any mass identification based on the arrival time at the detector as long as the product ions are extracted by a continuous electric field. This can be solved by time-dependent extraction fields, for which initially the electric field is switched off before it is suddenly generated by pulsing the potentials applied to the extraction electrons. This allows extraction of all product ions simultaneously, which again enables recording mass spectra based on the flight time of ions with different $m/q$-ratios. A typical mass spectrum obtained for the chemi-ionisation reaction of metastable neon with ground-state argon is displayed in Figure 3.21a. Besides products resulting from Penning ionisation of trace gases in the background vacuum ($H_2O^+$, $Ne^+$, $N_2^+$, $O_2^+$), the Penning ionisation product ($Ar^+$) and the associative ionisation product ($NeAr^+$) are the dominating species observed in the mass spectrum. The experimental mass resolution of the spectrometer utilising pulsed extraction fields was estimated from the $Ar^+$ peak resulting in $R = m/\Delta m \approx 40/0.1 = 400$.

The time-dependent extraction fields complicate the conversion from the experimentally recorded $t_{\mathrm{TOF}}$ to the final $m/z$-spectrum as the precise values of the extraction fields are unknown. For the experimental calibration of a TOF mass spectrum it is therefore handy to summarise all relevant experimental parameters of Equation (3.12) into a single constant $C_{\mathrm{exp}}$. The mass-to-charge-number-ratio ($m/z$) as function of $t_{\mathrm{TOF}}$ can then simply be written as

$$\frac{m}{z} = C_{\mathrm{exp}}(t_{\mathrm{TOF}} + t_{\mathrm{offset}})^2, \qquad (3.17)$$

with $t_{\mathrm{offset}}$ a fitting parameter accounting for the uncertainty in the definition of $t_{\mathrm{TOF}} = 0$. The TOF-MS detector can then be calibrated by fitting the measured $t_{\mathrm{TOF}}$ of particles with known $m/z$-ratios to Equation (3.17) as done in Figure 3.21b, resulting in a calibration constant of $C_{\mathrm{exp}} = 1.62$ and a time offset $t_{\mathrm{offset}} = 0.31$ $\mu$s.

While operating the TOF-MS detector with pulsed extraction fields, unwanted ions in the metastable beam, which might be generated by intrabeam Penning ionisation, are no longer discarded from the interaction region as long as the fields are switched off and might participated in undesirable ion-neutral reactions. To prevent any unwanted ions

(a)



(b)

(c)
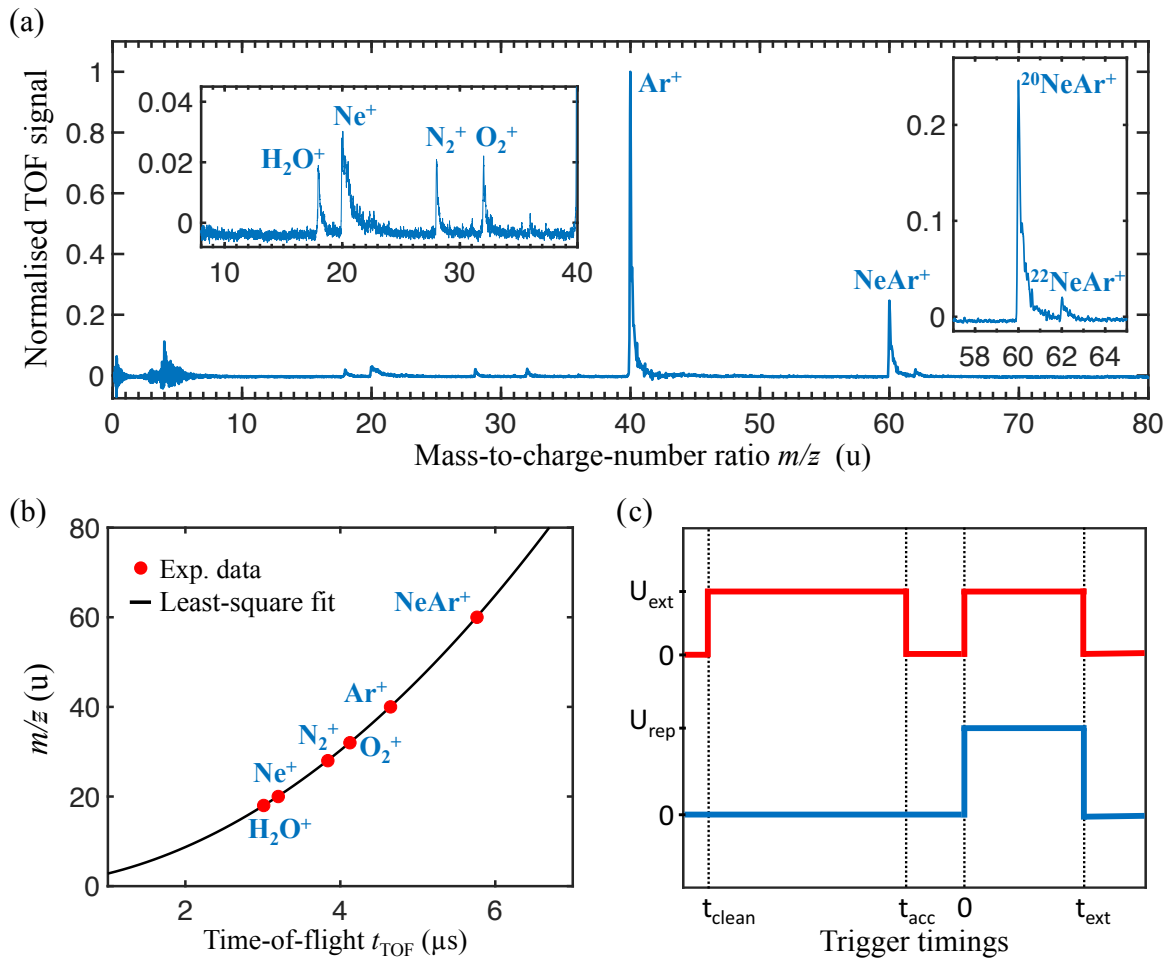
**Figure 3.21** (a) Time-of-flight mass spectrum of products of the chemi-ionisation reaction of metastable neon with argon. The mass spectrum was taken by simultaneously extracting all ions by pulsed electric fields. Intensities are normalised with respect to the strongest signal. Insets show magnifications of the mass spectrum as indicated by the x-axis values. (b) Experimentally recorded $t_{\text{TOF}}$ for particles with known $m/z$-ratios. The data is reproduced by a least-square fit of Equation (3.17) ($C_{\text{exp}} = 1.62$, $t_{\text{offset}} = 0.31\ \mu s$). (c) Typical switching sequences of the potentials applied to the extractor (red) and repeller (blue) electrode for one experimental cycle. A clean-up pulse is applied to the extractor electrode to prevent unwanted ions from entering the setup.

from entering the reaction region a clean-up pulse was applied to the extractor electrode. The resulting electric field deflects all incoming ions and prevents accumulation of ions in the detection region. Typical switching sequences of the potentials applied to the repeller and extractor electrodes are given in Figure 3.21c. Typical experimental timings are a clean-up pulse with a duration of 100 $\mu s$, followed by an accumulation time of 1 $\mu s$ and finally a 1 $\mu s$-extraction pulse ($t_{\text{clean}} = -101\ \mu s$, $t_{\text{acc}} = -1\ \mu s$, $t_{\text{ext}} = 1\ \mu s$, $U_{\text{rep}} = 3000$ V, $U_{\text{ext}} = 2235$ V).

## Time-of-flight data acquisition software

The data-acquisition of the TOF-MS data is done by a home-written program using the *LabVIEW* software package from *National Instruments*. The software allows control of all relevant parameters of the oscilloscope, which processes the signal obtained from the MCP, and directly visualises the acquired data in real time on a user friendly graphical-user interface (GUI) (Fig. 3.22).
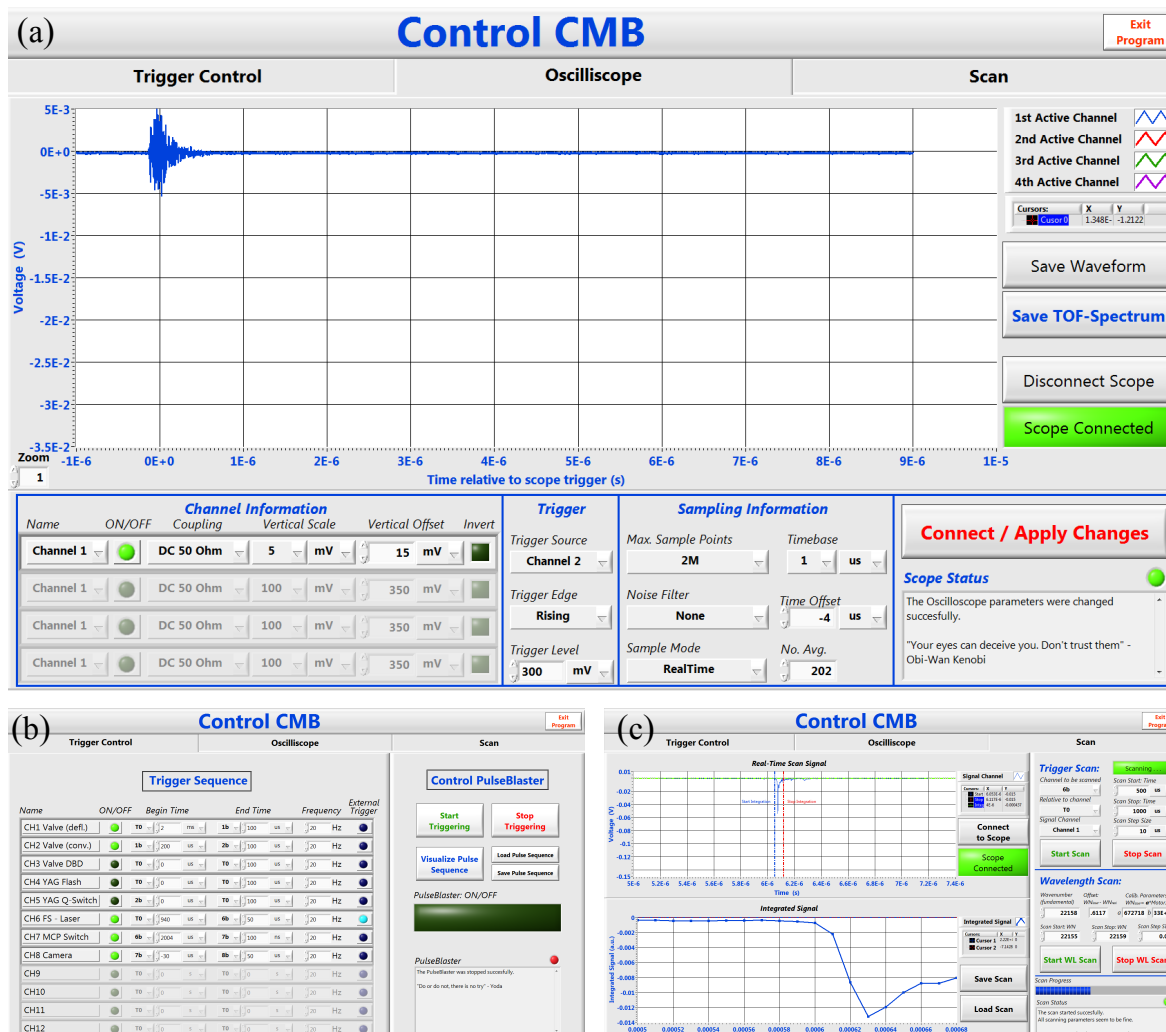


**Figure 3.22** GUI of the CMB control software displaying the tab for (a) the oscilloscope control and data acquisition, (b) the tab for the triggering-system control and (c) the tab for automatic scans of the laser and trigger timings.

The software allows controlled long-term averaging of data produced in many experimental cycles and provides a routine to standardise the data-acquisition process. The software also provides control of the triggering system and relevant ionisation lasers. The triggering system provides communication between different hardware devices of

the crossed-molecular beam setup utilising electronic 3.3 V-TTL pulses, which are produced by a commercially available delay generator (PulseBlasterESR-PRO from Spin-Core Technologies) capable of providing 24 independent programmable trigger pulses. Combining the trigger system and laser control with real-time data acquisition in a single software suite allows performing automatic scans of the TOF-MS signal with respect to certain trigger timings and recording scans with respect to the wavelength of the ionisation laser. This is very useful in optimising different aspects of the crossed-molecular-beam setup and additionally allows automatic recordings of REMPI spectra or valve-laser-delay scans as e.g. shown in Section 3.3.

### 3.5.3  Velocity-map imaging

Velocity-map imaging allows probing the dynamics of reaction and dissociation processes in gas-phase experiments [179]. It was first introduced by Eppink and Parker in 1997 [105, 178] as an advancement from standard ion imaging [104, 180, 181] and since then adapted in many areas of gas-phase research [15, 182, 183]. The principal of VMI detectors has been explained in detail elsewhere, e.g. Ref. [179], and here only the most relevant principals are described.

After ionisation, the reaction products are accelerated by an external electric field towards a position-sensitive particle detector. In a VMI spectrometer. the electric field is designed in such a way that all ions with the same initial velocity vector $\vec{v}_\mathrm{i}$ are mapped on the same point $P$ on the detector independent of their ionisation position as schematically illustrated in Figure 3.23a. The equipotential lines of a typical electric field, as e.g. used by the simple VMI detector described here, was visualised using SimIon and is presented in Figure 3.23b.

In a conventional detector the three-dimensional velocity distribution of products generated by a collision or photodissociation event is crushed on the two-dimensional surface of the particle detector. Particles with the same absolute velocity component perpendicular to the detection axis $v_{x,z}$ are mapped on the detector in a circle with radius $R$, which can be derived by Newton's equations of motion and is given by

$$R = Nd\sqrt{\frac{m}{2qU_\mathcal{E}}}v_\mathrm{x,z},\qquad(3.18)$$

with $N$ a magnification constant depending on the design of the electric field, $d$ the distance between the ionisation position and the detector plane and $U_\mathcal{E}$ the electrostatic potential at the point of ionisation [179]. The magnification constant $N$ is unique to each VMI-spectrometer and needs to be calibrated. For practical reasons, it is advantageous to summarise all experimental parameters into a single calibration constant $C_\mathrm{N}$.
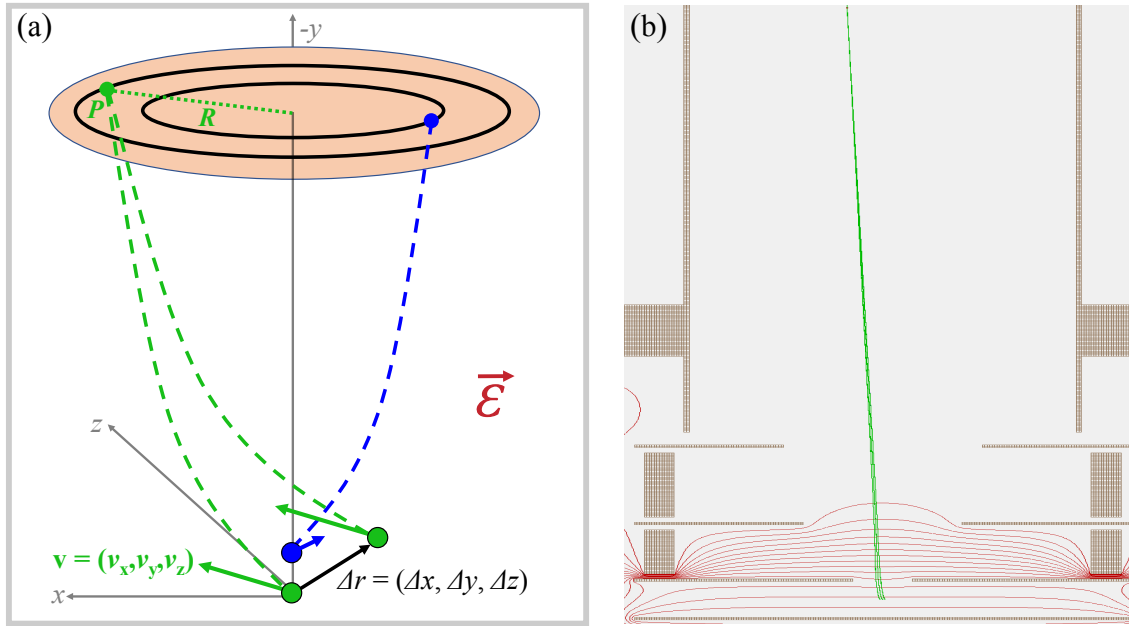
**Figure 3.23** (a) Schematic illustration of the working principle of a velocity-map-imaging detector. Ions with the same initial velocity are focused on the same point P on the detector, independent of their ionisation position. (b) Visualisation of the electric field generated by the ion-extraction electrodes under VMI-focusing conditions in our setup as simulated with SimIon. The red lines mark equipotential lines from 3000 V to 0 V in steps of 200 V.Green lines show typical trajectories of extracted ions generated in a cubic ionisation volume of $(1 \times 1 \times 1)$ mm$^3$ with same initial velocities.

The recoil velocity of an ion with a given $m/z$-ratio can then directly be determined from $R$ and the detector specific calibration constant using the relation

$$v_{x,z} = C_N R \sqrt{\frac{z}{m}}. \tag{3.19}$$

The VMI stack was characterised using the photodissociation process of molecular oxygen after multi-photon excitation by 225 nm laser radiation as described in detail in Ref. [178]. In short, after excitation by two photons to the $3d\pi(^3\Sigma_{1g})$-Rydberg state, a third laser photon can generate a superexcited O$_2^*$, which then directly dissociates into neutral oxygen atoms or first auto-ionises into O$_2^+(X\ ^2\Pi_g)$ or O$_2^+(a\ ^4\Pi_u)$. Absorption of a fourth photon can then result in the dissociation of the molecular ion or into ionisation of excited oxygen atoms from the direct neutral dissociation pathway. Both channels result in atomic oxygen ions (O$^+(^4S)$, O$^+(^2D)$) with a well-defined recoil velocity, which purely depends on the dissociation process and is independent of any experimental parameters. The dissociation channels relevant for the here described calibration are summarised in Table 3.2. A complete overview is given in Ref. [178].

If the dissociation laser is polarised in the detector plane, the $O_2$ molecules predominantly dissociate along the polarisation direction and imaging the dissociation products results in well-defined rings on the detector. The radii of these rings depend on the recoil velocity as described in Equation (3.18).

**Table 3.2** $O_2$ dissociation processes at 225 nm radiation according to Ref. [178].

| Label | Process [178] | $E_{kin}$ (eV) [178] | $v_{recoil}$ (m/s) |
|---|---|---|---|
| I | $O_2 \xrightarrow{3h\nu} O_2^* \to O(2p^4\ ^3P) + O^*(3p\ ^3P) \xrightarrow{1h\nu} O(^3P) + O^+(^4S)$ | 0.43 | 1610 |
| II | $O_2 \xrightarrow{3h\nu} O_2^* \to O(2p^4\ ^3P) + O^*(3p\ ^5P) \xrightarrow{1h\nu} O(^3P) + O^+(^4S)$ | 0.68 | 2025 |
| III | $O_2 \xrightarrow{3h\nu} O_2^* \to O_2^+(X\ ^2\Pi_g) \xrightarrow{1h\nu} O(2p^4\ ^3P) + O^+(^2D)$ | 1.34 | 2843 |
| VI | $O_2 \xrightarrow{3h\nu} O_2^* \to O(2p^4\ ^3P) + O^*(3s\ ^5S) \xrightarrow{1h\nu} O(^3P) + O^+(^4S)$ | 2.28 | 3708 |
| V | $O_2 \xrightarrow{3h\nu} O_2^* \to O_2^+(a\ ^4\Pi_u) \xrightarrow{1h\nu} O(2p^4\ ^3P) + O^+(^4S)$ | 3.25 | 4427 |

Technically, a pulsed molecular beam of 5 % molecular oxygen seeded in helium was produced by expanding 20 bar of the gas mixture into vacuum by the CRUCS valve. The resulting supersonic jet of $O_2$ molecules was intersected under an angle of 45°in the centre of the ion-extraction electrodes by the 225.05 nm-output of a Narrow Scan Radiant Dye dye laser (Narrow Scan from Radiant Dyes Laser & Acc. GmbH), pumped by a solid-state Nd:YAG laser (InnoLas SpitLight 1000). The extraction field was generated by applying a fixed voltage to the repeller and extractor electrode, while grounding the third and fourth electrode. The resulting field is displayed in Figure 3.23b. This field accelerated the ions towards a 75 mm MCP stack coupled to a phosphor (P46) screen. The different arrival time of products with different $m/z$-ratios at the detector allows detection of only specific ions by mass gating the detector. This was achieved by pulsing the MCP stack by an additional 500 V during the arrival time of the oxygen atoms, which takes the MCP from an idle state to being sensitive for arriving ions. Mass gating the detector significantly reduces the detection of unwanted background ions. The phosphor screen is read out by a fast camera and the resulting image is thresholded, centroided and event-counted [167] in real-time by a home-written software package. The resulting accumulated images are shown in Figures 3.24 and 3.25. To avoid any impact of Coulomb repulsion between generated ions, the laser power was reduced until on average less than one ion was detected per laser shot.

The width of the dissociation rings is a measure of the focusing ability of the detector, which can be tuned by adjusting the voltages applied to the repeller and extractor electrode as illustrated for the photodissociation process of $O_2$ in Figure 3.24. Experimentally, the best focusing conditions were found by adjusting the extractor voltages until the width of the rings were minimised. The best focusing condition was achieved for a ratio of $U_{ext}/U_{rep} = 2235\ V/3000\ V \approx 0.75$, which agrees with SimIon simulations.
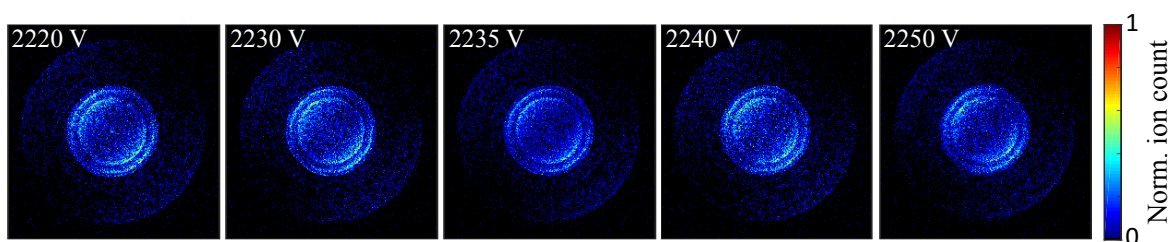
**Figure 3.24** VMI images of $O^+$ ions obtained from the photodissociation process of $O_2$ at 225.05 nm radiation.. The different panels show the same image for different extractor voltages as indicated in the figure. The voltage of the repeller was $U_{\text{rep}} = 3000$ V for all images. Best velocity resolution was obtained for $U_{\text{ext}} = 2235$ V. Images show the result of 30.000 experimental cycles with roughly 20.000 accumulated ions per image. Each images is normalised with respect to the pixel with highest intensity.

Figure 3.25a gives a VMI image of the same photodissociation process under the best focusing conditions and with greater statistics. Figure 3.25b shows the same data on a logarithmic scale, which accentuates the rings with weaker intensity occurring at larger radii. Integration of the VMI images over the angular coordinate results in the radial product distribution displayed in Figure 3.25c.

In total, five different rings could be distinguished which corresponds to the maxima labelled in the radial product distribution. Matching the radii of these rings with the well-known recoil velocities of the relevant $O_2$-dissociation products results in the calibration line displayed in Figure 3.25d. The same process was repeated for different repeller voltages (with $U_{\text{ext}} = 0.75 \cdot U_{\text{ext}}$), resulting in calibration constants of $C_{\text{N}} = 4.03 \cdot 10^{-12} \frac{\text{m}\sqrt{\text{kg}}}{\text{s pixel}}$, $3.30 \cdot 10^{-12} \frac{\text{m}\sqrt{\text{kg}}}{\text{s pixel}}$ and $2.86 \cdot 10^{-12} \frac{\text{m}\sqrt{\text{kg}}}{\text{s pixel}}$, for a repeller voltage of 3000 V, 2000 V and 1500 V respectively.[1]

Determining the calibration constant only allows determination of the relative velocity differences in the centre-of-mass frame. It is essential to also determine the zero-velocity origin of the laboratory frame to be able to also measure absolute velocities, which was done by directly imaging the atomic beams of helium and argon generated by both beam valves. The neutral rare gas atoms were ionised using the radiation of a femtosecond laser. The beam spots of the different carrier gases define the axes of the beams generated by the CRCUCS and Even-Lavie valve as shown in Figure 3.26a. The intersection of both axes defines the zero-velocity origin of laboratory frame as indicated in Figure 3.26b. The calibration obtained in Figure 3.25 together with the exact location of the origin of the laboratory frame allows an accurate measurement of the beam velocities, which are necessary for precise

---

[1] I acknowledge the students A. Cavadini and R. Röthlisberger for participating in the VMI-calibration experiments for $U_{\text{rep}}$=3000 V.
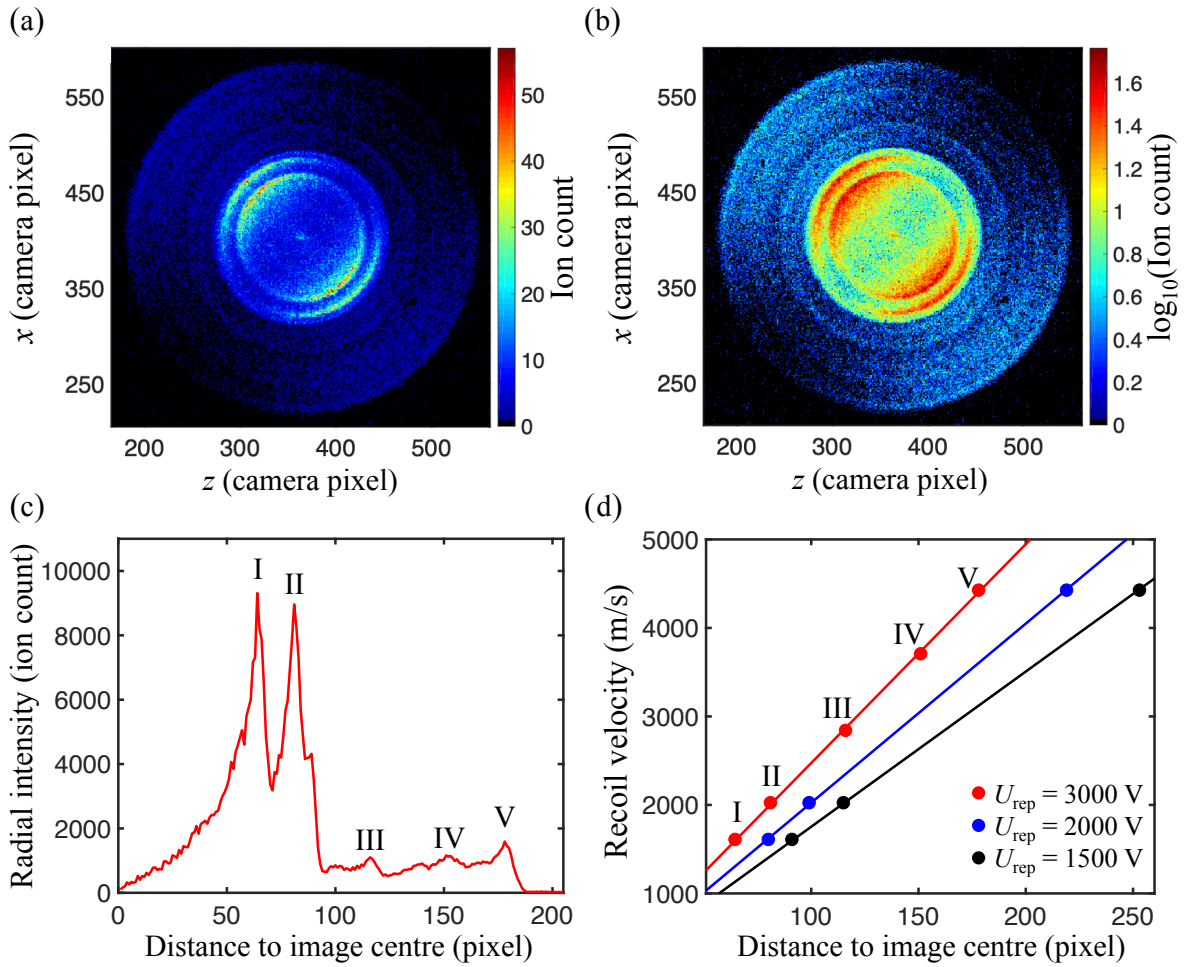
**Figure 3.25** Calibration of the VMI detector. (a) High-statistic VMI image of $O^+$ ions obtained from the photodissociation process of $O_2$ at 225.05 nm radiation. Images show the result of 500.000 experimental cycles with roughly 300.000 accumulated ions per image. (b) Same data as in (a) plotted on a logarithmic scale to accentuate rings with lower intensities. (c) Radial distribution obtained by integrating the VMI image over the angular coordinate. (d) Calibration lines obtained by relating the radii of the dissociation rings to the photodissocation processes listed in Table 3.2. Lines indicate least-square linear fits. Calibration was done for different repeller voltages ($U_{\text{ext}} = 0.75 \cdot U_{\text{ext}}$). The resulting calibration constants for different voltage configurations are given in the main text. Roman numbers in c) and d) indicate radii corresponding to the dissociation processes summarised in Table 3.2.

Monte-Carlo trajectory simulations as shown in Chapter 4. The visualisation of the beam axis also allowed the determination of the collision angle, resulting in a value of $\beta \approx 91°$.
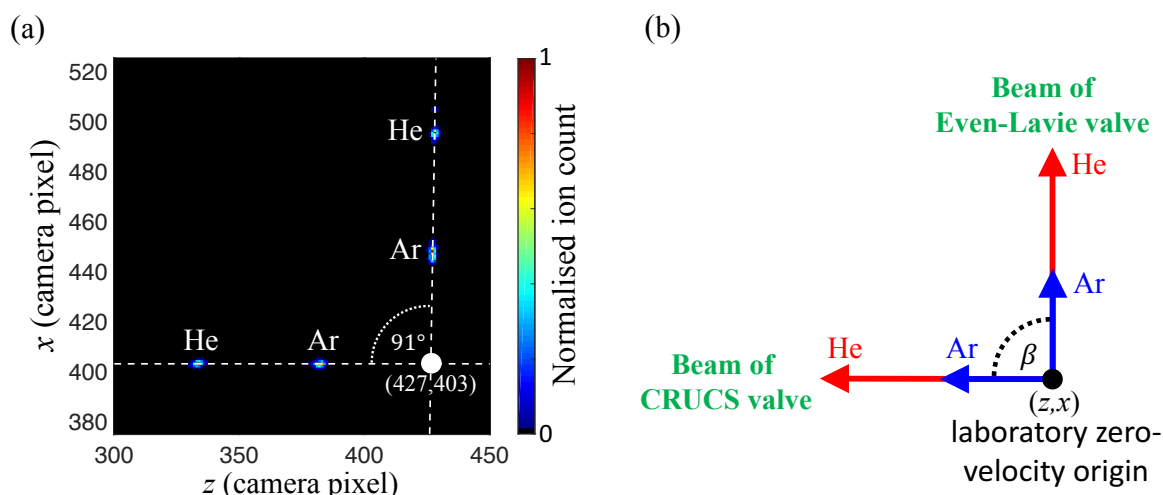
**Figure 3.26** Visualisation of the atomic and molecular beam axes. (a) Accumulation of several VMI images showing the atomic beams of helium and argon generated by the Even-Lavie and CRUCS valve. Each beam spot was measured separately, the images were then normalised and finally combined to the image shown here. The beam spots define the beam axes as indicated by the dashed white lines. The intersection of both lines defines the zero-velocity origin of the laboratory frame. The angle between both beam axes was determined to be $\beta \approx 91°$. (b) Schematic illustration of the beam axes for the Even-Lavie and CRUCS valve, including the laboratory zero-velocity origin and the collision angle $\beta$.

The VMI detector described here is very similar to the initial design by Eppink and Parker [105]. Since then, VMI spectrometers have been continuously improved and nowadays detectors with many electrodes are standard which enables velocity mapping of ions generated in much larger ionisation volumes and feature a significantly higher resolution [15,182–186]. The detector presented here was only meant as an initial tool to gain first experience with the new setup and narrow down possible target reactions. Due to its simplicity it was clear from the beginning that it had to be updated eventually to meet nowadays standards. A good detector has to be tailored for the exact needs of the investigated processes. This being said, for chemi-ionisation reactions, which are the topic of Chapters 5 and 6, the simple detector is not suited to gain valuable insights of the reaction dynamics due to two main reasons. As described in Section 3.5.2, mass selection utilising the different flight times of reaction productions with different mass-to-charge ratios is not straightforward for chemi-ionisation reactions and demands switching of the extraction fields. Pulsing the extraction voltages disturbs the carefully designed extraction fields and makes velocity-map imaging in combination with mass gating of the reaction products very difficult. In contrast, when the extraction fields are not switched only an accumulated image of all reaction products and background ions

can be achieved, which becomes complex for reactions involving polyatomic reactants. The second shortcoming of the current detector is its limited number of extraction electrodes, which makes it only suited for small ionisation volumes as e.g. achieved after laser ionisation of reactions resulting in neutral products. For these kind of experiments, the VMI detector presented here was very useful in characterising the fluorine radical discharge as it allowed to distinguish the fluorine radicals from the precursor molecule $F_2$ [127]. In chemi-ionisation reactions, however, the ionisation volume is not determined by the small cross section of the ionisation laser but by the overlap of the two intersecting beams, which is more than an order of magnitude larger. For such a large ionisation volume, a VMI stack with only a few electrodes as used here is not able to decouple the ionisation position from the velocity component of the product ions and no proper velocity mapping is possible. VMI detectors with a larger number of electrodes feature extraction fields with a softer focus which enables velocity-mapping conditions also for large ionisation volumes [184]. Both problems can be solved by implementing an electron-ion coincidence VMI detector [187] as e.g. recently introduced by the group of Edvardas Narevicius [45]. Such a detector works for large ionisation volumes and the combined information of electron and ion arrival times allows a software-based product identification which makes conventional mass gating obsolete. A similar detector is already under development in our laboratory and its implementation will significantly improve the information gained from chemi-ionisation reactions investigated by the crossed-molecular-beam setup.

**Velocity-map imaging software**

A reliable software package is needed for proper velocity-map imaging which processes the raw data obtained from the camera to thresholded, centroided and event-counted images. As discussed in Section 3.5.1, the long free-flight distance of the deflected molecular beam results in lower beam densities compared to conventional CMB setups which need to be compensated by higher experimental repetition rates. Therefore, a fast VMI analysis and acquisition software is needed, which allows for real time analysis and visualisation of the experimental data for repetition rates up to several hundred Hz.

For this purpose a new software was developed in our laboratory, which is completely written in *Python 3* and exploits the open-source *NumPy* library for fast processing and computation of multi-dimensional arrays and matrices. Communication between the program and the camera reading out the phosphor screen is provided by the *PyuEye-4.90.0.0* wrapper for uEye API functions. This makes the program compatible with all uEye cameras from IDS, which provide a broad selection of cost-efficient and

fast cameras well suited for reading out phosphor screens in velocity-map imaging applications. The software combines the control of all necessary camera properties, such as adjustment of the area-of-interest (AOI), exposure time and repetition rate, with a real-time data analysis including thresholding, centroiding and event counting, in a user-friendly graphical-user interface (GUI). The image of sequential shots is updated continuously and directly displayed in the GUI together with additional information as e.g. the number of accumulated shots and recorded ion hits. The program possesses a multi-threaded software structure to allow the processes connected to the data analysis and image visualisation happening independently from the camera control functions of the GUI. The GUI of the BASECC (**B**asel's **A**cquisition **S**oftware for **E**vent-**C**ounted and **C**entroided Images) Images software suit is shown in Figure 3.27a, together with image sections displaying the various stages of the data analysing algorithm.
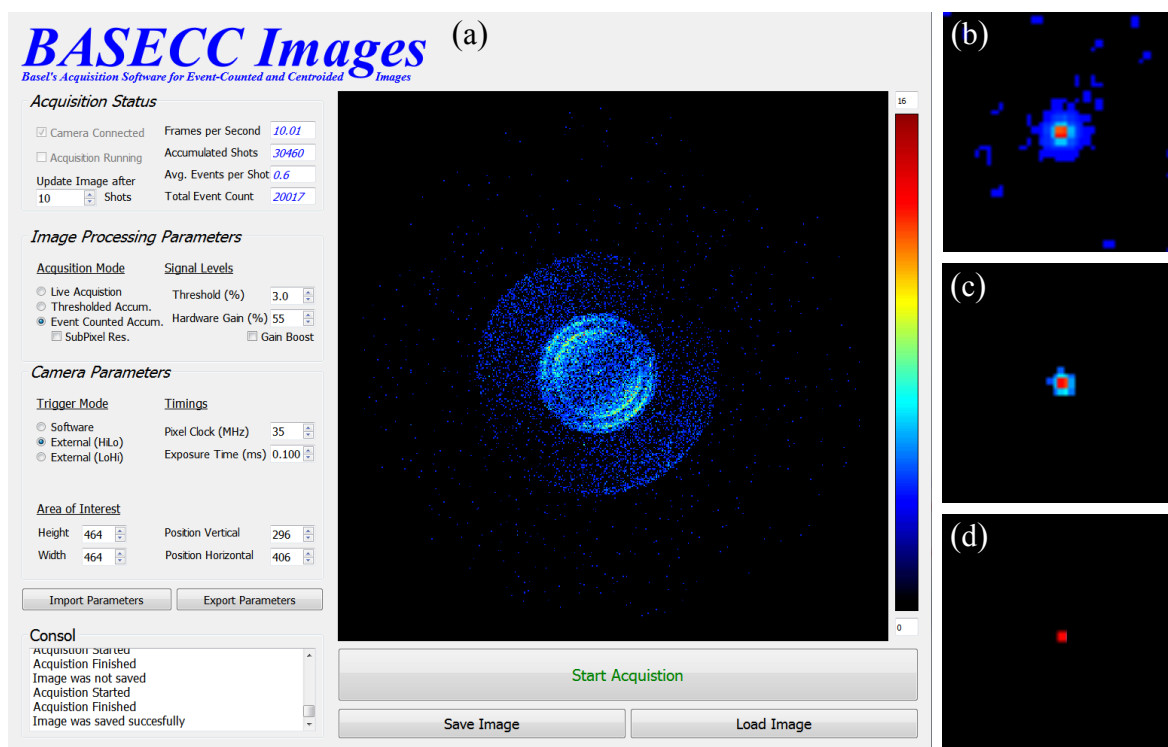


**Figure 3.27** (a) GUI of the VMI software. The software combines the control of all necessary camera properties with a real-time data analysis including thresholding, centroiding and event counting. The side panels show image sections displaying a single ion on the various steps of the data processing: (b) the raw data as obtained form the camera, (c) a thresholded image with removed background noise and (d) a centroided and event-counted image of a single ion.

The principles of thresholding, centroiding and event counting analysis have been described elsewhere [167]. In short, the raw images are first thersholded to remove signal caused by dark counts of the CMOS sensor and by background ions randomly hitting the MCP detector. In a second step, the remaining ion events, consisting out of spots spanning several dozen pixels, are reduced by a reliable and robust centre-of-mass algorithm to a single pixel, which represents the mean impact position of the ion. This process is known as centroiding. In a final step, these single-pixel events are even-counted over many experimental cycles into a single imaging matrix which makes the final thresholded, centroided and event-counted velocity-map image. The centre-of-mass centroiding algorithm employed in the software allows event-counting also with subpixel resolution [188, 189]. This possibility is also implemented in the software but is not used in the images displayed throughout this thesis. All relevant analysing parameters such as the threshold level can be directly adjusted by the operator. The software allows the operator to choose between three different acquisition modes; the *live-acquisition mode* displaying the raw data as recorded by the camera directly from the phosphor screen, the *thresholded accumulation mode* showing thresholded images and finally the *event-counted mode* for thresholded, centroided and event-counted images.

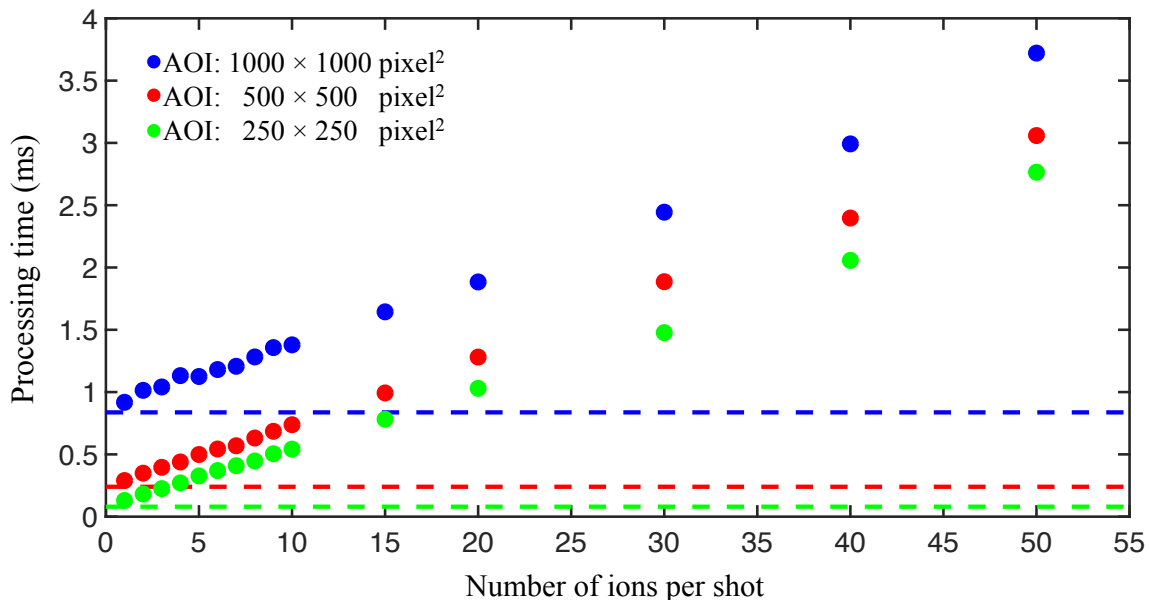The speed of the analysis algorithm for the event-counted images has been measured



**Figure 3.28** Processing time of the thresholding, centroiding and event-counting algorithm of the BASECC imaging software on a standard personal computer. The processing time of the thresholding step is independent of the number of detected ions per shot and is indicated for each area-of-interest (AOI) by the dashed vertical lines.

61

for randomly generated input matrices with a specified number of ion events. Each of these events consists in average out of ten adjacent pixels with a circular Gaussian intensity distribution, imitating experimentally recorded ion hits. The measured speed of the image-processing algorithm for several different area-of-interests (AOI) of the camera is displayed in Figure 3.28.

The processing time of the thresholding step is independent of the number of detected ions as indicated by the dashed lines in the figure. Typically VMI images are recorded with less than one ion per laser shot to avoid Coulomb interactions between multiple ions. The time necessary to read out the image from the camera was determined to be less than 1 ms for the largest AOI. Therefore, even for the biggest AOI the software package executes fast enough to perform image acquisition and real-time analysis up to an experimental repetition rate of several hundred Hz.

## 3.6   Summary

This chapter introduced a novel crossed-molecular-beam apparatus featuring an electrostatic deflector in one of the molecular beams, which allows the investigation of state- and geometry-specific effects in bimolecular reactions under single-collision conditions. The implementation of the electrostatic deflector introduces a new approach in controlling molecular reactants prior to collision events, which also allows the manipulation of molecules in strong-field seeking states [74], which makes the new setup a valuable addition to the existing CMB-landscape. The discharge source developed for the present setup is capable of producing high-density molecular beams of free radicals [127] and metastable species paving the way for the investigation of state- and conformer-specific effects in chemi-ionisation and radical reactions. The new setup features a combined detector to identify reaction products by time-of-flight mass spectrometry and probing reaction dynamics by velocity-map imaging. A summarising schematic overview of the new setup containing all relevant dimensions of the two crossed beams is given in Figure 3.29.

The power of the electrostatic deflector in separating molecules in different rotational states or in different structural isomers is in detail described in Chapter 4. The capabilities of the new setup for studying rotational-state and conformational effects in atom-molecule reactions are demonstrated in Chapters 5 and 6 on the chemi-ionisation reactions of metastable neon with carbonyl sulfide (OCS) and hydroquinone (HYQ), respectively.
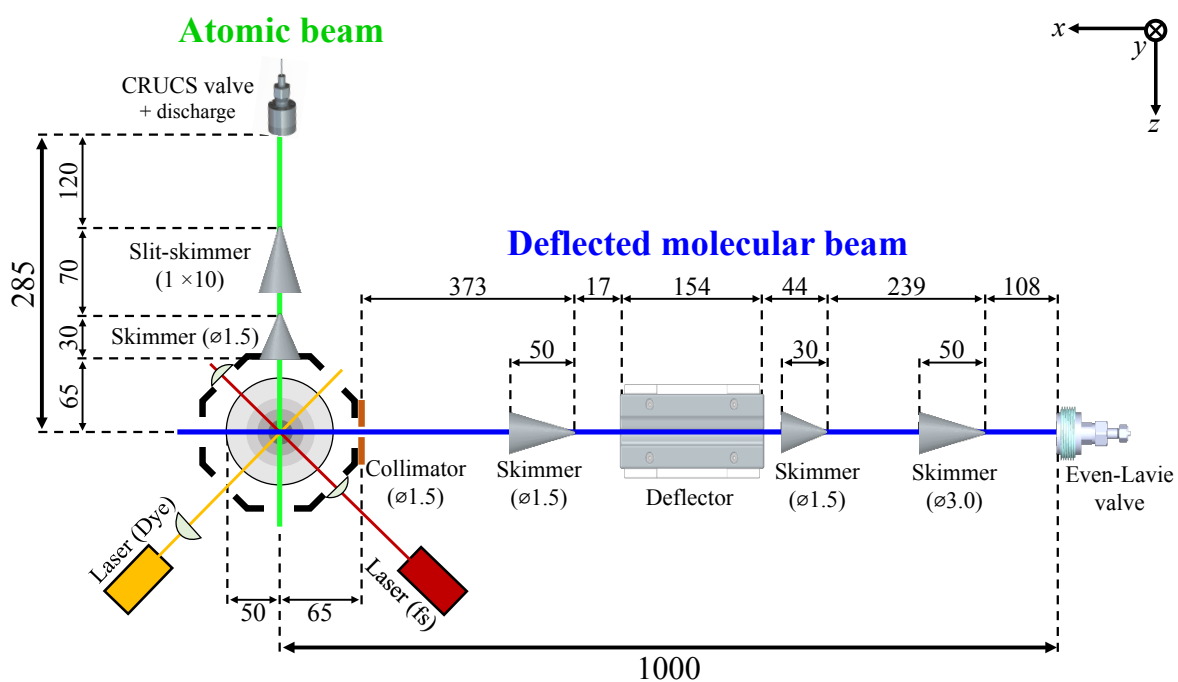
**Figure 3.29** Schematic overview of the novel crossed-molecular-beam apparatus. The deflected molecular beam crosses with an atomic beam of radicals or metastable species in the centre of a particle detector for time-of-flight mass spectrometry or velocity-map imaging. All dimensions are in millimetres.

# 4

# Deflecting strong-field-seeking molecules

The ability to separate different rotational states and conformers of one of the reaction partners is the unique feature of the crossed-molecular-beam setup described in this thesis. This chapter is dedicated to explain the theoretical background of separating different species by the interaction of their dipole moment with an external electric field, to describe the Monte-Carlo trajectory simulations used to predict the interaction of the molecular beam with the electric field of the deflector and to demonstrate with the examples of carbonyl sulfide (OCS) and hydroquinone how the new setup is able to separate different rotational states and conformers, respectively.

## 4.1   Molecules in external electric fields

The quantum-mechanical eigenstates of a molecule can be calculated by solving the Schrödinger equation, which is in its most general form given by

$$H\Psi = E\Psi, \tag{4.1}$$

where $\Psi$ denotes the wavefunction of the molecule, $E$ its internal energy and $H$ the Hamiltonian operator in the molecular centre-of-mass frame [190]. The internal energy of a molecule is given by the sum of the individual components for the electronic energy $E_{\mathrm{elec}}$, the vibrational energy $E_{\mathrm{vib}}$ and the rotational energy $E_{\mathrm{rot}}$ [191], i.e.

$$E = E_{\mathrm{elec}} + E_{\mathrm{vib}} + E_{\mathrm{rot}}. \tag{4.2}$$

In the experiments presented here all molecules are studied after the supersonic expansion of a molecular beam, which yields the overall majority of molecules in their

electronic and vibrational ground state, whereas multiple rotational states still can be populated. Therefore, this chapter focuses primarily on the rotational properties of molecules in external electric fields. While this section can only provide a reproducing summary on the theoretical aspects which are most relevant to the content of this thesis, extensive literature is available on this topic, e.g. see references [3, 192–194].

## 4.1.1 Rotating molecules

In the absence of any external field, the rotation of closed-shell molecules can be described by the field-free rotational Hamiltonian $H_{\mathrm{rot}}$. Here the molecules will be treated as rigid rotors. This approximation does not consider centrifugal distortion and vibrational averaging contributions, but the impact of these effects on the energy structure of the molecules is small compared to the contributions from the rigid rotor approximation and the effects generated by an external electric field and can be neglected for the deflection experiments of the molecules described in this thesis.

In this case, the field-free rotational Hamiltonian of closed-shell molecules can be expressed by components of the total angular moment $J$ and the principal moments of inertia $I$ along the three principal axis of the rigid rotor (here denoted by $a$, $b$, and $c$)

$$H_{\mathrm{rot}} = \frac{h^2}{4\pi^2} \left( \frac{J_a^2}{2I_a} + \frac{J_b^2}{2I_b} + \frac{J_c^2}{2I_c} \right),$$ (4.3)

with $h$ the Planck's constant [192, 193]. The rotational Hamiltonian can also be expressed in terms of the rotational constants defined as $A = h/8\pi^2 I_a$, $B = h/8\pi^2 I_b$ and $C = h/8\pi^2 I_c$ and is then given by [192, 193]

$$H_{\mathrm{rot}} = h \left( A J_a^2 + B J_b^2 + C J_c^2 \right).$$ (4.4)

Depending on the magnitude of their principal moments of inertia, polyatomic molecules can be classified into several groups. The most simple case is the **linear rotor** in which two moments of inertia are the same (i.e. $I_b = I_c$) and the third moment is zero ($I_a = 0$) as the distance of all atoms to the bond axis is zero [192, 193]. Molecules for which two moments of inertia are the same, but the third one is non-zero are commonly referred to as **symmetric tops** [192, 193]. Depending if the magnitude of the third moment of inertia is smaller than the other two (i.e. $I_a < I_b = I_c$) or larger ($I_a = I_b < I_c$), the molecules are known to have a prolate or oblate symmetry, respectively [192, 193]. Classically this can be described as a rotation about the longer or the shorter axis of an ellipse. **Spherical-top molecules** exhibit the special case in which the magnitude of all principal moments of inertia are identical ($I_a = I_b = I_c$) [192, 193]. Because of their symmetry, spherical top molecules exhibit no net dipole moment. The

majority of polyatomic molecules belong to the group of **asymmetric-top molecules**, which have three different moments of inertia ($I_a \neq I_b \neq I_c$) [192, 193].

Quantum-mechanically, the molecular rotations can be described in terms of the total angular momentum quantum number $J$, the quantum number $K$ of the projection of $\vec{J}$ onto the principal axis of the molecule and the quantum number $M$ of the projection of $\vec{J}$ on the space-fixed field-axis in the laboratory frame, with both $K$ and $M$ being elements of $\{-J, -J+1, ..., J\}$ [192, 193].

In the absence of an external electric field, the rotational energy does not depend on the orientation of the molecule in the laboratory frame and hence states which only differ in $M$ are degenerate. In the simple case of a linear top molecule, the projection of $J$ onto the principal rotation axis of the molecule is zero ($K = 0$) and the field-free energy levels can be expressed only in terms of $J$ and the rotational constant $B$ as [192]

$$E(J) = BJ(J + 1). \tag{4.5}$$

Due to its symmetry, also the energy levels for a spherical-top molecule can be given by Equation (4.5), with the only difference that for a linear-top molecule the energy levels are $(2J + 1)$-fold degenerated, whereas the spherical-top levels exhibit a $(2J + 1)^2$-fold degeneracy [192, 193]. For a symmetric-top molecule, $K \neq 0$ as the angular-momentum vector is not longer perpendicular to the principal axis of the molecule and the degeneracy is $2(2J + 1)$ for $K \neq 0$ and $(2J + 1)$ for $K = 0$. The energy levels for a symmetric-top molecule are defined as

$$E(J, K) = BJ(J + 1) + (A - B)K^2, \tag{4.6}$$

for prolate symmetry, and by

$$E(J, K) = BJ(J + 1) + (C - B)K^2, \tag{4.7}$$

in case of an oblate symmetric-top molecule [192]. For asymmetric-top molecules, the Schrödinger equation can not be solved analytically as the rotational Hamiltonian is not diagonal for the basis set of the quantum numbers $|J, K, M\rangle$. Whereas $J$ and $M$ remain "good" quantum numbers, $K$ is not anymore. However, the rotational quantum states are lying between the limiting cases of the prolate and oblate symmetric-top cases and hence the states for the asymmetric-top molecules can be expressed in terms of the pseudo-quantum numbers $K_a$ and $K_c$, which represent the projection of $J$ on the molecular axes $a$ and $c$, respectively (with $J \leq (K_a + K_c) \geq J + 1$) [195, 196]. The field-free energy levels of an asymmetric top-molecule can then be written in the form

$$E(J, K_a, K_c) = \frac{A + C}{2}J(J + 1) + \frac{A - C}{2}E_{\text{red}}(\kappa, K_a, K_c), \tag{4.8}$$

**Table 4.1** Classification of molecular rotors [192–194, 198]

| Rotor type | Moments of inertia | Rotational Constant | Energy levels | Degeneracy |
|---|---|---|---|---|
| Linear rotor | $I_a = 0; I_b = I_c$ | $A = undef.; B = C$ | $E(J) = BJ(J+1)$ | $(2J+1)$ |
| Prolate symmetric top | $I_a < I_b = I_c$ | A>B=C | $E(J, K) = BJ(J+1) + (A-B)K^2$ | $2(2J+1)$ |
| Oblate symmetric top | $I_a = I_b < I_c$ | A=B>C | $E(J, K) = BJ(J+1) + (C-B)K^2$ | $2(2J+1)$ |
| Spherical top | $I_a = I_b = I_c$ | $A = B = C$ | $E(J) = BJ(J+1)$ | $(2J+1)^2$ |
| Asymmetric top | $I_a \neq I_b \neq I_c$ | $A \neq B \neq C$ | $E(J, K_a, K_c) = \frac{A+C}{2}J(J+1) + \frac{A-C}{2}E_{\text{red}}(\kappa, K_a, K_c)$ | $(2J+1)^2$ |

where the reduced energy, $E_{\text{red}}$, is a tabulated, numerical value depending on Ray's asymmetry parameter $\kappa$ [197], which is defined as

$$\kappa = \frac{2B - A - C}{A - C}. \tag{4.9}$$

Alternatively, the different states can be defined in respect to the (pseudo-) asymmetric-top quantum number $\tau = K_a - K_c$, which takes the values of $\tau \in \{-J, -J+1, ..., J\}$. For an asymmetric-top molecule, every J state is $(2J+1)$-fold degenerate both in $\tau$ and in $M$, resulting into a total degeneracy of $(2J+1)^2$ in the absence of an external field [192, 193]. The main properties of the different rotor types are summarised in Table 4.1.

## 4.1.2 The Stark effect

If the rotating molecules discussed above are placed in an external electric field, also the interaction of the dipole moment of the molecule with the external electric field has to be considered. This contribution is known as the **Stark effect**, which is named after Johannes Stark, who was together with Antonino Lo Surdo the first to investigate the splitting of atomic energy levels in external electric fields [199–201].

As the external electric-field vector is fixed in the laboratory frame, whereas the dipole moment is fixed in the centre-of-mass frame of the molecule, there is a strong coupling between the different molecular rotational states and the external electric field. This coupling is described by the projection of the dipole moment $\vec{\mu}$ onto the electric field vector $\vec{\mathcal{E}}$ and is defined by the Stark Hamiltonian $H_{\text{Stark}}$ given by [192]

$$H_{\text{Stark}} = -\vec{\mu} \cdot \vec{\mathcal{E}}. \tag{4.10}$$

The rotational Hamiltonian operator $H_{\text{rot},\mathcal{E}}$ for a molecule in an external electric field is then a combination of the field-free rotational Hamiltonian $H_{\text{rot}}$ and the Stark term $H_{\text{Stark}}$

$$H_{\text{rot},\mathcal{E}} = H_{\text{rot}} + H_{\text{Stark}}. \tag{4.11}$$

Solving the appropriate Schrödinger equation gives the energies for a molecule in an external electric field. This can be done for numerous different electric field strengths

yielding the energy levels $E_{\text{Stark}}(\mathcal{E})$ as function of the electric field , which are known as the Stark energy curves. The Stark effect results in a shift and splitting of the rotational energy levels of the molecule. In an external electric field the $(2J + 1)$-degeneracy of the M-components is lifted into a total of (J+1) sublevels, with a two-fold degeneracy for all $M \neq 0$ - components $(E_{\text{Stark}}(|J, K, M\rangle) = E_{\text{Stark}}(|J, K, -M\rangle))$, while the $M = 0$ - levels are not degenerate [192].

In the case of an inhomogeneous electric field, the energy levels of the molecule vary depending on the field strength $\mathcal{E}(\vec{r})$, which depends on the spatial position of the molecule defined by the position vector $\vec{r}$. Therefore it experiences a force which pushes it towards positions with decreasing energy of its eigenstates. This force is called the **Stark force** $\vec{F}_{\text{Stark}}$ and is given by [192]

$$\vec{F}_{\text{Stark}} = -\vec{\nabla}E_{\text{Stark}}(\mathcal{E}(r)). \tag{4.12}$$

This force can also be defined in terms of the projection of the dipole moment of the molecule onto the electric-field axis

$$\vec{F}_{\text{Stark}} = \mu_{\text{eff}}(\mathcal{E})\vec{\nabla}\mathcal{E}(r), \tag{4.13}$$

with the **effective dipole moment** $\mu_{\text{eff}}(\mathcal{E})$ [198]

$$\mu_{\text{eff}}(\mathcal{E}) = -\frac{dE_{\text{Stark}}(\mathcal{E})}{d\mathcal{E}}. \tag{4.14}$$

The definition of Equation (4.13) provides an intuitive description on how the molecule behaves in an inhomogeneous electric field, as $\vec{F}_{Stark}$ is directly proportional to $\mu_{\text{eff}}(\mathcal{E})$. If the effective dipole moment for a given rotational state is negative $(\mu_{\text{eff}}(\mathcal{E}) < 0)$, i.e. the energy increases with stronger applied fields, the Stark force pushes the molecules to regions of weaker field strengths. Such molecules are known to be **weak-field seeking** [51]. On the contrary, molecules with a positive effective dipole moment $\mu_{\text{eff}}(\mathcal{E}) > 0$ are called **strong-field seekers** and are attracted to field maxima [51]. With increasing field strength, the dipole moment of the molecules tend to align with the external electric field, turning also weak-field-seeking states into strong-field seekers. In the limiting case of an infinitely strong electric field, the effective dipole moments of all rotational states approach the permanent dipole moment of the molecule. In general, for larger, polyatomic molecules with increasing moments of inertia the transition from weak- to strong-field-seeking states happens at weaker field strengths due to the coupling between their closely spaced rotational levels, making these molecules exclusively strong-field-seeking at experimentally relevant field strengths. Also molecules in the rotational ground-state align with the external field and are always strong-field seeking [74].

### 4.1.3 Population of rotational-quantum states

In thermal equilibrium, the normalised population fraction $N_i$ of a given rotational eigenstate $i$ with energy $E_i$ of a molecule is defined by the Boltzmann distribution

$$\frac{N_i}{N} = \frac{e^{-E_i/k_B T_{\mathrm{rot}}}}{\sum_i e^{-E_i/k_B T_{\mathrm{rot}}}}, \tag{4.15}$$

with $k_B$ the Boltzmann constant and $T_{\mathrm{rot}}$ the rotational temperature of the thermal assembly of molecules [3]. For the population difference between two states $i$ and $j$ it simplifies to

$$\frac{N_i}{N_j} = e^{-(E_i - E_j)/k_B T_{\mathrm{rot}}}. \tag{4.16}$$

In case the eigenstate is degenerate, also the degeneracy $g_M$ for the quantum number $M$ and the nuclear spin statistical weight $g_{ns}$ of this eigenstate has to be taken into account. The population weight $w_i(T_{\mathrm{rot}})$ of the energy state $E_i$ is then given by [202]

$$w_i(T_{\mathrm{rot}}) = \frac{g_M g_{ns} e^{-E_i/k_B T_{\mathrm{rot}}}}{\sum_i g_M g_{ns} e^{-E_i/k_B T_{\mathrm{rot}}}}. \tag{4.17}$$

## 4.2 Exploiting the Stark effect: Deflecting polar molecules

The Stark force can be exploited experimentally to control polar particles with a permanent electric dipole moment, which found widespread application in manipulating particles of atomic and molecular beams. Some examples of experimental applications of the Stark effect are Stark decelerators [28–30], electrostatic-multipole focusers [20–27] and velocity selectors [203, 204] for manipulating molecules in weak-field-seeking states, whereas alternating-gradient focusers [52–61], microwave-lens systems [62–65] and laser-based optical techniques [66–69] utilise the Stark force to gain control of strong-field seekers. One of the most versatile approaches, which can be applied for both weak- and strong-field-seeking states, is the principle of **electrostatic deflection**.

In 1921, Hartmut Kallmann and Fritz Reiche proposed that neutral particles with a permanent dipole moment can be deflected from their trajectories in the presence of an inhomogeneous field. Their theory treated both the Stark effect and its magnetic-field analogue, the Zeemann effect [70]. The first experimental deflection was then also realised using magnetic fields. In their groundbreaking experiment in 1922, Otto Stern and Walther Gerlach observed that a beam of ground-state silver atoms in an inhomogeneous, magnetic field are deflected into opposite directions depending on the spin of the unpaired 5s electron. This famous Stern-Gerlach experiment provided first experimental evidence that the spin angular momentum is quantised along the external field axis [71, 72]. A couple of years later in 1927, a student of Stern, Erwin Wrede was the first to demonstrate the principle of electrostatic deflection on molecular beams of different alkali halides and was able to give a first, rough estimate of the magnitude of the electric dipole moment of potassium iodide (KI) [73].

Another substantial improvement was then the deflector introduced by Chamberlain and Zorn in 1963, which was based on a two-wire design and featured improved inhomogeneous fields [205]. A similar approach also approximating two-wire fields, but featuring a trough-rod design, has more recently proven to be very successful in separating molecules in different rotational quantum states [75–77]. As the effective dipole moment, and hence the Stark force does depend on the rotational-quantum state of the molecule, molecules in different rotational states experience a different degree of deflection and hence can be spatially separated. The same design was also successfully applied in separating conformers of polyatomic molecules [60, 74, 78–82, 84, 85, 206] and in selecting different sizes of molecular clusters [74, 206, 207].

The electrostatic deflector used in the experiments described in this thesis was developed and designed by Ref. [165]. In contrast to the trough-rod design, the geometries of the deflector discussed here are shaped in an open mechanical structure, which supports stronger electric fields and have the additional advantage of not having a physical barrier along the deflection axis [165] (for technical details see Section 3.4).

The molecular beam setup used for separating individual rotational states and conformers by electrostatic deflection for the experiment reported in this thesis is schematically shown in Figure 4.1. The resulting, deflected molecular beam can then be ionised by a femto-second laser for analysis of the spatial beam composition as done in this chapter, or can be overlapped with a second beam to investigate bi-particle reactions which is the topic of Chapters 5 and 6. Different parts of the molecular beam can be selected by tilting the valve-deflector setup in respect with the detection region. All technical details of the setup are specified in Chapter 3.
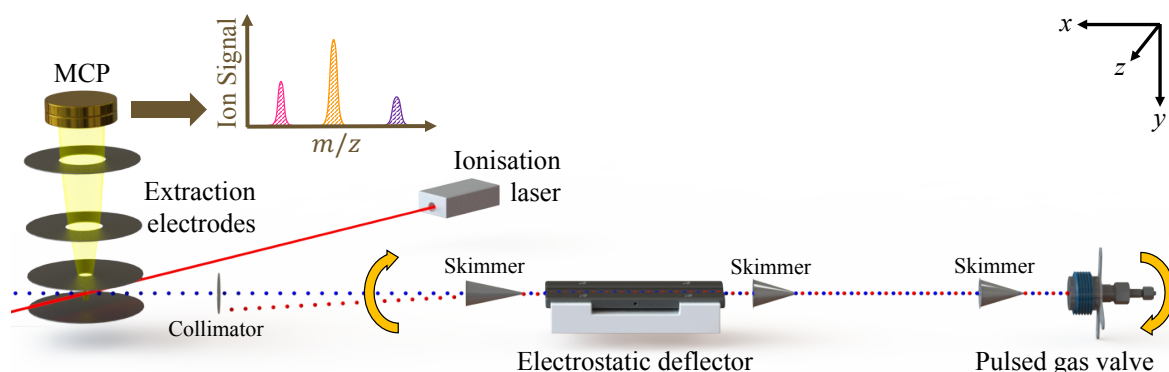
**Figure 4.1** Schematic of the experimental setup used to separate different rotational states and conformers of molecules by electrostatic deflection. Molecules are detected by TOF-mass spectrometry. The pulsed gas valve and the deflector can be tilted in conjunction with respect to the ionisation region as indicated by the orange arrows, which allows ionisation of different regions of the molecular beam.

## 4.3 Monte-Carlo trajectory simulations

For the analysis of the experimental results simulations of the behaviour of the molecules inside the inhomogeneous electric field of the deflector are essential. Additionally, such simulations play a crucial role in preparing and designing an experimental study as they provide information which, e.g. enables the selection of suitable molecules for deflection and the choice of the best suited inert seeding gases.

### 4.3.1 General introduction

Trajectories of molecules travelling from the source through the electrostatic deflector up to the reaction region were simulated using a Monte-Carlo approach implemented in home-written code [80, 84, 85], which has been adapted and extended for the deflector geometry and properties of the crossed-molecular-beam setup.

The theoretical base of the simulations is the interaction of the Stark force with the effective dipole moments of molecules in certain rotational states. The acceleration $\vec{a}$ the molecules undergo due to the Stark force is given by

$$\vec{a} = \frac{\vec{F}_{\text{Stark}}}{m} = \frac{\mu_{\text{eff}}(\mathcal{E})}{m}\vec{\nabla}\mathcal{E}(r). \tag{4.18}$$

For a constant field gradient, the acceleration is hence proportional to the ratio of the effective dipole moment over the mass $m$ of the molecule. The electrostatic deflector used here was designed to have only a non-zero component of the field-gradient along one axis, here defined along the Cartesian $y-$axis. In this case, the acceleration can be simplified into the 1D-expression

$$\ddot{y} = \frac{\mu_{\text{eff}}(\mathcal{E})}{m} \frac{\partial \mathcal{E}}{\partial y}. \tag{4.19}$$

The molecular trajectories propagating through a virtual experimental setup are calculated by numerical integration of the corresponding equations of motion using a Runge-Kutta algorithm [74, 84, 85]. The simulations are performed for a large number of molecules (typical 50k - 1M per quantum state) with a randomised starting assembly in a Monte-Carlo approach. Molecular trajectories which deviate so much from the beam axis that they collide with one of the skimmers or the deflector electrodes are discarded from the simulations. Molecules reaching the ionisation region are summarised depending on their final position along the $y$-axis into histograms, which can be directly compared to experimental deflection profiles.

### 4.3.2   Input parameters

The simulation requires several inputs whose accuracy towards the experimentally correct values determines the quality with which the simulations can reproduce, or predict, the experimentally obtained deflection profiles. The most important inputs are elucidated in the following paragraphs.

The **starting velocity distribution of the molecules** is given by a normal distribution, which mimics the experimental molecular beam directly after the supersonic expansion in the nozzle of the gas valve. The mean velocity of the particles along the molecular beam axis is here referred to as the beam velocity. The full-width-half maximum (FWHM) of this distribution along and perpendicular to the molecular beam direction are called the initial longitudinal and transverse velocity spread, respectively. The beam velocity of an experimental molecular beam can be directly measured in our setup by the calibrated VMI detector. The **initial spatial positions of the molecules** are given by a uniformly randomised distribution as the virtual nozzle opening.

The **physical geometries of the setup** and in particular the distance between the deflector and the ionisation region are essential for accurate simulations. The relevant dimensions have been extracted from a 3D-CAD model of the crossed-molecular-beam apparatus created with SOLIDWORKS and were confirmed by measuring the relevant

distances in the physical experimental setup. Note that the origin of the coordinate system in the simulations is placed at the position where the molecular beam will enter the deflector as shown in Fig 4.2.
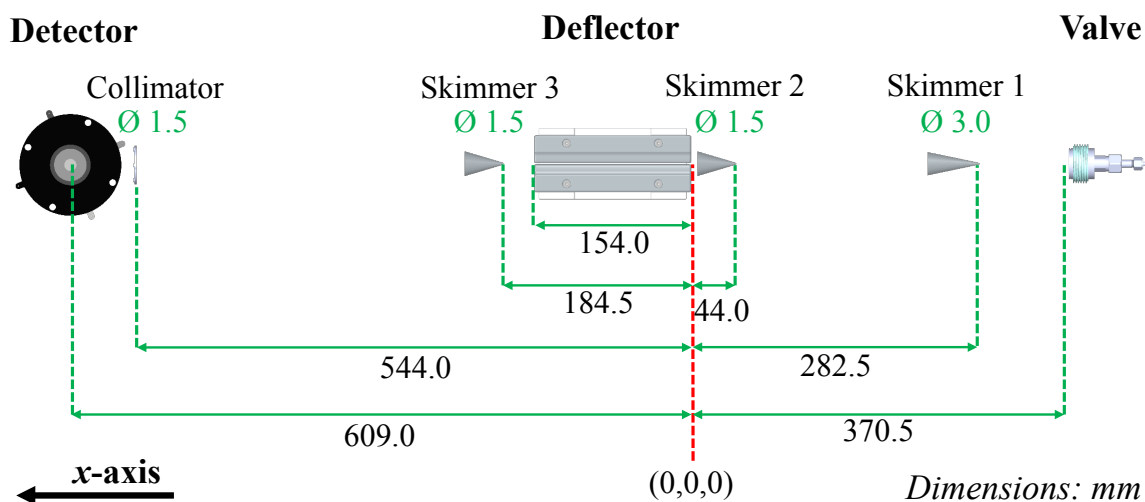


**Figure 4.2** Relevant dimensions of the experimental setup for the Monte-Carlo trajectory simulations. Especially the correct distance between the electrostatic deflector and the detector is crucial for reproducing experimentally obtained deflection profiles.

The **electric field of the deflector and its gradient** were calculated by the AC/DC module of the COMSOL Multiphysics software package. A cross section of the field in the centre of the deflector is shown in Figure 4.3 together with the partial electric-field gradients along all three Cartesian directions. The deflector geometry leads to a maximum of the electric field in the centre between the electrodes, which reaches a value of about 350 kV/cm for a potential difference of $\Delta V = 40$ kV applied across the deflector gap. The electric-field gradients along the $x-$ and $z-$axis are approximately zero in all relevant areas, whereas the field is strongly inhomogeneous along $y$. The deflector is positioned so that the molecular beam is placed 2.7 mm above the centre of the deflection electrodes as indicated by the white circle in Figure 4.3. For this arrangement, strong- and weak-field seeking molecules are deflected towards positive and negative $y$-coordinates, respectively.

The **Stark energy of the individual rotational states of the molecule** as function of the electric field strength is computed using the CMIStark software package [198], which numerically diagonalises the rotational Hamiltonian (Eq. (4.11)) for molecules in an external electric field. Other relevant molecule-specific parameters, e.g. the molecular mass and the size of the permanent dipole moment are obtained from the literature for the here investigated molecules.
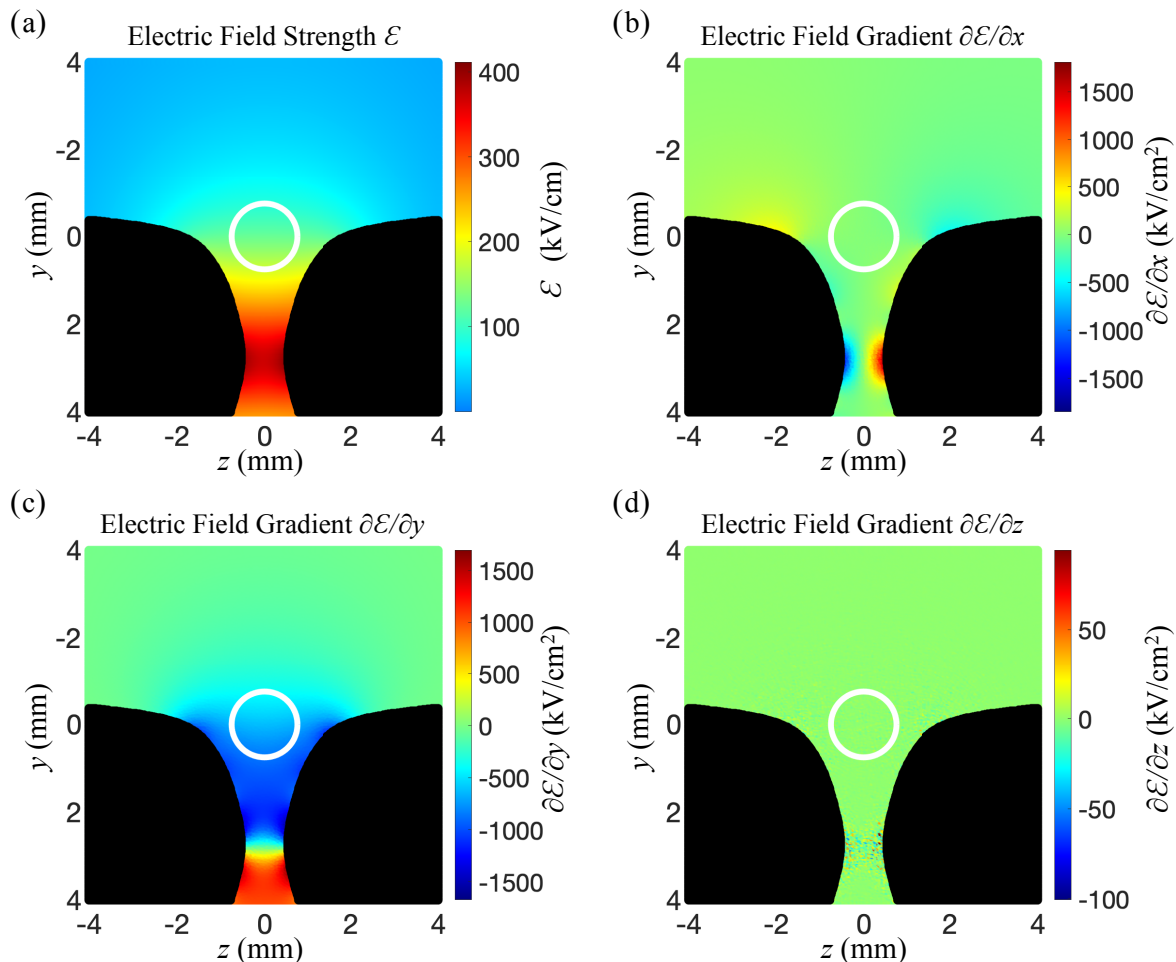
**Figure 4.3** (a) Cross sections of the electric field strength and gradients along the (b) $x$-, (c) $y$- and (d) $z$-direction for a potential difference of 40 kV on the deflector as calculated with COMSOL Multiphysics. The deflector electrodes are visualised in black and the position of the molecular beam is indicated by the white circle. The coordinate system is oriented as indicated in Figure 4.1.

## 4.3.3 Thermally averaged deflection profiles

Trajectory simulations are performed for individual quantum states $i$ yielding state-resolved density profiles $D_i$ of the molecular beam in the detection region. The thermally averaged deflection profile $D(T_{\mathrm{rot}})$ is then generated by weighting the state-resolved density profiles according to their thermal population weights $w_i(T_{\mathrm{rot}})$ (Eq. (4.17)) at a given rotational temperature $T_{\mathrm{rot}}$ according to [202]

$$D(T_{rot}) = \sum_i w_i(T_{\mathrm{rot}})D_i. \tag{4.20}$$

While reproducing experimental results, the rotational temperature of the molecules can be determined by matching the simulated thermally averaged density profiles to the experimental data by a least-square fitting procedure. If molecules with structural isomers are investigated, simulations are first run for each conformer separately and are then combined according to their populations given by the two-level Boltzmann distribution (Eq. (4.16)) assuming a thermal distribution at the temperature of the gas reservoir before expansion.

### 4.3.4   Impact of ionisation volume

Molecules in the interaction region are grouped into histograms according to their deflection position $y$. The sampling size of the histograms $d$ is closely coupled to the diameter of the experimental ionisation volume as both parameters directly effect how the spatial position of the deflected particles are averaged into the final deflection profile.

The impact of the histogram-sampling size on a simulated, undeflected beam profile is demonstrated in Figure 4.4a. A larger sampling size results into broadening of the beam profile due to an increased averaging range. For small histogram widths ($d < 0.5$ mm), the change in sampling size has only a negligible effect on the profile shape. It has to be noted that with a decreasing sampling width a larger number of molecules has to be simulated to obtain statistically converged deflection curves. E.g. the simulation profile with a sampling width of $d = 0.05$ mm in Figure 4.4a is not statically converged even for a total of 500.000 simulated molecules. The increasing computational power and calculation time makes simulations using such small histogram widths unpractical. Therefore, even for experimental data obtained for smaller ionsiation volumes, the sampling width of the simulation was not reduced below $d = 0.25$ mm throughout this thesis. That this assumption is sufficient to reproduce experimental deflection profiles obtained with a significant smaller ionisation diameter is illustrated in Figure 4.4b, which shows typical experimental deflection profiles of $OCS^+$ obtained by direct laser ionisation and in a chemi-ionisation reaction with $Ne^+$. In the latter case, the diameter of the reaction-ionisation volume is defined by the size of the overlapping molecular and atomic beams, which are both confined by collimators with a diameter of $d = 1.5$ mm directly before the reaction region. This data is nicely reproduced by a trajectory simulation assuming a sampling width of $d = 1.5$ mm. If a laser is used, the ionisation volume is defined by the beam waist of the laser beam. In this case a fs-laser was used which was strongly focused into the interaction region by a focusing lens with focal length of 70 mm. Its beam waist was experimentally determined to be $w \approx 30$ $\mu$m.
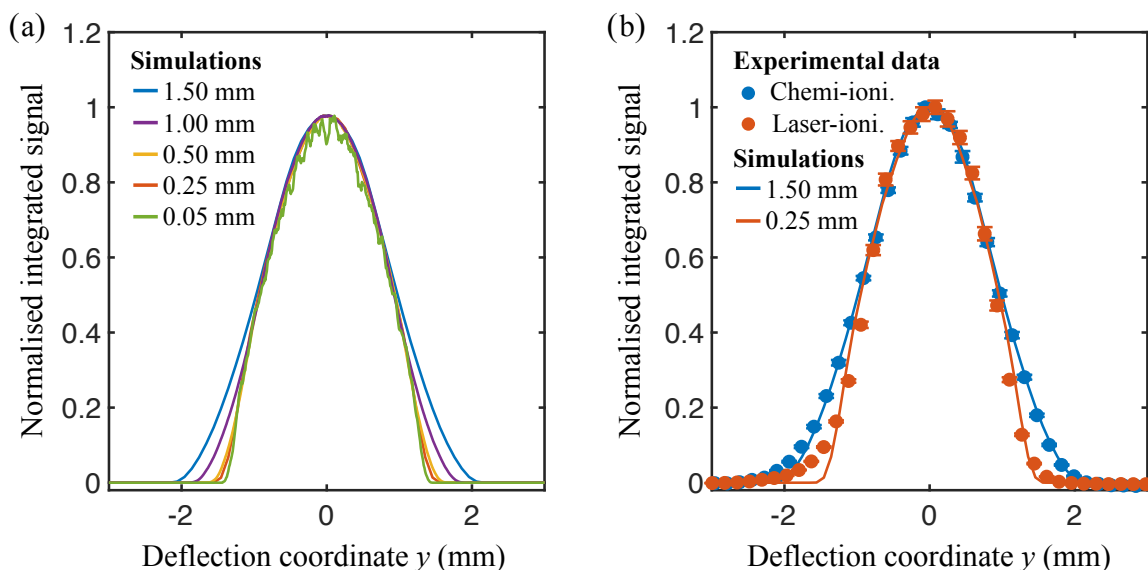
**Figure 4.4** (a) Trajectory simulations of an undeflected beam of OCS for different histogram-sampling widths and (b) a comparison to typical experimental deflection profiles of $OCS^+$ obtained by direct laser ionisation and in a chemi-ionisation reaction with $Ne^*$.

Statistically converged simulations with such a small sampling width are very time intensive. Therefore a histogram sampling size of $d = 0.25$ mm was used to simulate the experimental data obtained by the small ionisation volume of a laser, which is sufficient as can be seen from the direct comparison of simulation and experimental results (Fig. 4.4b). Furthermore, it has to be considered that the experimental step size between two data points along $y$ is typically $\sim 0.25$ mm, which makes a smaller sampling width in the simulations unnecessary as the difference in the resolution will not be resolved in the experimental data.

### 4.3.5  Technical structure and computation times

The core of the simulations is based on the CMIfly-code [74], which was adjusted by Daniel Rösch in Basel to the BaselFly-code to reproduce the results of a setup combining a deflected molecular beam with an ion trap [84, 85]. This version was then finally adapted to reproduce the deflection profiles of the crossed-molecular-beam setup presented here. The current program structure is summarised in the schematic flow diagram of Figure 4.5.

Briefly, the main calculation solving the equation of motion to obtain the molecular trajectories are done by a home-written Fortran 90 code (*Basel_Fly.f90*). The random starting distributions of the molecules are generated by the Fortran 90 script
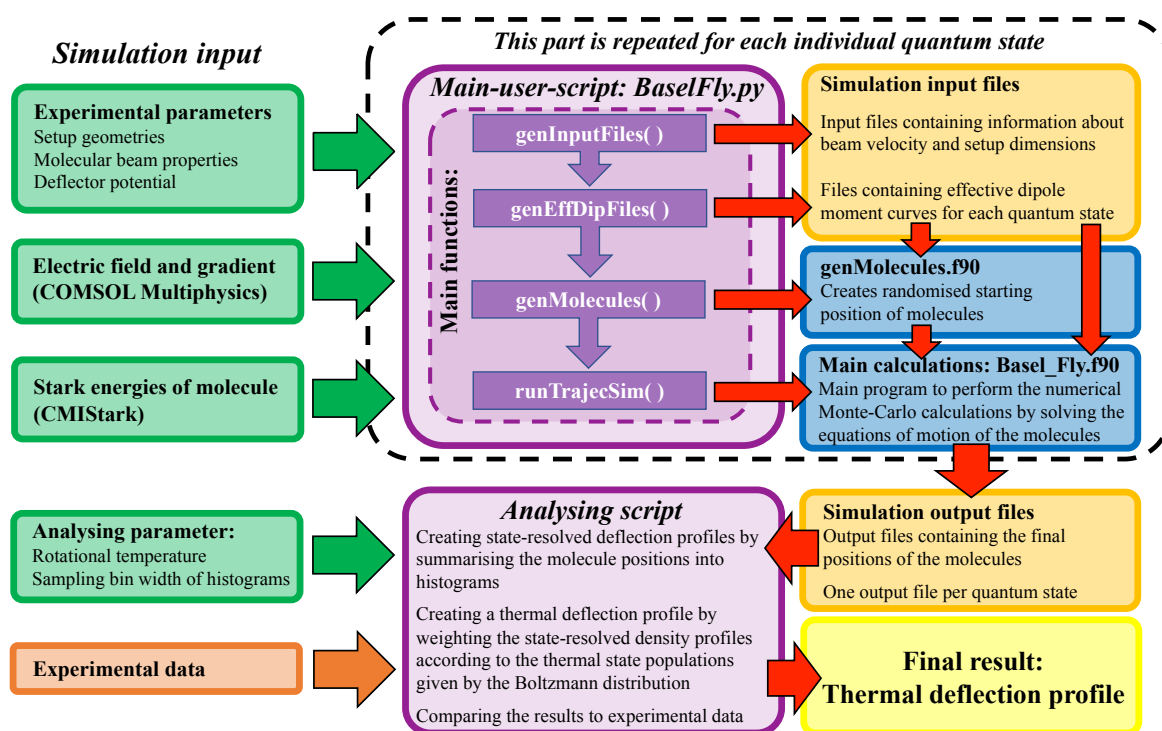
**Figure 4.5** Flow diagram of the Monte-Carlo trajectory simulations used to reproduce experimental deflection profiles. User-defined inputs are shown in green, Python scripts in purple and Fortran 90 code in blue.

*genMolecules.f90.* A user-friendly python script serves as a wrapper, which takes the necessary simulation input (setup geometries, molecular beam properties, deflector potential, electric field and gradient, Stark energies), creates necessary input files for the Fortran codes and coordinates the overall program execution. This process is iteratively executed for each individual quantum state. A final python script uses the raw output data from the main calculation program to create state-resolved deflection profiles by summarising the final spatial positions of the simulated particles into histograms with a user defined sampling width. In a last step, a thermal deflection profile is created by weighting the state-resolved deflection profiles according to the thermal state population given by the Boltzmann distribution for a given rotational temperature. This thermal deflection profile can then directly be compared to experimentally obtained deflection data.

The calculation time for simulating an individual quantum state for a sampling size of 50.000 takes at least several seconds on a fast desktop computer. Although this might seem short, the overall calculating time for molecules which have many rotational states populated in the molecular beam adds up to many hours. This is in particular true for asymmetric top molecules with reasonable small rotational constants. In this case $(2J + 1)(J + 1)$ calculations have to be performed per $J$-state, which adds up to a

total of 20336 calculations to include all quantum states from $J = 0$ till $J = 30$. For the here used calculator (takes $\sim 9$ s per quantum state with 50k particles) this leads to a total calculation time of $\sim 51$ hrs when all $J$-states are calculated sequentially. To significantly reduce the calculation time, the code has been modified to process all rotational $J$-states in a parallel manner. The gained computational speed is shown in Figure 4.6 for the simulation of all quantum states up to $J = 30$ of a typical asymmetric top molecule (here hydroquinone) and a sampling size of 50.000 molecules per quantum state. The calculation time of the parallelised code was a factor 10 shorter compared to standard sequential processing.
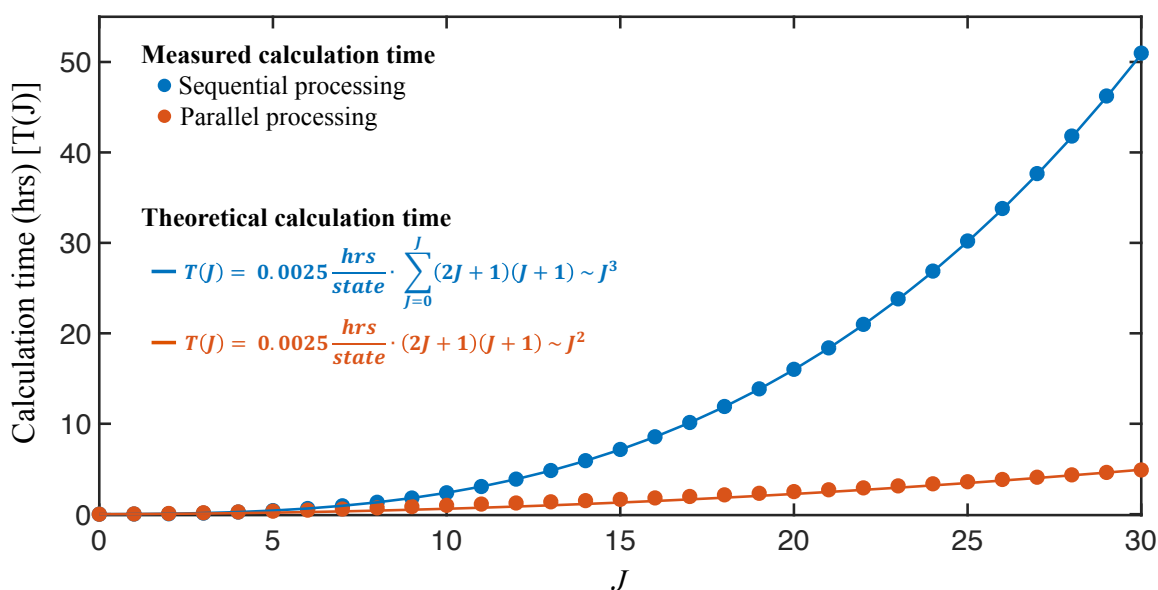


**Figure 4.6** Measured calculation time of trajectory simulations for an asymmetric top molecule (hydroquinone) as function of $J$. The experimental data is reproduced by the expected theoretical calculation time. In sequential processing the calculation of an individual quantum state is only started after the previous has been finished. Contrary, in parallel processing the calculation of the individual $J$-states are started at the same time and their individual quantum states are calculated simultaneously. For each individual quantum state 50.000 molecules are flown with an average calculation time of 9 s $\sim 0.0025$ hrs per quantum state.

## 4.4 Experimentally deflecting strong-field seekers

In this section it is demonstrated how the electrostatic deflector in the crossed-molecular-beam setup can be used to prepare reactants in individual rotational states or conformers using the examples of carbonyl sulfide (OCS) and hydroquinone, respec-

tively. The experimental setup to record the deflection profiles for both molecules was shown previously in Figure 4.1. The prepared molecular beams of OCS and hyrdro-quinone are later used to investigate rotational state- and conformer-specific chemi-ionisation reactions, which are described in Chapters 5 and 6, respectively.

### 4.4.1 Separating rotational states: the example of OCS

OCS is a benchmark molecule for electrostatic deflection [74, 75, 77, 165, 208, 209]. Due to its accurately known Stark effect it is an ideal molecule to test and calibrate a new deflection setup as it allows to closely match the experimental data with trajectory simulations. Here it serves as an example to demonstrate how different rotational states of a molecule can be spatially separated depending on their effective dipole moment-to-mass ratio.

As the deflection experiments are performed after a supersonic expansion of OCS, it can be assumed that nearly all molecules are cooled down to their electronic and vibrational ground state, which are $X^1\Sigma^+$ and $|00^00\rangle$, respectively. Furthermore, only the most abundant isotope $^{16}O^{12}C^{32}S$ is considered, which has zero nuclear spin and hence no hyperfine structure in the ground state. OCS can be classified as a linear rotor and hence its rotation can be fully described in terms of the two quantum numbers $|JM\rangle$. All relevant molecular parameters are summarised in Table 4.2.

**Table 4.2** Molecular parameters of OCS relevant for electrostatic deflection

| Molecule | Mass (g/mol) | $\mu_{\mathrm{perm}}$ (D) | B (MHz) |
|:---:|:---:|:---:|:---:|
| $^{16}O^{12}C^{32}S$ | 60 | 0.715196 [210] | 6081.4921(30) [211] |

The Stark energies and resulting effective dipole moments as function of the external electric field strength for the lowest rotational states of OCS are shown in Figure 4.7a and 4.7b, respectively. The light-blue shaded area in Figure 4.7b indicates the electric field strength at the position where the molecular beam enters the electrostatic deflector with an applied potential difference of 30 kV. The sign of the effective dipole moment in this area determines if a molecule in the certain rotational state will behave as a strong- or weak-field seeker while passing the deflector.

Experimental deflection profiles of OCS were recorded by expanding 10 bar of a mixture of 1000 ppm OCS (Sigma Aldrich) seeded in helium into vacuum by an Even-Lavie valve. The resulting supersonic jet of OCS molecules was guided through the electrostatic deflector and then multiphoton-ionised with fs-laser radiation (7 mW, 50 Hz). The resulting ions were detected by TOF-mass spectrometry. Integrating the TOF
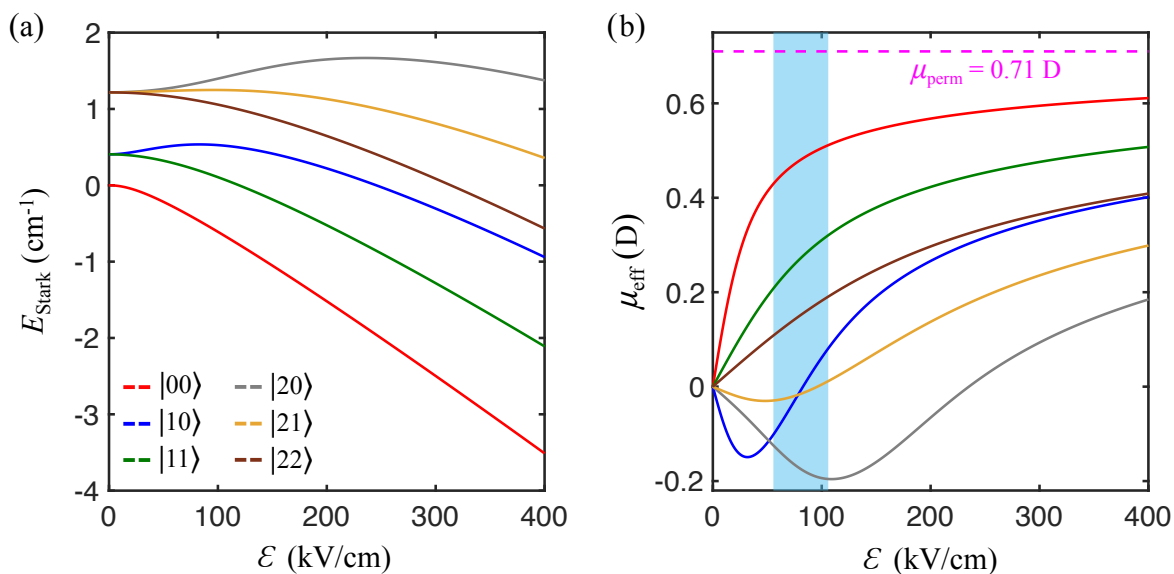
**Figure 4.7** (a) Stark energy curves as calculated with CMIStark [84] and (b) effective dipole moments as function of the external electric field strength for the few lowest rotational states of OCS. Colours for the effective dipole moments in (b) are the same as indicated for the Stark curves in (a). The light-blue shaded area indicates the electric field strength at the position of the molecular beam entering the electrostatic deflector carrying a potential difference of 30 kV.

peak of the $OCS^+$ product for different tilting angles of the molecular beam machine yielded the final beam-density profiles. Typical beam-density profiles for a deflector voltage of 0 kV, i.e. an undeflected molecular beam, and for a deflector voltage of 30 kV are shown together with the corresponding Monte-Carlo trajectory simulations in Figure 4.8. The deflection coordinate $y$ represents the offset from the centre of the undeflected molecular beam.

When a potential was applied to the deflector, the profile of the molecular beam broadened and shifted towards higher deflection coordinates in comparison to the undeflected beam profile. This behaviour could be reproduced by the Monte-Carlo trajectory simulations, which showed that different rotational states $|JM\rangle$ were deflected to a different degree. The rotational ground state $|00\rangle$ has the largest effective dipole moment and hence was deflected the most, resulting in a complete separation of the $|00\rangle$-state from all other rotational states at high deflection coordinates ($y = 2.5 - 3.0$ mm). Also highly strong field seeking is the $|11\rangle$-state. For the relevant field strengths, the effective dipole moments of the $|10\rangle$- and $|21\rangle$-states is close to zero and hence molecules in these rotational states are barely deflected. From all relevant populated states only molecules in the rotational state $|21\rangle$ posses a negative effective dipole moment and hence are weak-field seeking, which results into a deflection towards negative deflection
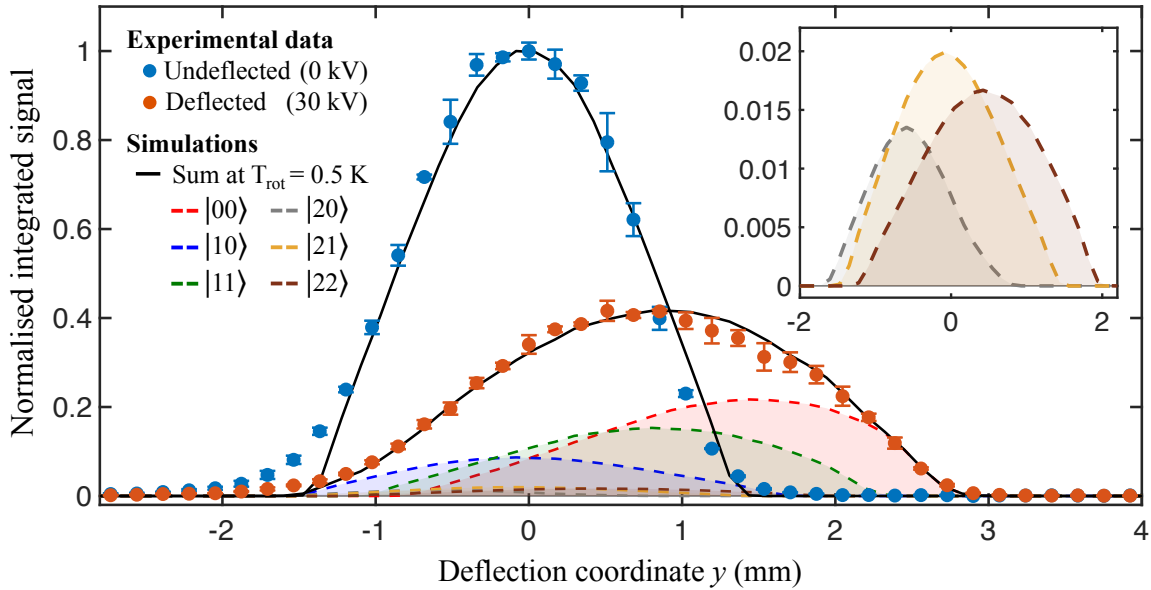
**Figure 4.8** Experimental deflection profiles of OCS at deflector voltages 0 kV and 30 kV with corresponding Monte-Carlo trajectory simulations for different rotational states $|JM\rangle$ assuming a rotational temperature of $T_{rot} = 0.5$ K. The error bars represent the standard error of 3 individual measurements in which each data point was averaged over 200 experimental cycles. Inset gives a close-up of the simulated state-specific deflection profiles for the quantum states associated with $J=2$.

coordinates as shown in the inset of Figure 4.8.

Utilising the difference in deflection for individual rotational states, the Monte-Carlo Simulations could be used to determine the populations of the individual rotational states and assign a rotational temperature of $T_{rot} = 0.5$ K to the molecular beam, assuming thermal populations during the expansion process.

The degree of deflection of individual rotational states and hence also the ability to separate them depends on several experimental parameters with the most important ones being the velocity of the molecular beam, its rotational temperature, the distance between the deflector and the detection region and finally the strength of the inhomogeneous electric field and its gradient inside the deflector. Exemplary, the effect of the latter is demonstrated in Figure 4.9, which shows experimental deflection curves of OCS for different applied electric potentials across the deflector electrodes. The applied potential at the deflector is directly related to the electric field strength ($\vec{\mathcal{E}} = -\vec{\nabla}V$). All experimental deflection curves were reproduced with Monte-Carlo trajectory simulations with the same input parameters with the only exception of the parameter for the deflector voltage which was varied accordingly. All experimental results were reproduced by simulations assuming the same rotational temperature $T_{rot} = 0.5$ K used
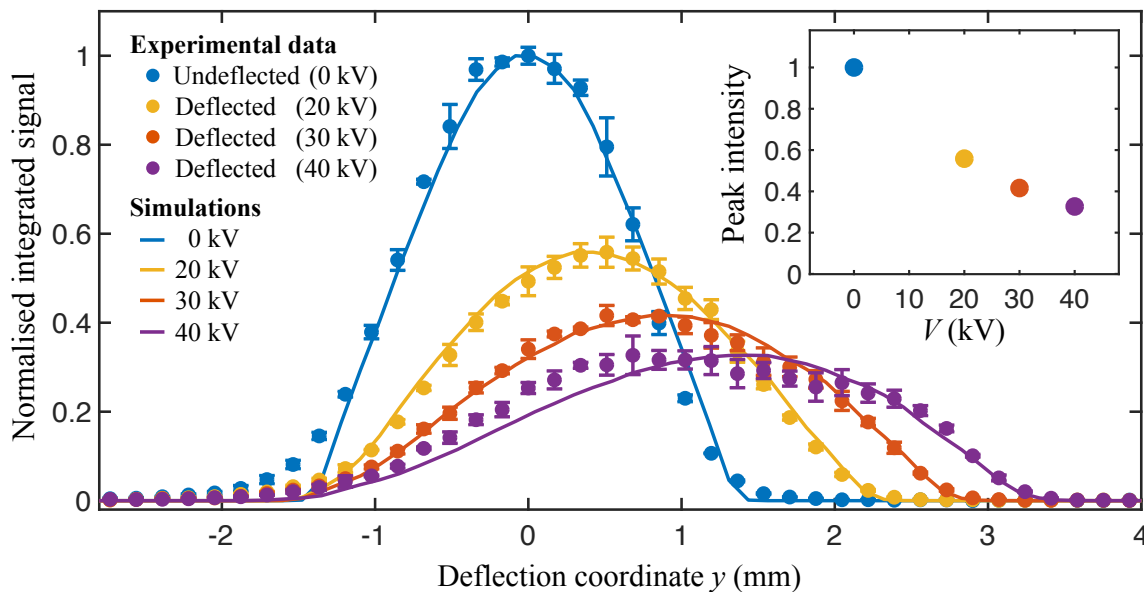
**Figure 4.9** OCS deflection profile for different potentials applied to the electrostatic deflector together with thermally averaged Monte-Carlo trajectory simulations. All simulations are performed with the exact same parameters, only the parameter for the potential was varied accordingly. All traces could be reproduced with the same rotational temperature ($T_{\text{rot}} = 0.5$ K) of the molecular beam. The error bars represent the standard error of 3 individual measurements in which each data point was averaged over 200 experimental cycles. The inset gives the normalised peak intensities of the deflection curves obtained with different applied deflector voltages $V$.

for thermal population averaging of the individual rotational states. Using the same rotational temperature for all simulated profiles is consistent with having the same experimental parameters for the supersonic expansion in all measurements.

The data clearly shows stronger deflection and hence also increased separation of different rotational states for higher applied voltages (i.e. stronger electric fields). However, it also has to be noted that with increased deflection the molecules are dispersed over a larger area and hence the beam densities at a given deflection coordinate decreases, as shown by the dependence of the peak intensities on the applied deflector voltages in the inset of Figure 4.9. For the shown data, the peak intensity of the deflection profile obtained with a deflector voltage of 40 kV is almost a factor 2 smaller than the peak intensity of a 20 kV-deflection profile. This effect is of particular importance if the deflected molecular beam is being used to investigate reactions with small reaction cross sections for which the quantity of the resulting products are close to the experimental sensitivity threshold of the detection setup. In such cases it might be beneficial to accept less deflection and hence smaller separation of rotational states while having

the trade-off of increased signal levels.

## 4.4.2   Separating conformers: the example of hydroquinone

Hydroquinone (HYQ, also known as 1,4-benzenediol or quinol) is the structural para-isomer of dihydroxybenzene ($C_6H_4(OH)_2$), consisting out off two hydroxyl groups bound to a benzene ring. The rotation of the hydroxyl group around its single bond with the benzene ring is inhibited, which results in a rotational barrier of approximately 790 cm$^{-1}$ [212]. This gives rise to two planar and energetically stable conformers, hereafter called *trans-* and *cis-*HYQ depending on the relative orientation of the two hydroxyl groups as shown in Fig 4.10a and b, respectively. The zero-point energy level of the *trans-*conformer lies 10.22 cm$^{-1}$ lower than the one of the cis-conformer [213], resulting in a nearly equal population of both conformers at room temperature (Fig. 4.10c).
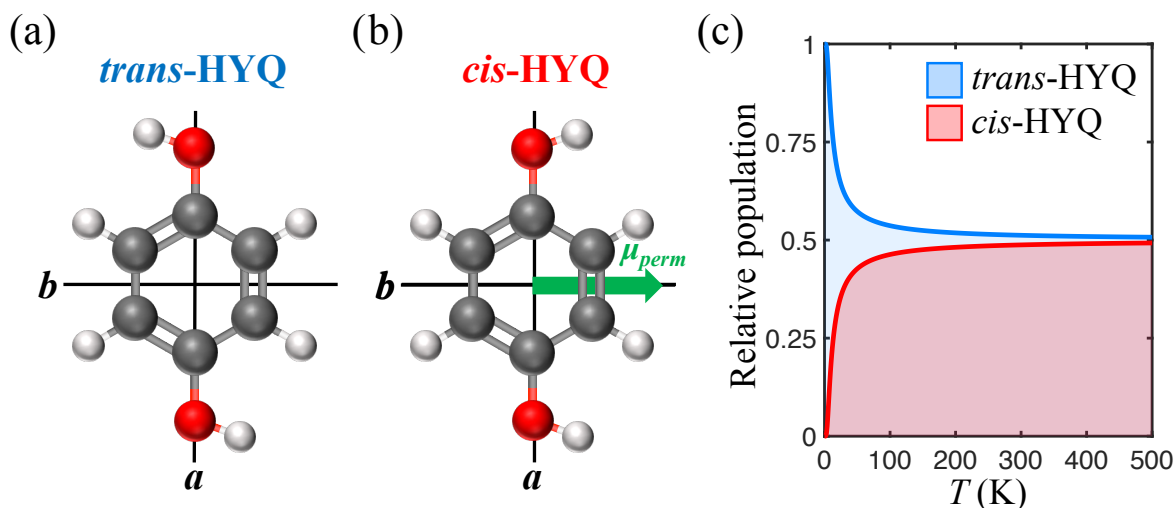


**Figure 4.10** Molecular structures of (a) *trans-* and (b) *cis-*hydroquinone with the principal axis of inertia. The *c*-axis is perpendicular to the figure plane. For *trans-*HYQ the bond dipole moments cancel each other, whereas for the *cis-*conformer the dipole moments and up into a net dipole moment along the b axis as indicated by the green arrow. Colours of atoms: grey (carbon), red (oxygen), white (hydrogen). (c) Relative populations of both conformers as function of temperature.

For the *cis-*rotamer the O-H bond dipoles of the two hydroxyl group add up to a net, permanent dipole moment of $\mu_{\mathrm{perm}} = 2.38$ D orientated along the $b$ principal axis [214]. Contrary, the *trans-*conformer has no net dipole moment due to its structural symmetry. Having a strong polar and a completely apolar rotamer makes hydroquinone a prime target for electrostatic deflection experiments. All relevant parameters of both conformers of HYQ are given in Table 4.3. HYQ is an asymmetric top molecule

and hence its rotational state are described in terms of the two quantum numbers $J$ and $M$ and the two pseudo-quantum numbers $K_a$ and $K_c$. *Cis*-HYQ belongs to the $C_{2v}$-symmetry point group with the main symmetry axis along $b$, whereas the *trans*-rotamer has a $C_{2h}$-symmetry with $c$ being the main symmetry axis. Both molecules have three pairs of interchangeable hydrogen nuclei which lead, under consideration of the symmetry of their rotational wave functions, to the nuclear spin statistical weights (nssw) depending on the values for $K_a$ and $K_c$ as shown in Table 4.3 [213].

**Table 4.3** Molecular parameters of HYQ relevant for electrostatic deflection. Abbrev.: NSSW (nuclear spin statistical weight), o (odd $K_{a,c}$), e (even $K_{a,c}$).

| Conformer | Mass (g/mol) | $\mu_{\mathrm{perm}}$ (D) [214] | Rotational constants (MHz) | NSSW [213] |
|---|---|---|---|---|
| *trans*-HYQ | 110.112 | $\mu_{\mathrm{A}} = 0.00$ $\mu_{\mathrm{B}} = 0.00$ $\mu_{\mathrm{C}} = 0.00$ | A = 5615.1 B = 1481.7 [213] C = 1172.8 | $(K_a K_c)$ (oe),(ee): 7 (oo),(eo): 9 |
| *cis*-HYQ | 110.112 | $\mu_{\mathrm{A}} = 0.00$ $\mu_{\mathrm{B}} = 2.38$ $\mu_{\mathrm{C}} = 0.00$ | A = 5614.1 B = 1481.6 [214] C = 1172.7 | $(K_a K_c)$ (ee),(oo): 7 (eo),(oe): 9 |

The Stark energy curves of both conformers as calculated with CMIStark are shown together with the effective dipole moment of the *cis*-conformer for all rotational quantum states up to $J = 2$ in Figure 4.11. In an experimentally relevant electric field, for *cis*-HYQ the size of the effective dipole moment decreases for quantum states belonging to higher rotational quantum number $J$. Molecules in higher quantum states are hence less effected by external electric fields. For very strong electric fields, the effective dipole moment of all states will eventually approach the size of the permanent dipole moment.

First experimental electrostatic deflection and separation of the two HYQ-conformers was performed by You et al. using a deflector featuring a trough-rod design [206]. In comparison to their study, the setup described here features stronger inhomogeneous electric fields and a colder supersonic expansion, allowing for an overall stronger deflection and better separation of both conformers.

To obtain experimental deflection profiles, a sample of HYQ (Sigma Aldrich, > 99 %) was placed in the sample cartridge of a heatable Even-Lavie valve, from which it was co-expanded with 90 bar of helium. As the vapour pressure of HYQ at room temperature was not sufficient to create a dense molecular beam, the Even-Lavie valve containing the sample was heated to a temperature of $T_{\mathrm{valve}} = 130$ °C. The resulting supersonic beam, containing both HYQ-conformers, was guided through the electrostatic deflector and then ionised by a fs-laser (2.9 mW, 50 Hz). Ionic products were detected by TOF-mass spectrometry. Analogously to the deflection profile of OCS, the TOF-mass
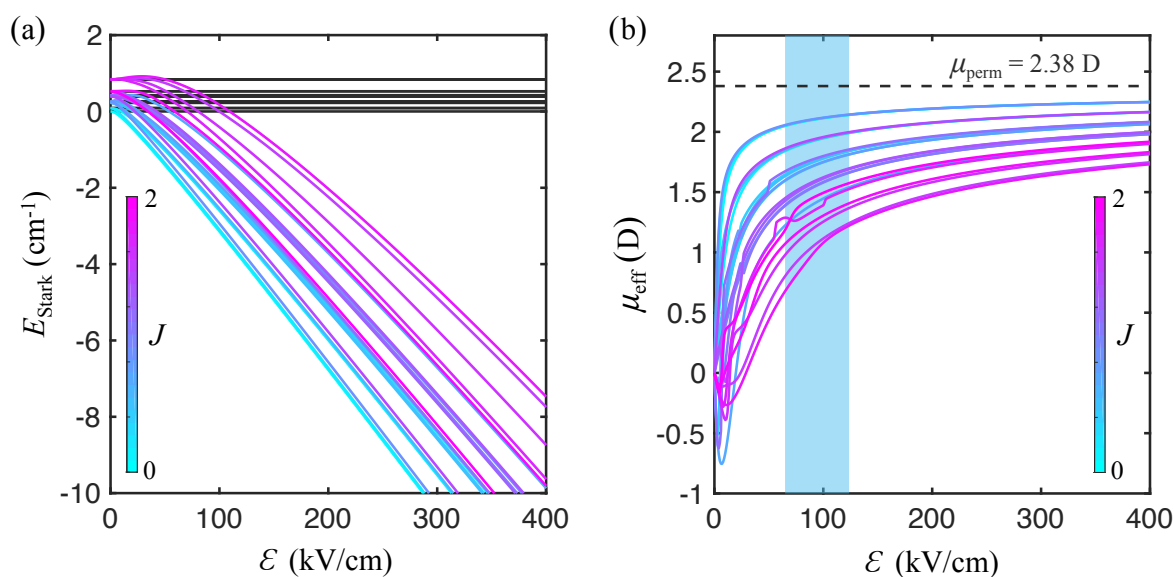
**Figure 4.11** (a) Stark energy curves as calculated with CMIStark [84] and (b) effective dipole moments as function of the external electric field strength for the lowest rotational states of cis-hydroquinone. The colour gradient indicates the individual rotational states with the total angular momentum quantum number $J = 0$ to $J = 2$, respectively from light blue to purple. The Stark energy of the trans-conformer is indicated in (a) by black lines. The light-blue shaded area indicates the electric field strength at the position of the molecular beam entering the electrostatic deflector carrying a potential difference of 35 kV.

peak of HYQ$^+$ was integrated for different tilting angles of the molecular beam machine, resulting in the experimental deflection profile shown in Figure 4.12a. As the applied detection method was not conformer-specific, only the overall deflection profile of both conformers could be recorded. The individual behaviour of both conformers could be disentangled with the help of Monte-Carlo trajectory simulations, for which both conformers were first simulated separately with a sampling size of 100k molecules per quantum state. The resulting state-specific deflection profiles were then averaged according to the rotational temperature of the beam $T_{rot}$, while accounting for the degeneracy and nuclear spin statistical weight of each quantum state. Finally, the two conformer-specific profiles were combined to the overall deflected profile according to their relative populations given by the temperature of the gas reservoir $T_{valve}$.

The direct comparison of experimental results and simulation data shows that when a potential difference of $V = 35$ kV was applied to the deflector, the *cis*-rotamer clearly shifted to higher deflection coordinates and by that separated from the undeflected *trans*-conformer. This is in clear contrast to the profile recorded with no potential difference applied to the deflector for which both conformers spatially overlap as shown
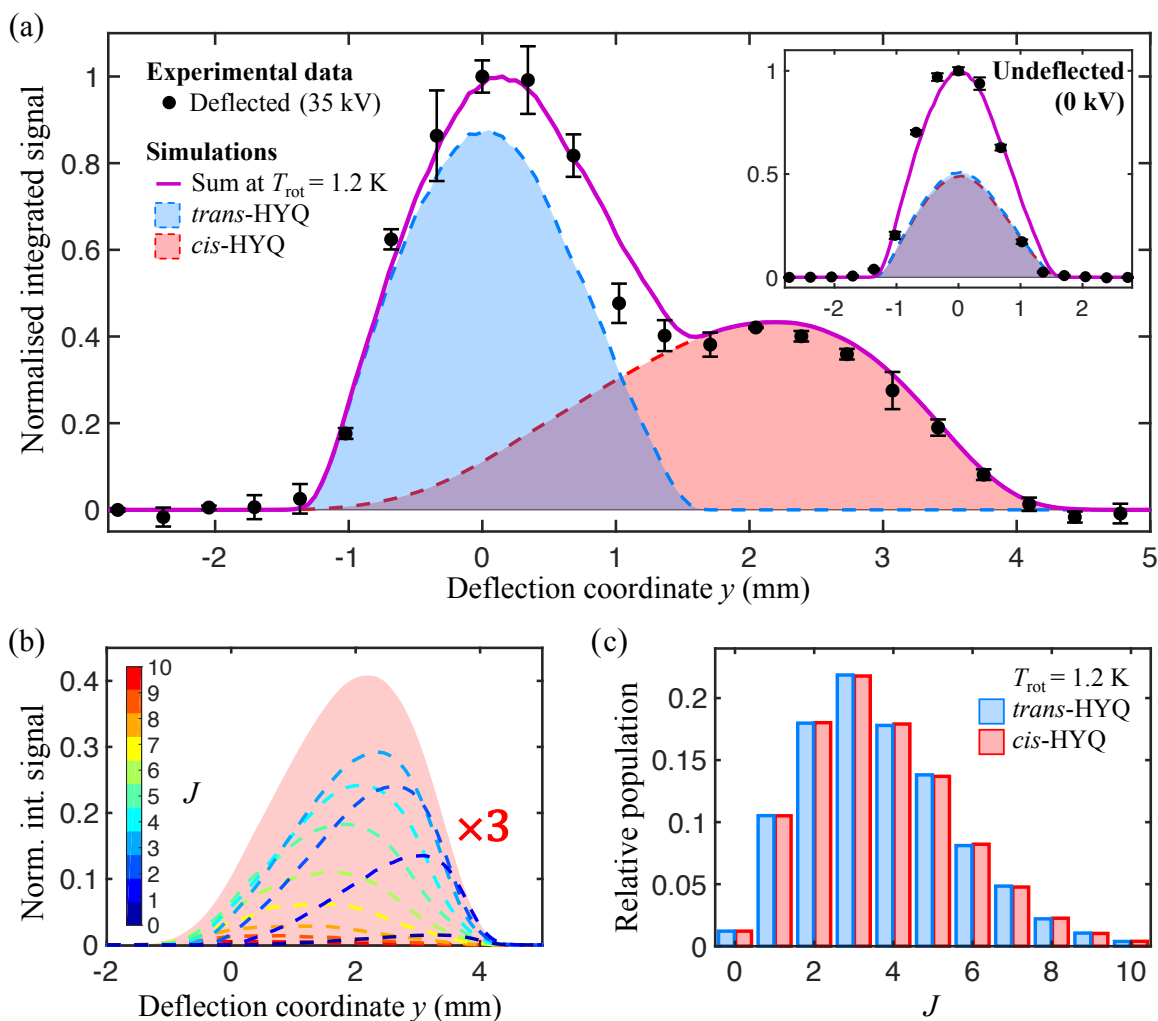
**Figure 4.12** Experimental deflection profile of HYQ together with Monte-Carlo trajectory simulations for the *trans*- and *cis*-rotamers, assuming a rotational beam temperature of $T_{rot} = 1.2$ K . The inset shows the beam profile obtained with a switched-off deflector. The error bars represent the standard error of three individual measurements in which each data point was averaged over 2000 experimental cycles. (b) Contribution of the state-specific deflection profiles summed over quantum states with the same angular momentum quantum number $J$ towards the deflected *cis*-conformer. For clarity, all profiles are magnified by a factor 3. (c) Relative populations of all quantum-states summed over $J$ for $T_{rot} = 1.2$ K.

in the inset of Figure 4.12a.

The contribution of molecules in different rotational states towards the deflection profile of the *cis*-conformer is given in Figure 4.12b. For clarity, only the state-specific deflection profiles summed over quantum states with the same angular momentum quantum number $J$ are shown. Only the relevant populated rotational states are considered (see Fig 4.12c). As expected from the effective dipole moments shown in Figure 4.11b, quan-

tum states with smaller $J$ are deflected more. In contrast to OCS, all relevant quantum states of HYQ are strong-field seeking for the given experimental field strength.

Because the degree of deflection strongly depends on the quantum state of the molecule, a rotationally cold molecular beam is essential for good separation of both conformers. This was investigated by measuring experimental deflection profiles of HYQ for different temperatures of the pulsed gas valve. Changing the valve temperature has a direct impact on several parameters of the created molecular beam, including (i) the mean beam velocity, (ii) the relative population of the conformers in the beam, (iii) the beam density and (iv) the population of the rotational states. The values of these parameters for the investigated valve temperatures are summarised in Table 4.4.

**Table 4.4** Molecular beam parameters of HYQ for different expansion temperatures.

| $T_{valve}$ (°C) | Beam velocity (m/s) | *Cis*-population (%) | Signal levels | $T_{rot}$ (K) |
| --- | --- | --- | --- | --- |
| 130 | 2257 | 49.09 | 0.07 | 1.2 |
| 150 | 2323 | 49.13 | 0.31 | 1.7 |
| 170 | 2380 | 49.17 | 0.66 | 2.5 |
| 190 | 2427 | 49.21 | 1 | 3.9 |

The mean velocity of the HYQ-beam was measured using the VMI detector. The population of the *cis*-rotamer directly follows from the two level Boltzmann distribution and is barely effected for the investigated temperature range. The absolute beam density can not be straightforwardly measured in our setup, but the relative signal levels of different measurements were obtained from TOF-MS traces. Finally, the rotational beam temperature was conducted by direct comparison of experimental deflection profiles and trajectory simulations.

Whereas the small change in the beam velocity and in the relative population of the conformers has only a small impact on the overall deflection profile, the population of the individual rotational states is critical for good separation of the two rotamers of HYQ. This is illustrated in Figure 4.13, in which experimental deflection profiles of HYQ for different temperatures of the expansion valve are shown together with trajectory simulations.

 All data was reproduced using simulations with the same input parameters, only the beam velocity, the population of the conformers and the rotational temperature of the beam has been adjusted accordingly. All data was normalised to exclude the effect of different signal levels for the time being.

As can be seen in the insets of Figure 4.13, the relative population of the rotational states shifts to higher $J$ for an increasing valve temperature. Because molecules in higher rotational states have a smaller dipole moment and are deflected less, the separation between the undeflected *trans*-conformer and *cis*-HYQ decreases with increas-
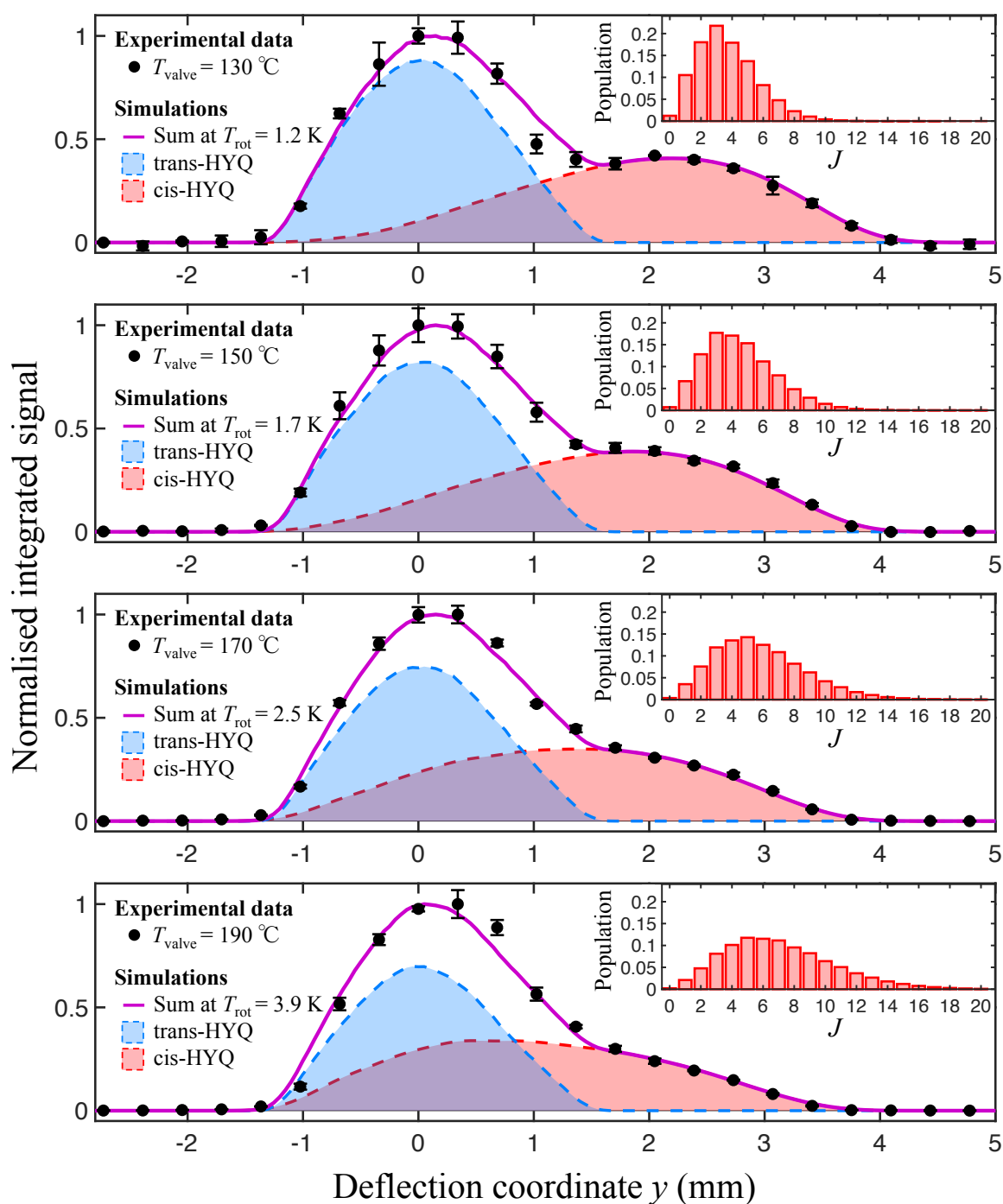
**Figure 4.13** Experimental deflection profile of *cis*- and *trans*-HYQ for different temperatures of the gas valve. All simulations were performed with the exact same parameters, only the valve temperature, beam velocity and rotational temperature was adjusted accordingly. Insets show the rotational population distribution.

ing rotational temperature. E.g., for the deflection profile obtained at $T_{valve} = 130$ °C, mainly the highly strong-field seeking rotational states at low $J$ are populated, leading to a clear separation of both HYQ-conformers. In contrast, for a rotationally warmer molecular beam created with a valve temperature of $T_{valve} = 190$ °C, the separation of both conformers is significantly worse, which emphasises the importance of a cold supersonic beam.

Nevertheless, it can not be neglected that the increased vapor pressure of the sample for higher valve temperatures significantly increases the beam density and hence the experimental signal levels of the experiment. For the shown data, the signal levels almost increased by a factor of 15 between the experiments conducted at $T_{valve} = 130$ °C and $T_{valve} = 190$ °C (see Tab. 4.4). While designing a study to investigate conformational effects in gas-phase reactions, these two factors, rotational coldness and density of the molecular beam, have to be carefully balanced to achieve good separation between the conformers on one hand and overall sufficient signal levels on the other hand.

## 4.5 Conclusion

It was demonstrated on the example of OCS that the electrostatic deflector of the new crossed-molecular-beam setup can be used to separate individual rotational states, depending on their effective dipole moment. Although a complete separation was only achieved for the rovibrational ground state at high deflection coordinates, a unique distribution of rotational-state populations was established in the beam at each deflection coordinate. This enables the investigation of state-specific effects in bimolecular reactions as demonstrated in Chapter 5.

Analogously, the electrostatic deflector allows the separation of rotational isomers as demonstrated with the apolar *trans*- and the polar *cis*-conformer of hydroquinone. The resulting molecular beam of spatially separated rotational isomers provides an ideal starting point for geometry-specific reaction experiments, which will be the topic of Chapter 6.

# 5

# Rotational-state resolved chemi-ionisation reaction of Ne$^{*}$ + OCS

The novel crossed-molecular-beam setup allows the investigation of state-specific effects of neutral bimolecular reactions under single-collision conditions. In this chapter, the capabilities of the new apparatus are demonstrated on the chemi-ionisation reaction of metastable neon atoms with rotationally state-selected carbonyl sulfide (OCS) molecules. It was observed that the branching ratio between the Penning and dissociative ionisation pathways, respectively leading to the OCS$^{+}$ and S$^{+}$ reaction products, strongly depends on the initial rotational state of OCS. The associative ionisation product was not observed.

## 5.1  Introduction

Chemi-ionisation reactions play an important role in many areas including plasma and discharge processes [215–218] and the chemistry of the terrestrial atmosphere [219, 220]. The term chemi-ionisation describes the reactive collision of an electronically exited metastable species $A^{*}$ with a ground-state atom or molecule $B$ resulting in an ionic reaction product. Ionisation only occurs when the excitation energy of the metastable species is larger than the ionisation energy of the collision partner [128,221]. It is generally understood that chemi-ionisation reactions follow a barrier-less reaction
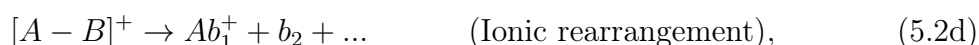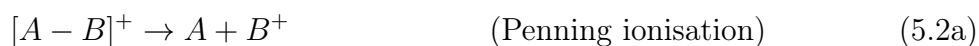
pathway proceeding via two intermediate collision complexes [128, 129]. The reaction can then be described as

$$A^* + B \rightleftharpoons [A-B]^* \rightarrow [A-B]^+ + e^-. \tag{5.1}$$

After the collision, the first excited collision complex ($[A-B]^*$) auto-ionises resulting in the ionic intermediate ($[A-B]^+$) from which the reaction can evolve via several different pathways. The ionic intermediate can break up resulting in a neutral atom $A$ and an ionic product $B^+$, commonly known as the Penning ion (Eq. 5.2a). If the ionic intermediate complex is stable, only a single product is formed in the reaction, which is called the associative ion (Eq. 5.2b). In case of a molecular co-reactant, also dissociative ionisation (Eq. 5.2c) and ionic rearrangement (Eq. 5.2d) are possible [128, 221, 222]. The different reaction pathways can be summarised by

$$[A-B]^+ \rightarrow A + B^+ \qquad \text{(Penning ionisation)} \tag{5.2a}$$

$$[A-B]^+ \rightarrow AB^+ \qquad \text{(Associative ionisation)} \tag{5.2b}$$

$$[A-B]^+ \rightarrow A + b_1^+ + b_2 + ... \quad \text{(Dissociative ionisation)} \tag{5.2c}$$

$$[A-B]^+ \rightarrow Ab_1^+ + b_2 + ... \qquad \text{(Ionic rearrangement)}, \tag{5.2d}$$

where $b_i$ with $i = 1, 2, ...$ represents possible dissociation fragments of the molecular collision partner $B$. The number of neutral and ionic fragments strongly depends on the target molecule and the energy available in the reaction.

The ionisation of neutral trace gas impurities by metastable rare gas atoms was first described by Frans Michel Penning in 1927 during his study of low-pressure gas discharges for the development of new light bulbs in the *Philips Natuurkundig Laboratorium* [223]. Since then, the details of the underlying reaction mechanism of chemi-ionisation reactions was topic of many gas-phase experiments utilising molecular-beam techniques [128, 221, 222]. Nowadays, chemi-ionisation reactions are understood to proceed via two main reaction mechanisms [128, 224–227]. In the indirect *radiative mechanism*, the target particle is ionised by the absorption of a virtual photon, which is emitted by the metastable atom relaxing to its ground state [128, 225, 227]. In the direct *exchange mechanism*, an electron of the collision partner is transferred into the inner-shell vacant orbital of the metastable atom, stimulating the ejection of the highly-excited electron [128, 227–229]. For the *exchange mechanism*, proper overlap of the interacting orbitals is essential, which makes it a highly stereo-specific process [128, 227, 229]. Both reaction mechanisms coexist in a chemi-ionisation reaction, but their respective contributions strongly vary with the collision energy [227]. The *radiative mechanism* predominates at low-collision energies under subthermal conditions. Contrary, chemi-ionisation reactions mainly proceed via the *exchange mechanism* at

high-collision energies, when the short-range part of the interaction is being probed. Remarkable progress has been made in the last years in unravelling the mechanistic details of chemi-ionisation reactions at very low collision energies [41, 43, 45–48, 230–235], as for example the observation of different reactivities of ortho- and para-hydrogen in the chemi-ionisation reaction with metastable helium, where the faster reactivity of ortho-hydrogen could be explained by stronger long-range interactions [236].

The importance of steric effects in chemi-ionisation reactions was observed in a number of experimental studies, where the metastable rare gas atom was oriented using external magnetic fields, resulting in strong orientation effects on the reaction outcome including differences in the branching ratio between the Penning and associative ionisation pathways [44, 46, 47, 232, 237–239]. Analogously, the molecular collision partner was oriented prior to reaction, initially by linearly polarised laser photodissociation experiments [240] and later using an electrostatic hexapole in combination with rotatable orientation fields [241–246]. These experiments also showed strong steric effects of the reaction mechanism which could be explained by the overlap of the molecular orbitals with the vacant orbital of the metastable species. Recently, joined experimental and theoretical work investigating chemi-ionisation reactions between metastable rare gas atoms and small molecules showed strong anisotropies in the intermolecular interactions that controls the stereo-dynamics in the entrance channel of these reactions [129, 227, 247–258]. The common observation throughout these studies is that orbital overlap plays a crucial role in the reaction mechanism and that in case of molecular reactants the direction of approach of the metastable species strongly impacts the reaction outcome.

To our knowledge, so far no experimental studies have been performed which directly compare the impact of different rotational states of the molecular reactant on the different pathways of a chemi-ionisation reaction. Presented here are first experimental results in which the novel crossed-molecular-beam apparatus was used to investigate effects of the rotational state of carbonyl sulfide (OCS) on the chemi-ionisation reaction with metastable neon. The reaction of OCS with metastable rare gas atoms has been investigated before using Penning-ionisation electron spectroscopy [259, 260], photoemission spectroscopy [261, 262] and CMB experiments which revealed strong anisotropies in the interaction potentials [263, 264]. In general, the reaction $Ne^*$ + OCS can proceed via different pathways yielding different reaction products: the Penning ionisation (PI) products $OCS^+$ and Ne, the associative ionisation (AI) product ($NeOCS^+$) or dissociative-ionisation (DI) products of OCS. In the latter case, multiple products are possible depending on the amount of energy available in the reaction [262]. The effect of different rotational states of OCS on the different reaction pathways is experimentally investigated in the following.

## 5.2   Experimental setup

The experimental setup has been described in detail in Chapter 3 and is schematically summarised in Figure 5.1.
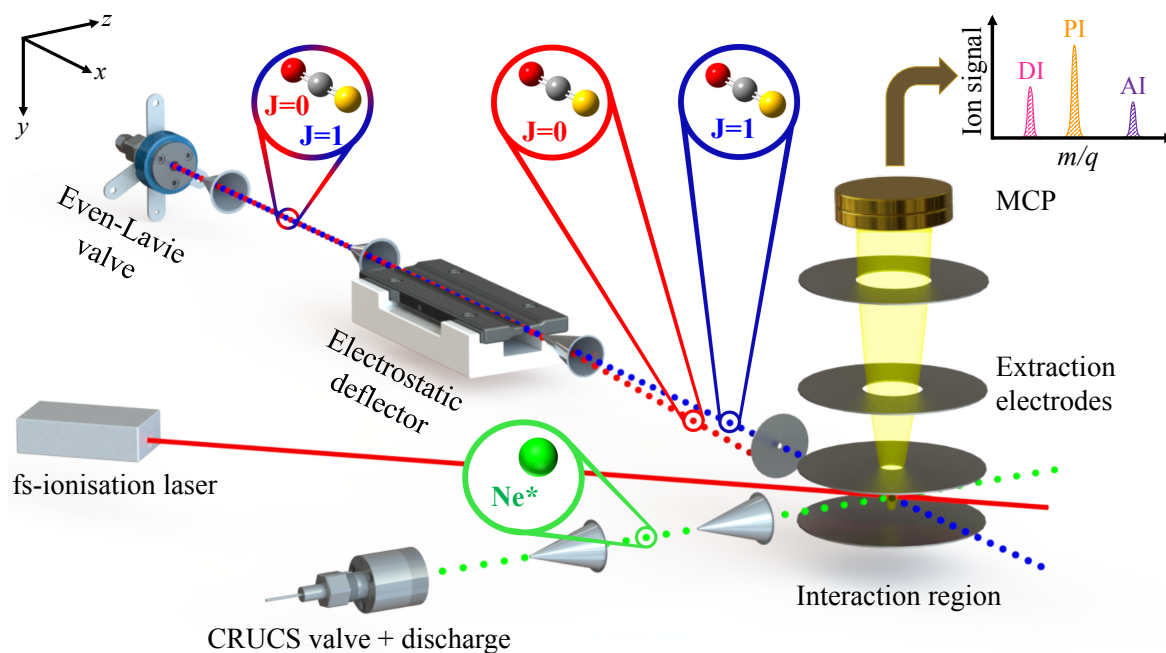


**Figure 5.1** Schematic of the experimental setup used for the investigation of the chemi-ionisation reaction of OCS with metastable neon. The electrostatic deflector allows spatial separation of OCS molecules in different rotational states as schematically illustrated for OCS in the ground-state ($J = 0$, red dots) and first excited rotational state ($J = 1$, blue dots). After crossing the OCS beam with an atomic beam of metastable neon atoms (green dots), the resulting product ions are detected by a time-of-flight mass spectrometer. This allows identification of the dissociative-ionisation (DI), Penning-ionisation (PI) and associative-ionisation (AI) reaction products. Different parts of the deflected OCS beam can be overlapped with the metastable neon beam in the collision region by tilting the OCS molecular-beam setup with respect to the collision chamber. The deflected molecular beam can be analysed by ionising the neutral OCS molecules by femtosecond-laser radiation [111].

In short, a pulsed molecular beam of 2000 ppm OCS (Sigma Aldrich) seeded in helium was produced by expanding 10 bar of the gas mixture into vacuum. The resulting supersonic jet of OCS molecules was guided through the electrostatic deflector, which allows spatial separation of the different rotational states of OCS. The deflected beam of OCS molecules was then intersected with a beam of metastable neon atoms in a time-of-flight mass spectrometer. The beam of metastable neon atoms in the $(2p^5 3s)\ ^3P_2$ and $^3P_0$ states were generated in a supersonic expansion of neon gas (stagnation pres-

sure 25 bar) through a pulsed plate-discharge source. Different parts of the deflected beam containing different compositions of OCS molecules in different rotational states were overlapped with the second molecular beam in the collision region by tilting the OCS molecular-beam setup with respect to the collision chamber. This allowed studying state-specific chemi-ionisation reactions of OCS in different rotational states. The collision energy of the chemi-ionisation reaction was determined to be approximately 0.3 eV.

To characterise the neutral deflected OCS beam, the neutral OCS molecules was multiphoton-ionised in the collision chamber using the radiation of a femtosecond laser.

## 5.3 Results

### 5.3.1 State-specific spatial separation of OCS

Before performing state-specific bimolecular collision experiments, it is essential to characterise the deflected OCS beam. Details on the principle of electrostatic deflection and how it can be used to separate different rotational states are given in Chapter 4 together with a description of the underlying Monte-Carlo trajectory simulations.

Experimentally, the supersonic jet of deflected OCS molecules was multiphoton-ionised with fs-laser radiation and the resulting $OCS^+$ ions were detected by TOF-mass spectrometry. Integrating the mass peak of the $OCS^+$ product for different tilting angles of the molecular beam machine yielded the beam-density profiles shown in Figure 5.2. The deflection coordinate $y$ represents the offset from the centre of the undeflected molecular beam. Experimental beam-density profiles at deflector voltages of 0 kV and 30 kV are shown together with the corresponding Monte-Carlo trajectory simulations. When the deflector was turned on, the molecular beam was broadened and clearly shifted towards higher deflection coordinates due to the different deflection of different rotational states of OCS. The spatial separation of different rotational states of OCS was previously demonstrated [75, 209]. The current setup did not allow for a state-selective detection, but the degree of deflection of individual rotational states $|JM\rangle$ of OCS could be inferred from a comparison of the experimental deflection profiles to the ones obtained from trajectory simulations. Here, $J$ and $M$ stand for the quantum numbers of the rotational angular momentum and its projection on the electric-field axis, respectively. Assuming thermal populations in the expansion, a rotational temperature $T_{rot} = 0.55(7)$ K was determined for the molecular beam of OCS molecules. The uncertainty quoted for the rotational temperature represents the uncertainty of the fit of the simulated thermally averaged density profiles to the experimental data.
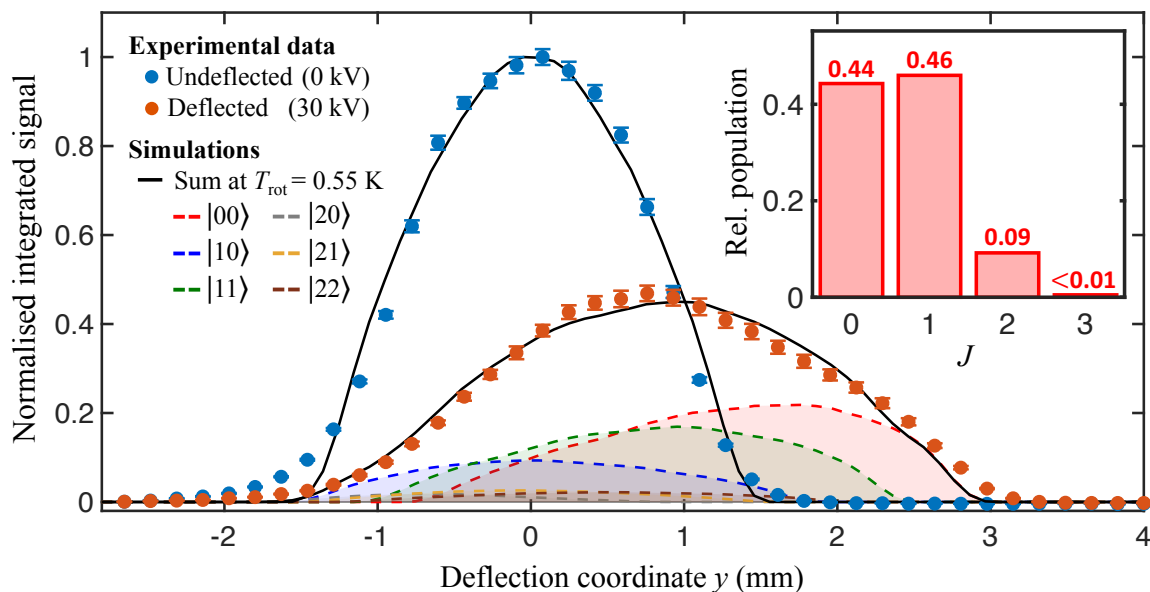
**Figure 5.2** Experimental deflection profiles of OCS at deflector voltages 0 kV and 30 kV (blue and red data points, respectively) with corresponding Monte-Carlo trajectory simulations for different rotational states $|JM\rangle$ (dashed lines). The black lines represent the sum of the individual rotational-state-specific deflection profiles weighted by the rotational populations assuming a rotational temperature of $T_{rot} = 0.55$ K. The error bars represent the standard error of ten individual measurements in which each data point was averaged over 1000 experimental cycles. Inset: Thermal populations of rotational levels of OCS summed over states with quantum number $J$ considering degeneracies at $T_{rot} = 0.55$ K [111].

The slightly higher rotational temperature compared to measurements presented in Section 4.4.1 can be explained by the higher OCS concentration in the gas mixture used in the current experiments (2000 ppm) compared to the one used for the measurements in Section 4.4.1 (1000 ppm). This results in slightly less efficient cooling during the expansion process and finally a marginally higher rotational temperature.

The rotational states $|00\rangle$ and $|11\rangle$ were highly strong-field seeking at the present electric-field strengths. Although a complete separation was only achieved for the rovibrational ground state $|00\rangle$ at high deflection coordinates (Fig. 5.2), a unique distribution of rotational-state populations was established in the beam at each deflection coordinate. This enables the determination of state-specific reaction rates from measurements of state-averaged reaction rates at different deflection coordinates [80].

Analysing the composition of the initial molecular beam showed that it consists of more than 95 % of OCS monomers and that eventual molecular cluster contributions to the deflection profile of the monomer or the investigated reaction are negligible (see Appendix A).

## 5.3.2 Time-of-flight mass analysis of Ne* + OCS

The chemi-ionisation reaction was investigated by crossing the molecular beam of OCS with a beam of metastable neon ions. The product ions generated by chemi-ionisation in the collision region were accelerated towards the detector by pulsing the extraction fields for 1 $\mu$s as described in Section 3.5.2. A typical TOF mass spectrum of the reaction products is displayed in Figure 5.3. Different reaction products are separated according to their mass-to-charge-number ratio ($m/z$).
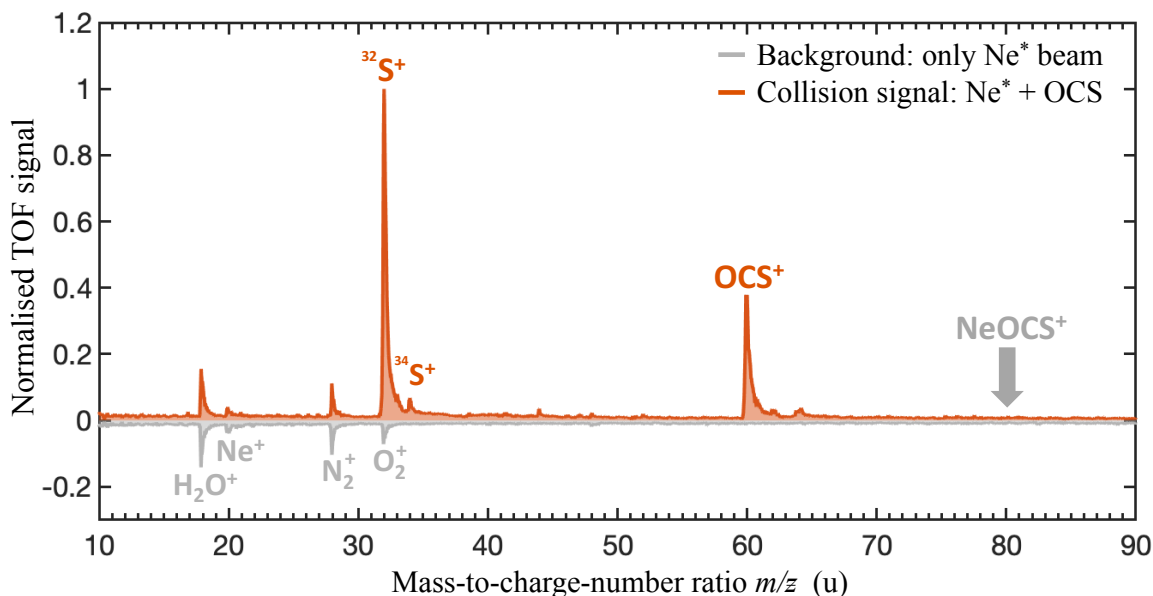


**Figure 5.3** Time-of-flight mass spectrum of products of the chemi-ionisation reaction Ne* + OCS. Intensities are normalised with respect to the strongest signal. The trace corresponding to the background experiment without the OCS beam is inverted for clarity. The signals of the ionic products originating from Penning- and dissociative-ionisation reaction pathways (OCS$^+$ and S$^+$, respectively) are indicated. The associative-ionisation product NeOCS$^+$ is not observed within the sensitivity limits of the present experiment [111].

Besides products resulting from the Penning ionisation of trace gases in the background vacuum (H$_2$O$^+$, N$_2$$^+$, O$_2$$^+$), the product of the Penning-ionisation pathway (OCS$^+$) and the dissociation product S$^+$ are the dominating species observed in the mass spectrum. From the integral of the relevant signals in the TOF mass spectrum, a total branching ratio between the Penning- and dissociative-ionisation products (PI:DI) of 1:2.5 could be determined. As can be seen from the list of possible reaction products given in Table 5.1 [262], other ionic products from the dissociation pathway besides S$^+$ are energetically unavailable considering the excitation energy of metastable neon

**Table 5.1**  Different reaction pathways for Ne$^*$ + OCS and required energies [262]

| Products | Electronic state | Energy [265] | References |
|---|---|---|---|
| *Ionic reaction pathways* | | | |
| OCS$^+$ | $X^2\Pi$ | 11.19 eV | [266] |
| | $A^2\Pi$ | 15.08 eV | [266] |
| | $B^2\Sigma^+$ | 16.04 eV | [266] |
| | $C^2\Sigma^+$ | 17.96 eV | [266] |
| CO + S$^+$ | $X^1\Sigma^+, {}^4S$ | 13.55 eV | [267] |
| | $a^3\Pi^+, {}^4S$ | 19.56 eV | [267] |
| CO$^+$ + S | $X^2\Sigma^+, {}^3P$ | 17.20 eV | [267] |
| CS$^+$ + O | $X^2\Sigma^+, {}^3P$ | 18.18 eV | [268] |
| CS + O$^+$ | $X^1\Sigma^+, {}^4S$ | 20.46 eV | |
| *Neutral reaction pathways* | | | |
| CO + S | $X^1\Sigma^+, {}^3P$ | 3.29 eV | [269] |
| CS + O | $X^1\Sigma^+, {}^3P$ | 6.85 eV | [270] |
| C + S + O | ${}^3P, {}^3P, {}^3P$ | 14.28 eV | [267, 270] |

(16.6 eV for Ne($^3$P$_2$) and 16.7 eV for Ne ($^3$P$_0$)) and the present collision energy of 0.3 eV. Table 5.1 gives only the most relevant ionic and neutral reaction channels and does not display reaction channels to products with higher excited electronic states. For a complete list please refer to Ref. [262]. In the current experiments, no ionisation laser was used and hence only the ionic reaction products could be analysed with the TOF-MS method, while the products of neutral channels were not detected.

The associative ionisation product at $m/z$ =80 u was not observed, but it cannot be ruled out that part of the signal at $m/z$ =60 u is due to predissociation of a weakly bound AI complex. Previous studies have shown that the formation of the associative ionisation complex strongly decreases with increasing collision energy [46, 128, 238, 271–273]. Furthermore, in case of molecular co-reactants vibrational or rotational excitation of the ionic collision complex further reduces the formation of stable associative ions by their predissociation into the according Penning-ionisation product [235, 239]. This finally results in overall less formed AI complexes for molecular collision partners even at lower collision energies [46, 235]. Therefore, for the present collision energy of 0.3 eV we expect the contribution of the AI pathway to be negligible. In the current setup using only TOF mass spectrometry, it is not possible to distinguish if OCS$^+$ is generated by direct Penning ionisation or through predissociation of a short-lived associative ionisation complex. This distinction should become possible

in the near future by the implementation of an ion-electron coincidence VMI detector. The small $Ne^+$ signal in the spectrum is attributed to intra-beam $Ne^*$-$Ne^*$ Penning ionisation which is also present in the background experiment with only the $Ne^*$ beam (grey inverted trace in Fig. 5.3). Moreover, the $Ne^+$ signal did not decrease when the Ne beam was overlapped with the OCS expansion suggesting that possible ion-molecule reactions $Ne^+$ + OCS do not play a major role under the present conditions.

### 5.3.3 Chemi-ionisation reaction of $Ne^*$ with rotational-state selected OCS

The chemical reactivity of the different rotational states of OCS was probed by overlapping different parts of the deflected OCS beam with the $Ne^*$ expansion in the collision chamber. TOF mass spectra of ionic reaction products were recorded for different tilting angles of the OCS molecular beam setup while keeping the position of the $Ne^*$ beam fixed. Reaction-deflection profiles for both the Penning- and dissociative-ionisation products were obtained by plotting the integrated TOF signals of the products as a function of the deflection coordinate $y$. These profiles reflect the chemical reactivity of OCS in the distribution of rotational states varying across the deflected beam. The raw profiles for the reaction products from the Penning- and dissociative-ionisation channels obtained with both undeflected and deflected molecular beams are displayed in Figure 5.4a. The according normalised profiles are shown in Figure 5.4b. The profile of the dissociative-ionisation product was corrected for a small background signal at the same mass-to-charge-number ratio $m/z = 32$ u originating from Penning ionisation of trace molecular oxygen in the background vacuum which does not vary as a function of the deflection coordinate.

 The undeflected profiles of the Penning-ionisation and dissociative-ionisation products, in which the individual rotational states of OCS were not spatially separated, overlap. By contrast, a clear shift between the Penning-ionisation and dissociative-ionisation products was observed for the reaction profiles corresponding to the deflected beams. We attribute these differences to different reaction probabilities of individual rotational states in the two reaction pathways.

Qualitatively, the effect of the rotational states of OCS on the reactivity on the different reaction pathways can be seen from the shift in the reaction-deflection profiles shown in Figure 5.4. Quantitatively, the contribution of each rotational state to the Penning- and dissociative-ionisation reaction-deflection profiles was determined by fitting a weighted sum of state-specific simulated profiles to the experimental data. In these fits, the properties of the molecular beam were fixed to the values obtained from fits of simulations to the fs-laser deflection profiles (see Sec. 5.3.1) and only the weights
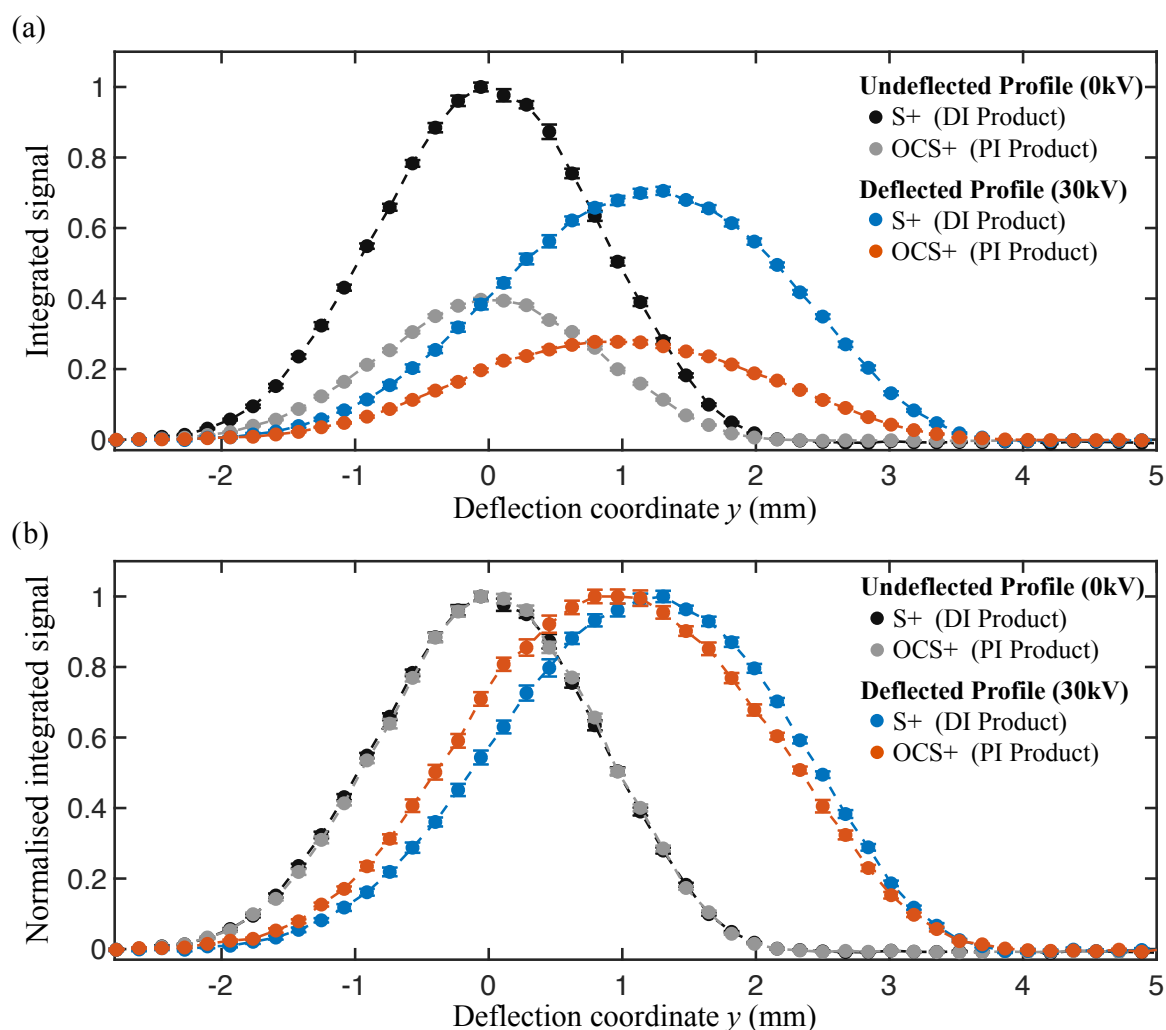
(a)



(b)



**Figure 5.4** (a) Raw and (b) normalised chemi-ionisation reaction-deflection profiles of OCS + Ne* recorded for the Penning-ionisation (PI) and dissociative-ionisation (DI) products obtained with deflected and undeflected beams. The error bars represent the standard error of 15 individual traces in which each data point was averaged over 1000 experimental cycles. In the normalised data a clear shift of the profiles associated with the PI and DI products is visible when the OCS molecules in different rotational states are spatially separated by the deflector (red and blue data points). The different shifts of the PI and DI product profiles are attributed to different reactivities of individual rotational states in the two reaction pathways. In clear contrast, for the profiles associated with the PI and DI products in the experiments with undeflected beams (black and grey data points) no shift is visible [111]. Dashed lines are only drawn to guide the eye.

of the individual rotational profiles in the sum was adjusted. Furthermore, as the beam waist of the fs-laser focus ($w \approx 30~\mu$m) is much smaller than the width of the Ne* beam ($d \approx 1.5$ mm), the different sampling volumes in the fs-laser ionisation and reaction

experiments were taken into account in the simulations (for details see Sec. 4.3.4). The resulting larger ionisation volumes causes slightly different shapes of the simulated reaction-deflection profiles due to averaging effects, which are fully understood as in greater detail described in Section 4.3.4.

Comparison of the laser-deflection profile with trajectory simulations in Section 5.3.1 showed that in the initial molecular OCS beam rotational states associated with $J=3$ or higher were barely populated and hence can be neglected. Therefore, in the following analysis only rotational states up to a total angular quantum number of $J=2$ were considered, which still resulted in six relevant state-specific simulated deflection profiles ($|00\rangle, |10\rangle, |11\rangle, |20\rangle, |21\rangle, |22\rangle$ for $|JM\rangle$). Considering all of these deflection profiles by giving them individual weights during the fitting procedure led to overfitting of the experimental data and did not provide meaningful results. It was thus necessary to restrict the number of independent fitting parameters. Considering that any orientation imparted by the field of the deflector should dephase during the transit over 45 cm from the exit of the deflector assembly [274], it can be assumed that all OCS molecules are isotropically oriented in the scattering region. Therefore, all $M$ states associated with a specific rotational state $J$ were weighted with a degeneracy factor $g_M = 1$ for $M = 0$ and $g_M = 2$ for $M > 0$ in the fit. This permitted to reduce the number of independent parameters to three weights for the simulated deflection profiles for $J=0$, 1, and 2, which were constructed by summing the $M$-state-specific deflection profiles according to their degeneracy factor. The fitting procedure is described in greater detail in Appendix B.1. The results of this analysis are shown in Figure 5.5.

As can be seen from the relative fitted weights of the different rotational states to the Penning- and dissociative-ionisation reaction-deflection profiles in the insets of Figures 5.5a and 5.5b, the individual states contribute with different efficiencies to the Penning- and dissociative-ionisation pathways. From the relative weights ($w_{J,\mathrm{DI}}$ and $w_{J,\mathrm{PI}}$), a ratio between the contribution of the dissociative- and the Penning-ionisation reaction pathway $R_J$ for each rotational state with quantum number $J$ was calculated to be

$$R_0 = w_{0,\mathrm{DI}}/w_{0,\mathrm{PI}} = 1.48(5),$$
$$R_1 = w_{1,\mathrm{DI}}/w_{1,\mathrm{PI}} = 0.57(13),\qquad(5.3)$$
$$R_2 = w_{2,\mathrm{DI}}/w_{2,\mathrm{PI}} = 0.20(58).$$

The same analysis was done for the raw data before normalisation (see Appendix B.1). In this case, the ratios also include the overall state-independent branching ratio (BR) of dissociative to Penning ionisation, which was determined to be $DI/PI = 2.5$ (see Sec. 5.3.2). The ratios of the Penning- and dissociative-ionisation pathway for each $J$-state including the branching ratio $R_{J,\mathrm{BR}}$ calculated from the relative fitted weights
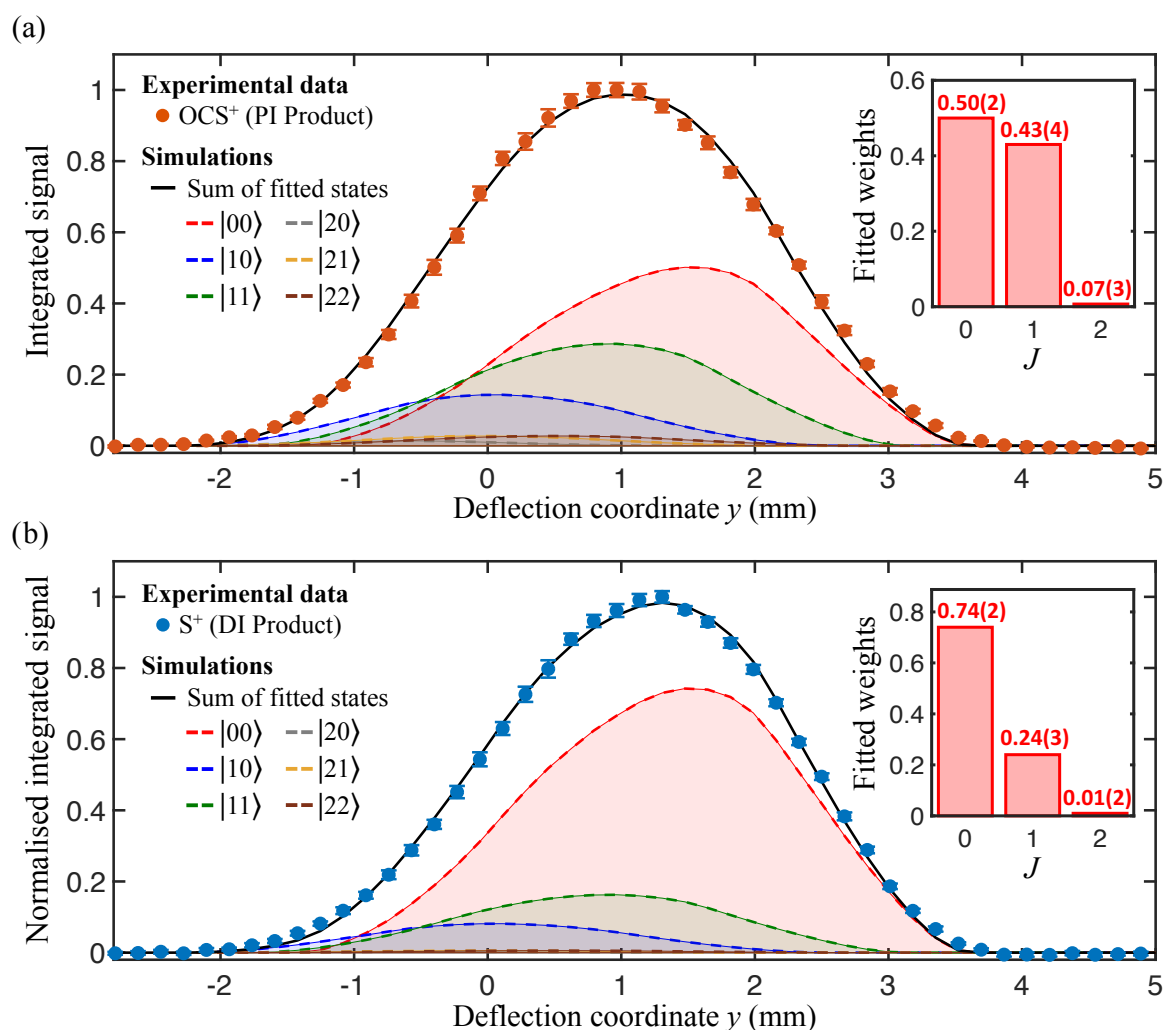
(a)



(b)



**Figure 5.5** Least-square fits of state-specific simulated reaction-deflection profiles to the experimental data for (a) the Penning- and (b) the dissociative-ionisation products [111]. Only the rotational states $J = 0, 1, 2$ significantly populated in the molecular beam were taken into account (see inset in Figure 5.2). Insets: Relative fitted weights of the individual rotational states ($J$) of OCS contributing to the reaction-deflection profiles. The uncertainties represent the fit errors.

of the raw deflection profiles are then given by

$$R_{0,\mathrm{BR}} = 3.77(9),$$
$$R_{1,\mathrm{BR}} = 1.44(21),$$
$$R_{2,\mathrm{BR}} = 0.52(99).$$

(5.4)

In a final step, it was possible to calculate the relative reactivity of the $J{=}0$ and $J{=}1$-states for the different reaction pathways. This ratio is independent of the overall

branching ratio and is given by

$$\frac{R_0}{R_1} = \frac{R_{0,\mathrm{BR}}}{R_{1,\mathrm{BR}}} = 2.6(6). \tag{5.5}$$

This value needs to be corrected for the initial thermal populations of $J$=0 and $J$=1 in the molecular beam, which was determined by the trajectory simulations in Section 5.3.1 to be $0.44/0.45 = 0.95$. Overall, it can then be said that OCS molecules in the rotational ground state $J$=0 are about a factor 2.7(6) more reactive in dissociative ionisation (yielding $S^+$) than in Penning ionisation (producing $OCS^+$) in comparison to the $J = 1$ state.

All uncertainties only represent the fit errors. Please note especially the large uncertainties for the ratios associated to the $J$=2-quantum state. Due to the small initial population in the molecular beam of molecules with $J$=2-rotational states, their impact on the different chemi-ionisation reactions could not be determined with a higher accuracy.

The above results originate from a fitting procedure, which assumes that molecules in rotational state with the same $J$ but different values for $M$ have the same reactivity towards the chemi-ionisation reaction with neon. Although this does not have to be true, this assumption had to be made to prevent overfitting of the experimental data. To validate the results given above, an alternative approach was taken to reduce the degrees of freedom in the fitting procedure. Instead of fixating the $M$-dependent degeneracy, in the second approach all molecules in rotational states associated with the total angular-quantum number $J$=2 were neglected. This is a reasonable assumption considering that the relative population of molecules in the $J$=2-rotational state was determined to be less than 10 % in the molecular OCS beam, as was determined from a comparison of the laser deflection-profile to trajectory simulations in Section 5.3.1. In contrast to the previous approach, this fitting procedure used independent fit weights for the deflection profiles of the $|10\rangle$ and $|11\rangle$ and hence allowed an individual contribution of these states. The results obtained by this alternative fitting procedure are very similar to the fit weights determined assuming a fixed $M$-dependent degeneracy and hence validate the above results (see Appendix B.2).

## 5.4   Discussion

The above experimental results provide clear evidence of an increased reactivity of molecules in the rotational ground state towards dissociative ionisation compared to molecules in the rotational states associated with $J$=1. This section aims to provide a first attempt towards a qualitative explanation of the observed experimental phenomena. At the moment of this writing, the exact reaction mechanism leading to

the observed different reactivities for different rotational states is still unknown to the author and hence it has to be stressed that the following is only a very preliminary proposal for understanding the underlying atom-molecule interactions based on previous studies of similar reaction systems.

As described in the introduction, the chemi-ionisation proceeds via two distinct reaction mechanisms, the indirect *radiative mechanism* predominating at subthermal conditions and the direct *exchange mechanism* prevailing at thermal collisions [128, 224–227, 229]. For the relative high collision energy of the experimental collision data presented here ($E_{col}$ = 0.3 eV), it can be expected in a first assumption that the reaction proceeds primarily via the *exchange mechanism*. In this case, the orbital overlap between the metastable rare gas atom and the molecular orbitals should play an important role and a strong geometrical dependence on the reaction outcome can be expected [129, 227, 247–258]. Previous studies on the chemi-ionisation reaction of metastable neon with ammonia showed that stereo-dynamic effects strongly impact if the reaction proceeds via the Penning ionisation or the dissociative ionisation pathway. Ionisation caused by an electron exchange from a molecular orbital associated with the lone pair of $NH_3$ led to the Penning ionisation product ($NH_3^+$), while removable of the electron from an N-H bonding orbital resulted into the dissociative ionisation products $NH_2^+$ and H [231, 247, 275]. A similar mechanism can be expected to govern the interaction of the present system $Ne^*$ + OCS.

As can be seen from Table 5.1, the ionic states of OCS energetically available in a chemi-ionisation reaction with metastable neon are the $X^2\Pi$, $A^2\Pi$ and $B^2\Sigma^+$ electronic states. Previous experiments investigating the reaction of $He^*$ + OCS using Penning ionisation electron spectroscopy (PIES) showed that the Penning ionisation reaction predominately populates the electronic $X^2\Pi$ and $B^2\Sigma^+$ states, whereas the $A^2\Pi$ is not appreciably populated [260, 263]. The results are very similar when neon was used as the metastable co-reactant [259]. Therefore, the $A^2\Pi$-state will be neglected in the following qualitative discussion, but surely it needs to be considered for a complete future analysis.

A previous study using photoelectron-photoion coincidence (PEPICO) spectroscopy on the dissociative ionisation of OCS at a photon energy of 21.21 eV showed that stable $OCS^+$ ions are almost exclusively formed via the ionic ground state $X^2\Pi$, while only a small fraction of stable $OCS^+$ could be assigned to the A-state [276]. The same study showed that $OCS^+$ ions in the $B^2\Sigma^+$ state exclusively dissociate forming $S^+$ ions and CO. Similar results regarding the dissociative characters of the electronic states of $OCS^+$ were shown by theoretical [277–279] and experimental studies [277, 278, 280–286]. Furthermore, although strongly vibrationally excited $OCS(X^2\Pi)^+$ can dissociate as well [284], it can be seen from Penning ionisation electron spectra pre-

sented in Ref. [259, 263] that by the chemi-ionisation reaction of OCS with He* only low vibrational states of the $X^2\Pi$ are populated on the grounds of Franck–Condon factors. Therefore, for the context of this discussion, it can be assumed that the ionic ground state is stable and hence leads to the formation of the Penning ionisation product OCS$^+$. Contrary, OCS$^+$ ions in the electronic $B^2\Sigma^+$ state dissociate, finally resulting in the reaction products S$^+$ and CO [279, 284].

The PIES data for He* + OCS also showed that the $B^2\Sigma^+$ state is more strongly populated than the ionic ground state [259, 260, 263]. Assuming that the $B^2\Sigma^+$ state is predominately dissociative while the $X^2\Pi$ is stable, the chemi-ionisation reaction is then expected to yield more dissociative-ionisation products than Penning ions. This qualitatively agrees with the observed experimental state-independent branching ratio of OCS$^+$ : S$^+$ = 1 : 2.5.

To include possible stereo-dynamic effects of the reaction, it is necessary to examine the relevant molecular orbitals of OCS associated to the ionic states. Molecules in the ionic ground state $X^2\Pi$ and the excited $B^2\Sigma^+$ state are formed by ionisation from the $3\pi$ and $9\sigma$ orbitals, respectively [264]. The electron density of these orbitals was calculated previously by Ohno and co-workers in the context of investigating the Penning ionisation reaction of OCS with metastable helium [263, 264]. For a visualisation of the electron densities of the relevant orbitals please refer to Ref. [264]. In general, it can be said that the electron distribution of the $3\pi$ orbital is predominately located around the carbon and sulphur atom with large regions extending in the perpendicular direction to the C=S double bond. Contrary, the electron distribution of the $9\sigma$ orbital is mainly located along the molecular bond axis. A perpendicular approach of the neon atom with respect to the molecular bond axis should favour an ionisation of OCS in the ionic ground state, whereas an approach along the bond axis should lead to the formation of OCS$^+$ in $B^2\Sigma^+$. Therefore, by purely looking at the involved ionic states and the spatial arrangement of the associated molecular orbitals, a strong steric dependency of the different reaction pathways can be expected. A perpendicular approach should favour the formation of the Penning ion OCS$^+$, whereas an approach along the bond axis has an increased probability of resulting in the dissociative ionisation products S$^+$ + CO.

The central question then remains why molecules in different rotational states posses different reactivities towards the Penning and dissociative ionisation pathways. This has to our knowledge not yet been studied for a comparable chemi-ionisation systems as investigated here. Therefore, it can only be speculated that different rotational states lead to different directional approaches between the molecule and the metastable neon. The interactions in the system are represented by the potential energy surface, which was calculated by Patrik Straňák using the analytical approach developed by Pirani

and coworkers [227, 248, 252, 253, 256, 287]. It assumes that at long intermolecular distances the metastable neon atom has a strong isotropic character, similar to that of an alkali atom, whereas at intermediate till short intermolecular distances the neon atom undergoes a strong polarisation of its highly excited 3s-electron cloud. The polarised neon atom features an ionic core, which can be described by assigning it a partial charge. The analytical model used takes all relevant intermolecular forces into account, including the dispersion, induction and van der Waals interactions, the attraction between the effective charge of the polarised neon atom and the molecular multipoles as well as small charge-transfer and electrostatic contributions. For details about the theory please refer to Refs. [227, 248, 252, 253, 256, 287] and for a detailed description of its application to the Ne$^*$ + OCS case, as presented here, see the dissertation of P. Straňák [142]. The resulting potential energy surface of OCS + Ne$^*$ is given in Figure 5.6.



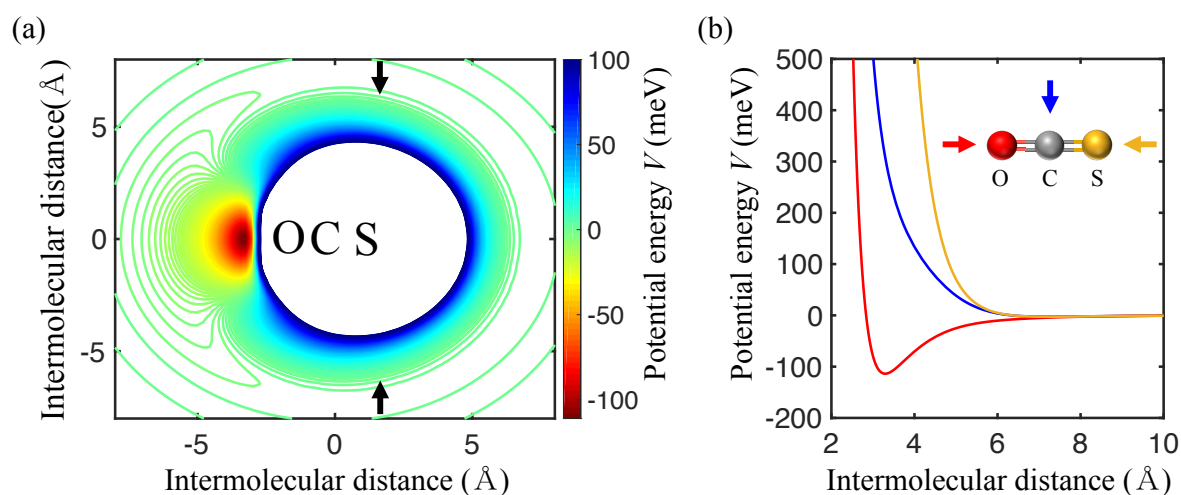**Figure 5.6** Analytical potential energy surface (PES) for the reaction of OCS + Ne$^*$ calculated by P. Straňák [142] based on a model described in Refs. [227, 248, 252, 253, 256, 287]. (a) Colour map of the PES in Cartesian coordinates. The labels indicate the positions of the atoms in the OCS molecule. Potential energies above +100 meV are not shown for clarity. The black arrows indicate the position of the missing attractive potential well at the sulphur side, which was observed for the reaction of He$^*$ + OCS [264], but which could not be reproduced by the analytical approach used here. (b) Interaction potential energy curves as function of the intermolecular distance between Ne$^*$ and OCS for several directional approaches as indicated in the inset of the figure: Linear approach towards the oxygen atom (red), perpendicular approach (blue) and linear approach towards the sulphur atom (yellow).

Qualitatively, the analytical PES surfaces for Ne$^*$ + OCS presented in Figure 5.6a agrees well with the interaction calculated for the reaction of He$^*$ + OCS presented in

Ref. [264], which was calculated ab-initio utilising the chemical resemblance between $He^*(2s)$ and $Li(2s)$. Only a weak attractive potential well positioned perpendicular to the molecular axis at the sulphur side, which originates from the degenerate nonbonding 3p orbitals extending around the C=S axis, could not be reproduced by the analytical model used here, even though it should also be present in the $Ne^*$ + OCS reaction. The approximate position of this potential well is indicated in Figure 5.6a by the black arrows. Furthermore, it has to be mentioned that it still remains to be seen in how far the given PES is also quantitatively accurate, as some properties, e.g. the size of the assumed partial charge on $Ne^*$, could only be estimated by comparing the present reaction to similar systems reported in the literature.

In the context of the theory developed by Pirani and coworkers, it might be speculated that in the entrance channel of the reaction the polar character of the OCS molecule introduces a strong polarisation of the metastable neon atom, similar to what was observed before in the reactions of $Ne^*$ + $N_2$ [257, 288], $Ne^*$ + $H_2O$ [249] and $Ne^*$ + $NH_3$ [253]. The resulting ionic core of the polarised $Ne^*$ atom would then generate a pronounced electric field, whose interaction with the electric multipoles of OCS would cause a re-orientation of the molecular axis towards a linear approach direction. The efficiency of this orientation would strongly hinge upon the effective dipole moment of the OCS molecule, which again depends on the initial rotational state. In this picture, molecules in the $J=0$ rotational state would undergo the strongest orientation in the entrance channel favouring a linear approach of the neon along the molecular axis. Such an approach would prefer the ionisation via the $9\sigma$ orbital leading towards the dissociative $B^2\Sigma^+$ state. The orientation efficiency should decrease for molecules in higher rotational states with smaller effective dipole moments, resulting in a higher probability for perpendicular approaches of the neon in respect to the molecular axis. This would increase the overlap of the inner-shell vacant orbital of the metastable atom with the $3\pi$-molecular orbital of OCS. Hence, for molecules in higher rotational states the formation of $OCS^+$ in the ionic ground state $X^2\Pi$ and therefore also the formation of the Penning ionisation product would be increased.

It has to be noted that such orientation effects should be in particular present for molecular interactions at low collision energies and in how far these effects play a role for the current experiments remains to be seen. Currently, ab-initio quantum-state calculations are being performed which should help to understand the precise nature of the chemi-ionisation reaction of $Ne^*$ + OCS.

## 5.5  Conclusion & Outlook

The results presented in this chapter demonstrate the utility of the novel crossed-molecular-beam setup to isolate individual rotational states of a molecule and study their reactivities in a bimolecular reaction. In the chemi-ionisation reaction of OCS with metastable neon, the Penning ionisation product ($OCS^+$) and the dissociative ionisation channel yielding $S^+$ were detected with a state-independent branching ratio of 1:2.5. The associative ionisation product was not observed. Investigating state-specific reactivities by separating different rotational states using inhomogeneous deflection fields showed that molecules in the rotational ground-state state have a higher reactivity towards the dissociative ionisation pathway than molecules in rotational states associated with $J=1$. Thus far, the details of the underlying reaction mechanism still remain unknown, but it can be speculated that the observed different reactivities of the individual rotational states are due to strong steric effects caused by different geometrical overlaps of relevant atomic and molecular orbitals, which play an important role in the *exchange mechanism* of chemi-ionisation reactions.

To further unravel the mechanistic details of the molecular interactions, it would be beneficial to gain additional information of the reaction products as well as possible reaction intermediates. This will become possible in the near future by the implementation of an ion-electron coincidence VMI detector into the current setup, which should enable simultaneous imaging of both the ionic reaction products and the emitted electrons. This should provide additional information about the involved ionic states in the reaction process and by that clarify the underlying reaction mechanism.

Furthermore, in the chemi-ionisation reaction experiments presented here no ionisation laser was used and hence the neutral reaction channels given in Table 5.1 could not be observed. Investigating these reaction pathways might be very interesting as it will increase the overall understanding of the atom-molecule interactions. In possible follow-up experiments, ionisation of the neutral reaction products could be done by the radiation of a femtosecond laser. This universal ionisation approach should yield sufficient experimental signal levels, but has the inherent drawback that the femtosecond laser would ionise and photodissociate neutral OCS molecules originating from the molecular beam. The resulting fragment ions in the spectrum would be difficult to distinguishing from the reaction products of the different chemi-ionisation pathways. A neater solution would be to ionise a specific neutral fragment, e.g. the CO-fragment, by resonance-enhanced multi-photon ionisation (REMPI). This method would be (almost) background free and has the additional advantage of being a state-specific detection technique. The downside of this technique is that the reaction products will be internally excited and with a narrow laser using REMPI only molecules in a specific

quantum-state can be detected simultaneously. This would significantly reduce experimental signal levels compared to using the radiation of a femtosecond laser, in which products in all states can be detected simultaneously. This drawback could be partially alleviated by using REMPI for atomic reaction products, which can only be excited to other electronic states. However, even then the detection efficiency of REMPI would be significantly smaller compared to the one achieved using a universal ionisation technique. If enough signal levels in experiments using state-specific detection can be obtained in the current setup, still remains to be seen.

The ability of the current setup to also investigate different reactivates caused by different geometrical structures of significant larger molecules is demonstrated in the next chapter on the example of the conformer-specific chemi-ionisation reaction of *trans*- and *cis*-hydroquinone with metastable neon.

# 6

# Conformationally-resolved chemi-ionisation reaction of Ne$^*$ + HYQ

Understanding the impact of molecular structure on the outcome of chemical reactions is a main objective in chemistry. In this chapter, the capability of the new crossed-molecular-beam setup to investigate conformational effects in bimolecular reactions under single-collision conditions is demonstrated with the example of the chemi-ionisation reaction of *trans*- and *cis*-hydroquinone with metastable neon. During these experiments, it was observed that formation of the dissociative-ionisation products was (almost) independent of the initial conformational and rotational state of the interacting hydroquinone molecule, while the reactivity towards forming the Penning ion (HYQ$^+$) seems to be conformational and rotational-state dependent. The reaction product of the associative-ionisation pathway was not observed.[1]

## 6.1   Introduction

The chemical structure of molecules strongly effects intermolecular interactions and chemical reactivity [289]. The importance of chemical structure becomes especially evident for biologically active molecules, whose proper functioning is crucially dependent on their correct geometrical shape [290, 291]. Even on smaller scales, molecular conformers are among the dominant forms of structural isomers. Thermal interconversion of conformers, i.e. the adiabatic transition from one conformational state to another, imposes great experimental challenges in performing conformation-dependent experimental studies as it makes the isolation and control of a single conformer an

ambitious task. This is especially true for molecular rotamers with small interconversion barriers. Due to these experimental difficulties, the precise impact of molecular conformers on chemical reactions is still poorly understood and so far only a small number of experimental studies under single-collision conditions investigating the impact of conformational effects on chemical reactivity in bimolecular collisions have been reported [292–294].

The experimental obstacles caused by the interconversion of conformers can be overcome by utilising the single-collision and low-temperature environment of supersonic beams, which efficiently suppresses thermal interconversion. Combining a supersonic expansion with the strong inhomogeneous electric field of an electrostatic deflector allows then preparation of molecules in specific conformational states depending on the different permanent dipole moments of the individual conformers [60, 74, 78, 79]. The resulting molecular beam of spatially separated conformers provides the ideal starting point to perform controlled, conformer-selective reaction experiments. This was demonstrated before in our laboratory for ionic reactions of *trans-* and *cis-*3-aminophenol with trapped Ca$^+$ ions [84, 85] and the cycloaddition reaction of *gauche-* and *s-trans-*2,3-dibromo-1,3-butadiene with sympathetically cooled propene ions [87], both revealing strong differences in the conformer-specific reactivities.

Here, the capability of the new crossed molecular beam setup to study the reactivity of individual conformers in neutral reactions is demonstrated on the chemi-ionisation reaction of metastable neon with the two conformational isomers of hydroquinone. Hydroquinone is the para-regioisomer of dihydroxybenzene ($C_6H_4(OH)_2$) and has an ionisation energy of 7.93 eV [295]. Hydroquinone is especially interesting from a fundamental point of view, because the rotation of the hydroxyl group around the bond with the benzene ring is inhibited, which gives rise to the apolar *trans-* and the polar *cis-*conformer ($\mu_{B,cis}$ = 2.38 D). This allows spatial separation of *trans-* and *cis-*HYQ by electrostatic deflection [206]. Investigating the specific reactivities of each conformer enables a direct comparison of two structural isomers with significantly different permanent dipole moments.

To our knowledge, the chemi-ionisation reaction of HYQ with a metastable rare gas atom was not yet investigated in a gas-phase collision experiment. But studies of Penning ionisation electron spectroscopy (PIES) with similar systems such as phenol [296], *p-*benzoquinone [297], aniline [296], thiophenol [296], and benzene [298] as well as dichlorobenzenes [299] and difluorobenzenes [300] have been reported, all showing strong anisotropies in the potential energy surface (PES) of the chemi-ionisation reaction with metastable helium.

The chemi-ionisation reaction of Ne$^*$ + HYQ can proceed via different reaction pathways resulting in the formation of the Penning (HYQ$^+$) and associative ion (NeHYQ$^+$)

as well as several dissociative ionisation products. As was described in the previous chapter, chemi-ionisation reactions proceed under thermal- and hyperthermal conditions predominantly via the direct *exchange* mechanism, which is contingent on sufficient overlap between the involved atomic and molecular orbitals and hence is strongly sterically dependent. Therefore, it can be expected that the outcome of the reaction should differ depending on the conformational state of the reactant. This is investigated in the following experiments.

## 6.2 Experimental setup

The novel crossed-molecular-beam apparatus has been described in detail in Chapter 3. A schematic illustration of the experimental setup used to investigate the chemi-ionisation reaction of conformer-selected HYQ with metastable neon is given in Figure 6.1. A molecular beam of hydroquinone was generated by placing a sample of HYQ (Sigma Aldrich, > 99 %) in the sample cartridge of a heatable Even-Lavie valve from which it was co-expanded with 90 bar of helium. The Even-Lavie valve with the sample catridge was heated to a temperature of $T_{\text{valve}} = 150$ °C to increase the vapour pressure of HYQ. This temperature was chosen as a compromise between sufficient signal levels and obtaining a cold molecular beam suited for electrostatic separation of the conformers (for details see Sec. 4.4.2). The resulting molecular beam contained both rotamers of HYQ in an approximately equal ratio of 51:49 (*trans*:*cis*) according to the Boltzmann factor at the valve temperature (see Sec. 4.1.3). The beam containing both HYQ conformers was guided through the inhomogeneous field of the electrostatic deflector, which resulted in a spatial separation of the the apolar *trans*- and the polar *cis*-conformer as indicated schematically in Figure 6.1. As the degree of deflection is determined by the interaction of the electric field with the effective dipole moments of HYQ molecules in certain rotational states, not only a separation of the different conformers was achieved, but also a spatial segregation of molecules in different rotational states along the deflection coordinate $y$.

The deflected beam of HYQ molecules was crossed with a beam of metastable neon atoms in the $(2p^5 3s)$ $^3P_2$ and $^3P_0$ states, which was generated in a supersonic expansion of neon gas (stagnation pressure 45 bar) through a pulsed plate-discharge source. Different parts of the deflected beam, containing unique compositions of HYQ rotamers in different rotational states, were overlapped with the second molecular beam in the collision region by tilting the HYQ molecular-beam setup with respect to the collision chamber. The resulting ionic reaction products were analysed by a time-of-flight mass spectrometer. This allowed the investigation of conformer- and state-specific
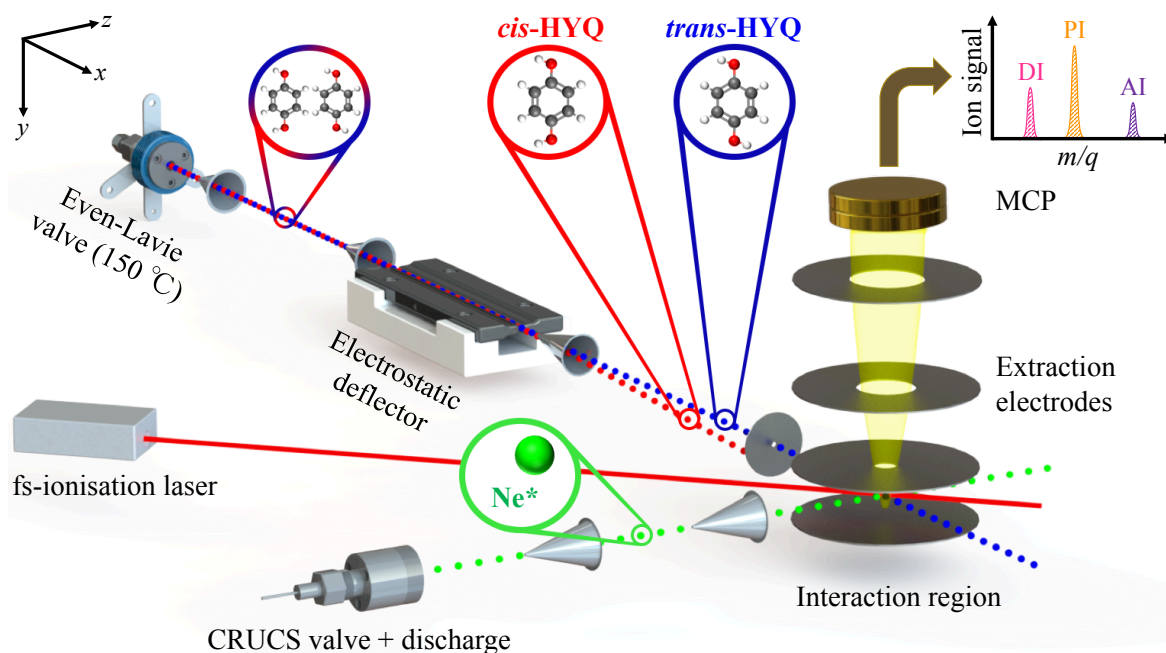
**Figure 6.1** Schematic of the experimental setup used for studying the chemi-ionisation reaction of hydroquinone with metastable neon. The Even-Lavie valve was heated to $T_{valve} = 150$ °C to reach sufficient beam densities. The electrostatic deflector allowed spatial separation of the *trans-* (blue dots) and *cis*-rotamers (red dots) of HYQ as schematically illustrated by the red and blue dots, respectively. After crossing the HYQ beam with an atomic beam of metastable neon atoms (green dots), the resulting product ions were detected by a time-of-flight mass spectrometer. This allowed the identification of the dissociative-ionisation (DI), Penning-ionisation (PI) and associative-ionisation (AI) reaction products. Different parts of the deflected HYQ beam could be overlapped with the metastable neon beam in the collision region by tilting the HYQ molecular-beam setup with respect to the collision chamber. Characterisation of the deflected molecular beam was possible by ionising the neutral HYQ molecules by femtosecond-laser radiation.

reactivities towards the different reaction pathways of the chemi-ionisation reaction of HYQ with metastable neon. The collision energy of the chemi-ionisation reaction was determined to be approximately 0.5 eV.

For analysis purposes, the deflected molecular beam was also multi-photon ionised by the radiation of a femtosecond laser. The resulting laser-deflection profile then allowed together with Monte-Carlo trajectory simulations the characterisation of the composition at different spatial positions of the beam.

## 6.3 Results & Discussion

### 6.3.1 Spatial separation of *trans*- and *cis*-HYQ

The principle of electrostatic deflection enabling the spatial separation of rotational states and conformers depending on their effective dipole moments was extensively described in Chapter 4, which also contains an in depth explanation of the Monte-Carlo simulations used to trace the trajectories of molecules passing through the deflection setup.

An experimental beam-density profile of a beam of HYQ molecules passing through a deflector carrying a potential difference of 35 kV is given in Figure 6.2a. The profile was obtained by integrating the TOF mass peak of photoionised $HYQ^+$ for different tilting angles of the molecular beam setup, in which the degree of deflection was measured as function of the deflection coordinate $y$, which represents the offset from the centre of the undeflected beam.

Although the detection technique used was not specific to the two conformational isomers, matching the Monte-Carlo trajectory simulations to the experimental data allowed an unambiguous determination of the deflection profiles for each individual conformer. This direct comparison revealed a clear spatial separation of the strongly deflected *cis*-rotamer from the apolar and hence undeflected *trans*-conformer. A similar separation for the two structural isomers of HYQ was confirmed previously using a conformer-specific detection technique [206]. When no potential difference was applied to the deflector, the beam-density profiles of both conformers spatially overlapped as shown in the inset of Figure 6.2a.

  The degree of archived deflection does strongly depend on the effective dipole moment of the manipulated HYQ molecules, which not only differs for its *trans*- and *cis*-conformation but also strongly depends on its rotational state. *Trans*-HYQ features no permanent dipole moment and hence no separation for molecules in different quantum states can be achieved. This is in clear contrast to molecules exhibiting a *cis*-geometry for which the effective dipole moment varies with the rotational state of the molecule, resulting in different deflection profiles for molecules in different rotational states. This is demonstrated by state-specific deflection profiles for all relevant populated states summed over $J$ in Figure 6.2b. In general, molecules in rotational states associated with a smaller total angular momentum $J$ have a larger effective dipole moment for experimentally relevant field strengths and were deflected more strongly (for details please refer to Section 4.4.2). The interaction of HYQ with the inhomogeneous electric field of the deflector thus resulted not only in a spatial separation of both structural isomers, but for the *cis*-rotamer also a segregation along the deflecting coordinate of
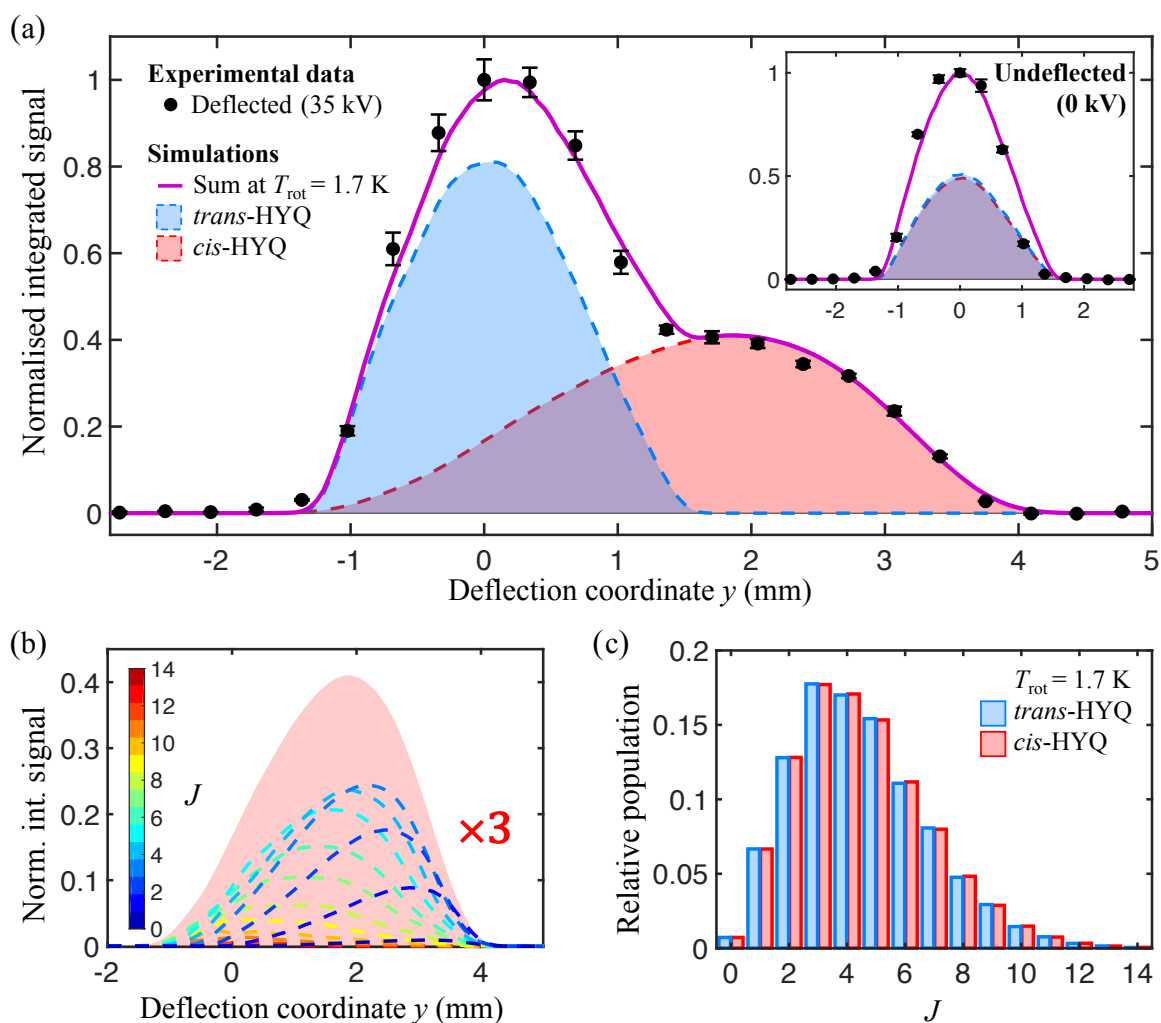
**Figure 6.2** Experimental deflection profile of HYQ obtained after multi-photon ionisation. The experimental data was reproduced by Monte-Carlo trajectory simulations for the *trans*- and *cis*-rotamers, assuming a rotational beam temperature of $T_{rot}$ =1.7 K. The inset shows the overlapping profiles of both conformers from an undeflected HYQ beam. The error bars represent the standard error of three individual measurements in which each data point was averaged over 2000 experimental cycles. (b) Contribution of the state-specific deflection profiles summed over quantum states with the same angular momentum quantum number $J$ towards the deflected *cis*-conformer. For clarity, all profiles are magnified by a factor 3. (c) Relative populations of all quantum-states summed over $J$ for $T_{rot}$ =1.7 K.

molecules in different rotational states was achieved. Matching the simulated deflection curves of *trans*- and *cis*-HYQ, which are averages of individual state-specific deflection profiles, to the experimentally obtained data allowed assigning a rotational temperature of $T_{rot}$ =1.7 K to the expanded molecular HYQ beam. The resulting relative populations of all quantum states summed over $J$ are given in Figure 6.2c.

## 6.3.2 Time-of-flight mass analysis of Ne* + HYQ

The chemi-ionisation reaction was investigated by overlapping the molecular beam of HYQ with an atomic beam of metastable neon. Time-of-flight mass spectrometry was performed by simultaneously extracting the ionic reaction products towards a time-sensitive detector by pulsed electric fields (see Sec. 3.5.2). A typical resulting time-of-flight mass spectrum of the chemi-ionisation reaction of Ne* with undeflected HYQ is shown in Figure 6.3.
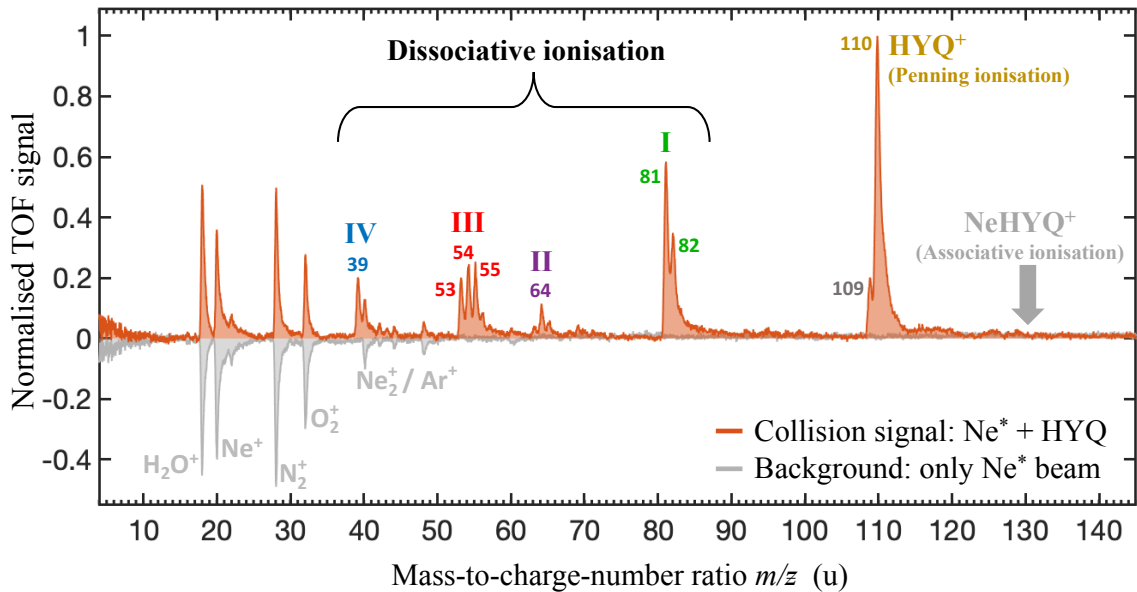


**Figure 6.3** Time-of-flight mass spectrum of products of the chemi-ionisation reaction of Ne* + HYQ. Intensities are normalised with respect to the strongest signal. The trace corresponding to the background experiment without the HYQ beam was inverted for clarity. Besides various peaks caused by Penning ionisation of background gases at smaller $m/z$-ratios, the Penning ionisation product (HYQ⁺) and various different dissociation fragments, labelled in roman numbers, are indicated in the spectrum. The different fragments are assigned in Table 6.1. The associative-ionisation product NeHYQ⁺ was not observed.

Besides the Penning ionisation product (HYQ⁺) at a mass-to-charge-number ratio of $m/z =110$, various ionic reaction products from the dissociative-ionisation pathway, labelled by Roman numbers, can be observed in the spectrum. The associative ion (NeHYQ⁺) was not detected within the sensitivity limits of the present measurement. Considering that earlier studies showed that the probability for the formation of the associative complex decreases with higher collision energies [46, 128, 238, 271–273], the lack of the associative ion in the spectrum was expected for the current collision energy of 0.5 eV. Still, it has to be mentioned that with the present experimental setup it is

not possible to distinguish if the HYQ$^+$ signal exclusively originates from the Penning ionisation reaction or also partially from predissociation of an unstable associative-ionisation complex. Although unlikely, in this case the reaction-deflection profile of HYQ$^+$, which is given in the next section, would be a superposition of the Penning- and associative-ionisation pathway.

The peaks at smaller mass-to-charge-number ratios could be assigned to Penning ionisation of trace gases in the background vacuum ($H_2O^+$, $N_2^+$, $O_2^+$). The spectrum also displays signals for Ne$^+$ and Ne$_2^+$, which can be attributed respectively to intra-beam Penning and associative ionisation between two metastable neon atoms. Both signals were already present in the trace of the background measurement (grey trace) with only the Ne$^*$ beam and did not change after overlapping it with the HYQ beam, which suggests that the ion-molecule reaction Ne$^+$ + HYQ can be neglected under the present experimental conditions.

The fragment ions stemming from dissociative ionisation in the spectrum could be identified based on their mass-to-charge-number ratio and using earlier studies on photodissociation of hydroquinone vapour [301], negative-ion mass spectrometry [302] and laser-induced photoionisation followed by TOF-MS [303]. Based on these references, the proposed reaction products for the signals observed in Figure 6.3 are summarised in Table 6.1 together with the experimentally determined branching ratios of the individual reaction channels.

**Table 6.1** Products and branching ratios of the chemi-ionisation reaction of Ne$^*$ + HYQ

| Label | Reaction products | Mass of ionic product (u) | Branching ratio |
|---|---|---|---|
| PI | $C_6H_6O_2^+$ | 110 | 1 |
| I | $C_5H_6O^+$ + CO | 82 | 0.61(4) |
|  | $C_5H_5O^+$ + HCO | 81 |  |
| II | $C_5H_4^+$ + CO + $H_2O$ | 64 | 0.04(1) |
| III | $C_3H_3O^+$ + $C_3H_3O$ | 55 | 0.43(3) |
|  | $C_3H_2O^+$ + $C_3H_4O$ | 54 |  |
|  | $C_3H_1O^+$ + $C_3H_5O$ | 53 |  |
| IV | $C_3H_3^+$ + $C_2H_3O$ + CO | 39 | 0.12(1) |

The branching ratios were determined by integrating the according signals in the TOF mass spectrum and are normalised for the value of the Penning ionisation product. The branching ratio of the Penning-ionisation pathway to the sum of all pathways assigned to dissociative ionisation was determined to be PI : DI = 1 : 1.2(1). Error

bars represent the standard error of 6 individual measurements averaged over 10.000 experimental cycles. Please note that in Figure 6.3 also a small signal at $m/z = 109$ can be observed, which originates from the dissociation of a single hydrogen atom from HYQ. This peak is not well resolved from the much larger peak associated with HYQ$^+$, which does not allow for a separate analysis by integration. Therefore, this dissociative-ionisation channel was not further investigated.

While analysing the data, it has to be considered that fragmentation of hydroquinone molecules could already take place in the heated gas nozzle or during the expansion process. For this purpose, the molecular beam of HYQ was analysed by TOF mass spectroscopy after general ionisation using a femtosecond laser. The resulting spectrum showed indeed signals for all ionic dissociation products given in Table 6.1 and furthermore also signals for the fragment ions $C_2H_2^+$ ($m = 26$ u), $C_2H_3^+$ (27 u), $C_2H_4^+$ (28 u), $CO^+$ (28 u) and $HCO^+$ (29 u) (see Appendix C), which were not observed in the chemi-ionisation reaction with metastable neon. The deflection profiles of all dissociation fragments (I-IV) obtained after photoionisation using a femtosecond laser showed exactly the same deflection behaviour as the photoionised HYQ$^+$ molecule (see Appendix C). This would not be the case if these fragments would already have been present in the initial molecular beam, because then the different dipole moments of the different fragments should have led to different deflection profiles. Contrarily, the same deflection behaviour for all fragments strongly indicates that the observed fragments are produced by photodissociation of the common precursor HYQ and that the molecular beam of HYQ is devoid of possible fragments. Further investigation of possible HYQ clusters showed that the HYQ beam consisted out of more than 97 % of monomers and that eventual molecular cluster contributions are negligible (Appendix C). Therefore, all fragments observed in the TOF-MS trace in Figure 6.3 can be assigned to products of the chemi-ionisation reaction of Ne$^*$ + HYQ.

### 6.3.3 Chemi-ionisation reaction of Ne$^*$ with conformer-selected HYQ

The chemical reactivity of *trans*- and *cis*-hydroquinone was probed by overlapping different parts of the deflected HYQ beam with the atomic beam of metastable neon. Integrating the relevant mass peaks of the TOF-MS traces obtained at different deflection coordinates $y$ resulted in the reaction-deflection profiles presented in Figure 6.4. These profiles reflect the chemical reactivities of *trans*- and *cis*-hydroquinone according to their relative conformational abundance and distribution of rotational states varying across the deflected HYQ beam as was determined in Section 6.3.1.

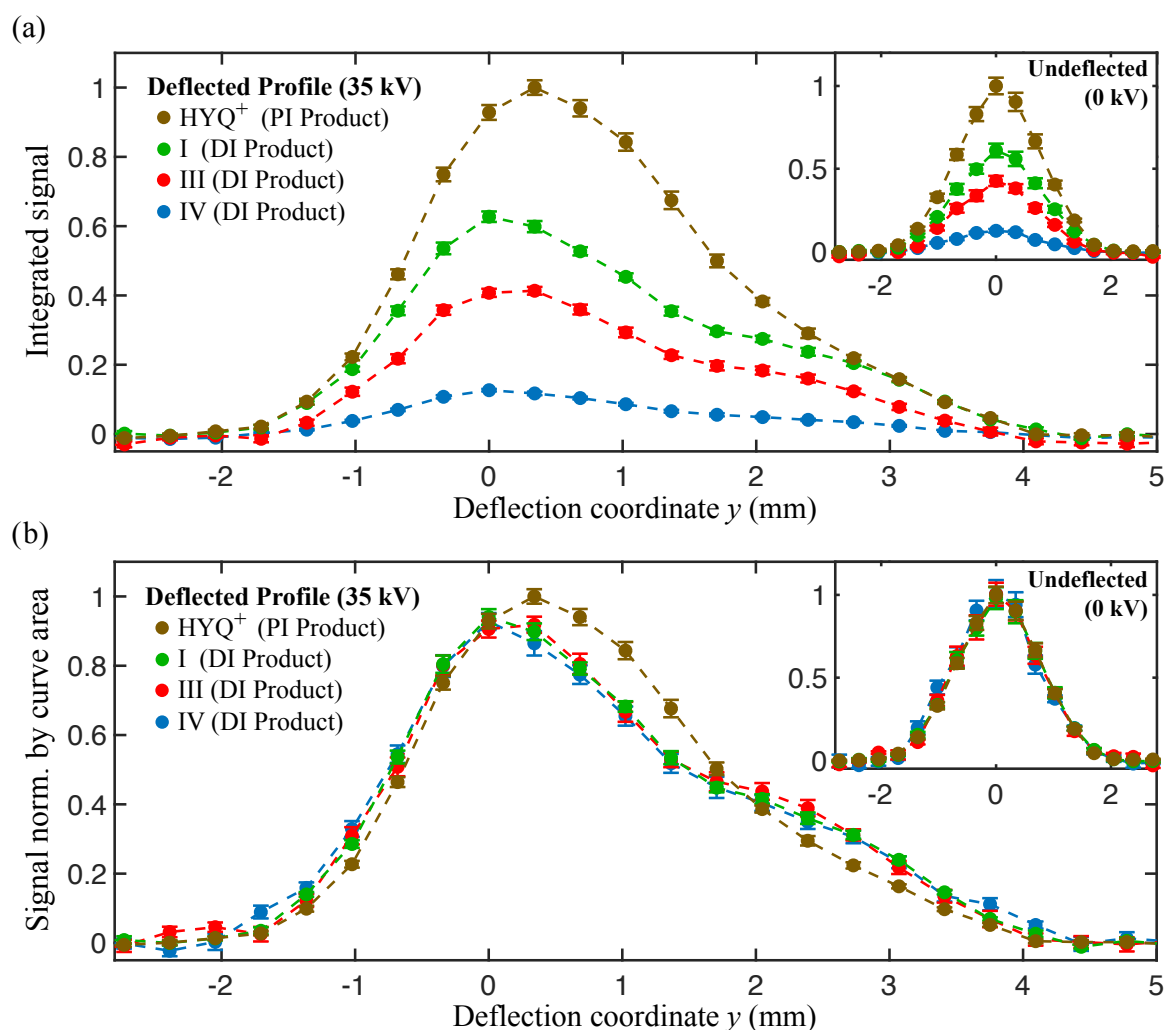Figure 6.4a presents the raw reaction-deflection profiles for the Penning-ionisation

(a)



(b)

**Figure 6.4** (a) Raw chemi-ionisation reaction-deflection profiles of HYQ + Ne* recorded for the Penning-ionisation product (HYQ⁺) and the different dissociative-ionisation products summarised in Table 6.1 for a deflected molecular beam. The error bars represent the standard error of 18 individual traces in which each data point was averaged over 10.000 experimental cycles. (b) Same deflection profiles, but normalised by the area below the curves, which is proportional to the number of detected ions. A clear shift of the profiles associated with the PI and DI products is visible in the data for the deflected molecular beam, while all dissociative-ionisation products follow the same deflection pattern. In clear contrast, for the profiles associated with the PI and DI products in the experiments with undeflected beams (insets in both figures) no shift is visible. Dashed lines are only drawn to guide the eye.

product (HYQ⁺) and the products of the dissociative-ionisation pathways I, III and IV as assigned in Table 6.1. The reaction profiles were normalised for the maximum signal obtained for the Penning-ionisation profile. Figure 6.4b shows the same deflection profiles, but in a representation in which each individual profile was normalised by the area

below the deflection curve. This area is proportional to the number of detected ions and hence Figure 6.4b gives the branching-ratio corrected reaction-deflection profiles. It is striking that all reaction-deflection profiles originating from a dissociative-ionisation pathway overlap in the normalised representation, while the reaction-deflection profile of the Penning-ionisation product is clearly different. This is in contrast to the data obtained for an undeflected HYQ beam, in which all reaction-deflection profiles independent of the reaction pathway followed the same deflection behaviour (inset of Fig. 6.4b). Therefore, we assign the different shapes of the dissociative- and the Penning-ionisation deflection profiles to different conformational and rotational reactivities of HYQ towards these reaction pathways.

The deflection profile of the ionic product from the dissociative-ionisation channel II was not included in Figure 6.4, because in the current measurements the extent of averaging was not sufficient to obtain a smooth deflection curve for this reaction channel. However, also the profile associated with the ionic product of reaction channel II seems to follow the deflection curve of the other dissociative-ionisation products as shown in Appendix D. Because all dissociative-ionisation products follow within the experimental uncertainties the same reaction-deflection curve, in the following analysis only the deflection curve of product channel I was considered exemplary for all dissociative-ionisation products.

To further quantify the experimental data and especially disentangle the contribution of the molecular conformation and rotational state towards the different deflection profiles, a series of least-square fits comparing the experimental data to trajectory simulations have been performed. In these fits, the properties of the molecular beam in the trajectory simulations were fixed to the values obtained from the fit of the simulation to the fs-laser deflection profile (Sec. 6.3.1). Only the parameter for the sampling volume was adjusted in the simulations to take into account the significantly larger size of the Ne$^*$ beam ($d \approx 1.5$ mm) compared to the beam waist of the fs-laser focus ($w \approx 30$ $\mu$m). The resulting larger ionisation volumes causes slightly different shapes of the simulated reaction-deflection profiles due to averaging effects, which are fully understood as in greater detail described in Section 4.3.4.

In a first step, the role of the geometrical difference between the two conformers, i.e. the orientation of the hydroxyl group with respect to the benzene ring, was investigated. This was done by fitting the contribution of the simulated deflection profiles associated with *trans*- and *cis*-HYQ to the experimental reaction-deflection profiles, while keeping the thermal rotational-state distribution of the molecular beam the same as was determined in Section 6.3.1 by matching the trajectory simulations to the laser-deflection profile. This approach allows free adjustment of the conformational reactivity within the least-square fit, while at the same time restricting the rotational-state reactivity to

121

be equal for all states. The impact of the conformational reactivity is quantitatively being expressed by a scaling constant $S_{cis}$, which scales the simulated deflection profile of the *cis*-conformer with respect to the deflection profile of *trans*-HYQ. This scaling is in reference to the initial populations of both conformers in the molecular beam. A scaling constant larger than 1 ($S_{cis} > 1$) thus expresses an increased reactivity of *cis*-HYQ towards the investigated reaction pathway compared to the *trans*-conformer, while a value below 1 hints for a decreased reactivity. The best values of $S_{cis}$ for the Penning- and dissociative ionisation profiles was determined by matching the sum of the simulated profiles for the *trans*- and scaled *cis*-conformer, obtained at a fixed rotational temperature of $T_{rot} = 1.7$ K, to the experimental reaction-deflection profiles in a least-square fitting approach. The results are given in Figure 6.5.

For both reaction pathways, the least-square fit resulted only in a small adjustment of the contribution of the *cis*-conformer, which corresponds to a reduced *cis*-specific reactivity of around 8 % and 6 % compared to *trans*-HYQ for the Penning and dissociative-ionisation pathway, respectively. These results suggest that the contribution of the conformational-reactivity to the observed effects are small.

It is striking that the experimental reaction-deflection profile for the dissociative-ionisation pathway (here represented by product I) is nicely reproduced by the trajectory simulations with only very small adjustments to the simulated conformational-deflection profiles (Fig. 6.5b, $S_{cis} \approx 0.94$). Furthermore, also the state-specific reactivities are the same for all populated states as they were fixed during the fit procedure. This implies that the reactivity of HYQ towards dissociative-ionisation in the chemi-ionisation reaction with metastable neon is not effected by its conformation or rotational quantum state.

This is in clear contrast to the data concerning the Penning-ionisation pathway, which could not be reproduced by simulations when only the conformational reactivities were adjusted while keeping the rotational reactivities fixed. Even for the best fit obtained, the discrepancy between the simulated and experimental deflection profile is significant (Fig. 6.5a), which suggests that the observed shift between the dissociative-ionisation and Penning-ionisation deflection profiles cannot (only) be explained by a difference in conformational reactivity.

In an alternative analysis, the reactivity of both HYQ conformers was kept the same, but instead the contribution of the rotational states towards the reaction-deflection profile of the Penning product was analysed. For such a large molecule as HYQ, many rotational states are populated even in a rotationally-cooled supersonic beam. Therefore, a least-square fitting analysis which allows an independent contribution for each individual rotational state is practically not feasible and restrictions to the fit procedure had to be applied. For that reason, it was investigated which thermal assembly of
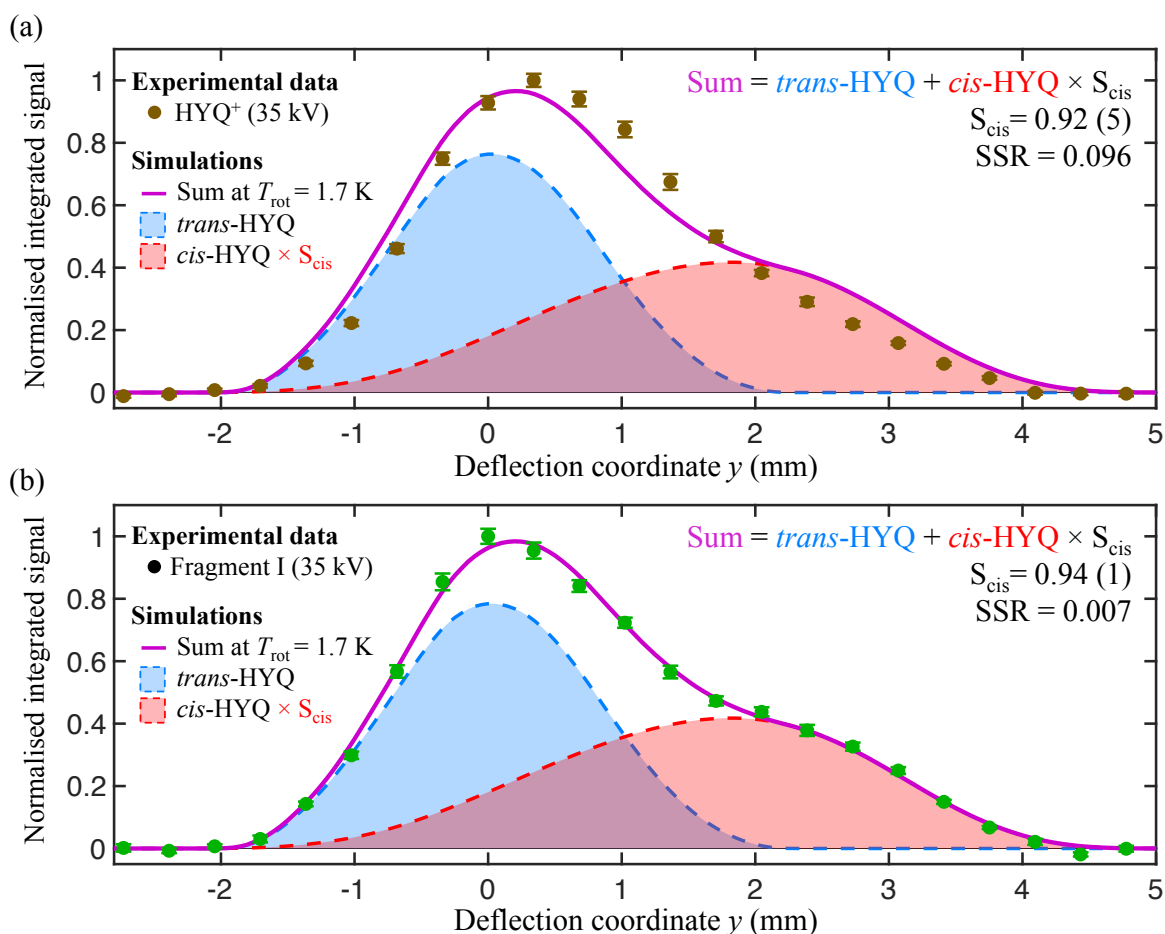
(a)



(b)



**Figure 6.5** Least-square fits of conformer-adjusted simulated reaction-deflection profiles to the experimental data for (a) the Penning- and (b) the dissociative-ionisation reaction pathway (exemplary shown for channel I). The thermal population of the rotational states was fixed to a rotational temperature of $T_{rot} = 1.7$ K, but the contribution of the *cis*-HYQ deflection profile was adjusted in a least-square fitting approach. The fit equation is given in the top right of the figure together with the values for the fitted scaling constant $S_{cis}$, which best reproduced the experimental data. The errors represent the fit uncertainties. The quality of the fits is expressed by the sum of squared residuals (SSR).

rotational states would best reproduce the experimental data. Although this approach will not result in specific reactivities of individual states, it should give an indication if rotational states associated with larger $J$-quantum number have an increased or decreased reactivity towards the Penning-ionisation pathway. Please note that in principle for this analysis purely the rotational states of the *cis*-conformer are relevant, as the rotational states of the apolar trans-conformer were not separated by the deflector and hence all equally contribute to the *trans*-HYQ deflection profile. During this procedure, the contribution of the two conformers were kept fixed to their abundance

in the deflected molecular HYQ beam, which was determined by the laser-deflection profile (Sec. 6.3.1).

The best match for the Penning-ionisation reaction-deflection profile was achieved for a thermal assembly of rotational states associated with a rotational temperature of $T_{rot} = 2.3$ K, as show in Figure 6.6a. Figure 6.6b gives a direct comparison of the relative populations of all quantum states summed over $J$ for a temperature of $T_{rot} = 2.3$ K and $T_{rot} = 1.7$ K, at which the best fits were obtained for the Penning-ionisation and dissociative-ionisation deflection profiles (Fig. 6.5b), respectively.
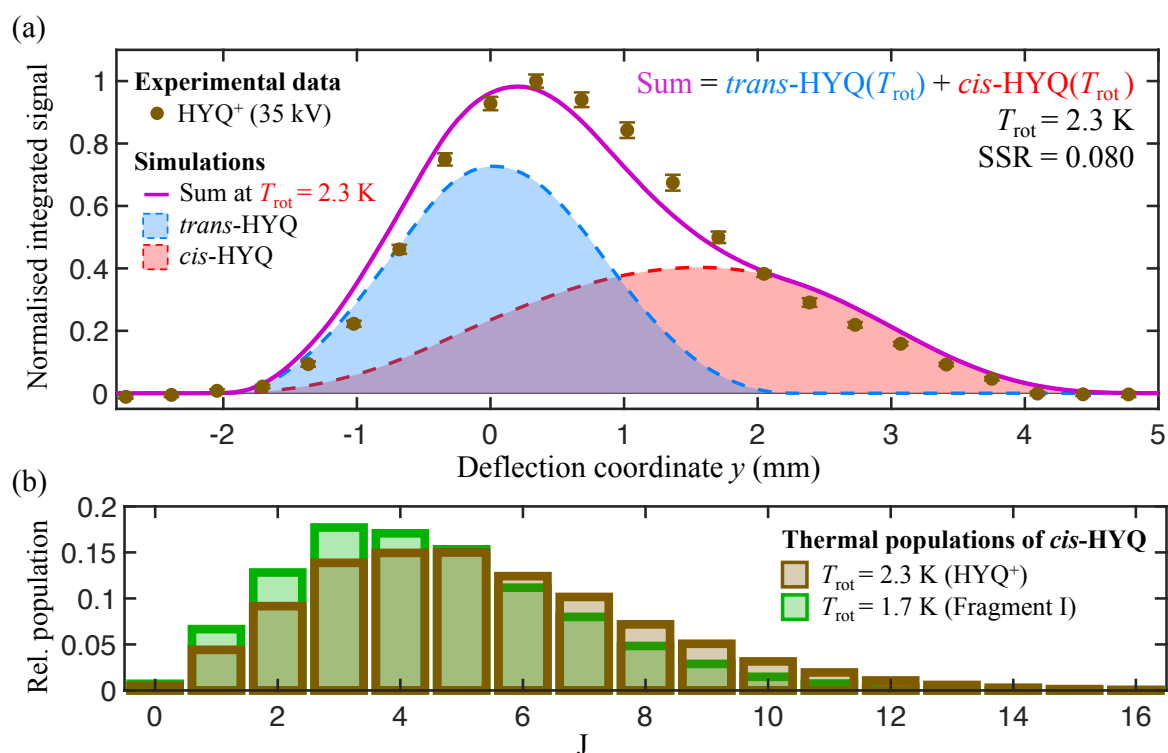


**Figure 6.6** (a) Best match of thermal trajectory simulations to the experimental reaction-deflection profile of the Penning-ionisation product. The simulated deflection profiles change as a function of the rotational temperature as indicated in the figure by $cis$-HYQ($T_{rot}$) and $trans$-HYQ($T_{rot}$). The rotational temperature was adjusted until the best reproduction of the experimental data was achieved. The contribution of the two conformers were kept fixed to their abundance in the deflected molecular HYQ beam. The simulations obtained for a rotational beam temperature of $T_{rot} = 2.3$ K provided the best match with the experimental deflection profile of the Penning ion. (b) Relative population of the $cis$-conformer for the rotational temperatures which reproduced best the experimental data for the Penning-ionisation pathway ($T_{rot} = 2.3$ K) and the dissociative-ionisation pathway ($T_{rot} = 1.7$ K, Fig. 6.5b).

This comparison suggests that HYQ molecules in energetically higher rotational sates have an increased reactivity towards the Penning-ionisation pathway. However,

also the least-square fit given in Figure 6.6a does not present a satisfactory reproduction of the experimental results.

Another attempt was made to better reproduce the experimental data by adjusting the thermal rotational-state distribution and the contribution of the two conformers, simultaneously. Although this resulted in a slightly better overall match (as shown in Appendix E), the fit yielded both an unreasonable high rotational temperature of $T_{rot} = 5.5$ K and an excessively large contribution of the *cis*-conformer (factor 4.8 higher than the contribution of *trans*-HYQ). Upon further investigation, it seems that the resulting fit has a very shallow optimisation minimum, which cannot be trusted as the simultaneous adjustment of both the rotational temperature and contribution of the conformers resulted in too many degrees of freedom for a trustworthy fit.

Furthermore, it has to be said that assuming a rotational reactivity based on a thermal distribution is very speculative and might not reproduce the actual physical interaction between HYQ and metastable neon. Especially, the results of Chapter 5 suggest a strong difference in the reactivity of molecules in different rotational states. As it is not feasible to disentangle the contribution of each rotational state by a pure fitting approach, hopefully future theoretical investigations will contribute some additional insights in how much the rotational and conformational state of HYQ impacts the reaction outcome. When theoretically calculated conformational- and rotational reactivities of the reaction would become available in the future, these could be implemented into the Monte-Carlo trajectory simulations which then should be able to reproduce the experimental data significantly better than the fits presented here.

So far, no theoretical calculations investigating the interaction of conformer-selected HYQ with metastable neon have been done yet, but a few assumptions towards the reaction mechanism can be formulated based on the experimental results presented here. First, because the reaction-deflection profiles of the different dissociative-ionisation pathways all follow the same deflection pattern, it can be speculated that for all these pathways the reaction proceeds via the same entrance channel resulting in the same reaction intermediate, which only then dissociates into the different product fragments. Second, the formation of this reaction intermediate seems to be independent of the initial conformational or rotational state of the HYQ molecule. This assumption is based on the fact that the reactive-deflection profile can be nicely reproduced by Monte-Carlo trajectory simulations assuming the same rotational and conformational distribution as was determined from comparison to the laser-deflection profile (Fig 6.5b). And finally, the reactive interaction leading to formation of the Penning ion seems to be dependent on both the initial conformer and rotational state of the HYQ molecule. This can be concluded from the observation that the reaction-deflection profile cannot be reproduced by assuming the same conformational and rotational state populations as was

125

determined for the initial molecular HYQ beam (Fig 6.5a). What causes this dependence is at the current moment still unknown and also very hard to speculate. Previous studies on the similar case of He$^*$ + phenol ($C_6H_6O$) showed a strong anisotropy in the potential energy surface, in particular a strong attractive potential well around the oxygen atom [296]. Similar to what was speculated for the Ne$^*$ + OCS reaction, the strong anisotropy might lead to different approach directions depending on the conformational and rotational state of the molecule, which differ in their effective dipole moment. The resulting different approaches ultimately might result in different probabilities for formation of the Penning ion. This is still far from a satisfactory explanation of the observed experimental phenomena, but hopefully future theoretical investigations will add some additional information which will help to better understand the state and conformational effects observed here.

## 6.4 Conclusion & Outlook

Although there are still a few open questions, the experimental results presented in this chapter showed that the new crossed-molecular-beam setup can be used to investigate conformational effects in bimolecular reactions. In particular, for the chemi-ionisation reaction of HYQ + Ne$^*$, the Penning ion (HYQ$^+$) was observed as the dominating reaction product alongside several ionic products originating from different dissociative-ionisation reaction pathways. Their respective branching ratios could be determined by TOF mass spectrometry. Formation of the associative ion was not observed.

Spatial separation of *trans*- and *cis*-HYQ, in combination with a unique distribution of rotational states along the deflection coordinate, allowed the investigation of conformational and rotational effects on the reaction outcome. This revealed a clear difference between the Penning- and the dissociative-ionisation pathways. Comparison to Monte-Carlo trajectory simulations showed that the formation of the dissociative-ionisation products in the chemi-ionisation reaction seems to be independent of the initial conformational or rotational state of HYQ, while the Penning-ionisation pathway showed a clear conformational and rotational dependency. However, the great number of involved rotational states makes a quantitative analysis purely based on experimental results very challenging, which explains why the rotational and conformational contributions towards the reaction mechanism could not be disentangled satisfactorily. This might become possible by future theoretical calculations, which should eventually allow a forward convolution of the trajectory simulations based on theoretical conformational and rotational reactivities.

To investigate and disentangle the conformational and rotational impact on the chem-

ical reactivity, it would be interesting to perform experiments as done here while only having a single conformer being populated in the molecular beam at once. This would experimentally disentangle the conformational from the rotational dependency, as for each conformer the rotational effects could be investigate in a separate measurement. Such experiments would demand chemical separation of the conformers and would make it necessary to keep them from interconverting during the full duration of the measurement. This is for a molecule like hydroquinone, for which the two different conformers easily interconvert through a reasonable small rotational barrier, extremely challenging, but could be attempted for molecules having significantly more stable conformers. Currently, such experiments are attempted in our laboratory with 1,2-dibromoethylene ($C_2H_2Br_2$), whose barrier for interconversion from *trans*- to the *cis*-conformer, although still unknown, should be significantly larger than for the hydroquinone rotamers. These experiments should lead to an understanding which might also be beneficial for the interpretation of the experimental result presented here.

# 7

# Conclusion & Outlook

This thesis reported the design, construction and characterisation of a novel crossed-molecular-beam setup, which aims to investigate state- and conformational effects in bimolecular reactions under single-collisions conditions. The distinctive feature of the new setup is an electrostatic deflector integrated into one of the molecular beams, which allows the spatial separation of polar molecules in different rotational states or conformations depending on their respective effective dipole moments [74]. In contrast to many crossed-beam setups previously reported [10, 12–19], the apparatus introduced here allows especially the control and manipulation of molecules in strong-field seeking states prior to the reaction. This enables in particular the study of large, polyatomic molecules which are exclusively strong-field seeking at electric field strengths relevant for experimental investigations. The second beam source is equipped with a home-build discharge unit which allows the generation of metastable rare gases as well as radicals to serve as co-reactants in the collision with the state- or conformation-selected molecular beam [127, 142]. A time-of-flight mass spectrometer allows the detection and identification of the reaction products as well as the determination of mass-specific relative integral cross sections. Ionic reaction products can be mass-specifically detected by pulsed ion-extraction fields, while neutral reaction products can be observed after the universal multiphoton ionisation of a femtosecond laser or the state-specific resonance-enhanced multiphoton ionisation (REMPI) using a Dye-Nd:YAG laser combination. A mass-gated velocity-map-imaging detector enables the observation of differential cross sections of specific reaction products. Although this has been proven to work successfully for photodissociation experiments, it has not yet been used for the investigation of bimolecular reactions. Mainly because only chemi-ionisation reactions have been investigated so far with the new setup, whose resulting ionic reaction products demand switching of the extraction fields for mass-specific detection. This imposes experimental difficulties for the simple VMI

detector used, which have not been overcome yet. Updating the present VMI detector should therefore be a priority as discussed later.

The capabilities of the new apparatus were demonstrated in first proof-of-principle experiments studying the class of chemi-ionisation reactions. The investigation of rotational-state selected OCS molecules with metastable neon atoms revealed that the branching ratio between the dissociative-ionisation pathway leading to $S^+$ and the formation of the Penning ion $OCS^+$ strongly depends on the initial rotational sate of the OCS molecule. Specifically, the reactivity of OCS molecules in the rotational ground state towards dissociative ionisation is enhanced compared to the $J$=1 state [111]. Other ionic products of dissociative-ionisation pathway besides $S^+$ were not observed as they were energetically unavailable considering the excitation energy of metastable neon and the experimental collision energy.

The chemi-ionisation reaction of metastable neon with spatially separated *trans-* and *cis*-hydroquinone resulted in the formation of the Penning ion $HYQ^+$ and several polyatomic dissociative-ionisation products. For all dissociative-ionisation products detected, no dependence of the reactivity on the initial conformational or rotational state of the hydroquinone molecule was observed. This is in clear contrast to the reactivities for the formation of the Penning ion, which seemed to be dependent on the initial rotational state of hydroquinone as well as on its molecular conformation. Due to the complexity caused by many rotational states populated in the initial molecular beam, the final conformational and rotational contributions of the reacting HYQ molecules could not yet be disentangled satisfactorily. This should become possible in the future when theoretically calculated state- and conformational reactivities will be implemented into trajectory simulations, which should then be able to reproduce the experimental results better than existing simulations. In both chemi-ionisation reactions, the associative ion was not observed as was expected considering the high collision energies of the performed experiments.

Although the studies of both reactions showed clear experimental evidence of state- and, for the case of hydroquinone, also conformational effects, the underlying reaction mechanisms are not yet fully understood and further theoretical as well as potential experimental investigations are necessary to achieve a final understanding of the chemical processes causing the observed state- and conformation-dependence of the reactivities.

# 7.1 Technical improvements of the CMB setup

Although it was shown that the novel crossed-molecular-beam setup is already suited to produce scientifically interesting observations, as for every other experimental apparatus only continuous improvements will enable its full potential and will keep it at the highest scientific standard.

As extensively discussed at the end of Section 3.5.3, the simple initial design of the VMI detector used here needs to be upgraded as it is not suited for large ionisation volumes and does not work correctly when the extraction fields have to be switched. Both these drawbacks became apparent while investigating chemi-ionisation reactions. For these reactions, the ionisation volume is defined by the cross sectional area of the intersecting beams, which is significantly larger than the ionisation volume of neutral reaction products ionised by a focused laser beam. Furthermore, mass-specific detection of the ionic reaction products need time-varying electric fields. Therefore, an upgrade towards an ion-electron coincidence VMI detector [187] with significantly softer extraction fields is already scheduled in our laboratory and should be implemented soon in the existing setup. Such a detector should work for large ionisation volumes and the combined arrival times of the electrons and ions should allow a software-based identification of neutral and ionic reaction products without the need to switch the extraction fields. Furthermore, the added ability to detect the emitted electrons should provide additional information about the ionic states involved in the reaction, which would be very useful for further clarification of the underlying reaction mechanism. The benefit of an ion-electron coincidence VMI detector for the investigation of chemi-ionisation reactions has been demonstrated before [45].

Another useful upgrade for the investigation of chemi-ionisation reactions would be the ability to quench certain metastable states to be able to perform reactive collisions with metastable-rare-gas beams containing only a single excited state. Several methods are available including magnetic [163] and optical deflection [164] as well as optical quenching using a discharge lamp [156–159] or laser radiation [160–162]. Implementation of any of these techniques into the existing setup should be straightforward.

Finally, recent experiments have shown that the spatial separation achieved by the electrostatic deflector can be improved by introducing a movable knife edge into the path of the deflected molecular beam [79]. Implementing such a knife edge should directly have an impact on the quality of the acquired data with the current setup, because a better separation of molecules in different rotational or conformational states should directly improve the resolution of the obtained reaction-deflection profiles.

This provides only a selection of possible technical upgrades, but already these should have a direct impact on the quality of the gained information and should hence further

improve the ability of the novel crossed-molecular-beam setup to investigate conformational and state-specific effects in bimolecular reactions.

## 7.2  Potential future reactions

Chapters 5 and 6 presented pioneering experiments on state- and conformationally-resolved chemi-ionisation reactions. These results as well as a series of recent experimental studies [41, 43–48, 129, 227, 230–235, 238, 239, 249–258] showed that the investigation of chemi-ionisation reactions in the gas-phase still reveals interesting insights into the fundamentals of chemical reactions and should be pursuit further with the new setup presented here. Chemi-ionisation reactions directly produce ionic reaction products [128]. This has the great experimental advantage, compared to collisions leading to purely neutral products, that the resulting ions can be directly detected without a preceding ionisation step, which results in an overall higher detection efficiency. The subsequently higher experimental signal levels make chemi-ionisation reactions the ideal target system for crossed-molecular beam experiments, especially for the first characterisation and validation of a newly constructed setup. Nevertheless, also other reaction systems should be amenable for investigation with the given apparatus.

Widely studied by crossed-beam setups are radical reactions featuring large reactive cross sections, which also have proven to provide sufficient signal levels for the investigation under single-collision conditions [10, 12–19]. A first step towards these reactions has already been done by the development and implementation of a reliable discharge source for the generation of cold and dense radical beams into the existing setup [127, 142]. Compared to conventional crossed-beam apparatuses for which the valve-detection distance generally not exceeds 20 cm, the deflected molecular beam of the setup introduced here has a free-flight distance of approximately one meter. This distance is imperative to the spatial separation achieved by the electrostatic deflector and thus can not be reduced significantly. The large distance leads to strongly reduced beam densities in the reaction region, which is even further decreased by the dispersion of the molecular beam as consequence of the electrostatic deflection. Beam densities for a similar setup have been determined previously for deflected beams of water seeded in neon [76] and methyl vinyl ketone seeded in helium [81], which were around $C_{beam} \approx 1 \times 10^8$ cm$^{-3}$ for both beams. Such low beam densities provide strong challenges towards achieving sufficiently high experimental signal levels in crossed-beam setups. A first step to overcome this obstacle would be to operate the experiment at higher repetition rates to compensate the inherent loss in sensitivity by

faster data accumulation. Therefore, the new apparatus has been set up to be able to perform 200 duty cycles per second, which is significantly more than the 10 Hz used in most setups previously reported [10, 12–19]. Furthermore, the experiments would need to be carried out using an efficient universal detection technique such as obtained after ionisation using a femtosecond laser or after (soft) electron impact ionisation [304], which both allows to record all products simultaneously independent of their quantum state. Although also commercial Nd:YAG laser systems for repetition rates exceeding 200 Hz have become available (e.g. the Spitlight DPSS series from Innolas), the reduced efficiency accompanying state-selective REMPI detection might not be sufficient for the low collision rates expected for the current setup. It still remains to be seen in how far acceptable signal levels even for universal detection techniques can be achieved for radical reactions investigated with the novel crossed-molecular-beam setup.

For both chemi-ionisation as well as radical reactions a wide range of different molecules are suited as co-reactants. Regarding the investigation of conformational effects, the target molecules need to fulfil several criteria [74, 80, 84]. The different conformational states need to differ sufficiently in their permanent dipole moments to allow for a successful spatial separation of the conformers by electrostatic deflection. Furthermore, it is crucial that the molecules can be expanded into supersonic beams with sufficient densities, either because their vapour pressure at room temperature already suffices or because it can be increased enough by heating the expansion nozzle. A final consideration is the relative population of the individual conformers in the molecular beam, which is determined by their respective energy difference. It is very beneficial when both conformers are populated in the beam sufficiently to achieve adequate signal levels for the reaction of both isolated conformers. However, the relative population of different conformers can in principle still be adjusted by optical pumping using infrared lasers as demonstrated previously [305]. This is experimentally challenging and has not been implemented yet, but could be a consideration for future experiments.

So far, the electrostatic deflector has already been used to spatially separate conformers of a wide range of molecules including aromatic compounds [60, 78, 79], 2,3-dibromobuta-1,3-diene [80] and methyl vinyl ketone [81], all of which would be amenable for the investigation in conformationally-resolved scattering experiments with metastable or radical species using the crossed-molecular-beam setup presented here.

Analogue to the experiments investigating the ionic reaction of nuclear-spin isomers of water with $N_2H^+$ ions [86], also the neutral reaction of spatially-separated *para-* and *ortho-*$H_2O$ molecules with metastable rare gases or even radicals as collision partners

could provide an interesting target system.

To further emphasise the capabilities of the new setup, also the possibility to investigate conformational effects of biomolecules should be mentioned. Important ground work in this respect has already been done by the experimental separation of the conformers of the dipeptide Ac-Phe-Cys-NH$_2$ with a similar electrostatic deflector as used throughout the experiments described in this thesis [82]. Such experiments would require the development and implementation of a laser-desorption setup [306, 307] for the generation of a molecular beam carrying intact dipeptides. Finally, the electrostatic deflector also has been proven to be able to select different sizes of molecular clusters [74, 206, 207], which opens up the possibility of studying effects of different cluster sizes in neutral collisions.

## 7.3   Concluding remark

Due to experimental challenges caused by the interconversion of molecular conformers in thermal assemblies, the precise impact of structural effects in isolated bimolecular reactions are still poorly understood. The author is confident that the novel crossed-molecular-beam setup presented in this dissertation should serve as a great tool for further investigations of conformational- as well as state-specific effects in bimolecular collisions of fully neutral reactants under single-collision conditions.

# Appendices

## A Composition of the OCS beam

The composition of the OCS beam in the experiments described in Chapter 5 was analysed by ionising the molecular beam using femtosecond-radiation followed by TOF-mass analysis. To perform experiments with a pure beam of OCS molecules, it is essential to reduce the formation of molecular clusters during the beam expansion. As can be seen in Figure A.1, the amount of molecular OCS clusters in the beam strongly depends on the OCS concentration in the expanded gas mixture. For a concentration
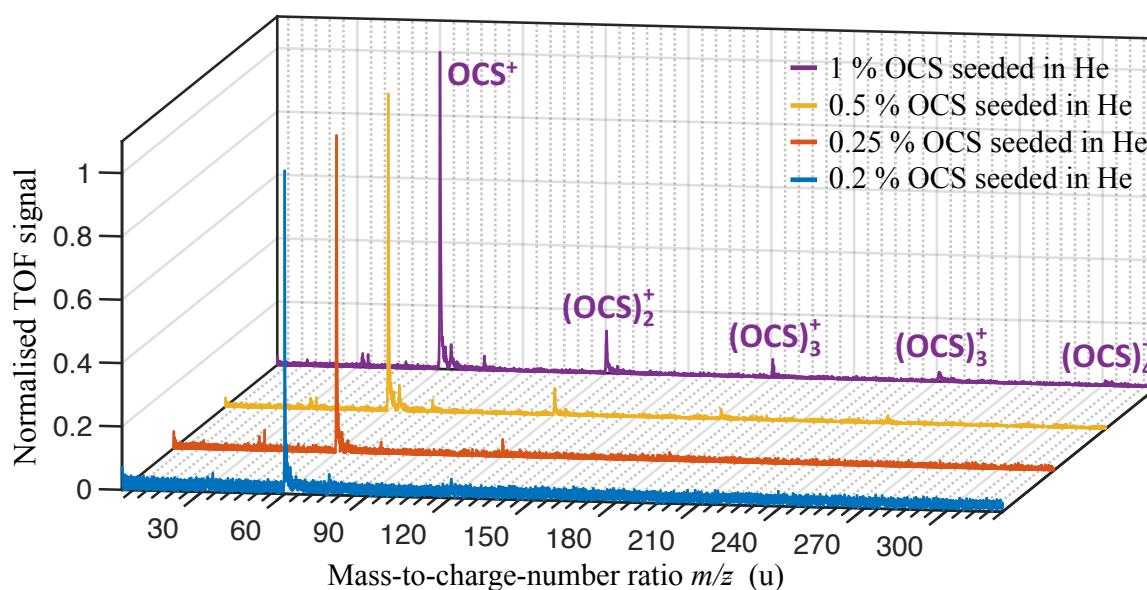


**Figure A.1** Time-of-flight mass spectrum of an OCS beam with different seeding concentrations as indicated in the legend. For a concentration of 1 % OCS in helium a significant fraction of the molecular beam consists of molecular OCS clusters. Diluting the initial gas mixture results in a strong reduction of observed clusters.

of 1 % OCS in helium, a significant fraction of the molecular beam consists of molecular OCS clusters. Diluting the initial gas mixture results in a strong reduction of observed clusters. For the experiments presented in Chapter 5, a concentration of 0.2 % OCS in helium was chosen as a compromise between having a negligible cluster contribution while at the same time ensuring enough signal levels to be able to investigate the chemi-ionisation reaction with metastable neon.

## Appendix A

The TOF mass spectrum of a molecular beam of 0.2 % OCS seeded in helium is given in Figure A.2.
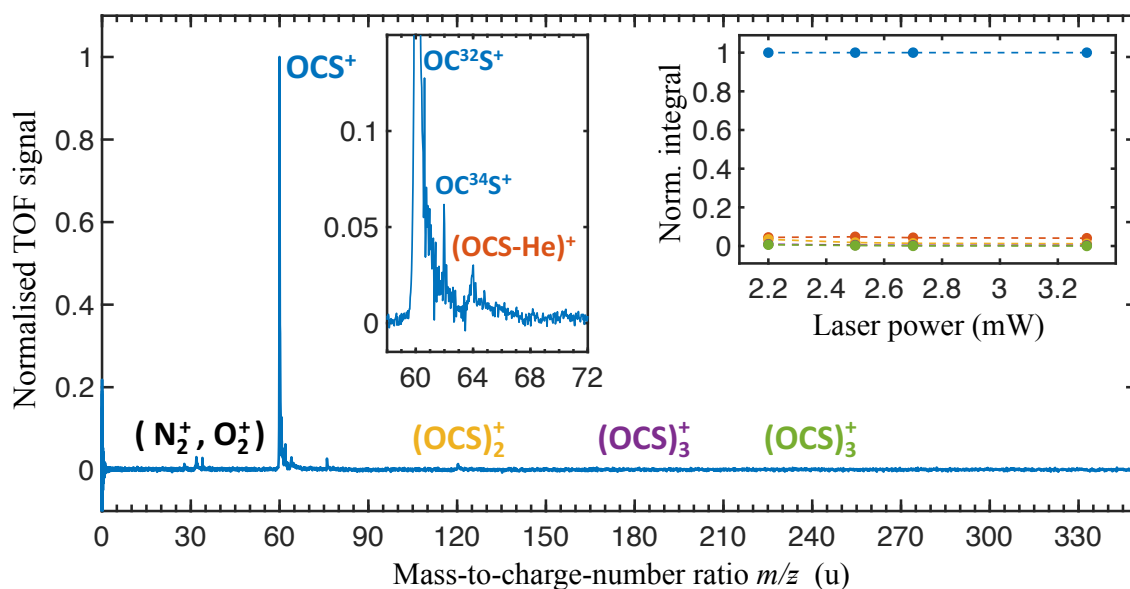


**Figure A.2** Time-of-flight mass spectrum of a molecular beam of 0.2 % OCS seeded in helium measured at a laser power of 2.7 mW. Left inset: Magnification of the TOF-MS spectrum as indicated by the axes values. Right inset: Integrals of the OCS and cluster peaks for different laser powers. The value is normalised for the integral of the OCS monomer for each laser power. Colours are the same as the peak labels in the main figure. Dashed lines are drawn to guide the eye.

Besides some small contributions of trace gases in the background vacuum ($N_2^+$, $O_2^+$), only small fractions of OCS-He and molecular clusters are present in the molecular beam. To check for possible photodissociation of the clusters caused by the radiation of the fs-laser, the power of the laser was reduced until it was not sufficient anymore to ionise OCS. If dissociation of the clusters would play a significant role, the relative populations of the clusters should increase with decreasing laser power. This is not the case as shown in the inset of Figure A.2. Based on these measurements it was concluded that at a concentration of 0.2 % OCS seeded in helium more than 95 % of the resulting molecular beam consists out of OCS monomers. The combined fraction of OCS-He and molecular OCS clusters was determined to be less than 5 %. It has to be mentioned that the OCS-He peak is spatially not very well separated from the OCS monomer peak. This makes a quantitative analysis by integration difficult, resulting in an overestimation of the He-OCS quantity in the beam.

# B  Numerical analysis of the Ne$^*$ + OCS data

This is a short summary of the numerical analysis regarding the data of the chemi-ionisation reaction of Ne$^*$ + OCS, which was presented in Chapter 5. The different contributions of the rotational states towards forming the PI and DI products are determined by matching a weighted sum of state-specific simulated profiles to the experimental data by a least-square fitting algorithm. The shape and position of the state-specific profiles were determined by matching the trajectory simulations to deflection profiles of the initial molecular beam obtained by fs-laser ionisation. As the beam waist of the fs-laser focus ($w \approx 30\ \mu$m) is much smaller than the width of the second molecular beam ($d \approx 1.5$ mm), the simulated deflection profiles obtained for laser ionisation were adjusted for the ionisation volume expected in chemi-ionisation reactions as described in detail in Section 4.3.4. The resulting simulated deflection profiles were compared to the experimental data.

The input in this fitting procedure are the normalised simulated state-specific deflection profiles $d_{JM}$ and the experimental reaction-deflection profiles $S_{PI}$ and $S_{DI}$ for the Penning and dissociative-reaction product, respectively. The general fit equation used for all relevant rotational states is given by

$$S = w_{00}\ d_{00} + w_{10}\ d_{10} + w_{11}\ d_{11} + w_{20}\ d_{20} + w_{21}\ d_{21} + w_{22}\ d_{22}, \qquad \text{(B.1)}$$

with $w_{JM}$ the fitting parameters for scaling the simulated deflection profiles for a given state $|JM\rangle$.

As described in Section 5.3.3, it was necessary to reduced the number of independent fitting parameters to prevent overfitting of the data. For this purpose, two approaches were followed. In the first, all $M$ states associated with a specific rotational state $J$ were weighted with a fixed degeneracy factor, whereas in the second approach the rotational states associated with $J{=}2$ were neglected.

## B.1  Method 1: Assuming degeneracy of M-states

As no explicit orientation effects are expected, all $M$ states associated with a specific rotational state $J$ were weighted with a degeneracy factor $g_M = 1$ for $M = 0$ and $g_M = 2$ for $M > 0$ in the fit. In this case, the fit weights for individual state-specific deflection profiles for a certain $J$ are related to each other, e.g. the weights for the state-specific deflection profiles associated with $|10\rangle$ and $|11\rangle$ can be related by $2w_{10}{=} w_{11}$. The fit equation for the Penning-ionisation reaction data is then given by

$$S_{PI} = w_{00,PI}\ d_{00} + w_{10,PI} \cdot (d_{10} + 2 \cdot d_{11}) + w_{20,PI}\ \cdot (d_{20} + 2 \cdot d_{21} + 2 \cdot d_{22}). \quad \text{(B.2)}$$

## Appendix B

Analogously, the same can be done for the dissociative ionisation pathway by

$$S_{DI} = w_{00,DI} \, d_{00} + w_{10,DI} \cdot (d_{10} + 2 \cdot d_{11}) + w_{20,DI} \cdot (d_{20} + 2 \cdot d_{21} + 2 \cdot d_{22}). \quad (B.3)$$

**Fit weights obtained for normalised experimental data**

In a first step, the fit weights were determined using the normalised experimental deflection profiles. This results in the individual contributions of the rotational states corrected for the state-independent branching ratio between the different pathways. The fit weights determined by a least-square fitting approach using the above equations to reproduce the normalised experimental data by simulated deflection profiles are given in Table B.1. Please note that this table contains the normalised fit weights, i.e. the sum of all state-specific contributions is equal to 1. The contributions of all states $w_J$ with the same total angular quantum number $J$ are given by the sum of the state-specific weights $w_{JM}$, e.g. the total contribution of $J{=}1$ is given by $w_1 = w_{10} + w_{11} = 3 \cdot w_{10}$. These values are also given in Table B.1 and are the final contributions which are represented in the inset of Figure 5.5. From the relative contributions of the

**Table B.1** Values for the fit weights assuming degeneracy of M-states

| Penning-ionisation pathway | | Dissociative-ionisation pathway | |
|---|---|---|---|
| $w_{00,PI}{=}\ 0.502(20)$ | $w_{0,PI}{=}\ 0.502(20)$ | $w_{00,DI}{=}\ 0.742(15)$ | $w_{0,DI}{=}\ 0.742(15)$ |
| $w_{10,PI}{=}\ 0.143(14)$ | $w_{1,PI}{=}\ 0.430(43)$ | $w_{10,DI}{=}\ 0.081(11)$ | $w_{1,DI}{=}\ 0.244(33)$ |
| $w_{11,PI}{=}2 \cdot w_{10,PI}{=}\ 0.287(29)$ | | $w_{11,DI}{=}2 \cdot w_{10,DI}{=}\ 0163(22)$ | |
| $w_{20,PI}{=}\ 0.014(006)$ | | $w_{20,DI}{=}\ 0.003(5)$ | |
| $w_{21,PI}{=}2 \cdot w_{20,PI}{=}\ 0.027(13)$ | $w_{2,PI}{=}0.069(32)$ | $w_{21,DI}{=}2 \cdot w_{20,DI}{=}\ 0.006(10)$ | $w_{2,DI}{=}\ 0.014(24)$ |
| $w_{22,PI}{=}2 \cdot w_{20,PI}{=}\ 0.027(13)$ | | $w_{22,DI}{=}2 \cdot w_{20,DI}{=}\ 0.006(10)$ | |

rotational states, a ratio between the contribution of the dissociative- and the Penning-ionisation reaction pathway $R_J$ for each rotational state with quantum number $J$ can be calculated. These ratios were determined to be

$$R_0 = w_{0,\mathrm{DI}}/w_{0,\mathrm{PI}} = 1.48(5)$$
$$R_1 = w_{1,\mathrm{DI}}/w_{1,\mathrm{PI}} = 0.57(13) \qquad (B.4)$$
$$R_2 = w_{2,\mathrm{DI}}/w_{2,\mathrm{PI}} = 0.20(58).$$

These ratios can now be compared between the different rotational states. Dividing the ratio between the DI and PI of $J{=}0$ by the same ratio for $J{=}1$, results in a factor of 2.6(6). Because the fit was done with the normalised simulation profiles, until here the initial populations of the rotational states were not yet taken into account. The

fs-laser profile gives a ratio between the state populations summed over $J$=0 and $J$=1 of $0.44/0.45 = 0.953$, which also includes the degeneracy factor of $g_M = 1$ for $M = 0$ and $g_M = 2$ for $M > 0$. Correcting the ratio between $J$=0 and $J$=1 with the ratio of the thermal populations $(2.6/0.953)$, **gives the result that the ratio of the reactivity of the DI and the PI process is for $J$=0 a factor 2.7(6) bigger than the same ratio for $J$=1.** All quoted uncertainties are the standard deviations of the fit, propagated according to the used mathematical operators.

**Fit weights obtained for raw experimental data**

The same analysis as above was done for the raw data before normalisation. The raw experimental deflection profiles with the least-square fits of the state-specific simulated profiles are shown in Figure B.1. The relative fitted weights of the individual rotational states of OCS summed over all states with the same $J$ considering the $M$-dependent degeneracy factors are given in the top right of the figure. From the relative contributions of the rotational states, a ratio between the contribution of the individual rotational states towards the dissociative- and the Penning-ionisation reaction pathway can be calculated. For analysing the raw data as done here, these ratios also include the overall state-independent branching ratio (BR) of dissociative to Penning ionisation, which was determined to be $DI/PI = 2.5$ (see Sec. 5.3.2). These ratios $R_{J,\mathrm{BR}}$ including the state-independent branching ratio were determined to be

$$R_{0,\mathrm{BR}} = 3.77(9)$$
$$R_{1,\mathrm{BR}} = 1.44(21) \tag{B.5}$$
$$R_{2,\mathrm{BR}} = 0.52(99).$$

Please note that these values were also obtained by assuming a fixed $M$-dependent degeneracy as described above.

(a)



(b)
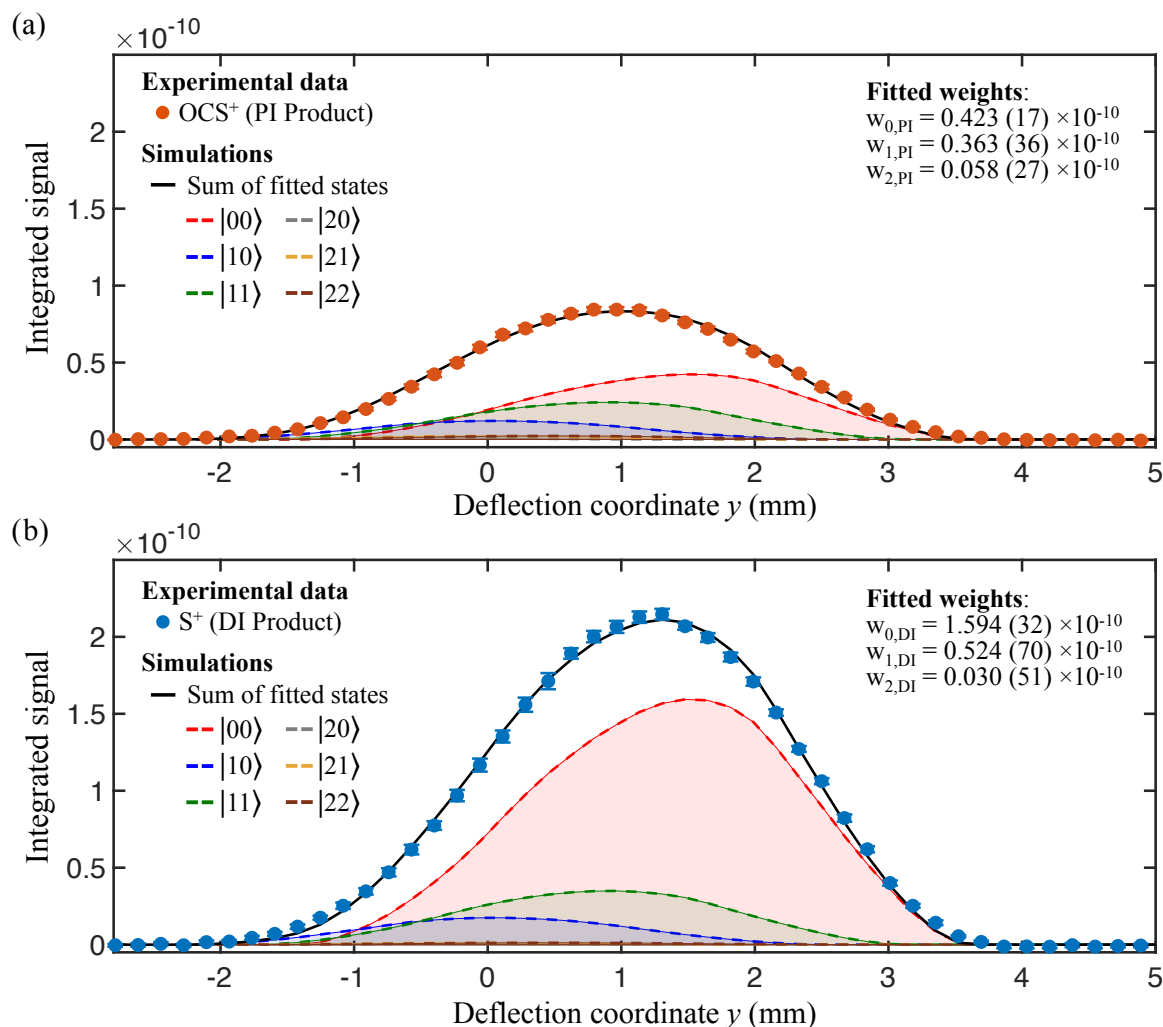
**Figure B.1** Least-square fits of state-specific simulated reaction-deflection profiles to the raw experimental data for (a) the Penning- and (b) the dissociative-ionisation products [111]. Only the rotational states $J = 0, 1, 2$ significantly populated in the molecular beam were taken into account (see inset in Figure 5.2). Relative fitted weights of the individual rotational states of OCS summed over all states with the same $J$ are given in the top right. The uncertainties represent the fit errors.

## B.2 Method 2: Neglecting contributions of J=2-states

To validate the results obtained in the previous section, an alternative approach to reduce the degrees of freedom in the fitting procedure was taken. Instead of fixating the $M$-dependent degeneracy as done in the previous section, in the approach described here all molecules in rotational states associated with the total angular quantum number $J=2$ were neglected. The physical reasoning behind this approach is that the molecular OCS beam contained less than 10 % of molecules in rotational states associated with $J=2$ (see Sec. 5.3.1). This approach was only performed for the normalised

data, which results in the branching-ratio corrected values. The used fit equation to reproduce the experimental Penning-ionisation deflection profile by the simulated profiles neglecting all $J = 2$-states is then given by

$$S_{PI} = w_{00,PI} \ d_{00} + w_{10,PI} \ d_{10} + w_{11,PI} \ d_{11}, \tag{B.6}$$

and analogously for the dissociative ionisation profile by

$$S_{DI} = w_{00,DI} \ d_{00} + w_{10,DI} \ d_{10} + w_{11,DI} \ d_{11}. \tag{B.7}$$

The resulting fit weights using the above equations to reproduce the experimental reaction-deflection profiles are given in Table B.2. Please note that this table contains the normalised fit weights, i.e. the sum of all state-specific contributions is equal to 1. The contributions of all states $w_J$ with the same total angular quantum number $J$ are given by the sum of the state-specific weights $w_{JM}$, e.g the total contribution of $J{=}1$ is given by $w_1 = w_{10} + w_{11}$. These values are also given in Table B.2.

**Table B.2** Values for the fit weights neglecting $J{=}2$-states

| Penning-ionisation pathway | | Dissociative-ionisation pathway | |
|---|---|---|---|
| $w_{00,PI}= 0.515(21)$ | $w_{0,PI}= 0.515(21)$ | $w_{00,DI}= 0.749(16)$ | $w_{0,DI}= 0.749(16)$ |
| $w_{10,PI}= 0.215(16)$ | $w_{1,PI}= 0.485(48)$ | $w_{10,DI}= 0.099(12)$ | $w_{1,DI}= 0.251(36)$ |
| $w_{11,PI}= 0.270(32)$ | | $w_{11,DI}= 0.152(24)$ | |

All quoted uncertainties are the standard deviations of the fit. The contributions given in Table B.2, which were determined by a fitting procedure which neglects the rotational states associated with $J{=}2$, are very similar to the fit weights summarised in Table B.1 obtained after fixating the $M$-dependent degeneracy. The only appreciable differences are the values obtain for the $|10\rangle$-state, which are slightly higher when the $J{=}2$-state was neglected. This could have been expected, considering that the state-specific deflection profile of the barely deflected $|10\rangle$-state has the largest spatial overlap with the deflection profiles of all states associated with $J{=}2$. In the absence of these deflection profiles, the state-specific deflection profile of the $|10\rangle$ tries to compensate the contributions of the missing $J{=}2$-state deflection profiles.

# C   Composition of the HYQ beam

A typical TOF mass spectrum of a HYQ beam taken after general ionisation with a femtosecond laser is given in Figure C.1
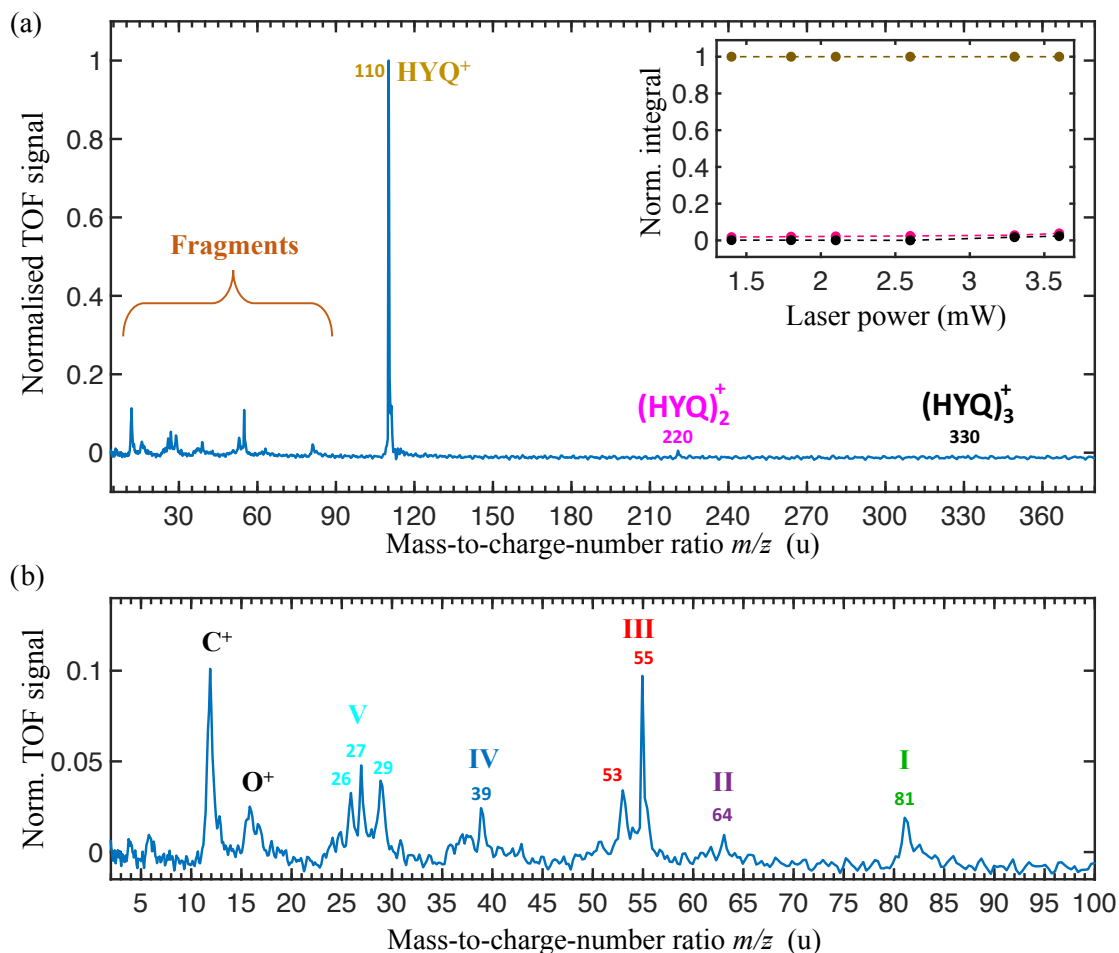


**Figure C.1** (a) Time-of-flight mass spectrum of a molecular HYQ beam measured at a femtosecond-laser power of 3.3 mW. The peak associated to the HYQ monomer dominates the spectrum. A small trace of the HYQ dimer is also visible, while the signal-to-noise ratio of the current spectrum is not sufficient to detect clusters of higher order. Inset: Integrals of the HYQ monomer and cluster peaks for different laser powers. The value is normalised for the integral of the HYQ monomer for each laser power. Colours are the same as the peak labels in the main figure. Dashed lines are drawn to guide the eye. (b) Magnification of the lower $m/z$-area, showing fragments of HYQ. The labels of the fragments are the same as given in Table 6.1.

Only small fractions of $(HYQ)_n$-clusters are present in the molecular beam. To check for possible photodissociation of the clusters, the power of the laser was reduced until it was not sufficient anymore to ionise the HYQ monomer. If dissociation of the clusters would play a significant role, the relative populations of the clusters should

increase with decreasing laser power. This is not the case as shown in the inset of Figure C.1. Based on these measurements it was concluded that the ratio of HYQ monomers to the sum of all clusters is 97 % : 3 %.

Also some small traces originating from HYQ fragmentation (I-V, $C^+$, $O^+$) are visible in the spectrum. Labelling of the fragments is the same as given in Table 6.1 and the main text of Chapter 6. To determine if the fragments were already present in the expanding molecular beam or only caused by photodissociation using the femtosecond laser, a laser-deflection profile was taken for all relevant fragments (Fig. C.2).
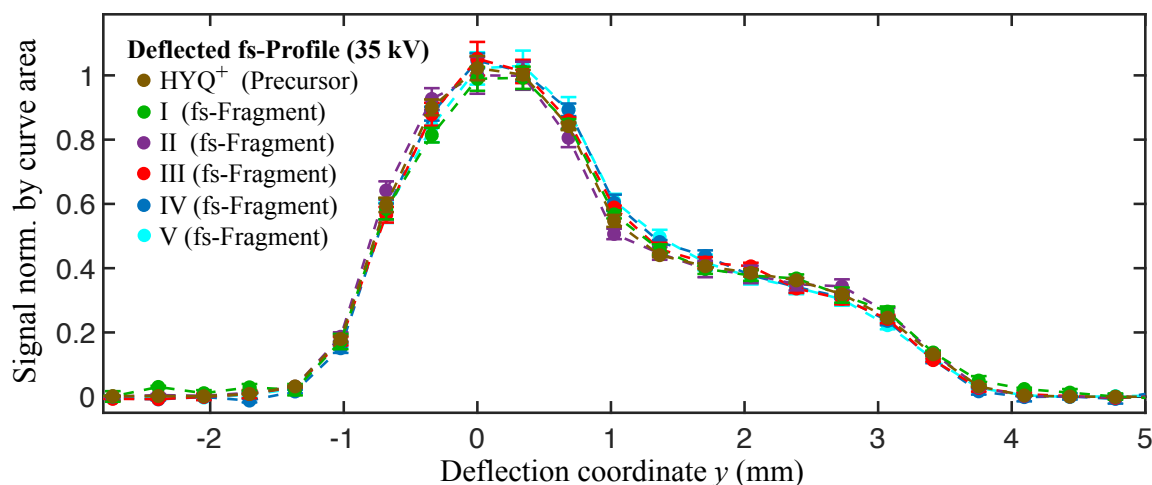


**Figure C.2** Experimental deflection profile of HYQ and its fragments obtained after multi-photon ionisation with a femtosecond laser. The fragments are labelled as given in Table 6.1. Each dataset is normalised by its curve area. All fragments follow the same deflection pattern as the HYQ monomer, confirming that these fragments are purely originating from laser photodissociation and are not present in the original molecular beam.

These laser-deflection profiles all showed exactly the same deflection behaviour as the deflection profile of the $HYQ^+$ ion. This strongly suggests that these fragments were not present in the initial molecular beam, because then the different dipole moments of the different fragments should have led to different deflection profiles. Contrarily, the same deflection behaviour for all fragments strongly indicates that the observed fragments are products by photodissociation processes of the common precursor HYQ. Fragmentation down to atomic ions ($C^+$, $O^+$) only occurred after ionisation with the femtosecond laser and was not observed in the chemi-ionisation reaction. Therefore, it was not further considered here.

# D   Deflection profile of reaction product II in Ne* + HYQ

The dissociative-ionisation products associated with channel II, as assigned in Table 6.1 of the main text, has the smallest signal-to-noise ratio for all investigated reaction products. Therefore, the performed averaging for the experiments reported in Chapter 6 was not sufficient to obtain a smooth deflection profile for this reaction channel. Also the profile associated with the ionic product of reaction channel II seems to follow the deflection curve of the other dissociative-ionisation products as shown in Figure D.1. However, the signal-to-noise ratio of the data associated with channel II is significantly less compared to the other dissociative-ionisation channels. More averages would be needed to make a final statement about the deflection behaviour of the ionic product associated with reaction channel II.
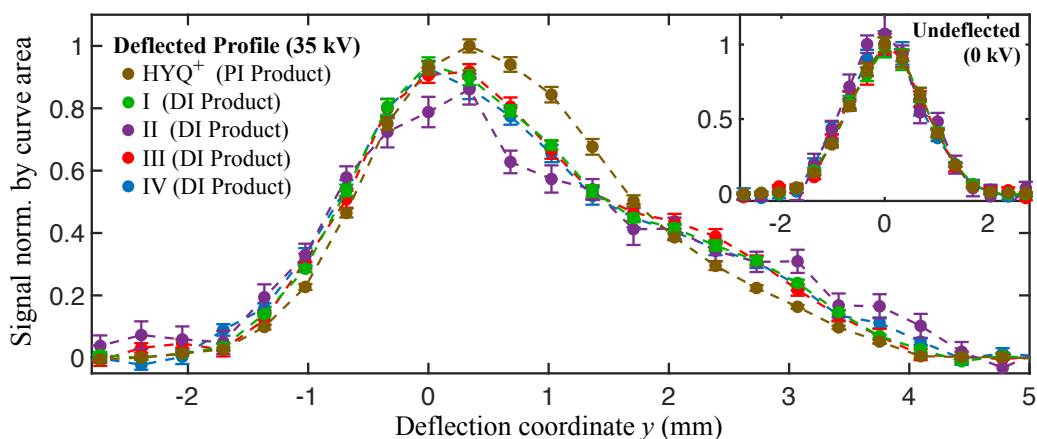


**Figure D.1** Chemi-ionisation reaction-deflection profiles of HYQ + Ne* recorded for the Penning-ionisation product (HYQ$^+$) and the different dissociative-ionisation products summarised in Table 6.1 for a deflected molecular beam. The profiles have been normalised by the area below the curves, which is proportional to the number of detected ions. This figure also shows the data associated with reaction channel II. The deflection profile of ionic product II seems to follow the same deflection pattern as the other dissociative-ionisation products, but the quality of the data is not sufficiently good to make a final statement. More averaging would be needed. The error bars represent the standard error of 18 individual traces in which each data point was averaged over 10.000 experimental cycles. Inset: Reaction profiles of an undeflected molecular HYQ beam.

# E  Least-square fit of Penning-ion deflection profile

The experimental reaction-deflection profile for the Penning-ionisation product was reproduced by adjusting both the thermal rotational-state distribution as well as the contribution of the two conformers in a least-square fitting approach. The results are shown in Figure E.1. Although this resulted in a decent match between experimental

(a)



(b)
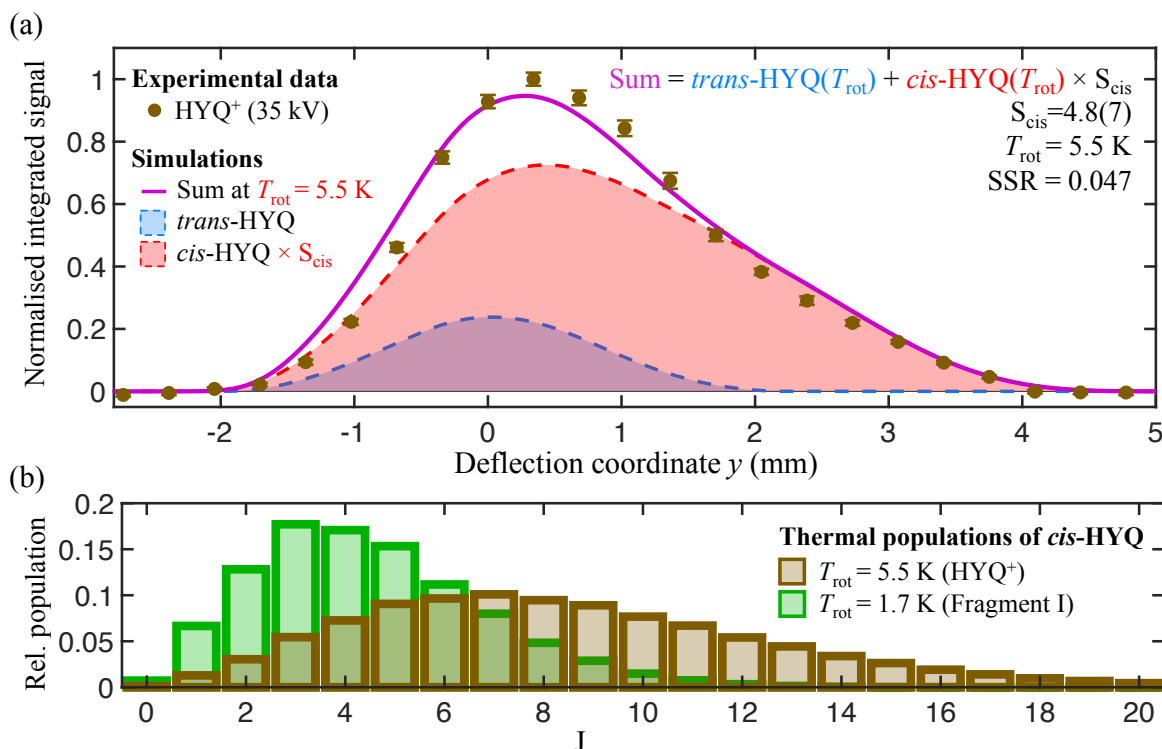
**Figure E.1** Least-square fits of simulated reaction-deflection profiles to the experimental data for (a) the Penning- and (b) the dissociative-ionisation reaction pathway (exemplary shown for channel I). During the fit both the contribution of the *cis*-conformer as well as the rotational temperature were adjusted. The fit equation is given in the top right of the figure together with the values for the fitted scaling constant $S_{cis}$ and the best matching rotational temperature $T_{rot}$, which best reproduced the experimental data. The errors represent the fit uncertainties. The quality of the fit is expressed by the sum of squared residuals (SSR). (b) Relative population of the *cis*-conformer for the rotational temperatures which reproduced best the experimental data for the Penning-ionisation pathway ($T_{rot} = 5.5$ K) and the dissociative-ionisation pathway ($T_{rot} = 1.7$ K, Fig. 6.5b), which were obtained in a least-square fit which also includes the conformational reactivates.

data and simulations, the fit assumed both an unreasonable high rotational temperature of $T_{rot} = 5.5$ K and an excessively large contribution of the *cis*-conformer (factor 4.8 higher than the contribution of *trans*-HYQ). Upon further investigation, it seems that

the resulting fit has a very shallow optimisation minimum, which can not be trusted as the simultaneous adjustment of both the rotational temperature and contribution of the conformers resulted in too many degrees of freedom for a trustworthy fit.

# Bibliography

[1] B. Hölldobler and E.O. Wilson, *The Ants*, 1st ed. (Harvard University Press, Cambridge, MA, 1990).

[2] P. Atkins, *What is chemistry?*, 1st ed. (Oxford University Press, Oxford, 2013).

[3] P. Atkins, J. de Paula and J. Keeler, *Atkins' Physical Chemistry*, eleventh ed. (Oxford University Press, Oxford, 2018).

[4] R.D. Levine, *Molecular Reaction Dynamics* (Cambridge University Press, Cambridge, 2005).

[5] M. Brouard and C. Vallance, editors, *Tutorials in Molecular Reaction Dynamics* (The Royal Society of Chemistry, Oxford, 2012).

[6] T.H. Bull and P.B. Moon, Discuss. Faraday Soc. **17**, 54 (1954).

[7] E.H. Taylor and S. Datz, J. Chem. Phys. **23** (9), 1711 (1955).

[8] D.R. Herschbach, Discuss. Faraday Soc. **33**, 149 (1962).

[9] Y.T. Lee, J.D. McDonald, P.R. LeBreton and D.R. Herschbach, Rev. Sci. Instrum. **40** (11), 1402 (1969).

[10] Y.T. Lee, Science **236**, 793 (1987).

[11] D.R. Herschbach, Angew. Chem. Int. Ed. **26** (12), 1221 (1987).

[12] P. Casavecchia, N. Balucani and G.G. Volpi, Annu. Rev. Phys. Chem. **50**, 347 (1999).

[13] K. Liu, Annu. Rev. Phys. Chem. **52** (1), 139. (2001).

[14] R.I. Kaiser and A.M. Mebel, Int. Rev. Phys. Chem. **21** (2), 307 (2002).

[15] M.N. Ashfold, N.H. Nahler, A.J. Orr-Ewing, O.P.J. Vieuxmaire, R.L. Toomes, T.N. Kitsopoulos, I.A. Garcia, D.A. Chestakov, S.M. Wu and D.H. Parker, Phys. Chem. Chem. Phys. **8**, 26 (2006).

[16] K. Liu, J. Chem. Phys. **125**, 132307 (2006).

[17] H. Pan, K. Liu, A. Caracciolo and P. Casavecchia, Chem. Soc. Rev. **46**, 7517 (2017).

[18] T. Wang, T. Yang, C. Xiao, Z. Sun, D. Zhang, X. Yang, M.L. Weichman and D.M. Neumark, Chem. Soc. Rev. **47**, 6744 (2018).

# Bibliography

[19] H. Li and A.G. Suits, Phys. Chem. Chem. Phys. **22**, 11126 (2020).

[20] S.R. Gandhi, T.J. Curtiss, Q.X. Xu, S.E. Choi and R.B. Bernstein, Chem. Phys. Lett. **132**, 6 (1986).

[21] J. Reuss, in *Atomic and Molecular Beam Methods*, edited by Giacinto Scoles, Vol. 1, Chap. 11 (Oxford University Press, Oxford, 1988), pp. 276–289.

[22] D.H. Parker and R.B. Bernstein, Annu. Rev. Phys. Chem. **40**, 561 (1989).

[23] J.J. van Leuken, W.H.W. van Amerom, J. Bulthuis, J.G. Snijders and S. Stolte, Annu. Rev. Phys. Chem. **99**, 15573 (1995).

[24] J.J. van Leuken, J. Bulthuis, S. Stolte and J.G. Snijders, Chem. Phys. Lett. **260**, 595 (1996).

[25] A. Gijsbertsen, H. Linnartz, G. Rus, A. Wiskerke, S. Stolte, D. Chandler and J. Kłos, J. Chem. Phys. **123**, 224305 (2005).

[26] P.Y. Tsai, D.C. Che, M. Nakamura, K.C. Lin and T. Kasai, Phys. Chem. Chem. Phys. **12**, 2532 (2010).

[27] M. Brouard, H. Chadwick, S.D.S. Gordon, B. Hornung, B. Nichols, J. Kłos, F.J. Aoiz and S. Stolte, J. Chem. Phys. **141**, 164306 (2014).

[28] H.L. Bethlem, G. Berden and G. Meijer, Phys. Rev. Lett. **83**, 1558 (1999).

[29] J.J. Gilijamse, S. Hoekstra, S.Y.T. van de Meerakker, G.C. Groenenboom and G. Meijer, Science **313**, 1617 (2006).

[30] L. Scharfenberg, J. Kłos, P.J. Dagdigian, M.H. Alexander, G. Meijer and S.Y.T. van de Meerakker, Phys. Chem. Chem. Phys. **12**, 10660 (2010).

[31] N. Vanhaecke, U. Meier, M. Andrist, B.H. Meier and F. Merkt, Phys. Rev. A **75**, 031402 (2007).

[32] E. Narevicius, C. Parthey, A. Libson, J. Narevicius, I. Chavez, U. Even and M.G. Raizen, New J. Phys. **9**, 358 (2007).

[33] A.W. Wiederkehr, M. Motsch, S.D. Hogan, M. Andrist, H. Schmutz, B. Lambillotte, J.A. Agner and F. Merkt, J. Chem. Phys. **135**, 214202 (2011).

[34] K. Dulitz, M. Motsch, N. Vanhaecke and T.P. Softley, J. Chem. Phys. **140**, 104201 (2014).

[35] T. Cremers, S. Chefdeville, N. Janssen, E. Sweers, S. Koot, P. Claus and S.Y.T. van de Meerakker, Phys. Rev. A **95**, 043415 (2017).

[36] M. Kirste, X. Wang, H.C. Schewe, G. Meijer, K. Liu, A. van der Avoird, L.M. Janssen, K.B. Gubbels, G.C. Groenenboom and S.Y.T. van de Meerakker, Science **338**, 1060 (2012).

[37] A. von Zastrow, J. Onvlee, S.N. Vogels, G.C. Groenenboom, A. van der Avoird and S.Y.T. Van De Meerakker, Nat. Chem. **6**, 216 (2014).

[38] S.N. Vogels, T. Karman, J. Kłos, M. Besemer, J. Onvlee, A. van der Avoird, G.C. Groenenboom and S.Y.T. van de Meerakker, Nat. Chem. **10**, 435 (2018).

[39] T. de Jongh, M. Besemer, Q. Shuai, T. Karman, A. van der Avoird, G.C. Groenenboom and S.Y.T. van de Meerakker, Science **368**, 626 (2020).

[40] V. Plomp, Z. Gao, T. Cremers, M. Besemer and S.Y.T. van de Meerakker, J. Chem. Phys. **152**, 091103 (2020).

[41] A.B. Henson, S. Gersten, Y. Shagam, J. Narevicius and E. Narevicius, Science **338**, 234 (2012).

[42] B. Bertsche, J. Jankunas and A. Osterwalder, Chimia **68**, 256 (2014).

[43] A. Klein, Y. Shagam, W. Skomorowski, P.S. Żuchowski, M. Pawlak, L.M. Janssen, N. Moiseyev, S.Y. van de Meerakker, A. van der Avoird, C.P. Koch and E. Narevicius, Nat. Phys. **13**, 35 (2017).

[44] S.D.S. Gordon, J.J. Omiste, J. Zou, S. Tanteri, P. Brumer and A. Osterwalder, Nat. Chem. **10**, 1190 (2018).

[45] B. Margulis, J. Narevicius and E. Narevicius, Nat. Comm. **11**, 1 (2020).

[46] J. Zou and A. Osterwalder, J. Chem. Phys. **153**, 104306 (2020).

[47] S.D.S. Gordon and A. Osterwalder, Int. Rev. Phys. Chem. **39**, 109 (2020).

[48] P. Paliwal, N. Deb, D.M. Reich, A. van der Avoird, C.P. Koch and E. Narevicius, Nat. Chem. **13**, 94 (2021).

[49] W.H. Wing, Prog. Quantum Electron. **8** (3-4), 181 (1984).

[50] W. Ketterle and D.E. Pritchard, Appl. Phys. B **54** (5), 403 (1992).

[51] H.L. Bethlem and G. Meijer, Int. Rev. Phys. Chem. **22** (1), 73 (2003).

[52] D. Kakati and D.C. Lainé, J. Phys. E: At. Sci. Instrum. **4**, 269 (1971).

[53] H.L. Bethlem, A.J.A. van Roij, R.T. Jongma and G. Meijer, Phys. Rev. Lett. **88**, 133003 (2002).

[54] M.R. Tarbutt, H.L. Bethlem, J.J. Hudson, V.L. Ryabov, V.A. Ryzhov, B.E. Sauer, G. Meijer and E.A. Hinds, Phys. Rev. Lett. **92**, 173002 (2004).

[55] H.L. Bethlem, M.R. Tarbutt, J. Küpper, D. Carty, K. Wohlfart, E.A. Hinds and G. Meijer, J. Phys. B: At. Mol. Opt. **39**, 263 (2006).

[56] K. Wohlfart, F. Filsinger, F. Grätz, J. Küpper and G. Meijer, Phys. Rev. A **78**, 033421 (2008).

[57] T.E. Wall, S. Armitage, J.J. Hudson, B.E. Sauer, J.M. Dyne, E.A. Hinds and M.R. Tarbutt, Phys. Rev. A **80**, 043407 (2009).

[58] K. Wohlfart, F. Grätz, F. Filsinger, H. Haak, G. Meijer and J. Küpper, Phys. Rev. A **77**, 031404 (2008).

[59] S. Putzke, F. Filsinger, H. Haak, J. Küpper and G. Meijer, Phys. Chem. Chem. Phys. **13**, 18962 (2011).

[60] F. Filsinger, U. Erlekam, G. von Helden, J. Küpper and G. Meijer, Phys. Rev. Lett. **100**, 133003 (2008).

[61] F. Filsinger, G. Meijer, H. Stapelfeldt, H.N. Chapman and J. Küpper, Phys. Chem. Chem. Phys. **13**, 2076 (2011).

[62] H. Odashima, S. Merz, K. Enomoto, M. Schnell and G. Meijer, Phys. Rev. Lett. **104**, 253001 (2010).

[63] S. Merz, N. Vanhaecke, W. Jäger, M. Schnell and G. Meijer, Phys. Rev. A **85**, 063411 (2012).

[64] S. Spieler, W. Zhong, P. Djuricanin, O. Nourbakhsh, I. Gerhardt, K. Enomoto, F. Stienkemeier and T. Momose, Mol. Phys. **111**, 1823 (2013).

[65] K. Enomoto, N. Hizawa, Y. Furuta, N. Hada and T. Momose, J. Phys. B: At. Mol. Opt. **52**, 035101 (2019).

[66] H. Stapelfeldt, H. Sakai, E. Constant and P.B. Corkum, Phys. Rev. Lett. **79**, 2787 (1997).

[67] B.S. Zhao, H.S. Chung, K. Cho, S.H. Lee, S. Hwang, J. Yu, Y.H. Ahn, J.Y. Sohn, D.S. Kim, W.K. Kang and D.S. Chung, Phys. Rev. Lett. **85**, 2705 (2000).

[68] R. Fulton, A.I. Bishop and P.F. Barker, Phys. Rev. Lett. **93**, 243004 (2004).

[69] X.N. Sun, L.Y. Kim, B.S. Zhao and D.S. Chung, Phys. Rev. Lett. **115**, 223001 (2015).

[70] H. Kallmann and F. Reiche, Zeitschrift für Physik **6** (1), 352 (1921).

[71] O. Stern, Zeitschrift für Physik **7** (1), 249 (1921).

[72] W. Gerlach and O. Stern, Zeitschrift für Physik **9** (1), 349 (1922).

[73] E. Wrede, Zeitschrift für Physik **44** (4), 261 (1927).

[74] Y.P. Chang, D.A. Horke, S. Trippel and J. Küpper, Int. Rev. Phys. Chem. **34**, 557 (2015).

[75] J.H. Nielsen, P. Simesen, C.Z. Bisgaard, H. Stapelfeldt, F. Filsinger, B. Friedrich, G. Meijer and J. Küpper, Phys. Chem. Chem. Phys. **13**, 18971 (2011).

[76] D.A. Horke, Y.P. Chang, K. Dlugolecki and J. Küpper, Angew. Chem. Int. Ed. **53**, 11965 (2014).

[77] S. Trippel, T. Mullins, N.L. Müller, J.S. Kienitz, R. González-Férez and J. Küpper, Phys. Rev. Lett. **114**, 103003 (2015).

[78] F. Filsinger, J. Küpper, G. Meijer, J.L. Hansen, J. Maurer, J.H. Nielsen, L. Holmegaard and H. Stapelfeldt, Angew. Chem. Int. Ed. **48**, 6900 (2009).

[79] S. Trippel, M. Johny, T. Kierspel, J. Onvlee, H. Bieker, H. Ye, T. Mullins, L. Gumprecht, K. Długołęcki and J. Küpper, Rev. Sci. Instrum. **89**, 096110 (2018).

[80] A. Kilaj, H. Gao, D. Tahchieva, R. Ramakrishnan, D. Bachmann, D. Gillingham, O.A. von Lilienfeld, J. Küpper and S. Willitsch, Phys. Chem. Chem. Phys. **22**, 13431 (2020).

[81] J. Wang, A. Kilaj, L. He, K. Długołęcki, S. Willitsch and J. Küpper, J. Phys. Chem. A **124**, 8341 (2020).

[82] N. Teschmit, D.A. Horke and J. Küpper, Angew. Chem. Int. Ed. **57**, 13775 (2018).

[83] S. Willitsch, Adv. Chem. Phys. **162**, 307 (2017).

[84] Y.P. Chang, K. Dlugolecki, J. Küpper, D. Rösch, D. Wild and S. Willitsch, Science **342**, 98 (2013).

[85] D. Rösch, S. Willitsch, Y.P. Chang and J. Küpper, J. Chem. Phys. **140**, 124202 (2014).

[86] A. Kilaj, H. Gao, D. Rösch, U. Rivero, J. Küpper and S. Willitsch, Nat. Commun. **9** (2018).

[87] A. Kilaj, J. Wang, P. Straňák, M. Schwilk, U. Rivero, L. Xu, O.A. von Lilienfeld, J. Küpper and S. Willitsch, Nat. Commun. **12** (1), 1 (2021).

[88] J.E. Lennard-Jones, Proc. R. Soc. Lond. A **106** (738), 463 (1924).

[89] J.N. Israelachvili, *Intermolecular and Surface Forces*, 3rd ed. (Academic Press, London, San Diego, 2011).

[90] F. London, Zeitschrift für Physik **63** (3-4), 245 (1930).

[91] Y.T. Lee, Angew. Chem. Int. Ed. **26** (10), 939 (1987).

[92] E. Greene, R. Roberts and J. Ross, J. Chem. Phys. **32** (3), 940 (1960).

[93] S. Datz, D.R. Herschbach and E.H. Taylor, J. Chem. Phys. **35** (5), 1549 (1961).

[94] D.R. Herschbach, J. Chem. Phys. **33** (6), 1870 (1960).

[95] D. Herschbach, G. Kwei and J. Norris, J. Chem. Phys. **34** (5), 1842–1843 (1961).

## Bibliography

[96] E.F. Greene and J. Ross, Science **159** (3815), 587 (1968).

[97] J.C. Polanyi, Angew. Chem. Int. Ed. **26** (10), 952 (1987).

[98] W.C. Wiley and I.H. McLaren, Rev. Sci. Instrum. **26** (12), 1150 (1955).

[99] M. Ashfold and J. Howe, Annu. Rev. Phys. Chem. **45** (1), 57 (1994).

[100] R.N. Zare, Annu. Rev. Anal. Chem. **5**, 1 (2012).

[101] K. Liu, R.G. Macdonald and A.F. Wagner, Int. Rev. Phys. Chem. **9** (2), 187 (1990).

[102] A. Schiffman and D.W. Chandler, Int. Rev. Phys. Chem. **14** (2), 371 (1995).

[103] H. Kohguchi and T. Suzuki, Annu. Rep. Prog. Chem., Sect. C: Phys. Chem. **98**, 421 (2002).

[104] D.W. Chandler and P.L. Houston, J. Chem. Phys. **87** (2), 1445 (1987).

[105] A.T.J.B. Eppink and D.H. Parker, Rev. Sci. Instrum. **68**, 3477 (1997).

[106] M.D. Morse, in *Atomic, Molecular, and Optical Physics: Atoms and Molecules*, edited by F.B. Dunning and G.H. Randall, Vol. 29, 1st ed., Chap. 2 (Academic Press, New York, 1996), pp. 21–48.

[107] H. Pauly, *Atom, Molecule, and Cluster Beams* (Springer, Berlin, 2000).

[108] A.M. Wodtke and Y.T. Lee, J. Phys. Chem **89** (22), 4744 (1985).

[109] K.H. Kramer and R.B. Bernstein, J.Chem. Phys. **42** (2), 767 (1965).

[110] C. Amarasinghe, C.A. Perera and A.G. Suits, J. Chem. Phys **152** (18), 184201 (2020).

[111] L. Ploenes, P. Straňák, H. Gao, J. Küpper and S. Willitsch, Mol. Phsy. **119** (17-18), e1965234 (2021).

[112] G. Sanna and G. Tomassetti, *Introduction to Molecular Beams Gas Dynamics* (Imperial College Press, London, 2005).

[113] D.R. Miller, in *Atomic and Molecular Beam Methods*, edited by Giacinto Scoles, D. Bassi, U. Buck and D. Lainé, Vol. 1, Chap. 2 (Oxford University Press, Oxford, 1988), pp. 18–53.

[114] W. Demtröder, *Laser Spectroscopy Vol. 2: Experimental Techniques*, 4th ed. (Springer, Berlin, 2008).

[115] T.E. Wall, J. Phys. B **49** (24), 243001 (2016).

[116] N.R. Hutzler, H.I. Lu and J.M. Doyle, Chem. Rev. **112** (9), 4803 (2012).

[117] C.T. Rettner, E.E. Marinero, R.N. Zare and A.H. Kung, J. Phys. Chem. **88** (20), 4459 (1984).

[118] H. Ashkenas and F.S. Sherman, Rarefied Gas Dyn. **3** (20), 84 (1966).

[119] U. Even, J. Jortner, D. Noy, N. Lavie and C. Cossart-Magos, J. Chem. Phys. **112**, 8068 (2000).

[120] U. Even, EPJ Tech. Instrum. **2**, 1 (2015).

[121] U. Even, Adv. Chem. **1**, 1 (2014).

[122] C. Antoine, Compt. rend. **107**, 681 (1888).

[123] C. Antoine, Compt. rend. **107**, 1143 (1888).

[124] E. Terres, F. Gebert, H. Hülsemann, H. Petereit, H. Toepsch and W. Ruppert, Brennst.-Chem. **36**, 272 (1955).

[125] P. Linstrom and W. Mallard, *NIST Chemistry WebBook, NIST Standard Reference Database Number 69*, National Institute of Standards and Technology, Gaithersburg, https://webbook.nist.gov/cgi/cbook.cgi?ID=C123319&Mask=4&Type=ANTOINE&Plot=on, Online accessed on 07.09.2021.

[126] J. Grzesiak, M. Vashishta, P. Djuricanin, F. Stienkemeier, M. Mudrich, K. Dulitz and T. Momose, Rev. Sci. Instrum. **89**, 113103 (2018).

[127] P. Straňák, L. Ploenes, S. Hofsäss, K. Dulitz, F. Stienkemeier and S. Willitsch, Rev. Sci. Instrum. **92** (10), 103203 (2021).

[128] P.E. Siska, Rev. Mod. Phys. **65**, 337 (1993).

[129] S. Falcinelli, F. Pirani, P. Candori, B.G. Brunetti, J.M. Farrar and F. Vecchiocattivi, Front. Chem. **7**, 445 (2019).

[130] Y. Segev, N. Bibelnik, N. Akerman, Y. Shagam, A. Luski, M. Karpov, J. Narevicius and E. Narevicius, Sci. Adv. **3** (3), e1602258 (2017).

[131] I.C. Lu, W.J. Huang, C. Chaudhuri, W.K. Chen and S.H. Lee, Rev. Sci. Instrum. **78** (8), 083103 (2007).

[132] M. Van Beek and J. Ter Meulen, Chem. Phys. Lett. **337** (4-6), 237 (2001).

[133] K. Ikejiri, H. Ohoyama, Y. Nagamachi, T. Teramoto and T. Kasai, Chem. Phys. Lett. **379** (3-4), 255–260 (2003).

[134] H. Lewandowski, E.R. Hudson, J. Bochinski and J. Ye, Chem. Phys. Lett. **395** (1), 53 (2004).

[135] S. Davis, D.T. Anderson, G. Duxbury and D.J. Nesbitt, J. Chem. Phys. **107** (15), 5661 (1997).

## Bibliography

[136] Z. Ren, M. Qiu, L. Che, D. Dai, X. Wang and X. Yang, Rev. Sci. Instrum. **77** (1), 016102 (2006).

[137] C. Abeysekera, B. Joalland, Y. Shi, A. Kamasah, J.M. Oldham and A.G. Suits, Rev. Sci. Instrum. **85**, 116107 (2014).

[138] L. Ploenes, D. Haas, D. Zhang, S.Y.T. van de Meerakker and S. Willitsch, Rev. Sci. Instr. **87**, 053305 (2016).

[139] U. Kogelschatz, Plasma Chem. Plasma P. **23** (1), 1 (2003).

[140] K. Luria, N. Lavie and U. Even, Rev. Sci. Instrum. **80** (10), 104102 (2009).

[141] R. Brandenburg, Plasma Sources Sci. Technol. **26**, 053001 (2017).

[142] P. Straňák, *Ph.D. thesis*, University of Basel, Basel (in preparation).

[143] B. Yan, P.F.H. Claus, B.G.M. Van Oorschot, L. Gerritsen, A.T.J.B. Eppink, S.Y.T. van de Meerakker and D.H. Parker, Rev. Sci. Instrum. **84** (2), 023102 (2013).

[144] V. Plomp, Z. Gao, T. Cremers and S.Y. van de Meerakker, Phys. Rev. A **99** (3), 033417 (2019).

[145] A. Bogaerts, E. Neyts, R. Gijbels and J. Van der Mullen, Spectrochim. Acta B: Atomic Spectroscopy **57** (4), 609 (2002).

[146] N.S.J. Braithwaite, Plasma Sources Sci. Technol. **9** (4), 517 (2000).

[147] Y.P. Raizer, *Gas Discharge Physics* (Springer, Berlin, 1991).

[148] E.E. Muschlitz Jr, Science **159** (3815), 599 (1968).

[149] J. Grzesiak, T. Momose, F. Stienkemeier, M. Mudrich and K. Dulitz, J. Chem. Phys. **150** (3), 034201 (2019).

[150] D.C. Morton, Q. Wu and G.W.F. Drake, Can. J. Phys **84** (2), 83 (2006).

[151] S.S. Hodgman, R.G. Dall, L.J. Byron, K.G.H. Baldwin, S.J. Buckman and A.G. Truscott, Phys. Rev. Lett. **103** (5), 053002 (2009).

[152] R.S. Van Dyck Jr, C.E. Johnson and H.A. Shugart, Phys. Rev. A **4** (4), 1327 (1971).

[153] E.B. Saloman and C.J. Sansonetti, J. Phys. Chem. Ref. Data **33** (4), 1113 (2004).

[154] M. Zinner, P. Spoden, T. Kraemer, G. Birkl and W. Ertmer, Phys. Rev. A **67** (1), 010501 (2003).

[155] N.E. Small-Warren and L.Y.C. Chiu, Phys. Rev. A **11** (6), 1777 (1975).

[156] E. Fry and W. Williams, Rev. Sci. Instrum. **40** (9), 1141 (1969).

[157] H. Hotop, J. Lorenzen and A. Zastrow, J. Electron. Spectrosc. **23** (3), 347 (1981).

[158] Y. Harada and H. Ozaki, Jpn. J. Appl. Phys. **26**, 1201 (1987).

[159] K. Kato, D.W. Fitzakerley, M.C. George, A.C. Vutha, M. Weel, C.H. Storry, T. Kirchner and E.A. Hessels, Phys. Rev. A **86** (1), 014702 (2012).

[160] F.B. Dunning, T.B. Cook, W.P. West and R.F. Stebbings, Rev. Sci. Instrum. **46** (8), 1072 (1975).

[161] T.D. Gaily, M.J. Coggiola, J.R. Peterson and K.T. Gillen, Rev. Sci. Instrum. **51** (9), 1168 (1980).

[162] J. Guan, V. Behrendt, P. Shen, S. Hofsäss, T. Muthu-Arachchige, J. Grzesiak, F. Stienkemeier and K. Dulitz, Phys. Rev. Appl. **11** (5), 054073 (2019).

[163] C. Weiser and P.E. Siska, Rev. Sci. Instrum. **58** (11), 2124 (1987).

[164] A. Aspect, N. Vansteenkiste, R. Kaiser, H. Haberland and M. Karrais, Chem. Phys. **145** (2), 307 (1990).

[165] J.S. Kienitz, K. Długołęcki, S. Trippel and J. Küpper, J. Chem. Phys. **147**, 024304 (2017).

[166] J.S. Kienitz, *Ph.D. thesis*, University of Hamburg, Hamburg (2016).

[167] B.Y. Chang, R.C. Hoetzlein, J.A. Mueller, J.D. Geiser and P.L. Houston, Rev. Sci. Instrum. **69** (4), 1665 (1998).

[168] D. Townsend, M.P. Minitti and A.G. Suits, Rev. Sci. Instrum. **74**, 2530 (2003).

[169] J. Onvlee, S.N. Vogels, A. von Zastrow, D.H. Parker and S.Y.T. van de Meerakker, Phys. Chem. Chem. Phys. **16** (30), 15768 (2014).

[170] A.E. Cameron and D.F. Eggers J r, Rev. Sci. Instrum. **19** (9), 605 (1948).

[171] V.H. Dibeler, Anal. Chem. **26** (1), 58–65 (1954).

[172] U. Even and B. Dick, Rev. Sci. Instrum. **71** (12), 4421 (2000).

[173] E. de Hoffmann and V. Stroobant, *Mass spectrometry: Principles and Applications*, 3rd ed. (John Wiley & Sons, New York, 2007).

[174] R.J. Cotter, *Time-of-Flight Mass Spectrometry: Instrumentation and Applications in Biological Research*, 1st ed. (American Chemical Society, Washington DC, 1997).

[175] C. Weickhardt, F. Moritz and J. Grotemeyer, Mass Spectrom. Rev. **15** (3), 139 (1996).

[176] B. Mamyrin, Int. J. Mass Spectrom. **206** (3), 251 (2001).

# Bibliography

[177] U. Boesl, Mass Spectrom. Rev. **36** (1), 86 (2017).

[178] D.H. Parker and A.T.J.B. Eppink, J. Chem. Phys. **107** (7), 2357 (1997).

[179] B.J. Whitaker, editor, *Imaging in Molecular Dynamics: Technology and Applications* (Cambridge University Press, Cambridge, 2003).

[180] A.G. Suits, L.S. Bontuyan, P.L. Houston and B.J. Whitaker, J. Chem. Phys. **96** (11), 8618 (1992).

[181] L.S. Bontuyan, A.G. Suits, P.L. Houston and B.J. Whitaker, J. Phys. Chem. **97** (24), 6342 (1993).

[182] A. Chichinin, K.H. Gericke, S. Kauczok and C. Maul, Int. Rev. Phys. Chem. **28** (4), 607 (2009).

[183] D.W. Chandler, P.L. Houston and D.H. Parker, J. Chem. Phys. **147** (1), 013601 (2017).

[184] J.J. Lin, J. Zhou, W. Shiu and K. Liu, Rev. Sci. Instrum. **74** (4), 2495 (2003).

[185] D. Yuan, S. Yu, W. Chen, J. Sang, C. Luo, T. Wang, X. Xu, P. Casavecchia, X. Wang, Z. Sun, D.H. Zhang and X. Yang, Nat. Chem. **10** (6), 653 (2018).

[186] V. Plomp, Z. Gao and S.Y.T. van de Meerakker, Mol. Phys. **119** (1), e1814437 (2021).

[187] J.A. Davies, J.E. LeClaire, R.E. Continetti and C.C. Hayden, J. Chem. Phys. **111** (1), 1 (1999).

[188] A.S. Tremsin, J.V. Vallerga, O.H.W. Siegmund and J.S. Hull, Proc. SPIE **5164**, 113 (2003).

[189] J.H. Jungmann, A. Gijsbertsen, J. Visser, J. Visschers, R.M.A. Heeren and M.J.J. Vrakking, Rev. Sci. Instrum. **81** (10), 103112 (2010).

[190] E. Schrödinger, Phys. Rev. **28** (6), 1049 (1926).

[191] C. Eckart, Phys. Rev. **47** (7), 552 (1935).

[192] W. Gordy and R.L. Cook, *Microwave Molecular Spectra*, 3rd ed. (John Wiley & Sons, New York, 1984).

[193] R.N. Zare, *Angular Momentum* (John Wiley & Sons, New York, 1988).

[194] P.W. Atkins and R.S. Friedman, *Molecular Quantum Mechanics*, 5th ed. (Oxford University Press, Oxford, 2011).

[195] G.W. King, R.M. Hainer and P.C. Cross, J. Chem. Phys. **11** (1), 27 (1943).

[196] J. Küpper, F. Filsinger, G. Meijer and H. Stapelfeldt, in *Methods in Physical Chemistry*, edited by R. Schäfer and P. C. Schmidt, 1st ed., Chap. 1 (Wiley Online Library, Hoboken, 2012), pp. 1–28.

[197] B.S. Ray, Zeitschrift für Physik **78** (1-2), 74 (1932).

[198] Y.P. Chang, F. Filsinger, B.G. Sartakov and J. Küpper, Comp. Phys. Comm. **185**, 339 (2014).

[199] J. Stark, Annalen der Physik **348** (7), 965 (1914).

[200] J. Stark and G. Wendt, Annalen der Physik **348** (7), 983 (1914).

[201] A.L. Surdo, Il Nuovo Cimento **7** (1), 335 (1914).

[202] F. Filsinger, J. Küpper, G. Meijer, L. Holmegaard, J.H. Nielsen, I. Nevo, J.L. Hansen and H. Stapelfeldt, J. Chem. Phys. **131**, 064309 (2009).

[203] S.A. Rangwala, T. Junglen, T. Rieger, P.W. Pinkse and G. Rempe, Phys. Rev. A **67** (4), 043406 (2003).

[204] S. Willitsch, M.T. Bell, A.D. Gingell, S.R. Procter and T.P. Softley, Phys. Rev. Lett. **100** (4), 043203 (2008).

[205] G.E. Chamberlain and J.C. Zorn, Phys. Rev. **129** (2), 677 (1963).

[206] H.S. You, J. Kim, S. Han, D.S. Ahn, J.S. Lim and S.K. Kim, J. Phys. Chem. A **122** (5), 1194 (2018).

[207] S. Trippel, Y.P. Chang, S. Stern, T. Mullins, L. Holmegaard and J. Küpper, Phys. Rev. A **86**, 033202 (2012).

[208] S. Trippel, T. Mullins, N.L. Müller, J.S. Kienitz, J.J. Omiste, H. Stapelfeldt, R. González-Férez and J. Küpper, Phys. Rev. A **89** (5), 051401 (2014).

[209] E.T. Karamatskos, S. Raabe, T. Mullins, A. Trabattoni, P. Stammer, G. Goldsztejn, R.R. Johansen, K. Długołecki, H. Stapelfeldt, M.J.J. Vrakking, S. Trippel, A. Rouzée and J. Küpper, Nat. Commun. **10**, 1 (2019).

[210] J.M.L.J. Reinartz and A. Dymanus, Chem. Phys. Lett. **24**, 346 (1974).

[211] K. Tanaka, H. Ito, K. Harada and T. Tanaka, J. Chem. Phys. **80**, 5893 (1984).

[212] K. Kim and K. Jordan, Chem. Phys. Lett. **241** (1-2), 39 (1995).

[213] S.J. Humphrey and D.W. Pratt, J. Chem. Phys. **99** (7), 5078 (1993).

[214] W. Caminati, S. Melandri and L.B. Favero, J. Chem. Phys. **100** (12), 8569 (1994).

[215] T.D. Märk and H.J. Oskam, Phys. Rev. A **4**, 14452 (1971).

# Bibliography

[216] F. Massines, P. Segur, N. Gherardi, C. Khamphan and A. Ricard, Surf. Coat. Technol. **174**, 8 (2003).

[217] Z. Chang, N. Jiang, G. Zhang and Z. Cao, J. Appl. Phys. **115** (10), 103301 (2014).

[218] N. Mamedov, N. Shchitov, D. Kolodko, I. Sorokin and D. Sinel'nikov, Tech. Phys. **63** (8), 1129–1136 (2018).

[219] M. Alagia, N. Balucani, P. Candori, S. Falcinelli, F. Pirani, R. Richter, M. Rosi, S. Stranges and F. Vecchiocattivi, Rend. Lincei **24** (1), 53 (2013).

[220] S. Falcinelli, F. Pirani and F. Vecchiocattivi, Atmosphere **6** (3), 299 (2015).

[221] A. Niehaus, Ber. Bunsenges. Phys. Chem. **77** (8), 632 (1973).

[222] B. Brunetti and F. Vecchiocattivi, in *Cluster Ions*, edited by C. Y. Ng, T. Baer and I. Powis (John Wiley and Sons Ltd, New York, 1993), p. 360–445.

[223] F.M. Penning, Naturwissenschaften **15** (40), 818 (1927).

[224] W.H. Miller, J. Chem. Phys. **52** (7), 3563 (1970).

[225] W. Miller and H. Morgner, J. Chem. Phys. **67** (11), 4923 (1977).

[226] R.W. Gregor and P.E. Siska, J. Chem. Phys. **74** (2), 1078 (1981).

[227] S. Falcinelli, J.M. Farrar, F. Vecchiocattivi and F. Pirani, Acc. Chem. Res. **53**, 2248 (2020).

[228] H. Hotop and A. Niehaus, Zeitschrift für Physik **228** (1), 68 (1969).

[229] K. Ohno, H. Mutoh and Y. Harada, J. Am. Chem. Soc. **105** (14), 4555 (1983).

[230] E. Lavert-Ofir, Y. Shagam, A.B. Henson, S. Gersten, J. Kłos, P.S. Żuchowski, J. Narevicius and E. Narevicius, Nat. Chem. **6** (4), 332 (2014).

[231] J. Jankunas, K. Jachymski, M. Hapka and A. Osterwalder, J. Chem. Phys. **142** (16), 164305 (2015).

[232] J. Zou, S.D. Gordon and A. Osterwalder, Phys. Rev. Lett. **123** (13), 133401 (2019).

[233] N. Bibelnik, S. Gersten, A.B. Henson, E. Lavert-Ofir, Y. Shagam, W. Skomorowski, C.P. Koch and E. Narevicius, Mol. Phys. **117** (15-16), 2128 (2019).

[234] K. Dulitz, T. Sixt, J. Guan, J. Grzesiak, M. Debatin and F. Stienkemeier, Phys. Rev. A **102**, 022818 (2020).

[235] S. Tanteri, S.D. Gordon, J. Zou and A. Osterwalder, J. Phys. Chem. A **125** (46), 10021 (2021).

[236] Y. Shagam, A. Klein, W. Skomorowski, R. Yun, V. Averbukh, C.P. Koch and E. Narevicius, Nat. Chem. **7** (11), 921 (2015).

[237] D. Watanabe, H. Ohoyama, T. Matsumura and T. Kasai, J. Chem. Phys. **125** (8), 084316 (2006).

[238] S.D. Gordon, J. Zou, S. Tanteri, J. Jankunas and A. Osterwalder, Phys. Rev. Lett. **119** (5), 053001 (2017).

[239] J. Zou, S.D.S. Gordon, S. Tanteri and A. Osterwalder, J Chem. Phys. **148** (16), 164310 (2018).

[240] M.S. de Vries, G.W. Tyndall, C.L. Cobb and R.M. Martin, J. Chem. Phys. **86** (5), 2653 (1987).

[241] H. Ohoyama, H. Kawaguchi, M. Yamato, T. Kasai, B. Brunetti and F. Vecchiocattivi, Chem. Phys. Lett. **313** (3-4), 484 (1999).

[242] M. Yamato, S. Okada, V. Wei-Keh Wu, H. Ohoyama and T. Kasai, J. Chem. Phys. **113** (16), 6673 (2000).

[243] M. Yamato, H. Ohoyama and T. Kasai, J. Phys. Chem. A **105** (13), 2967 (2001).

[244] S. Okada, H. Ohoyama and T. Kasai, Chem. Phys. Lett. **355** (1-2), 77 (2002).

[245] K. Koizumi, H. Ohoyama and T. Kasai, Chem. Phys. Lett. **378** (5-6), 486 (2003).

[246] S. Okada, H. Ohoyama and T. Kasai, J. Chem. Phys. **119** (14), 7131 (2003).

[247] M.B. Arfa, B. Lescop, M. Cherid, B. Brunetti, P. Candori, D. Malfatti, S. Falcinelli and F. Vecchiocattivi, Chem. Phys. Lett. **308** (1-2), 71 (1999).

[248] F. Biondini, B.G. Brunetti, P. Candori, F. De Angelis, S. Falcinelli, F. Tarantelli, F. Pirani and F. Vecchiocattivi, J. Chem. Phys. **122** (16), 164308 (2005).

[249] N. Balucani, A. Bartocci, B. Brunetti, P. Candori, S. Falcinelli, F. Palazzetti, F. Pirani and F. Vecchiocattivi, Chem. Phys. Lett. **546**, 34 (2012).

[250] B. Brunetti, P. Candori, D. Cappelletti, S. Falcinelli, F. Pirani, D. Stranges and F. Vecchiocattivi, Chem. Phys. Lett. **539**, 19 (2012).

[251] B.G. Brunetti, P. Candori, S. Falcinelli, F. Pirani and F. Vecchiocattivi, J. Chem. Phys. **139** (16), 164305 (2013).

[252] S. Falcinelli, A. Bartocci, P. Candori, F. Pirani and F. Vecchiocattivi, Chem. Phys. Lett. **614**, 171 (2014).

[253] S. Falcinelli, A. Bartocci, S. Cavalli, F. Pirani and F. Vecchiocattivi, J. Chem. Phys. **143** (16), 164306 (2015).

# Bibliography

[254] S. Falcinelli, M. Rosi, S. Cavalli, F. Pirani and F. Vecchiocattivi, Chem. Eur. J. **22** (35), 12518 (2016).

[255] S. Falcinelli, A. Bartocci, S. Cavalli, F. Pirani and F. Vecchiocattivi, hem. Eur. J. **22** (2), 764 (2016).

[256] S. Falcinelli, F. Vecchiocattivi and F. Pirani, Commun. Chem. **3** (1), 1 (2020).

[257] S. Falcinelli, F. Vecchiocattivi, J.M. Farrar, B.G. Brunetti, S. Cavalli and F. Pirani, Chem. Phys. Lett. **778**, 138813 (2021).

[258] S. Falcinelli, F. Vecchiocattivi, J.M. Farrar and F. Pirani, J. Phys. Chem. A **125** (16), 3307 (2021).

[259] V. Čermák, J. Electron Spectrosc. Relat. Phenom. **9**, 419 (1976).

[260] C.E. Brion and D.S.C. Yee, J. Electron Spectrosc. Relat. Phenom. **12**, 77 (1977).

[261] D.W. Setser, Int. J. Mass Spectrom. Ion Phys. **11**, 301 (1971).

[262] M. Tsuji, M. Matsuo and Y. Nishimura, Int. J. Mass Spectrom. Ion Phys. **34**, 273 (1980).

[263] N. Kishimoto, T. Horio, S. Maeda and K. Ohno, Chem. Phys. Lett. **379**, 332 (2003).

[264] T. Horio, S. Maeda, N. Kishimoto and K. Ohno, J. Phys. Chem. A **110**, 11010 (2006).

[265] C. Moore, Atomic Energy Levels, Natl. Bur. Stand. (US) Circ. No. **467** (1949).

[266] R. Frey, B. Gotchev, W.B. Peatman, H. Pollak and E.W. Schlag, Int. J. Mass Spectrom. Ion Processes **26** (2), 137 (1978).

[267] P. Krupenie, Natl. Stand. Ref. Data Ser., Natl. Bur. Std. (US) **5** (1966).

[268] N. Jonathan, A. Morris, M. Okuda, K.J. Ross and D.J. Smith, Faraday Discuss. Chem. Soc. **54**, 48 (1972).

[269] V.H. Dibeler and J.A. Walker, J. Opt. Soc. Am. **57** (8), 1007 (1967).

[270] L.C. Lee and D.L. Judge, J. Chem. Phys. **63**, 2782 (1975).

[271] R.H. Neynaber and G.D. Magnuson, Phys. Rev. A **14** (3), 961 (1976).

[272] B. Brunetti, F. Vecchiocattivi and G.G. Volpi, J. Chem. Phys. **84** (1), 53 (1986).

[273] C.A. Arango, M. Shapiro and P. Brumer, J. Chem. Phys. **125** (9), 094315 (2006).

[274] J.S. Kienitz, S. Trippel, T. Mullins, K. Długołęcki, R. González-Férez and J. Küpper, Chem. Phys. Chem. **17**, 3740 (2016).

[275] J. Jankunas, B. Bertsche, K. Jachymski, M. Hapka and A. Osterwalder, J. Chem. Phys. **140** (24), 244302 (2014).

[276] S. Morse, M. Takahashi, J.H.D. Eland and L. Karlsson, Int. J. Mass Spectrom. **184** (1), 67 (1999).

[277] M.J. Hubin-Franskin, J. Delwiche, P.M. Guyon, M. Richard-Viard, M. Lavollée, O. Dutuit, J.M. Robbe and J.P. Flament, Chem. Phys. **209** (2-3), 143 (1996).

[278] W. Chen, M. Hochlaf, P. Rosmus, G. He and C. Ng, J. Chem. Phys. **116** (13), 5612 (2002).

[279] D.M. Hirst, Mol. Phys. **104** (1), 55 (2006).

[280] J. Eland, Int. J. Mass Spectrom. Ion Phys. **12** (4), 389 (1973).

[281] B. Brehm, R. Frey, A. Küstler and J.H.D. Eland, Int. J. Mass Spectrom. Ion Phys. **13** (3), 251 (1974).

[282] R.G. Orth and R.C. Dunbar, Chem. Phys. **45** (2), 195 (1980).

[283] J.P. Maier and F. Thommen, Chem. Phys. **51** (3), 319 (1980).

[284] Y. Hikosaka, H. Hattori, T. Hikida and K. Mitsuke, J. Chem. Phys. **107** (8), 2950 (1997).

[285] S. Stimson, M. Evans, C. Ng, C.W. Hsu, P. Heimann, C. Destandau, G. Chambaud and P. Rosmus, J. Chem. Phys. **108** (15), 6205 (1998).

[286] C. Chang, C.Y. Luo and K. Liu, J. Phys. Chem. A **109** (6), 1022 (2005).

[287] S. Falcinelli, F. Vecchiocattivi and F. Pirani, Phys. Rev. Lett. **121** (16), 163403 (2018).

[288] S. Falcinelli, F. Vecchiocattivi and F. Pirani, Sci. Rep. **11** (1), 1 (2021).

[289] E.L. Eliel and S.H. Wilen, *Stereochemistry of Organic Compounds* (, , 1994).

[290] H. Frauenfelder, S.G. Sligar and P.G. Wolynes, Science **254** (5038), 1598 (1991).

[291] E.G. Robertson and J.P. Simons, Phys. Chem. Chem. Phys. **3** (1), 1 (2001).

[292] L. Khriachtchev, A. Domanskaya, K. Marushkevich, M. Räsänen, B. Grigorenko, A. Ermilov, N. Andrijchenko and A. Nemukhin, J. Phys. Chem. A **113** (29), 8143 (2009).

[293] C.A. Taatjes, O. Welz, A.J. Eskola, J.D. Savee, A.M. Scheer, D.E. Shallcross, B. Rotavera, E.P. Lee, J.M. Dyke, D.K. Mok, D.L. Osbornand and C.J. Percival, Science **340** (6129), 177 (2013).

[294] H.Y. Lin, Y.H. Huang, X. Wang, J.M. Bowman, Y. Nishimura, H.A. Witek and Y.P. Lee, Nat. Commun. **6** (1), 1 (2015).

# Bibliography

[295] A. Oikawa, H. Abe, N. Mikami and M. Ito, Chem. Phys. Lett. **116** (1), 50 (1985).

[296] N. Kishimoto, M. Furuhashi and K. Ohno, J. Electron Spectrosc. Relat. Phenom. **113** (1), 35 (2000).

[297] N. Kishimoto, K. Okamura and K. Ohno, J. Chem. Phys. **120** (23), 11062 (2004).

[298] M. Yamazaki, S. Maeda, N. Kishimoto and K. Ohno, J. Chem. Phys. **122** (4), 044303 (2005).

[299] K. Imura, N. Kishimoto and K. Ohno, J. Phys. Chem. A **105** (40), 9111 (2001).

[300] K. Imura, N. Kishimoto and K. Ohno, J. Phys. Chem. A **105** (25), 6073 (2001).

[301] M. Akopyan, V. Kleimenov and A. Feofilov, High Energy Chem. **34** (2), 107 (2000).

[302] I. Hassan, J. Pavlov, R. Errabelli and A.B. Attygalle, J. Am. Soc. Mass Spectrom. **28** (2), 270 (2016).

[303] W.L. Holstein, M.R. Hammer, G.F. Metha and M.A. Buntine, Int. J. Mass Spectrom. **207** (1-2), 1 (2001).

[304] P. Casavecchia, F. Leonori, N. Balucani, R. Petrucci, G. Capozza and E. Segoloni, Phys. Chem. Chem. Phys. **11** (1), 46 (2009).

[305] B.C. Dian, A. Longarte and T.S. Zwier, Science **296** (5577), 2369 (2002).

[306] D.M. Hercules, R. Day, K. Balasanmugam, T.A. Dang and C. Li, Anal. Chem. **54** (2), 280 (1982).

[307] A.M. Rijs and J. Oomens, editors, *IR Spectroscopic Techniques to Study Isolated Biomolecules* (Springer, Berlin, 2015).

# List of Figures

## List of Figures

# List of Tables